

UNIVERSITY OF SÃO PAULO
SÃO CARLOS SCHOOL OF ENGINEERING

SEYED REZA AMINI NIAKI

Effects of inter particle friction on the meso-scale hydrodynamics of dense
gas-solid fluidized flows

São Carlos

2018

SEYED REZA AMINI NIAKI

Effects of inter particle friction on the meso-scale hydrodynamics of dense
gas-solid fluidized flows

Thesis submitted to the São Carlos School of
Engineering, University of São Paulo, for the degree
of Doctor of Science in Mechanical Engineering.

Concentration area: Thermal and Fluid Mechanics

Supervisor: Prof. Dr. Fernando E. Milioli

THIS IS THE CORRECTED VERSION.
THE ORIGINAL THESIS CAN BE FOUND
AT THE MECHANICAL
ENGINEERING DEPARTMENT AT EESC-USP

São Carlos

2018

I AUTHORIZE THE TOTAL OR PARTIAL REPRODUCTION OF THIS WORK,
THROUGH ANY CONVENTIONAL OR ELECTRONIC MEANS, FOR STUDY AND
RESEARCH PURPOSES, SINCE THE SOURCE IS CITED.

Catalog card prepared by Patron Service at "Prof. Dr. Sergio
Rodrigues Fontes" Library at EESC/USP

A517e Amini Niaki, Seyed Reza
Effects of inter particle friction on the meso-scale
hydrodynamics of dense gas-solid fluidized flows / Seyed
Reza Amini Niaki; Thesis directed by Fernando Eduardo
. Milioli. -- São Carlos, 2018

 Doctorate (Thesis) - Graduate Program in Mechanical
Engineering and Research Area in Thermal and Fluids of the
School of Engineering of São Carlos at University of São
Paulo, 2018.

 1. Two-fluid modeling. 2. Sub-grid modeling. 3. Highly
resolved simulation. 4. Gas-solid flow. 5. Fluidization.
6. Particle-particle interaction. I. Title.

SEYED REZA AMINI NIAKI

Efeitos da fricção inter-partículas na hidrodinâmica de meso-escala de escoamentos
gás-sólido fluidizados densos

Tese apresentada à Escola de Engenharia de São Carlos da Universidade de São Paulo, para obtenção do título de Doutor em Ciências – Programa de Pós – Graduação em Engenharia Mecânica.

Área de concentração: Térmica e Fluidos

Orientador: Prof. Dr. Fernando E. Milioli

ESTE EXEMPLAR TRATA – SE DA
VERSÃO CORRIGIDA.
A VERSÃO ORIGINAL ENCONTRA-
SE DISPONÍVEL JUNTO AO
DEPARTAMENTO DE
ENGENHARIA MECANICA DA
EESC-USP.

São Carlos

2018

AUTORIZO A REPRODUÇÃO E DIVULGAÇÃO TOTAL OU PARCIAL DESTES TRABALHOS, POR QUALQUER MEIO CONVENCIONAL OU ELETRÔNICO, PARA FINS DE ESTUDO E PESQUISA, DESDE QUE CITADA A FONTE.

Ficha catalográfica elaborada pela Biblioteca Prof. Dr. Sérgio Rodrigues
Fontes da EESC/USP

A517e Amini Niaki, Seyed Reza
Efeitos da fricção inter-partículas na hidrodinâmica de meso-escala de escoamentos gás-sólido fluidizados densos / Seyed Reza Amini Niaki ; orientador Fernando Eduardo Milioli. -- São Carlos, 2018.

Tese (Doutorado) - Programa de Pós-Graduação em Engenharia Mecânica e Área de Concentração em Termociências e Mecânica dos Fluidos -- Escola de Engenharia de São Carlos da Universidade de São Paulo, 2018.

1. Modelagem de dois fluidos. 2. Modelagem sub-malha.
3. Simulação altamente resolvida. 4. Escoamento gás-sólido.
5. Fluidização. 6. Interações partícula-partícula.
I. Título.

FOLHA DE JULGAMENTO

Candidato: Bacharel **SEYED REZA AMINI NIAKI**.

Título da tese: "Efeitos da fricção inter-partículas na hidrodinâmica de meso-escala de escoamentos gás-sólido fluidizados densos".

Data da defesa: 21/11/2018.

Comissão Julgadora:

Resultado:

Prof. Dr. **Fernando Eduardo Milioli**
(Orientador)
(Escola de Engenharia de São Carlos/EESC)

Aprovado

Prof. Associado **Luben Cabezas Gómez**
(Escola de Engenharia de São Carlos/EESC)

Aprovado

Prof. Titular **Antonio Castelo Filho**
(Instituto de Ciências Matemáticas e de Computação/ICMC-USP)

APROVADO

Prof. Dr. **Rodrigo Béttega**
(Universidade Federal de São Carlos/UFSCar)

APROVADO

Prof. Dr. **Anderson Antonio Ubices de Moraes**
(Universidade Federal de São Carlos/UFSCar)

APROVADO

Coordenador do Programa de Pós-Graduação em Engenharia Mecânica:
Prof. Associado **Gherhardt Ribatski**

Decano da Comissão de Pós-Graduação:
Prof. Associado **Luís Fernando Costa Alberto**

ACKNOWLEDGEMENTS

Firstly, I would like to express my sincere gratitude to my advisor Prof. Fernando Eduardo Milioli for the continuous support of my Ph.D. study and related research, for his patience, motivation, and immense knowledge. His guidance helped me in all the time of research and writing of this thesis.

I am also grateful to Dra. Chris Milioli for her invaluable advices and constructive suggestions during these four years. In particular, I am very grateful for her inestimable assistance regarding the MFIX code implementations and modifications, as well as regarding the filtering procedure that was applied

My sincere thanks also goes to Prof. Gherhardt Ribatski, Prof. Luben Cabezas Gomez, and Prof. Oscar Rodriguez for all the scientific discussions we had and for teaching their disciplines.

I thank my fellow office mates Joseph Mouallem and Norman Chavez in for the stimulating discussions, for the weeks we were working together before deadlines, and for all the fun we have had in the last four years.

I will forever be thankful to Fatemeh Gholi Zadeh. He has been always providing me encouragements and guidance through my academic and professional career.

Last but not the least, I would like to thank my parents Mehrmah and Mahmood and to my brother and sister, Bahador and Mona for supporting me spiritually throughout writing this thesis and my life in general. I literally cannot put in words how much being on my side means to me.

ABSTRACT

AMINI NIKAI, S. R. **Effects of inter particle friction on the meso-scale hydrodynamics of dense gas-solid fluidized flows**. 2018. 138p. Thesis (Doctor of Science) – São Carlos School of Engineering, University of São Paulo, São Carlos, 2018.

Gas-solid fluidized bed reactors are widely applied in chemical and energy industries, and their design and scale-up are virtually empirical, extremely expensive and time consuming. This scenario has motivated the development of alternative theoretical tools, and two-fluid modeling, where gas and particulate are both treated as interpenetrating continuum phases, has appeared as a most promising approach. Owing to the large domains to be resolved in real-scale fluidized bed reactors, only filtered modeling approaches are feasible, and closure models become necessary to recover sub-grid effects that are filtered by the very coarse numerical grids that are imposed owing to computational limitations. Those closure models, which in hydrodynamic formulations account for filtered interphase momentum exchanges and filtered and residual stresses in the phases, can be derived from results of highly resolved simulations (HRS) performed over small size domains under refined numerical grids. One widely practiced approach consists of applying two-fluid modeling under micro-scale defined closures, generally known as microscopic two-fluid modeling. This approach includes microscopic closures for solid phase stresses derived from the kinetic theory of granular flows (KTGF), which accounts for kinetic-collisional effects only, and is adequate to dilute flows. Otherwise, the conventional KTGF does not account for interparticle friction effects, and its application to dense flow conditions is quite questionable. In this work a literature available modified version of KTGF is applied which also accounts for interparticle friction, and highly resolved simulations are performed for dense flow conditions in order to evaluate the effects of friction over relevant filtered parameters (namely effective drag coefficient, filtered and residual stresses). Ranges of domain average solid volume fractions and gas Reynolds numbers are considered (macro-scale conditions) embracing dense gas-solid fluidized flows from suspensions up to pneumatic transport. The MFIX open source code is used in all the simulations, which are performed over 2D periodical domains for a unique monodisperse particulate. The HRS results (i.e. meso-scale flow fields) are filtered over regions compatible with grid sizes in large scale simulations, and the relevant filtered parameters of concern are derived and classified by

ranges of other filtered parameters taken as independent variables (filtered solid volume fraction, filtered slip velocity, and filtered kinetic energy of solid velocity fluctuations, which are referred to as markers). Results show that the relevant filtered parameters of concern are well correlated to all of those filtered markers, and also to all of the imposed macro-scale conditions. Otherwise, interparticle friction showed no significant effects over any filtered parameter. It is recognized that this issue clearly requires further investigation notably regarding the suitability of the markers that were assumed for classifying the filtered results. The current work is intended as a contribution for future developments of more accurate closure models for large scale simulations of gas-solid fluidized flows.

Keywords: Two-fluid modeling, Sub-grid modeling, Highly resolved simulation, Gas-solid flow, Fluidization, Particle-particle interaction.

RESUMO

AMINI NIKAI, S. R. **Efeitos da fricção inter-partículas na hidrodinâmica de meso-escala de escoamentos gás-sólido fluidizados densos**. 2018. 138p. Tese (Doutorado) – Escola de Engenharia de São Carlos, Universidade de São Paulo, São Carlos, 2018.

Reatores de leito fluidizado de escoamento gás-sólido são largamente utilizados nas indústrias química e de energia, e o seu projeto e escalonamento são virtualmente empíricos, extremamente caros e demorados. Este cenário tem motivado o desenvolvimento de ferramentas teóricas alternativas, e a modelagem de dois fluidos, onde gás e particulado são ambos tratados com fases contínuas interpenetrantes, tem surgido como uma aproximação muito promissora. Devido aos grandes domínios a serem resolvidos em reatores de leito fluidizado de escala real, apenas aproximações de modelagem filtradas são viáveis, e modelos de fechamento tornam-se necessários para recuperar efeitos sub-malha que são filtrados pelas malhas numéricas grosseiras que são impostas devido as limitações computacionais. Estes modelos de fechamento, que em formulações hidrodinâmicas respondem principalmente por trocas de momentum filtradas entre fases e tensões filtradas e residuais nas fases, podem ser obtidos de resultados de simulações altamente resolvidas (SAR) realizadas em domínios de dimensões reduzidas sob malhas numéricas refinadas. Uma aproximação largamente praticada consiste na aplicação de modelagem de dois fluidos sob fechamentos definidos na micro-escala, genericamente conhecida como modelagem microscópica de dois fluidos. Esta aproximação inclui fechamentos microscópicos para tensões da fase sólida obtidos da teoria cinética dos escoamentos granulares (TCEG), que considera apenas efeitos cinéticos-colisionais, e é adequada para escoamentos diluídos. Por outro lado, a TCEG convencional não leva em conta efeitos de fricção interpartículas, e sua aplicação para condições densas de escoamento é bastante questionável. Neste trabalho aplica-se uma versão modificada da TCEG disponível na literatura que também leva em conta fricção interpartículas, e simulações altamente resolvidas são realizadas para condições de escoamentos densos visando avaliar os efeitos da fricção sobre os parâmetros filtrados relevantes (coeficiente de arrasto efetivo, tensões filtradas e residuais). Considera-se faixas de frações volumétricas de sólido e números de Reynolds do gás médios no domínio (condições de macro-escala) abrangendo escoamentos gás-sólido fluidizados densos desde suspensões até transporte pneumático. O código aberto MFIX é utilizado

em todas as simulações, que foram executadas sobre domínios periódicos 2D para um único particulado monodisperso. Os resultados das SAR (i.e., campos de escoamento de meso-escala) foram filtrados sobre regiões compatíveis com tamanhos de malha praticados em simulações de grandes escalas, e os parâmetros filtrados relevantes de interesse são calculados e classificados por faixas de outros parâmetros filtrados tomados como variáveis independentes (fração volumétrica de sólido filtrada, velocidade de deslizamento filtrada, e energia cinética das flutuações de velocidade da fase sólida filtrada, que são referidos como marcadores). Os resultados mostram que os parâmetros filtrados relevantes de interesse são bem correlacionados com todos os marcadores, e também com todas as condições de macro-escala impostas. Por outro lado, a fricção interpartículas não mostrou efeitos significativos sobre qualquer parâmetro filtrado. Reconhece-se que este aspecto claramente requer investigações adicionais, notadamente com respeito à adequação dos marcadores que foram considerados para classificação dos resultados filtrados. O trabalho corrente é posto como uma contribuição para o desenvolvimento futuro de modelos de fechamento mais acurados para simulações de grandes escalas de escoamentos gás-sólido fluidizados.

Palavras-chave: Modelagem de dois fluidos, Modelagem sub-malha, Simulação altamente resolvida, Escoamento gás-sólido, Fluidização, Interações partícula-partícula

LIST OF FIGURES

Figure 1 – Schematic representation of gas fluidized beds in different regimes.....	33
Figure 2 – Schematics of the bin discharge problem.....	53
Figure 3 – Snapshot of the bin discharge.	54
Figure 4 – Solid discharge rate in g/s as a function of time (s).	55
Figure 5 – Snapshot of the particle volume fraction field.	58
Figure 6 – Three-markers binning procedure (for particular filter size, $\langle \phi_s \rangle$ and $\langle \text{Re}_g \rangle / \langle \text{Re}_g \rangle_{susp}$)	59
Figure 7 – Time evolution of the domain average axial gas velocity in the simulation for $\langle \phi_s \rangle = 0.35$ and $\langle \text{Re}_g \rangle / \langle \text{Re}_g \rangle_{susp} = 1$	62
Figure 8 – Plots of solid volume fraction in the domain inside the statistical steady state regime, for simulations with dense domain average solid fractions $\langle \phi_s \rangle = 0.35, 0.45$ and 0.50 (columns), and gas Reynolds number ratios $\langle \text{Re}_g \rangle / \langle \text{Re}_g \rangle_{susp} = 1, 8.15, 16.30$ and 24.45 (rows), and $C_f = 0$. (blue and red related to solid and gas phase, respectively).	63
Figure 9 – Drag Coefficient Correction, H , as a function of the filtered solid volume fraction $\bar{\phi}_s$ for the domain average solid volume fractions $\langle \phi_s \rangle = 0.35, 0.45$ and 0.50 and for gas Reynolds number ratios $\langle \text{Re}_g \rangle / \langle \text{Re}_g \rangle_{susp} = 1$ and 8.15 . The results stand for different dimensionless filtered axial slip velocities \tilde{v}_{slip} / v_t (black and red), for the dimensionless filter size $\Delta_f / (v_t^2 / g) = 4.112$, and for various dimensionless filtered kinetic energy of the solid velocity fluctuations k_s / v_t^2 (with different thickness). All graphs for $C_f = 0$	65
Figure 10 – Dimensionless filtered solid pressure, $P_{fil,s} / (\rho_s v_t^2)$, as a function of the filtered solid volume fraction $\bar{\phi}_s$ for the domain average solid volume fractions $\langle \phi_s \rangle = 0.35, 0.45$ and 0.50 and for gas Reynolds number ratios $\langle \text{Re}_g \rangle / \langle \text{Re}_g \rangle_{susp} = 1$ and 8.15 . The results stand for different	

dimensionless filtered axial slip velocities \tilde{v}_{slip}/v_t (black and blue), for the dimensionless filter size $\Delta_f/(v_t^2/g)=4.112$, and for various dimensionless filtered kinetic energy of the solid velocity fluctuations k_s/v_t^2 (with different thickness). All graphs for $C_f = 0$ 69

Figure 11 – Dimensionless filtered solid dynamic viscosities $\mu_{fil,s}/(\rho_s v_t^3/g)$, as a function of the filtered solid volume fraction $\bar{\phi}_s$ for the domain average solid volume fractions $\langle\phi_s\rangle = 0.35, 0.45$ and 0.50 and for gas Reynolds number ratios $\langle Re_g \rangle / \langle Re_g \rangle_{susp} = 1$ and 8.15 . The results stand for different dimensionless filtered axial slip velocities \tilde{v}_{slip}/v_t (black and blue), for the dimensionless filter size $\Delta_f/(v_t^2/g)=4.112$, and for various dimensionless filtered kinetic energy of the solid velocity fluctuations k_s/v_t^2 (with different thickness). All graphs for $C_f = 0$ 72

Figure 12 – Dimensionless residual solid pressure, $P_{res,s}/(\rho_s v_t^2)$, as a function of the filtered solid volume fraction $\bar{\phi}_s$ for the domain average solid volume fractions $\langle\phi_s\rangle = 0.35, 0.45$ and 0.50 and for gas Reynolds number ratios $\langle Re_g \rangle / \langle Re_g \rangle_{susp} = 1$ and 8.15 . The results stand for different dimensionless filtered axial slip velocities \tilde{v}_{slip}/v_t (smaller: black and bigger: red), for the dimensionless filter size $\Delta_f/(v_t^2/g)=4.112$, and for various dimensionless filtered kinetic energy of the solid velocity fluctuations k_s/v_t^2 (with different thickness). All graphs for $C_f = 0$ 76

Figure 13 – Dimensionless residual solid dynamic viscosities, $\mu_{res,s}/(\rho_s v_t^3/g)$, as a function of the filtered solid volume fraction $\bar{\phi}_s$ for the domain average solid volume fractions $\langle\phi_s\rangle = 0.35, 0.45$ and 0.50 and for gas Reynolds number ratios $\langle Re_g \rangle / \langle Re_g \rangle_{susp} = 1$ and 8.15 . The results stand for different dimensionless filtered axial slip velocities \tilde{v}_{slip}/v_t (smaller: black and bigger: red), for the dimensionless filter size $\Delta_f/(v_t^2/g)=4.112$, and for various dimensionless filtered kinetic energy of the solid velocity fluctuations k_s/v_t^2 (with different thickness). All graphs for $C_f = 0$ 79

Figure 14 – Drag Coefficient Correction, H , as a function of the filtered solid volume fraction $\bar{\phi}_s$ for the domain average solid volume fractions $\langle\phi_s\rangle = 0.35, 0.45$ and 0.50 and for gas Reynolds number ratios $\langle Re_g \rangle / \langle Re_g \rangle_{susp} = 1$ and 8.15 . The results stand for particular dimensionless filtered

axial slip velocities \tilde{v}_{slip}/v_t , for the dimensionless filter size $\Delta f/(v_t^2/g)=4.112$, and two different interparticle friction coefficient, $C_f=0$ (full lines) and $C_f=0.3$ (dash lines). 83

Figure 15 – Dimensionless filtered solid pressure, $P_{fil,s}/(\rho_s v_t^2)$, as a function of the filtered solid volume fraction $\bar{\phi}_s$ for the domain average solid volume fractions $\langle\phi_s\rangle=0.35, 0.45$ and 0.50 and for gas Reynolds number ratios $\langle Re_g \rangle/\langle Re_g \rangle_{susp}=1$ and 8.15 . The results stand for particular dimensionless filtered axial slip velocities \tilde{v}_{slip}/v_t , for the dimensionless filter size $\Delta f/(v_t^2/g)=4.112$, and two different interparticle friction coefficient, $C_f=0$ (full lines) and $C_f=0.3$ (dash lines). 86

Figure 16 – Dimensionless filtered solid dynamic viscosities, $\mu_{fil,s}/(\rho_s v_t^3/g)$, as a function of the filtered solid volume fraction $\bar{\phi}_s$ for the domain average solid volume fractions $\langle\phi_s\rangle=0.35, 0.45$ and 0.50 and for gas Reynolds number ratios $\langle Re_g \rangle/\langle Re_g \rangle_{susp}=1$ and 8.15 . The results stand for particular dimensionless filtered axial slip velocities \tilde{v}_{slip}/v_t , for the dimensionless filter size $\Delta f/(v_t^2/g)=4.112$, and two different interparticle friction coefficient, $C_f=0$ (full lines) and $C_f=0.3$ (dash lines). 89

Figure 17 – Dimensionless residual solid pressure, $P_{res,s}/(\rho_s v_t^2)$, as a function of the filtered solid volume fraction $\bar{\phi}_s$ for the domain average solid volume fractions $\langle\phi_s\rangle=0.35, 0.45$ and 0.50 and for gas Reynolds number ratios $\langle Re_g \rangle/\langle Re_g \rangle_{susp}=1$ and 8.15 . The results stand for particular dimensionless filtered axial slip velocities \tilde{v}_{slip}/v_t , for the dimensionless filter size $\Delta f/(v_t^2/g)=4.112$, and two different interparticle friction coefficients, $C_f=0$ and 0.3 92

Figure 18 – Dimensionless residual solid dynamic viscosities, $\mu_{res,s}/(\rho_s v_t^3/g)$, as a function of the filtered solid volume fraction $\bar{\phi}_s$ for the domain average solid volume fractions $\langle\phi_s\rangle=0.35, 0.45$ and 0.50 and for gas Reynolds number ratios $\langle Re_g \rangle/\langle Re_g \rangle_{susp}=1$ and 8.15 . The results stand for particular dimensionless filtered axial slip velocities \tilde{v}_{slip}/v_t , for the dimensionless filter size $\Delta f/(v_t^2/g)=4.112$, and two different interparticle friction coefficient, $C_f=0$ (full lines) and $C_f=0.3$ (dash lines). 95

Figure 19 – Drag Coefficient Correction, H , as a function of the filtered solid volume fraction $\bar{\phi}_s$, for the domain average solid volume fractions $\langle\phi_s\rangle = 0.35, 0.45$ and 0.50 and for gas Reynolds number ratios $\langle Re_g \rangle / \langle Re_g \rangle_{susp} = 16.30$ and 24.45 . The results stand for different dimensionless filtered axial slip velocities \tilde{v}_{slip} / v_t (black and red), for the dimensionless filter size $\Delta_f / (v_t^2 / g) = 4.112$, and for various dimensionless filtered kinetic energy of the solid velocity fluctuations k_s / v_t^2 (with different thickness). All graphs for $C_f = 0$ 108

Figure 20 – Dimensionless filtered solid dynamic viscosities $P_{fil,s} / (\rho_s v_t^2)$, as a function of the filtered solid volume fraction $\bar{\phi}_s$ for the domain average solid volume fractions $\langle\phi_s\rangle = 0.35, 0.45$ and 0.50 and for gas Reynolds number ratios $\langle Re_g \rangle / \langle Re_g \rangle_{susp} = 16.30$ and 24.45 . The results stand for different dimensionless filtered axial slip velocities \tilde{v}_{slip} / v_t (black and blue), for the dimensionless filter size $\Delta_f / (v_t^2 / g) = 4.112$, and for various dimensionless filtered kinetic energy of the solid velocity fluctuations k_s / v_t^2 (with different thickness). All graphs for $C_f = 0$ 111

Figure 21 – Dimensionless filtered solid dynamic viscosities $\mu_{fil,s} / (\rho_s v_t^3 / g)$, as a function of the filtered solid volume fraction $\bar{\phi}_s$ for the domain average solid volume fractions $\langle\phi_s\rangle = 0.35, 0.45$ and 0.50 and for gas Reynolds number ratios $\langle Re_g \rangle / \langle Re_g \rangle_{susp} = 16.30$ and 24.45 . The results stand for different dimensionless filtered axial slip velocities \tilde{v}_{slip} / v_t (black and blue), for the dimensionless filter size $\Delta_f / (v_t^2 / g) = 4.112$, and for various dimensionless filtered kinetic energy of the solid velocity fluctuations k_s / v_t^2 (with different thickness). All graphs for $C_f = 0$ 114

Figure 22 – Dimensionless residual solid pressure, $P_{res,s} / (\rho_s v_t^2)$, as a function of the filtered solid volume fraction $\bar{\phi}_s$ for the domain average solid volume fractions $\langle\phi_s\rangle = 0.35, 0.45$ and 0.50 and for gas Reynolds number ratios $\langle Re_g \rangle / \langle Re_g \rangle_{susp} = 16.30$ and 24.45 . The results stand for different dimensionless filtered axial slip velocities \tilde{v}_{slip} / v_t (smaller: black and bigger: red), for the dimensionless filter size $\Delta_f / (v_t^2 / g) = 4.112$, and various dimensionless filtered kinetic energy of the solid velocity fluctuations k_s / v_t^2 (with different thickness). All graphs for $C_f = 0$ 117

Figure 23 – Dimensionless residual solid dynamic viscosities, $\mu_{res,s}/(\rho_s v_t^3/g)$, as a function of the filtered solid volume fraction $\bar{\phi}_s$ for the domain average solid volume fractions $\langle\phi_s\rangle = 0.35, 0.45$ and 0.50 and for gas Reynolds number ratios $\langle Re_g \rangle / \langle Re_g \rangle_{susp} = 16.30$ and 24.45 . The results stand for different dimensionless filtered axial slip velocities \tilde{v}_{slip}/v_t (smaller: black and bigger: red), for the dimensionless filter size $\Delta_f/(v_t^2/g) = 4.112$, and various dimensionless filtered kinetic energy of the solid velocity fluctuations k_s/v_t^2 (with different thickness). All graphs for $C_f = 0$ 120

Figure 24 – Drag Coefficient Correction, H , as a function of the filtered solid volume fraction $\bar{\phi}_s$ for the domain average solid volume fractions $\langle\phi_s\rangle = 0.35, 0.45$ and 0.50 and for gas Reynolds number ratios $\langle Re_g \rangle / \langle Re_g \rangle_{susp} = 16.30$ and 24.45 . The results stand for particular dimensionless filtered axial slip velocities \tilde{v}_{slip}/v_t , for the dimensionless filter size $\Delta_f/(v_t^2/g) = 4.112$, and two different interparticle friction coefficient, $C_f = 0$ (full lines) and $C_f = 0.3$ (dash lines). 124

Figure 25 – Dimensionless filtered solid pressure, $P_{fil,s}/(\rho_s v_t^2)$, as a function of the filtered solid volume fraction $\bar{\phi}_s$ for the domain average solid volume fractions $\langle\phi_s\rangle = 0.35, 0.45$ and 0.50 and for gas Reynolds number ratios $\langle Re_g \rangle / \langle Re_g \rangle_{susp} = 16.30$ and 24.45 . The results stand for particular dimensionless filtered axial slip velocities \tilde{v}_{slip}/v_t , for the dimensionless filter size $\Delta_f/(v_t^2/g) = 4.112$, and two different interparticle friction coefficient, $C_f = 0$ (full lines) and $C_f = 0.3$ (dash lines). 127

Figure 26 - Dimensionless filtered solid dynamic viscosities, $\mu_{fil,s}/(\rho_s v_t^3/g)$, as a function of the filtered solid volume fraction $\bar{\phi}_s$ for the domain average solid volume fractions $\langle\phi_s\rangle = 0.35, 0.45$ and 0.50 and for gas Reynolds number ratios $\langle Re_g \rangle / \langle Re_g \rangle_{susp} = 16.30$ and 24.45 . The results stand for particular dimensionless filtered axial slip velocities \tilde{v}_{slip}/v_t , for the dimensionless filter size $\Delta_f/(v_t^2/g) = 4.112$, and two different interparticle friction coefficient, $C_f = 0$ (full lines) and $C_f = 0.3$ (dash lines)..... 130

Figure 27 – Dimensionless residual solid pressure, $P_{res,s}/(\rho_s v_t^2)$, as a function of the filtered solid volume fraction $\bar{\phi}_s$ for the domain average solid volume fractions $\langle\phi_s\rangle = 0.35, 0.45$ and 0.50 and for gas Reynolds number ratios $\langle Re_g \rangle / \langle Re_g \rangle_{susp} = 16.30$ and 24.45 . The results stand for particular

dimensionless filtered axial slip velocities \tilde{v}_{slip}/v_t , for the dimensionless filter size $\Delta_f/(v_t^2/g) = 4.112$, and two different interparticle friction coefficients, $C_f = 0$ and 0.3 133

Figure 28 – Dimensionless residual solid dynamic viscosities, $\mu_{res,s}/(\rho_s v_t^3/g)$, as a function of the filtered solid volume fraction $\bar{\phi}_s$ for the domain average solid volume fractions $\langle\phi_s\rangle = 0.35, 0.45$ and 0.50 and for gas Reynolds number ratios $\langle Re_g \rangle / \langle Re_g \rangle_{susp} = 16.30$ and 24.45 . The results stand for particular dimensionless filtered axial slip velocities \tilde{v}_{slip}/v_t , for the dimensionless filter size $\Delta_f/(v_t^2/g) = 4.112$, and two different interparticle friction coefficient, $C_f = 0$ (full lines) and $C_f = 0.3$ (dash lines). 136

LIST OF TABLES

Table 1 – Microscopic two-fluid model.....	43
Table 2 – Modifications on the microscopic two-fluid model (Berzi and Vescovi, 2014).....	46
Table 3 – Filtered two-fluid model.....	49
Table 4 – Bin discharge simulation parameters (Schneiderbauer et al. 2012).....	54
Table 5 – Physical properties of gas and solid.....	56
Table 6 – Set up different simulation for fluidization.....	57

LIST OF ABBREVIATIONS AND ACRONYMS

CFB	Circulating Fluidized Bed
CFD	Computational Fluid Dynamics
DOE-USA	United States Department of Energy
FCC	Fluid Catalytic Cracking
FCCUs	Fluidized catalytic cracking units
HRS	Highly Resolved Simulation
KTGF	Kinetic Theory of Granular Flows
LSS	Large Scale Simulation
MFIX	Multiphase Flow with Interphase eXchange
NETL	National Energy Technology Laboratory
PTE	Pseudo-Thermal Energy
SIMPLE	Semi-Implicit Method for Pressure Linked Equations
TFM	Two-Fluid Model
TVD	Total Variation Diminishing

LIST OF SYMBOLS

B'_{gs}	Nm^{-3}	Fluctuation of gas-solid buoyancy force
C_f	-	Friction coefficient
C_D	-	Single particle drag coefficient
d_p	m	Particle diameter
e	-	Restitution coefficient for particle-particle collisions
e_{eff}	-	Effective restitution coefficient
Fr_{d_p}	-	Particle size based Froude number
g	ms^{-2}	Acceleration of gravity
g_0	-	Radial distribution function
H	-	Drag coefficient correction
I	-	Unit tensor
$J_{\text{coll,k}}$	$\text{Jm}^{-3}\text{s}^{-1}$	Rate of dissipation of granular energy by collisional damping
$J_{\text{coll,f}}$	$\text{Jm}^{-3}\text{s}^{-1}$	Rate of dissipation of granular energy by friction
J_{vis}	$\text{Jm}^{-3}\text{s}^{-1}$	Rate of dissipation of granular energy by viscous damping
k	$\text{m}^{-2}\text{s}^{-2}$	Kinetic energy
L	m	Characteristic length
\mathbf{f}	Nm^{-3}	Interface force
P	Nm^{-2}	Pressure
Re	-	Reynolds number
s	s^{-1}	Strain rate tensor due to viscous plus pressure effects
St	-	Stokes number
t	s	Time
T	K	Temperature
u'	ms^{-1}	Velocity fluctuation in the horizontal direction

v'	ms^{-1}	Velocity fluctuation in the vertical direction
\mathbf{v}	ms^{-1}	Velocity vector
V_t	ms^{-1}	Terminal settling gas velocity
y	m	Vertical (axial) Cartesian coordinate

Greek letters

β	$\text{kgm}^{-3}\text{s}^{-1}$	Micro-scale gas-solid drag coefficient
Γ_{slip}	$\text{Jm}^{-3}\text{s}^{-1}$	Rate of production of granular energy by gas-particle slip
Δf	m	Filter size
Δt	s	Time step
ε_p	-	Particle sphericity
θ	m^2s^{-2}	Granular temperature
k_s	$\text{kgm}^{-1}\text{s}^{-1}$	Granular thermal conductivity
λ	Nsm^{-2}	Bulk viscosity
μ	Nsm^{-2}	Dynamic viscosity
ρ	kgm^{-3}	Density
σ	Nm^{-2}	Deviatoric stress tensor
σ	ms^{-1}	Root mean square velocity
τ'	Nm^{-2}	Reynolds-like stress tensor
ϕ	-	Volume fraction

Subscripts

eff	-	Effective, or meso-scale related
f	-	Fluid
fil	-	Filtered
g	-	Gas phase

	-	Horizontal direction
l	-	Interface
j	-	Vertical direction
ℓ	-	A generic phase, either s or g
max	-	Maximum
p	-	Particle
<i>res</i>	-	Residual, or meso-scale related
s	-	Solid phase
<i>slip</i>	-	Slip
<i>susp</i>	-	Suspension

Other symbols

-	Filtered or volume averaged
*	Dimensionless parameter
~	Dimensionless parameter,
$\langle \rangle$	Domain volume average

CONTENTS

1	INTRODUCTION	31
1.1	Fluidization Regimes	33
1.2	Two – Fluid modeling of gas – solid flows	34
1.3	Literature.....	35
1.3.1	Highly resolved simulations of gas-solid fluidized flows	35
1.3.2	Interparticle friction in gas-solid flow modeling.....	38
1.4	Objective.....	39
2	METHODOLOGY	41
2.1	The conventional microscopic two-fluid model	41
2.2	The modified microscopic two-fluid model	45
2.3	Filtered two-fluid model	48
2.4	Numerical Procedure	51
2.5	Test of the friction model and set up of the interparticle friction coefficient	52
2.6	Simulations Set up	56
2.7	Filtering Procedure	58
3	RESULTS AND DISCUSSION.....	61
3.1	Case 1: 3 rd marker analysis	61
3.1.1	Statistical steady state regime.....	61
3.1.2	Flow Topology	62
3.1.3	Drag Coefficient Correction.....	64
3.1.4	Filtered pressure and dynamic viscosity of the solid phase.....	68
3.1.5	Residual pressure and dynamic viscosity of the solid phase.....	75
3.2	Case 2: interparticle friction analysis.....	82
4	CONCLUSION	98
	REFERENCES.....	102
	Appendices.....	105
	Appendix A – Case 1: Third marker analysis – results for high Reynolds number ratios... ..	107
	Appendix B – Case 2: Interparticle friction analysis – results for high Reynolds number ratios	123

1 INTRODUCTION

Fluidized-bed processes have operated commercially since the 1920s, beginning with the advent of the Winkler coal gasifier in Germany. Fluidized catalytic cracking units (FCCUs) for the production of high-octane gasoline and fluidized-bed reactors for making phthalic anhydride debuted in the 1940s (Cocco et al. 2014). Today, about three-quarters of all polyolefin are made in fluidized-bed processes. The development of a specialized zeolite catalyst for cracking heavy oil into various fractions enabled the commercialization of the FCC circulating fluidized beds (Leva et al. 1948). Fluidized beds are typically more complex to design, build, and operate than other types of reactors, such as packed-bed and stirred-tank reactors; scale-up of fluidized beds is highly expensive, time consuming and hard-working (Pangarkar 2014). Fluidized beds are prone to erosion and particle attrition caused by the moving particles. Solids losses can result in significant operating costs, especially when the solid particles are an expensive catalyst. The development of fluidized bed reactors is still a very much empirical science, based upon gradually scaled demonstration plants that involve both very high costs and excessive execution times (Wang et al. 1999). The current research proposition ultimately intends to contribute in the context of replacing those very expensive demonstration plants by computational simulation.

Accurate computational simulation of fluidized bed reactors requires accurate modeling, and no accurate modeling can be advanced without a rigorous description of the concerning very heterogeneous gas-solid flows. Those flows are characterized by very dynamic formation, composition and dissipation of entities such as gas bubbles and clusters of particulate, which manifest in a multitude of time and length scales, and profoundly affect mass transfer, heat transfer and chemical reaction rates. Owing to the commonly huge physical volumes that are involved in real scale fluidized bed reactors, only the so called large scale simulations (LSS) are feasible. LSS impose very coarse numerical grids, inside which any heterogeneity is filtered, and their effects are thereby lost. Therefore, if accuracy is desired, closure models must be added to the LSS formulations in order to recover sub-grid filtered effects. Generating sub-grid closures for LSS represents a formidable challenge for physicists and modelers. One way of performing that is through filtered results from Highly Resolved Simulations (HRS), where fine enough numerical grids are applied so that all possible scales of solid particle structures are captured.

The currently proposed research intends to contribute for the derivation of increasingly realistic filtered closure models for phase stresses and inter-phase interactions by means of computational experiment with microscopic two-fluid modeling, which is suitable for HRS of the concerning flows.

In gas-solid fluidized flows, for solid volume fractions up to 40%, solid phase stresses arising from particle-particle collisions are usually modeled following an analogy with the kinetic theory of dense gases (Lun et al. 1984). The so called kinetic theory of granular flows (KTGF) assumes that the collisions are inelastic and mostly binary. Those assumptions are quite fine for dilute conditions, but KTGF requires revision for dense flow conditions. In dense flow regimes, which are frequently referred to as frictional regimes particle-particle contacts are dominated largely by enduring multiple frictional contacts and, thus, kinetic theory does not apply.

In the current work the effects of frictional interactions among particles are considered in addition to the usual collisional effects usually accounted for by the conventional kinetic theory of granular flows. For that purpose, a modified version of KTGF is applied following on implementation developed by Berzi and Vescovi (2015) based on Chialvo et al. (2013) frictional model. The effects of the inclusion of frictional interactions on filtered parameters are evaluated having in view sub-grid model enhancement. A range of domain average solid fractions and gas Reynolds numbers are enforced which are typical of dense flow regimes.

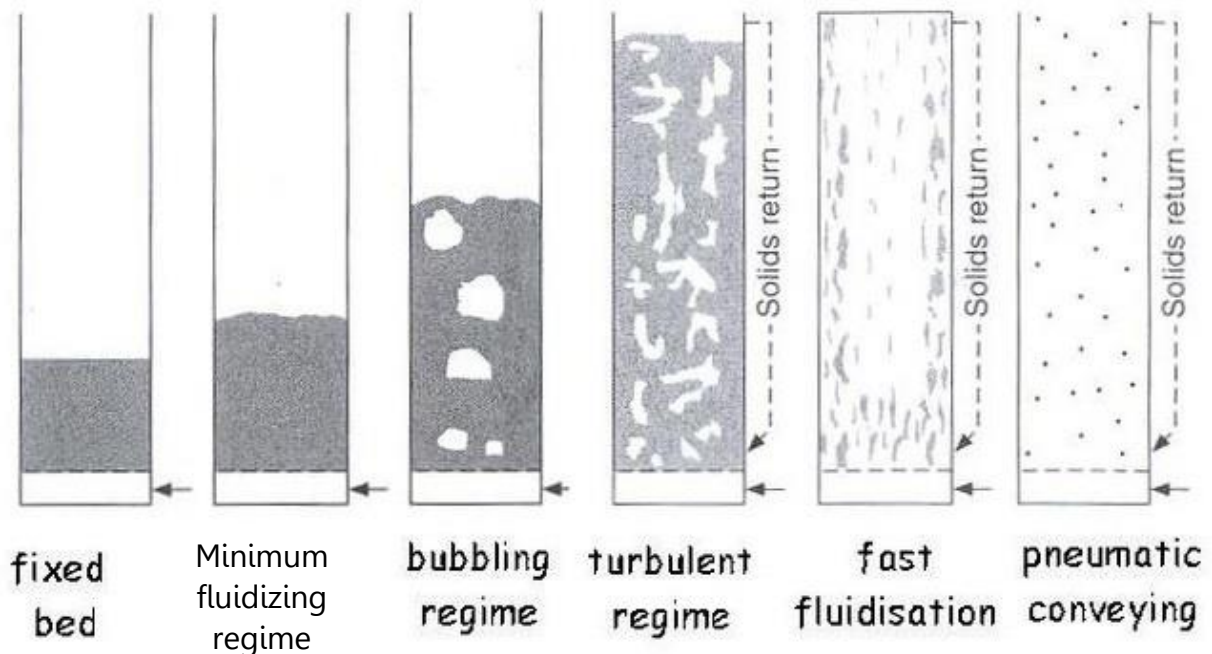
The present concern is turned to the application of high Stokes number particulates, which are typical of fluidized bed processes. A high Stokes number (frequently defined as the ratio of the particulate response time to the Kolmogorov time scale or other relevant time scales of the flow) means that the motion of individual particles is not affected by the carrying gas turbulence. The MFIX open source code is used in all the simulations, which are performed over 2D periodical domains for a unique high stokes number particulate.

An overview is presented next on gas-solid fluidization basics and the continuum modeling approach which is followed in this work. Then the concerning literature is revised both on highly resolved simulations and frictional effects, and the objectives of research are briefly summarized.

1.1 Fluidization Regimes

Gas-particle flows in fluidized beds exhibit a number of complex characteristics. Depending on the gas inlet conditions and particle properties, the fluidization of a bed of particles can fall into a number of different regimes (Figure 1).

Figure 1 – Schematic representation of gas fluidized beds in different regimes.



Source (Kunii and Levenspiel 2013)

When inlet gas velocity is small, the gas will seep through the particulate, and the bed of particles remains fixed. As the gas velocity is increased, so is its drag effect over the particulate, and a stage is reached when the drag force exceeds the gravity on the particles. At this condition the particles start moving and colliding, and the bed expands. At this so called minimum fluidization condition, the two-phase suspension that is formed exhibits a fluid like behavior. The particular velocity at which the fixed bed begins to expand is defined as the minimum fluidization velocity. At gas velocities higher than the minimum fluidization velocity bubbles of gas arise which ascend through a dense “emulsion” phase. A further gas velocity increase disrupts the bubbles into nonuniform very irregular gas voids characterizing the so called turbulent regime. Even higher gas velocities push the particles into a fast or rapid fluidization regime, and the topology turns to be

dominated by a dilute gas-solid flow full of particulate structures usually referred to as clusters. At still higher gas velocities the flow enters the pneumatic transport regime.

The current work is mostly concerned with high density flow conditions, where frictional effects may become dominant. However, high density regions inside the flow happen in all fluidized regimes, so that current analysis stands independently of flow regime.

Because of the importance of fluidized beds to the chemical industry, and the large amounts of capital invested in their operation, the ability to make engineering predictions of their performance characteristics is essential in design, planning, and optimization. Unfortunately, scaling up the experimental results from bench-scale fluidized beds is notoriously problematic (Kunii and Levenspiel 1991). The difficulty of scale-up is unsurprising considering the complex behavior exhibited by fluidized beds, which related to physical properties of the fluid and the particles, flow conditions, and vessel dimensions. Capturing all these effects with simple engineering correlations of operating conditions is impossible. Therefore, more rigorous and scientific models hold great practical value and have drawn increasing attention in the research community.

1.2 Two – Fluid modeling of gas – solid flows

In this work two-fluid modeling is applied, which is on Euler-Euler style approach where the phases, fluid and particulate, are both treated as continuum phases, respectively called gas and solid phases. In this modeling framework, the gas and solid phases are inter-penetrating and locally-averaged and inter phase interaction effects such as drag are considered in average as field effects. The volume averaged two-fluid model as derived by Anderson & Jackson (1968) is applied. The formulation requires closure modelling, notably for particulates treated as the continuum solid phase which requires the definition of suitable fluid properties.

Closures are usually set in terms of topological laws, constitutive laws, and transfer laws (Drew and Lahey 1993; Arnold et al. 1990). Topological laws define the spatial distribution of phase-specific quantities such as phase fractions and mass flow rates. Constitutive laws describe the rheological approach and physical properties of different phases such as viscosities and pressures. Transfer laws equations that describe different interactions between phases at the interface such as momentum exchanges by drag.

In the two-fluid model based on the kinetic theory of granular flows, besides the continuity and momentum conservation equations for the two phases, an additional conservation pseudothermal energy is resolved. This equation is an analogy with the continuum energy conservation equation, and provides a granular temperature analogous to the thermodynamic temperature concept (Gidaspow 1994). The granular temperature is associated with the fluctuating motion of particles just like temperature is associated with the fluctuating motion of molecules. The kinetic theory of granular flows based two-fluid model, which is applied in the present work, is known to capture characteristics such as bubble-like voids in dense gas-particle flows, as well as clusters and streamers in dilute flows (Agrawal 2001). The two-fluid model under closures from the kinetic theory of granular flows is usually called microscopic two-fluid model approach.

1.3 Literature

1.3.1 Highly resolved simulations of gas-solid fluidized flows

According to (Sundaresan 2000), two-fluid models including suitable filtered closures represent the most promising next generation models for multiphase reactors and, in this context, the formulation of realistic filtered models is a great challenge ahead. This particular issue has been addressed by a number of researchers on the basis of highly resolved computational experiments (or highly resolved simulations, HRS) with microscopic two-fluid modeling (Agrawal 2001; Andrews IV et al. 2005; Igci et al. 2008; Igci and Sundaresan 2011a; Milioli et al. 2013; Schneiderbauer and Pirker 2014; Sarkar et al. 2016). Besides making it clear the real necessity for filtered models, those works suggest that filtered models so produced from highly resolved computational experiments do require continuous improvement as more and more realistic approaches are pursued. The filtered models are also called meso-scale models since they are generated from computational experiments under grid refinements that are expected to capture all the solid phase scales of the flow, so that filtered meso-scale data can be derived.

In most cases, reduced domains are considered, which are extracted from the free stream in the core of the flow field, and periodic boundaries are applied. As periodic boundaries are applied, an extra gas phase pressure gradient is imposed in the vertical direction in order to impose a flow driving force. It is usual to consider an extra gas phase pressure gradient to exactly compensate the gravity acting on the gas-solid mixture. This idea is brought from fundamental studies on the

instabilities that develop in gas-solid flows owing to inter-particle inelastic collisions, which ultimately lead to clustering (Goldhirsch et al. 1993; Tan and Goldhirsch 1997). While those studies are valid for quasi-static conditions, where the particulate arranges itself in low velocity suspensions, it has been commonly assumed that the cluster formation mechanism that prevails is also relevant to any flow topology, from bubbling, to turbulent, to rapid gas-solid flows.

Following the above basic approach, Agrawal et al. (2001), Andrews IV et al. (2005), Igci et al. (2008), Igci et al. (2010), and Igci and Sundaresan (2011) developed highly resolved simulations aiming for filtered correlations for filtered and residual pressure and viscosity of the solid phase, and for the effective drag coefficient. Agrawal et al. (2001) characterized the Meso-scale of the gas-solid flow as comprised of solid coherent structures with dimensions from 10 to 100 times the particulate size. From their predictions the authors analyzed the effective drag coefficient, and the effective dynamic viscosity and pressure of the solid phase.

As observed by van der Hoef et al. (2006), Agrawal et al. (2001) showed that grid refinements of the order of 10 times the particulate size provided grid independent predictions for a particular case. They also showed that vertical boundary conditions of free slip, partial slip and periodic, do produce similar flow topologies.

Andrews IV et al. (2005) explicitly proposed ad hoc closures for the effective drag, residual viscosity and pressure of the solid phase. Igci et al. (2008) further extended the previous works of Agrawal et al. (2001) and Andrews IV et al. (2005), and showed that the filtered predictions depend on the sub-grid filter size. A posterior work also showed the filtered predictions to depend on the distance from walls (Igci and Sundaresan 2011b). Further extending the work reported in Igci et al. (2008), Igci and Sundaresan (2011) produced correlations for the filtered effective drag, pressure and viscosity of the solid phase, as a function of filter size and filtered solid volume fraction.

The effective drag coefficient was expressed in the form of a drag coefficient correction relating the actual effective drag coefficient to the filtered micro-scale drag coefficient, as previously done, for instance, by Zhang and Vander Heyden (2002). Igci et al. (2012) tested the correlations presented in Igci and Sundaresan (2011), including the wall corrections proposed in Igci et al. (2010), in coarse grid simulations of a riser flow. The comparisons against empirical data showed qualitative agreement, while quantitative differences still remained.

Following the same basics of the previous works, Parmentier et al. (2012) proposed a similar approach to deal with the filtered effective drag, except they did not apply periodic

boundaries but a small 2D bubbling bed configuration. Their correlations for the effective drag correction were alike those proposed in Igci and Sundaresan (2011), except for the inclusion of a macro-scale length scale in the filter size dependence of the drag coefficient correction. They also included a coarse grid dynamical adjustment analogous to the dynamic correction usually applied in large eddy simulation of turbulent flows. A test of their drag correction correlation in a coarse grid simulation of a bubbling bed set up recovered the correct bed expansion which came out from a highly resolved simulation. The model remained to be tested for more dilute flow configurations such as circulating fluidized beds.

Ozel et al. (2013) extended the work of Parmentier et al. (2012) by incorporating vertical periodic boundaries over 3D bubbling bed conditions, and also by extending the development to include stresses analyses as done by Agrawal et al. (2001). Their conclusions were similar to those of Parmentier et al. (2012).

In the above works (Agrawal 2001; Andrews IV et al. 2005; Igci et al. 2008; Igci and Sundaresan 2011a; Parmentier et al. 2012; Ozel et al. 2013), filtered parameters have been correlated to filter size and filtered solid volumetric fraction. It so happens that different patterns, ranging from very homogeneous to very heterogeneous, may occur for any particular values of filter size and filtered solid fraction. In order to account for the heterogeneity of the flow, Milioli et al. (2013) introduced an additional independent variable in filtered parameter correlation (named 2nd marker, while the solid volumetric fraction was named 1st marker). Models for filtered and residual pressures and viscosities were proposed in analogy with the Smagorinsky's turbulence viscosity model, thereby introducing the filtered scalar shear rate as 2nd marker. Also, a model for the effective drag coefficient correction was proposed including the filtered slip velocity as a 2nd marker.

Ozarkar et al. (2015) applied the sub-grid models of Milioli et al. (2013) to a large scale simulation of a bubbling fluidized bed, and compared results to experiment. They found a very good agreement between experiment and predictions for both bed expansion and pressure drop through the height of the bed. Schneiderbauer and Pirker (2014) followed the same path as Milioli et al. (2013), and found similar results.

Agrawal et al. (2013) extended the work of Milioli et al. (2013) by also proposing filtered models for the mass/heat diffusivity coefficient and for the interphase mass/heat transfer

coefficient; respectively accounting for the filtered scalar shear rate and the filtered slip velocity as 2nd marker.

Sarkar et al. (2016) developed new sub-grid models following the work of Milioli et al. (2013), except that based on 3D highly resolved simulations. Similar behavior of the effective drag coefficient correction, filtered and residual pressures and viscosities were observed, with some quantitative differences. Regarding the filtered and residual pressures and viscosities, a correlation to the filtered velocity as 2nd marker was also observed which was not seen on the previous results of Milioli et al. (2013). In addition to sub-grid model proposition, Sarkar et al. (2016) also developed a validation step by comparing predictions of a large scale simulation against experiment for a bubbling bed situation. A very good agreement between predictions and experiment was found for both bed expansion and pressure drop through the height of the bed.

1.3.2 Interparticle friction in gas-solid flow modeling

In two-fluid modeling, particulate phases are treated as continua, thereby requiring continuum properties to be defined. In microscopic two-fluid modeling this is done through the kinetic theory of granular flows (Jenkins and Savage 1983; Lun et al. 1984; Gidaspow 1994; Garzó and Dufty 1999). This theory is only valid for regions of dilute homogeneous flows, where collisional inelastic effects dominate particle-particle interactions. The real fluidized flows, however, are highly heterogeneous and comprise very dense regions that come close to particulate maximum packing. In these regions enduring frictional contact among particles predominate over collisional effects. Different procedures have been proposed for the treatment of transition regions between dilute and dense flows (Johnson and Jackson 1987; Schaeffer 1987; Syamlal et al. 1993; Srivastava and Sundaresan 2003; Chialvo and Sundaresan 2013; Berzi and Vescovi 2015).

Some approximations look for either the simple replacement of collisional by frictional effects above some high solid fraction (Schaeffer 1987; Syamlal et al. 1993), the generalized composition of collisional and frictional effects irrespective of solid concentration (Johnson and Jackson 1987), or the composition of those effects only above some limit on solid fraction (Srivastava and Sundaresan 2003).

Departing from a comparative analysis of those propositions, Pannala et al. (2009) performed two-fluid simulations using a simple heuristic interpolation between regions of collisional and frictional predominance to account for particle interactions. Through this procedure

they found results closer to experiment in comparison to the results under the previous assumptions, for a particular bin discharge application.

Following a more rigorous line of development, da Cruz et al. (2005) carried out a collisional/frictional analysis in dense packs through dynamic molecular simulation. They defined and showed the relevance of the so called inertial number (ratio between inertial forces and pressure) for the collisional/frictional transition between dilute and dense regions. The propositions of da Cruz et al. (2005) were adapted and implemented by Schneiderbauer et al. (2012) into the kinetic theory of granular flows of Jenkins and Savage (1983), with some success. More recently, rheological models even more rigorous have been proposed, based on modifications of the kinetic theory of granular flows (Chialvo and Sundaresan 2013; Berzi and Vescovi 2015).

Chialvo and Sundaresan (2013) used empirical frictional data to validate results of dynamic molecular simulations of homogeneous shear flows, which were then used to generate correlations for rheological parameters alternative to those provided by the granular kinetic theory of Garzó and Dufty (1999). Their developments provided new correlations incorporating the transition dilute/dense for the radial distribution function, and for effective viscosities and pressure for solid phases.

Berzi and Vescovi (2015) built over the previous analyses of Jenkins and Berzi (2010) and Chialvo and Sundaresan (2013) by applying the same method, except that their developments were performed over the granular kinetic theory of Jenkins and Savage (1983). Their conclusions were similar to those of Chialvo and Sundaresan (2013).

1.4 Objective

In this work two different features are investigated regarding their effects over the meso-scale hydrodynamics of dense gas-solid fluidized flows: (a) macro-scale conditions and (b) interparticle friction. The analysis are performed over filtered parameters derived from results of higher resolved simulations with microscopic two-fluid modeling. Regarding the macro-scale conditions, different gas flow average Reynolds number and solid fraction are enforced and relevant filtered parameters (such as the drag coefficient correction, filtered and residual viscosities and pressure) are evaluated as for the effects of those macroscopic features (the current concerning literature only shows analysis under low average gas Reynolds number typical of suspension like conditions).

Regarding interparticle friction, the usual closures for the microscopic two-fluid approach, which is provided by the kinetic theory of granular flows, is suitable for the inertial collisional-kinetic regime only. Heterogeneous fluidized flow fields, however, which also present regions of very high particle concentrations close to packing, do require that frictional effects are also accounted for. A modified kinetic theory is applied, following literature, in order to add interparticle friction effects. The present research evaluate the behavior of relevant filtered parameters as frictional effects are also accounted for.

2 METHODOLOGY

In this work a microscopic two-fluid model is used to perform highly resolved simulation of gas-solid fluidized bed, which includes a modification to account for interparticle friction. The concerning conventional formulation is described next, which is followed by the modified version including friction modeling. Following those description, a two-fluid filtered formulation is presented in order to define the relevant filtered parameters to be derived from the results of the intended highly resolved simulations (filtered parameters whose behavior are evaluated regarding the effects of both the macro-scale flow conditions and friction inclusion).

After all the formulation have been presented, then the numerical solution approach is described and the simulation set up defined (firstly for calibrating the frictional model, then to actually resolve the concerning gas-solid fluidized flows). To close this chapter, the filtering procedure is define which is applied for generating filtered parameters of concern.

2.1 The conventional microscopic two-fluid model

Two-fluid models are formally developed departing from conservative integral balances applied over control volumes including both phases. Leibniz and Gauss theorems are then applied over the integral balances providing local instantaneous conservative differential equations for both phases, and jump conditions describing interface interactions. It so happens that such formulation cannot be applied to particulate dispersed flows (since the inter-penetrating phases create discontinuities on each other so that the fundamental continuum hypothesis is violated).

To go around this difficulty, averaging procedures are applied, where interface interactions are treated in average, as continuum field effects between the phases. The resulting equations are the so called two-fluid formulation. Different averaging procedures can be applied (time, volumetric and ensemble), which are usually assumed equivalent (ergodicity hypothesis), thereby providing the same averaged equations. A comprehensive development of the two-fluid formulation can be found, for instance in research of (Ishii 1975) and (Enwald et al. 1996).

The two-fluid formulation considered in the present work is that developed by (Anderson and Jackson 1968) applying volumetric averaging, which was specially derived for gas-solid fluidized flows. The microscopic formulation that is used, which includes microscopic closures, is described next.

The continuity equations for the particle and gas phases are shown in Equations 2.1 and 2.2. Equations 2.3 and 2.4 show the particle and gas phase momentum balances, respectively. Here, ϕ_s is the volume fraction of solids; v_s and v_g are the velocities of the solid and gas phases, respectively; ρ_s and ρ_g are the densities; $\boldsymbol{\sigma}_s$ and $\boldsymbol{\sigma}_g$ are the stress tensors associated with the two phases; \mathbf{f} is the drag interaction force between the phases per unit volume (other interaction forces such as lift, virtual mass or history forces are disregarded as drag is dominant in gas-solid fluidized flows); and \mathbf{g} is the specific gravity force. Equations 2.5, 2.6 and 2.7 describe the drag model used in our simulations (Gidaspow 1994). β , C_D , d , μ_g and Re_g denote the drag coefficient for the suspension, the single particle drag coefficient, the particle diameter, gas viscosity and Reynolds number, respectively. This expression for the drag coefficient β applies to homogeneous flows, developed by Wen and Yu (Wen 1966).

The kinetic theory of granular flows provides a framework to write constitutive relationships for the particle-phase stresses, which are needed as closures for the momentum solid phase equations. The granular temperature, which appears in the kinetic-theory based constitutive model for the solid phase deviatoric stress tensor (See Equation 2.10), is given by the equation for pseudo-thermal energy (Equation 2.8). In this equation T is the granular temperature, \mathbf{q} is the diffusive flux of pseudo-thermal energy (PTE), and the second and third terms on the right hand side quantify the rates of production of PTE by shear and gas-particle slip, respectively. The fourth and the fifth terms account for the rates of dissipation of PTE through inelastic collisions and viscous damping, respectively. Here e denotes the coefficient of restitution for particle-particle collisions. Equations 2.9 and 2.19 are the kinetic-theory based constitutive models for the diffusive flux of PTE and the rate of dissipation of PTE through inelastic collisions, respectively.

Table 1 – Microscopic two-fluid model (Agrawal 2001)

Continuity and momentum conservation equations

$$\frac{\partial(\rho_s \phi_s)}{\partial t} + \nabla \cdot (\rho_s \phi_s \mathbf{v}_s) = 0 \quad (2.1)$$

$$\frac{\partial(\rho_g \phi_g)}{\partial t} + \nabla \cdot (\rho_g \phi_g \mathbf{v}_g) = 0 \quad (2.2)$$

$$\left[\frac{\partial(\rho_s \phi_s \mathbf{v}_s)}{\partial t} + \nabla \cdot (\rho_s \phi_s \mathbf{v}_s \mathbf{v}_s) \right] = -\nabla \cdot \boldsymbol{\sigma}_s - \phi_s \nabla \cdot \boldsymbol{\sigma}_g + \mathbf{f} + \rho_s \phi_s \mathbf{g} \quad (2.3)$$

$$\left[\frac{\partial(\rho_g \phi_g \mathbf{v}_g)}{\partial t} + \nabla \cdot (\rho_g \phi_g \mathbf{v}_g \mathbf{v}_g) \right] = -\phi_g \nabla \cdot \boldsymbol{\sigma}_g - \mathbf{f} + \rho_g \phi_g \mathbf{g} \quad (2.4)$$

Gas – Particle drag

$$\mathbf{f} = \beta (\mathbf{v}_g - \mathbf{v}_s) \quad \text{Gidaspow (1994)} \quad (2.5)$$

$$\beta = \frac{3}{4} C_D \frac{\rho_g \phi_g \phi_s |\mathbf{v}_g - \mathbf{v}_s|}{d_p e_p} (\phi_g)^{-2.65} \quad \text{Wen \& Yu (1966)} \quad (2.6)$$

$$C_D = \begin{cases} \frac{24}{\text{Re}_g} (1 + 0.15 \text{Re}_g^{0.687}) & \text{Re}_g < 1000 \\ 0.44 & \text{Re}_g \geq 1000 \end{cases} ; \quad \text{Re}_g = \frac{\phi_g \rho_g d |\mathbf{v}_g - \mathbf{v}_s|}{\mu_g} \quad (2.7)$$

Granular energy conservation equation

$$\left[\frac{\partial \left(\frac{3}{2} \rho_s \phi_s T \right)}{\partial t} + \nabla \cdot \left(\frac{3}{2} \rho_s \phi_s T \mathbf{v}_s \right) \right] = -\nabla \cdot \mathbf{q} - \boldsymbol{\sigma}_s : \nabla \mathbf{v}_s + \Gamma_{\text{slip}} - J_{\text{coll}} - J_{\text{vis}} \quad (2.8)$$

Pseudo – thermal energy flux vector (Lun et al. 1984)

$$\mathbf{q} = -\frac{\lambda^*}{g_o} \left\{ \left(1 + \frac{12}{5} \phi_s \eta g_o \right) \left(1 + \frac{12}{5} \eta^2 (4\eta - 3) \phi_s g_o \right) + \frac{64}{25\pi} (41 - 33\eta) \eta^2 \phi_s^2 g_o^2 \right\} \nabla T \quad (2.9)$$

Deviatoric stresses of the phases

$$\boldsymbol{\sigma}_t = \left[P_t - \left(\lambda_t + \frac{2}{3} \mu_t \right) (\nabla \cdot \mathbf{v}_t) \right] \mathbf{I} - 2\mu_t \mathbf{S}_t \quad ; \quad t = g, s \quad (2.10)$$

$$\mathbf{S}_i = \frac{1}{2}(\nabla \mathbf{v}_i + (\nabla \mathbf{v}_i)^T) - \frac{1}{3}(\nabla \cdot \mathbf{v}_i)\mathbf{I} \quad ; \quad i = g, s \quad (2.11)$$

$$\mu_g = \text{constant} \quad \lambda_g = 0 \quad (2.12)$$

Solid phase pressure

$$P_s = \rho_s \phi_s (1 + 4\eta \phi_s g_o) T \quad (2.13)$$

Kinetic - collisional granular viscosity

$$\mu_{s,k} = \left(\frac{2+\alpha}{3} \right) \left\{ \frac{\xi^*}{g_o \eta (2-\eta)} \left(1 + \frac{8}{5} \phi_s \eta g_o \right) \left(1 + \frac{8}{5} \eta (3\eta - 2) \phi_s g_o \right) + \frac{6}{5} \eta \mu_b \right\} \quad (2.14)$$

$$\lambda_{s,k} = \eta \mu_b - \frac{2}{3} \mu_{s,k} \quad (2.15)$$

$$\xi^* = \frac{\xi}{1 + \frac{2\beta\xi}{(\rho_s \phi_s)^2 g_o T}} \quad ; \quad \lambda^* = \frac{\lambda}{1 + \frac{6\beta\lambda}{5(\rho_s \phi_s)^2 g_o T}} \quad (2.16)$$

$$\xi = \frac{5\rho_s d \sqrt{\pi T}}{96} \quad ; \quad \mu_b = \frac{256\xi \phi^2 g_o}{5\pi} \quad ; \quad \lambda = \frac{75\rho_s d \sqrt{\pi T}}{48\eta(41-33\eta)} \quad ; \quad \eta = \frac{1+e}{2} \quad ; \quad \alpha = 1.6 \quad (2.17)$$

Rate of production of pseudo – thermal energy

$$\Gamma_{slip} = \frac{81\phi_s \mu_g^2 |\mathbf{v}_g - \mathbf{v}_s|^2}{g_o d_p^3 \rho_s (\pi T)^{0.5}} \quad (2.18)$$

Rate of dissipation of pseudo – thermal energy

$$J_{coll,k} = \frac{48}{\sqrt{\pi}} \eta (1-\eta) \frac{\rho_s \phi_s^2}{d} g_o T^{3/2} \quad (2.19)$$

$$J_{visc} = 3\beta T \quad (2.20)$$

Radial distribution function

$$g_o = \frac{1}{1 - (\phi_s / \phi_{s,max})^{1/3}} \quad ; \quad \phi_{s,max} = 0.65 \quad (2.21)$$

Volumetric continuity

$$\phi_g + \phi_s = 1 \quad (2.22)$$

2.2 The modified microscopic two-fluid model

The microscopic two-fluid model is modified in the sense that the conventional kinetic theory of granular flows (KTGF), which provides closures for solid phase stresses, is modified to incorporate frictional effects. The conventional KTGF applies wherever kinetic-collisional effects are dominant and frictional effects are supposed not to be significant. Typical gas-solid fluidized flows, however, are very heterogeneous and present regions of high solid concentrations where friction may become relevant.

In the current work the modification of the KTGF advanced by Berzi and Vescovi (2015) is applied, which is an adaptation of a previous approach developed by Chialvo and Sundaresan (Chialvo and Sundaresan 2013). Both of those approaches were discussed, implemented into the MFIX code, and tested by C.C. Milioli (Milioli 2016). Reported tests showed that both approaches give similar results, with Berzi and Vescovi's implementation providing for more accurate results in dilute regions.

The conventional KTGF was originally developed for describing the rheology of continuum solid phases derived from the motion of inelastic monodisperse spherical particulates, accounting for kinetic-collisional effects only (Jenkins and Savage 1983; Lun et al. 1984; Gidaspow 1994; Garzó and Dufty 1999). Such conditions are suitable for regions of the flow under dilute conditions, and modifications in the theory have been proposed for also embracing dense regions by introducing interparticle friction coefficients into the rheology description of the derived continuum solid phases (Chialvo and Sundaresan 2013; Berzi and Vescovi 2015).

Chialvo and Sundaresan (2013) developed their frictional modifications over the conventional kinetic theory approach of Garzó and Dufty (1999). They performed discrete element method simulations for shear flows of frictional particles, and also continuum simulations under closures from the kinetic theory approach of Garzó and Dufty. Then they proposed modifications into Garzó and Dufty's correlations so that the results of both simulations match. Specifically, they introduced additional frictional stresses, and replaced the original restitution coefficient and radial distribution function by an effective restitution coefficient and a modified radial distribution function, respectively. The new frictional stresses were formulated as a function of an interparticle friction coefficient and a term accounting for frictional generation. As a result, a modified algebraic KTGF model was advanced, with formulations composed of alternative equations providing smooth transitions between dilute and dense regions.

Berzi and Vescovi (Berzi and Vescovi 2015) simplified the modified KTGF of Chialvo and Sundaresan (2013) by taking care of transition and dense regions alone, where friction may be relevant, while dilute regions are treated through the conventional KTGF of Lun et al. (1984).

Table 2 presents the modifications on the microscopic two-fluid model as applied in the current work. Basically, the correlations for the pressure and dynamic viscosity of the solid phase, and for the rate of dissipation of pseudo-thermal energy by collisions have been changed to account for friction. The pressure of the solid phase is modified by introducing a new radial distribution function which accounts for friction when the solid volume fraction goes above 0.4. The viscosity of the solid phase and the rate of dissipation of pseudo-thermal energy by collisions are both obtained by adding the respective kinetic parts (as provided by the conventional KTGF, given in Table 1) to new frictional parts, when the solid volume fraction goes above 0.49. Definitions for the various terms in the correlations in Table 2 can be found in Berzi and Vescovi (Berzi and Vescovi 2015).

Table 2 – Modifications on the microscopic two-fluid model (Berzi and Vescovi, 2014).

$$P_s = \rho_s \phi_s T + f_1 \rho_s T \quad (2.23)$$

$$\mu_s = \begin{cases} \mu_{s,k} & \phi_s < 0.49 \\ \mu_{s,k} + \mu_{s,f} & \phi_s \geq 0.49 \end{cases} \quad (2.24)$$

$$\mu_{s,f} = \rho_s d_p f_2 \sqrt{T} \quad (2.25)$$

$$J_{\text{coll},f} = \begin{cases} J_{\text{coll},k} & \phi_s < 0.49 \\ J_{\text{coll},f} & \phi_s \geq 0.49 \end{cases} \quad (2.26)$$

$$J_{\text{coll},f} = \frac{\rho_s}{d_p} \frac{f_3}{L} (T)^{3/2} \quad (2.27)$$

Where

$$f_1 = 2(1+e)\phi_s G \quad (2.28)$$

$$f_2 = \frac{8J}{5\pi^{0.5}} (\phi_s G) \quad (2.29)$$

$$f_3 = \frac{12}{\pi^{0.5}} \phi_s G (1 - e_{\text{eff}}^2) \quad (2.30)$$

$$G = \phi_s g_o \quad (2.31)$$

$$L = \left[\frac{15(1 - e_{\text{eff}}^2)}{2J} \right]^{1/3} (L^*)^{2/3} \quad (2.32)$$

$$g_o = f \frac{2 - \phi_s}{2(1 - \phi_s)^3} + (1 - f) \frac{2}{(\phi_{s,\text{max}} - \phi_s)} \quad (2.33)$$

$$f = \begin{cases} 1 & \phi_s < 0.4 \\ \frac{\phi_s^2 - 0.8\phi_s + \phi_{s,\text{max}}(0.8 - \phi_{s,\text{max}})}{0.8\phi_{s,\text{max}} - 0.16 - \phi_{s,\text{max}}^2} & \phi_s \geq 0.4 \end{cases} \quad (2.34)$$

$$\phi_{s,\text{max}} = 0.58 + (0.636 - 0.58) \exp(-4.5 C_f) \quad (2.35)$$

$$J = \frac{(1 + e)}{2} + \frac{\pi}{4} \frac{(3e - 1)(1 + e)^2}{[24 - (1 - e)(11 - e)]} \quad (2.36)$$

$$e_{\text{eff}} = e - \left[\frac{3}{2} C_f \exp(-3 C_f) \right] \quad (2.37)$$

$$L^* = \left(\frac{f_2}{f_3} \right)^{1/2} \left[\frac{26(1 - e_{\text{eff}})}{15} \left(\frac{\phi_s - 0.49}{\phi_{rcp} - \phi_s} \right) + 1 \right]^{3/2} ; \quad \phi_{rcp} = 0.64 \quad (2.38)$$

2.3 Filtered two-fluid model

Filtering operators applied over the two-fluid model conservative equations (Equations 2.1 to 2.4) give rise to the filtered two-fluid model equations. In filtered formulations dependent variables, $f(\mathbf{x}, t)$, are described as a composition of a filtered part added to a sub-grid fluctuation or unresolved part, that is:

$$f(\mathbf{X}, t) = \bar{f}(\mathbf{X}, t) + f'(\mathbf{X}, t) \quad (2.39)$$

The filtered part is defined as:

$$\bar{f}(\mathbf{X}, t) = \int_{\mathbf{X}} f(\mathbf{X}, t) G(\mathbf{X}) d(\mathbf{X}) \quad (2.40)$$

The filter function $G(x)$ is a sub-grid space cut that limits the size of the smaller scales to be resolved. The sub-grid filter is usually made to match with the numerical grid volume V , so that $G(x) = 1/V$ for any $X \in V$. Therefore,

$$\bar{f}(\mathbf{X}, t) = \frac{1}{V} \int_V f(\mathbf{X}, t) dV \quad (2.41)$$

While filtering the two-fluid model equations some filtered products of dependent variables with phase fractions do appear which need to be developed. This is done by applying Favre or mass weighed averaging. For a phase l , either gas or solid.

$$\overline{\phi_l(\mathbf{X}, t) f_l(\mathbf{X}, t)} = \tilde{f}_l(\mathbf{X}, t) \bar{\phi}_l(\mathbf{X}, t) \quad (2.42)$$

$$\tilde{f}_l(\mathbf{X}, t) = \frac{\int_V \phi_l(\mathbf{X}, t) f_l(\mathbf{X}, t) dV}{\int_V \phi_l(\mathbf{X}, t) dV} \quad (2.43)$$

As seen the equations of the filtered two-fluid model are presented in Table 3, the filtering procedure gives rise to two new terms in the momentum equations, in addition to those in the unfiltered conservative differential equations (as given in Table 1). One of the new terms accounts for the fluctuations on the buoyancy exerted by the gas over the solid phase. This buoyancy fluctuation is usually composed with the filtered drag thereby defining an effective interface

interaction force, usually referred to as effective drag force owing to the predominance of the drag in gas-solid fluidized flows. The other new term accounts for residual stresses in both the phases.

Table 3 – Filtered two-fluid model.

Filtered continuity and momentum conservation equations

$$\frac{\partial(\rho_s \bar{\phi}_s)}{\partial t} + \nabla \cdot (\rho_s \bar{\phi}_s \tilde{\mathbf{v}}_s) = 0 \quad (2.44)$$

$$\frac{\partial(\rho_g \bar{\phi}_g)}{\partial t} + \nabla \cdot (\rho_g \bar{\phi}_g \tilde{\mathbf{v}}_g) = 0 \quad (2.45)$$

$$\left[\frac{\partial(\rho_s \bar{\phi}_s \tilde{\mathbf{v}}_s)}{\partial t} + \nabla \cdot (\rho_s \bar{\phi}_s \tilde{\mathbf{v}}_s \tilde{\mathbf{v}}_s) \right] = -\nabla \cdot \bar{\boldsymbol{\sigma}}_s - \nabla \cdot \boldsymbol{\tau}'_s - \bar{\phi}_s \nabla \cdot \tilde{\boldsymbol{\sigma}}_g + (\mathbf{B}'_{gs} + \bar{\mathbf{f}}) + \rho_s \bar{\phi}_s \mathbf{g} \quad (2.46)$$

$$\left[\frac{\partial(\rho_g \bar{\phi}_g \tilde{\mathbf{v}}_g)}{\partial t} + \nabla \cdot (\rho_g \bar{\phi}_g \tilde{\mathbf{v}}_g \tilde{\mathbf{v}}_g) \right] = -\bar{\phi}_g \nabla \cdot \tilde{\boldsymbol{\sigma}}_g - \nabla \cdot \boldsymbol{\tau}'_g - (\mathbf{B}'_{gs} + \bar{\mathbf{f}}) + \rho_g \bar{\phi}_g \mathbf{g} \quad (2.47)$$

Filtered volumetric continuity

$$\bar{\phi}_g + \bar{\phi}_s = 1 \quad (2.48)$$

Closures

Filtered deviatoric stresses and effective stresses

$$\tilde{\boldsymbol{\sigma}}_g = \left[\tilde{P}_g - \left(\lambda_g + \frac{2}{3} \mu_g \right) (\nabla \cdot \tilde{\mathbf{v}}_g) \right] \mathbf{I} - 2\mu_g \tilde{\mathbf{S}}_g = P_{\text{fil},g} \mathbf{I} - 2\mu_{\text{fil},g} \tilde{\mathbf{S}}_g \quad (2.49)$$

$$\bar{\boldsymbol{\sigma}}_s = \left[\bar{P}_s - \left(\lambda_s + \frac{2}{3} \mu_s \right) (\nabla \cdot \mathbf{v}_s) \right] \mathbf{I} - 2\bar{\mu}_s \tilde{\mathbf{S}}_s = P_{\text{fil},s} \mathbf{I} - 2\mu_{\text{fil},s} \tilde{\mathbf{S}}_s \quad (2.50)$$

Residual stresses

$$\boldsymbol{\tau}'_\ell = \rho_\ell \bar{\phi}_\ell \mathbf{v}_\ell \mathbf{v}_\ell - \rho_\ell \bar{\phi}_\ell \tilde{\mathbf{v}}_\ell \tilde{\mathbf{v}}_\ell = P_{\text{eff},\ell} \mathbf{I} - 2\mu_{\text{eff},\ell} \tilde{\mathbf{S}}_\ell \quad \ell = g, s \quad (2.51)$$

Filtered strain rate tensor

$$\tilde{\mathbf{S}}_\ell = \frac{1}{2} \left[\nabla \tilde{\mathbf{v}}_\ell + (\nabla \tilde{\mathbf{v}}_\ell)^T \right] - \frac{1}{3} (\nabla \cdot \tilde{\mathbf{v}}_\ell) \mathbf{I} \quad \ell = g, s \quad (2.52)$$

Filtered drag force

$$\bar{\mathbf{f}} = \overline{\beta(\mathbf{u} - \mathbf{v})} \quad (2.53)$$

Buoyancy fluctuation force

$$\mathbf{B}'_{gs} = -\left[\overline{\phi_s \nabla \cdot \boldsymbol{\sigma}_g} - \bar{\phi}_s \nabla \cdot \bar{\boldsymbol{\sigma}}_g\right] \approx -\left[\overline{\phi_s \nabla P_g} - \bar{\phi}_g \nabla \bar{P}_g\right] \quad (2.54)$$

Effective drag force

$$\beta_{\text{eff}} = \frac{\overline{\beta(\mathbf{v}_g - \mathbf{v}_s)}}{(\tilde{\mathbf{v}}_g - \tilde{\mathbf{v}}_s)} - \frac{\left[\overline{\phi_s \nabla P_g} - \bar{\phi}_s \nabla \bar{P}_g\right]}{(\tilde{\mathbf{v}}_g - \tilde{\mathbf{v}}_s)} \quad (2.55)$$

The coefficient β_{eff} given by Equation 54 is usually expressed in terms of a drag coefficient correction related to the filtered drag coefficient, $\bar{\beta}$, given by the microscopic model in Equation 6 as evaluated in terms of filtered variables (i.e. $\bar{\phi}_s, \bar{\phi}_g, \tilde{\mathbf{v}}, \tilde{\mathbf{u}}$). The drag coefficient correction is defined as:

$$H = 1 - \frac{\beta_{\text{eff}}}{\bar{\beta}} \quad (2.56)$$

Therefore, the effective drag force is cast as:

$$\mathbf{B}'_{gs} + \bar{\mathbf{f}} = (1 - H) \bar{\beta} (\tilde{\mathbf{u}} - \tilde{\mathbf{v}}) \quad (2.57)$$

The filtered and residual pressures and viscosities, which account for the filtered deviatoric and residual stresses in Table 3, are given by:

$$P_{\text{fil},g} = \tilde{P}_g - \frac{2}{3} \mu_g (\nabla \cdot \tilde{\mathbf{v}}_g) \quad (\text{assuming } \lambda_g = 0) \quad (2.58)$$

$$\mu_{\text{fil},g} = \mu_g \quad (2.59)$$

$$P_{\text{fil},s} = \bar{P}_s - \overline{\left(\lambda_s + \frac{2}{3} \mu_s\right)} (\nabla \cdot \mathbf{v}_s) \quad (2.60)$$

$$\mu_{\text{fil},s} = \bar{\mu}_s \quad (2.61)$$

$$P_{\text{res},\ell} = \frac{1}{3} \text{tr}(\boldsymbol{\tau}'_\ell) \quad (2.62)$$

$$\mu_{\text{res},\ell} = \frac{|\tau'_{\text{shear},\ell}|}{2|\tilde{\mathbf{S}}_{\text{shear},\ell}|} \quad (2.63)$$

2.4 Numerical Procedure

The complex system of coupled non-linear partial differential equations of the two-fluid models can only be solved by numerical procedures. There are different options available for that, such as the commercial codes CFX and Fluent, and the free open source code MFIX. All of those codes are stable, and widely used to solve two-phase flows under two-fluid modeling. Numerical models in commercial appliances like CFX and Fluent do not allow access to the source code, thereby preventing any modifications on formulations and boundary conditions. In the present work the MFIX code is used since it is free, and since it allows for code modifications, which are required.

MFIX (Multiphase Flow with Interphase exchanges) (Syamlal et al. 1993) is a numerical code specific for gas-solid flow simulations, which includes two-fluid based formulations, developed and made available by NETL (National Energy Technology Laboratory, DOE-USA). Its source code is open so that any modifications and implementations on both formulation and boundary conditions are allowed. MFIX is a FORTRAN written parallelized code. The governing equations in MFIX's two-fluid model are discretized through the finite volume method. The resulting numerical model is solved through a point by point numerical technique. Diffusive terms are discretized following the second order central differencing scheme.

For advection terms there are various alternative discretizing methods, ranging from the first order upwind method up to higher order TVD procedures. The pressure-velocity coupling is solved through the SIMPLE algorithm. The numerical code of MFIX is fully described in (Syamlal et al. 1993; Cabezas-Gómez et al. 2006), and tested some of the discretization procedures for advective terms in MFIX, and found the Superbee procedure to provide the best results for the simulation of a particular riser flow. This procedure is followed in the current work.

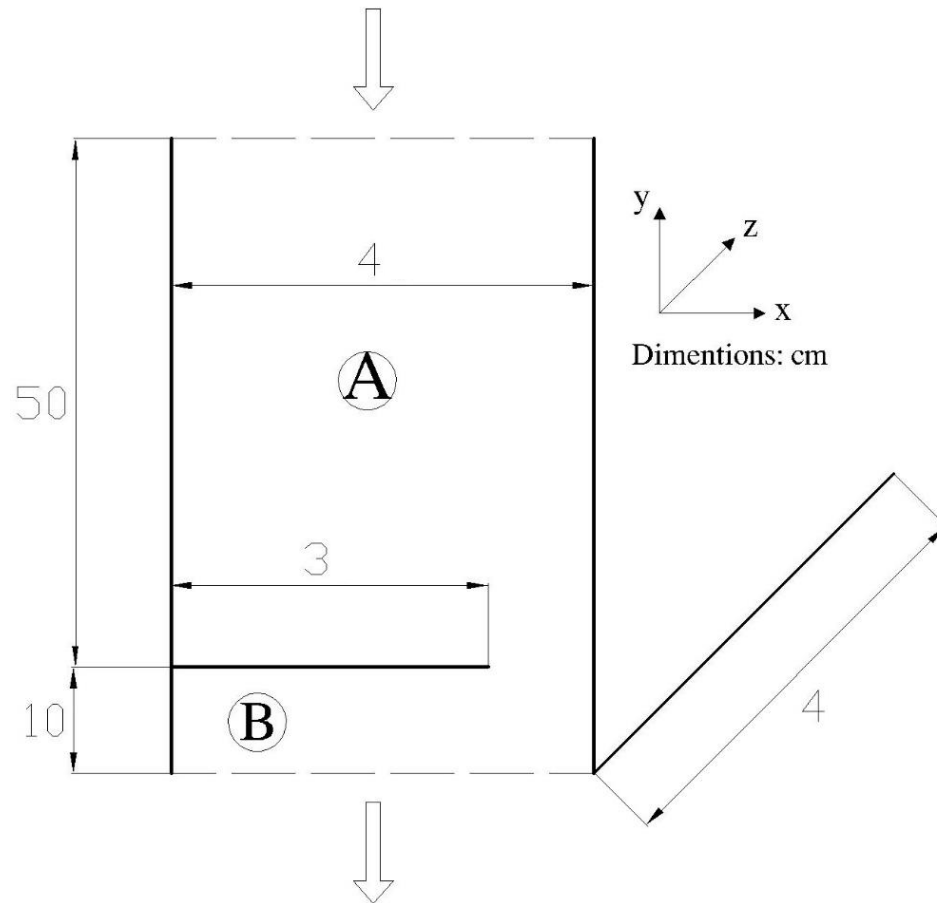
2.5 Test of the friction model and set up of the interparticle friction coefficient

Schneiderbauer et al. (2012) presents experimental results for a bin discharge application with a particulate size very close to that considered in the present work (See Table 5). Those results are used here with two different purposes: I. to evaluate the friction model implementation; II: to set up a suitable value for the interparticle friction coefficient to be applied on the simulations under fluidization conditions (See section 2.6). In order to do a bin discharge simulation is performed following Milioli (2016).

Bin discharge is an application where frictional effects are dominant. Experiment shows that, as the process starts, the discharge rate quickly reaches a plateau that is kept constant until the bin is almost empty. The magnitude of the plateau of discharge rate is a function of the interparticle friction coefficient.

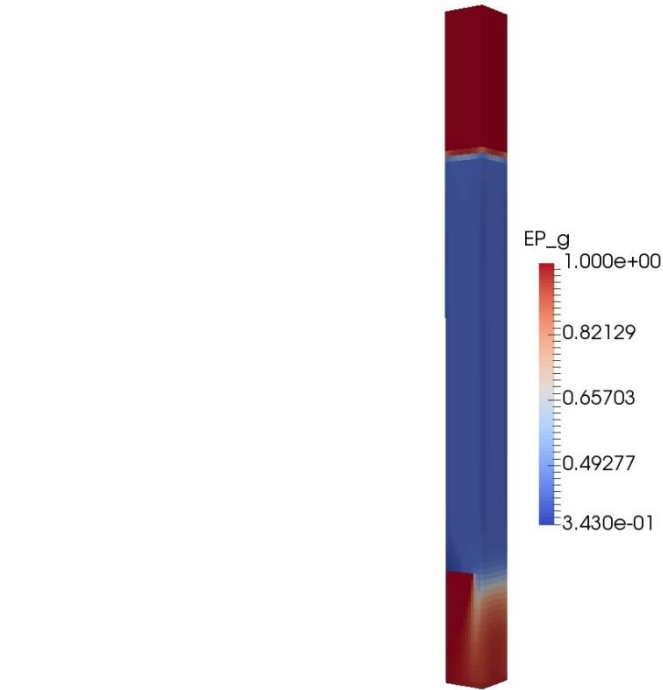
The simulation of the bin discharge application was done with the MFIX two-fluid model including the modifications to account for friction, as described in section 2.2. The schematics of the bin discharge problem is given in Figure 2 and the details of the simulation parameters are provided in Table 4. The simulations were performed on a fine mesh with $16 \times 120 \times 8$ grids in 3D, a resolution that ensures grid independence of the numerical solution. Alongside with partial-slip wall boundary conditions of Johnson & Jackson for the vertical boundaries, various interparticle friction coefficients were imposed ($C_f = 0.0, 0.1, 0.2, 0.3, 0.5$). The moment the simulation starts, solid starts discharging through the bin due to the effect of gravity. Figure 3 is an instantaneous snapshot of the solid discharge.

Figure 2 – Schematics of the bin discharge problem.



Source: Elaborated by the author

Figure 3 – Snapshot of the bin discharge.



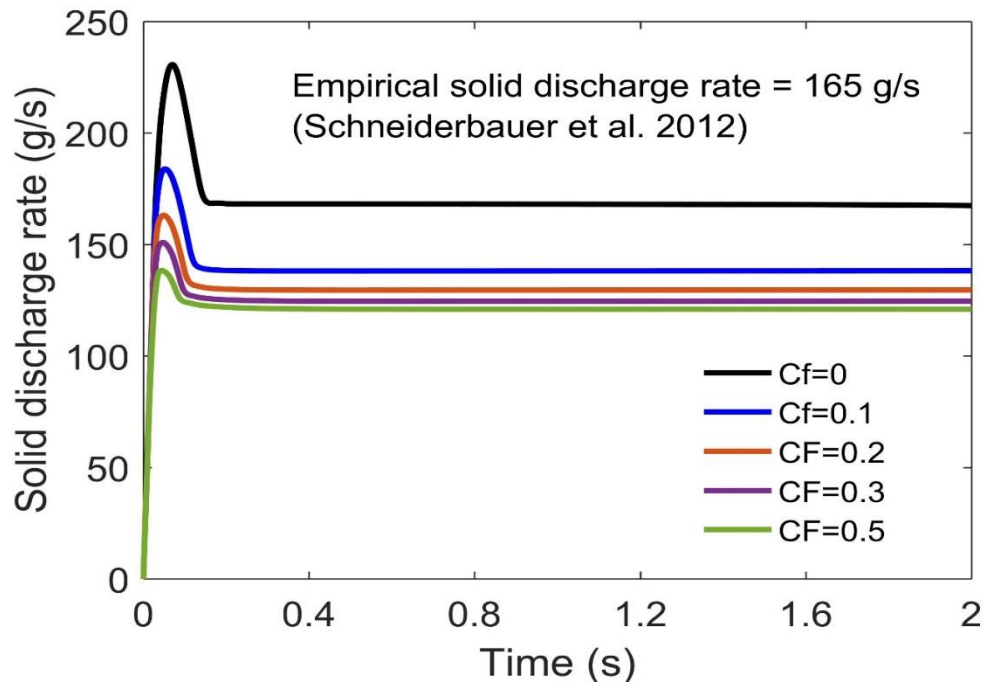
Source: Elaborated by the author

Table 4 – Bin discharge simulation parameters (Schneiderbauer et al. 2012)

Physical properties of gas and solid	Initial Conditions	Boundary Conditions
$d_p = 0.0875 \text{ cm}$	$T_g = 300 \text{ K}$	Inlet gas Pressure = $1.01 \times 10^6 \text{ g/cm} \cdot \text{s}^2$
$\rho_p = 2.5 \text{ g/cm}^3$	$P_g = 1.01 \times 10^6 \text{ g/cm} \cdot \text{s}^2$	Outlet gas Pressure = $1.01 \times 10^6 \text{ g/cm} \cdot \text{s}^2$
$\rho_g = 0.001224 \text{ g/cm}^3$	$P_s = 0$	Vertical walls: Johnson&Jackson (partial slip)
$\mu_g = 1.78 \times 10^{-4} \text{ g/cm} \cdot \text{s}$	$T = 1 \text{ cm}^2/\text{s}^2$	Horizontal wall insert (non-slip)
$e = 0.8$	$v_{g,x} = v_{g,y} = v_{g,z} = 0$	
	$v_{s,x} = v_{s,y} = v_{s,z} = 0$	
	$\phi_s = 0.58 \text{ (in A)}$	
	$\phi_s = 0.0 \text{ (in B)}$	

Figure 4 presents the computed temporal variation of the solid discharge rate (\dot{m}) for the various simulations under the different interparticle friction coefficient that were considered. At the beginning the discharge is characterized by a rapid increase of the mass flow rate, and a constant discharge rate is reached in less than 0.2 s. As seen, the expected plateau is reached even for $C_f = 0$, while its value does not match the experimental data (Schneiderbauer et al. 2012). It is known from experiment that the considered particulate presents an interparticle friction coefficient around 0.3, and that the plateau of solid discharge rate occurs at about 165 g/s. The present simulations, however, indicate that this plateau is found for a C_f approaching 0, which is in disagreement with experiment. The mispredictions is possibly related to differences of conditions between experiment and simulations. The experiment is performed for real particles (not perfectly spherical), and for a narrow range of particle sizes. The simulations, on the other hand, are done for spherical particles and for a unique average particle size. In view of the observed discrepancy, the experimental $C_f = 0.3$ is assumed in the current work.

Figure 4 – Solid discharge rate in g/s as a function of time (s).



Source: Elaborated by the author

2.6 Simulations Set up

Highly resolved simulations (HRS) are carried out for a typical fluid catalytic cracking particulate in a 2D periodic domain, under domain average gas Reynolds numbers and particle concentrations covering dense gas-fluidized topologies. The relevant parameter values of physical properties of gas and solid can be found in Table 5.

Table 5 – Physical properties of gas and solid

Physical properties of gas and solid		
d_p	$7.5 \times 10^{-6} \text{ m}$	Particle diameter
ρ_s	1500 Kg/m^3	Particle density
ρ_g	1.3 Kg/m^3	Gas density
μ_g	$1.8 \times 10^{-5} \text{ Kg/m.s}$	Gas viscosity
e	0.9	Coefficient of restitution
V_t	0.2184 m/s	Terminal settling velocity
V_t^2/g	0.00487 m	Characteristic length
V_t/g	0.0223 s	Characteristic time
$\rho_s V_t^2$	71.55 Kg/ms^2	Characteristic stress
Fr_{dp}	64.83	Froude number

The simulations were done by imposing the domain average solid volume fraction $\langle \phi_s \rangle$ at specific values for each simulation, 0.35, 0.45 and 0.50. $\langle \phi_s \rangle$ is enforced through the initial conditions, and is kept constant through the simulations owing to continuity and to the periodical boundaries. The domain average gas Reynold number is also set constant in each simulation at controlled values. The domain average gas Reynolds number $\langle Re_g \rangle$ based on particle diameter is defined as:

$$Re_p = \frac{\rho_g \langle v_{g,y} \rangle \langle \phi_s \rangle d_p}{\mu_g} \quad (2.64)$$

In the simulations for different $\langle \phi_s \rangle$, the ratio $\langle Re_g \rangle / \langle Re_g \rangle_{susp}$ was set unchanged, at values 1.00, 8.15, 16.30 and 24.45. This range was found suitable for producing streams closing towards pneumatic transport for the different $\langle \phi_s \rangle$ that were enforced. $\langle Re_g \rangle / \langle Re_g \rangle_{susp}$ stands for the ratio between the domain average gas Reynolds number and its value under suspension like conditions.

$\langle Re_g \rangle_{susp}$ results from imposing a gas pressure gradient in the axial direction of the domain that exactly matches the gravity acting on the gas-solid mixtures.

$$\frac{\Delta P_g}{Y_{\text{length}}} = \rho_s \langle \phi_s \rangle g + \rho_g \langle \phi_g \rangle g \quad (2.65)$$

Where Y_{length} is the length of the domain in the axial direction. Regarding the investigation of the effect of interparticle friction, all simulations were set for two different cases: $C_f = 0$ and $C_f = 0.3$. Table 6 shows the complete simulations schedule that was followed.

Table 6 – Set up different simulation for fluidization

		$\langle \phi_s \rangle$					
		0.35		0.45		0.50	
		Interparticle friction coefficient (C_f)					
		0.0	0.3	0.0	0.3	0.0	0.3
$\langle Re_g \rangle / \langle Re_g \rangle_{susp}$	1.00	Sim1	Sim5	Sim9	Sim13	Sim17	Sim21
	8.15	Sim2	Sim6	Sim10	Sim14	Sim18	Sim22
	16.30	Sim3	Sim7	Sim11	Sim15	Sim19	Sim23
	24.45	Sim4	Sim8	Sim12	Sim16	Sim20	Sim24

A two-dimensional square domain of 16×16 cm was considered under periodic boundaries in all directions. A numerical mesh of 128×128 grids was applied resulting a grid size of 1.25×1.25 mm (grid sizes between 1 and 2 mm do provide grid size reasonably independent filtered results Agrawal et al. 2001).

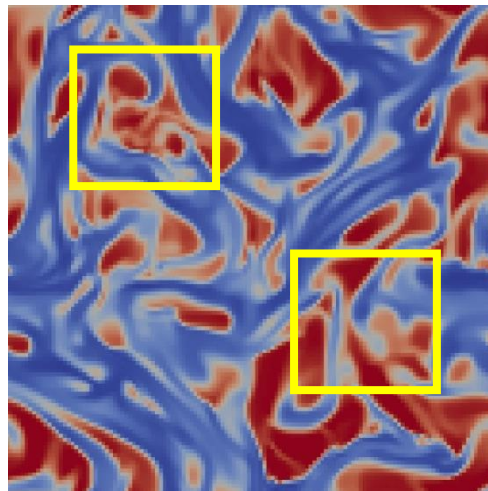
2.7 Filtering Procedure

The simulations give rise to fields of dependent variables over the grid mesh, and a filtering procedure with a filter size of 2cm (16 cells) on both directions is carried out providing for filtered data. A unique filter size is considered which is compatible with cell sizes in large-scale simulations.

Figure 5 shows an instantaneous snapshot of the particle volume fraction field in one of the performed simulations. As can be seen filtering over different regions at any given time are not equivalent as different regions will possibly hold different averaged solid volume fractions. Thus, one cannot simply lump the results obtained over all the regions; instead, the results must be grouped into bins based on suitable markers, and statistical averages must be performed within each bin to extract useful information.

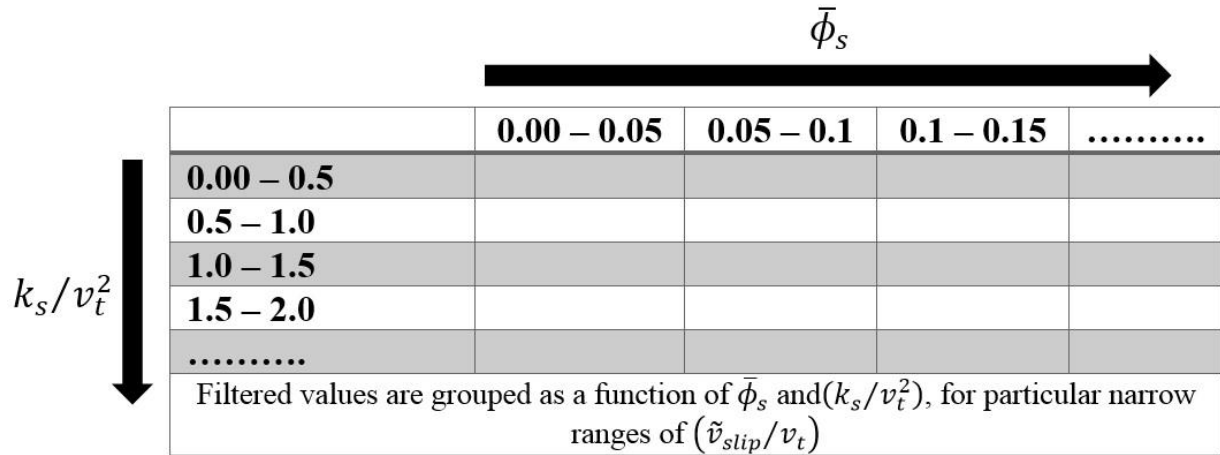
At first, following literature (Milioli et al. 2013), a two-marker filtering was considered, with the filtered solid volume fraction and the filtered slip velocity taken as 1st and 2nd marker, respectively. In this case, the filtered values are grouped in a double entry table, where the entries are the first and second markers. Thus, the obtained averages of all the filtered values are stored as functions of those two parameters.

Figure 5 – Snapshot of the particle volume fraction field.



Source: Elaborated by the author

Figure 6 – Three-markers binning procedure (for particular filter size, $\langle \phi_s \rangle$ and $\langle \text{Re}_g \rangle / \langle \text{Re}_g \rangle_{susp}$)



Source: Elaborated by the author

In order to improve the accuracy of the filtered results, so as to allow for a better assessment of frictional effects a 3rd marker was introduced. The filtered kinetic energy of the velocity fluctuations of the solid phase (k_s) was chosen as the additional marker owing to its relevance in gas-solid fluidized flows (Schneiderbauer 2017). k_s is defined as:

$$k_s = \frac{1}{2} \mathbf{v}_{s,i}'' \mathbf{v}_{s,i}'' \approx \frac{1}{2} \frac{tr(\tau'_{s,ij})}{\rho_s \bar{\phi}_s} \quad (2.66)$$

Where:

$$\mathbf{v}_s'' = \mathbf{v}_s - \tilde{\mathbf{v}}_s \quad (2.67)$$

In this work, binning is performed for the filtered solid volume fraction as a 1st marker, and filtered kinetic energy of solid velocity fluctuations as a 2nd marker, for narrow ranges of filtered slip velocity as a 3rd marker. Figure 6 illustrates this three-marker binning procedure.

The storage of filtered data is done over 64×80 bins, meaning 64 gaps of filtered solid volume fraction and 80 gaps of filtered kinetic energy of the solid (this binning resolution was found adequate based on previous works (Sarkar et al. 2016)). In summary, one must consider a suitable number of snapshots of the flow field in the statistical steady state regime (See section 3.1.1), so that good averaging statistics are collected. Then a window (filter) is defined over the domain comprising a number of numerical cells. Averaging over this region provides averaged or filtered data. The window is made to move in space all over the domain and in time through the

various snapshots, and the collected averaged data are classified by ranges of suitable markers and stored in bins.

3 RESULTS AND DISCUSSION

Ultimately, the goals of this research are summarized in two cases as:

Case 1: 3rd marker analysis: Analyses are provided for relevant filtered parameters (H , $P_{\text{fil},s}$, $\mu_{\text{fil},s}$, $P_{\text{eff},s}$, $\mu_{\text{res},s}$), for $\langle\phi_s\rangle = 0.35, 0.45, 0.50$ and gas Reynolds number ratios $\langle\text{Re}_g\rangle/\langle\text{Re}_g\rangle_{\text{susp}} = 1.00, 8.15, 16.30, 24.45$. Results are shown for the filtered parameters as a function of inside filtered parameters ($\bar{\Phi}_s, \tilde{V}_{\text{slip}}, k_s$) and the macro-scale parameters of ($\langle\phi_s\rangle$ and $\langle\text{Re}_g\rangle/\langle\text{Re}_g\rangle_{\text{susp}}$) that were imposed.

Case 2: Interparticle friction analysis: Analyses are carried out similar to those of case 1, but including interparticle friction. In this case results for $C_f = 0.3$ are compared against those of case 1 for $C_f = 0$.

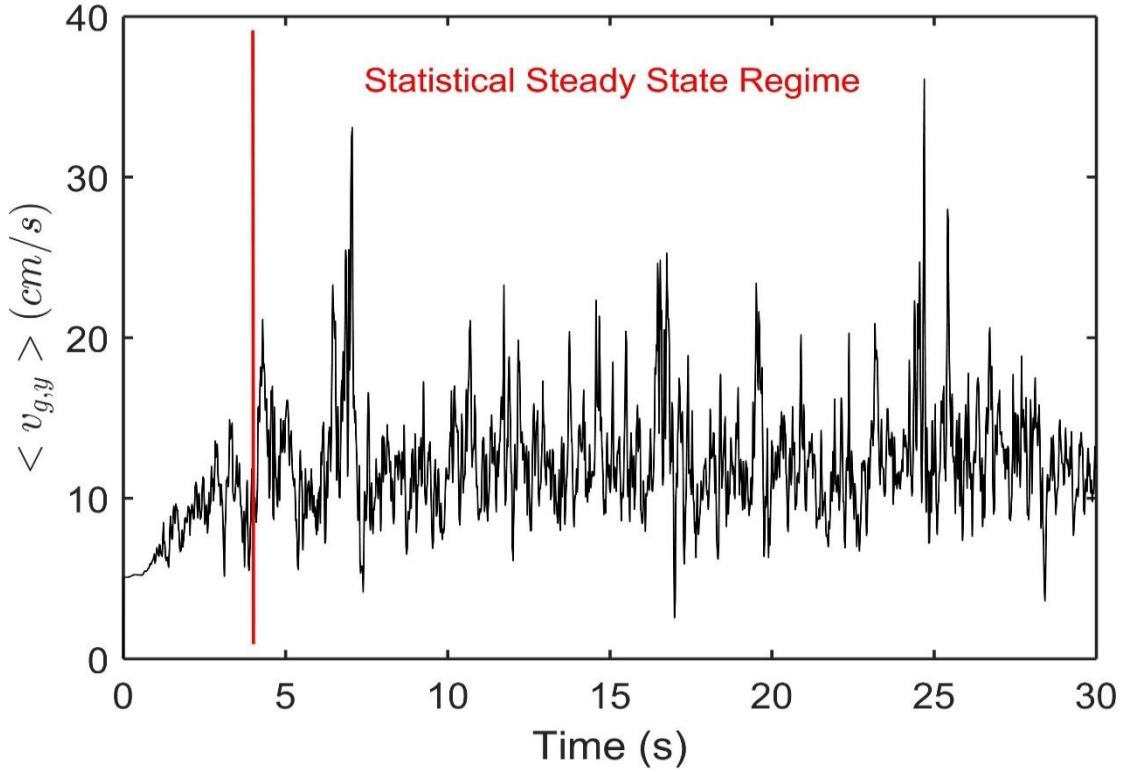
3.1 Case 1: 3rd marker analysis

Among the various filtered parameters of interest, the current analysis concentrates on the drag coefficient correction H (Equation 2.56), the solid residual pressure and viscosity $P_{\text{res},s}$ and $\mu_{\text{res},s}$ (Equation 2.62 and Equation 2.63) and the solid filtered pressure and viscosity $P_{\text{fil},s}$ and $\mu_{\text{fil},s}$ (Equation 2.60 and Equation 2.61). Before addressing those results, the statistical steady state regime and the flow topology are briefly described.

3.1.1 Statistical steady state regime

All the results presented in this work were obtained under statistical steady state conditions. Rigorously this condition is reached when all the statistical moments of all flow variables start to oscillate in time around well-defined averages. In gas-solid fluidized flows, however, statistical steady state is usually assumed when the mean value of the relevant variables reach their well-defined averages. Figure 7 illustrates this situation for the domain average gas velocity from one of the performed simulations. Departing from an initial condition (zero), the domain average gas velocity evolves through the numerical iterations (and in time) over a transient stage, until the statistical steady state regime is reached.

Figure 7 – Time evolution of the domain average axial gas velocity in the simulation for $\langle \phi_s \rangle = 0.35$ and $\langle \text{Re}_g \rangle / \langle \text{Re}_g \rangle_{\text{susp}} = 1$

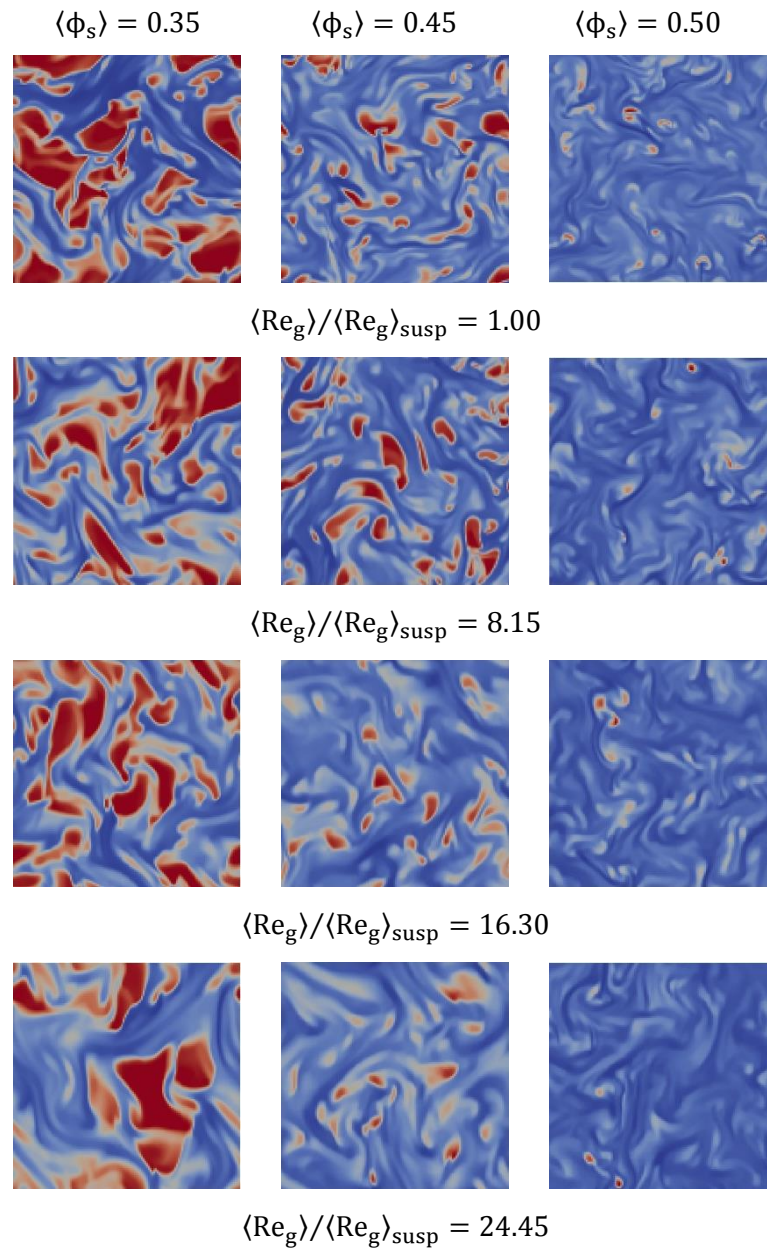


Source: Elaborated by the author

3.1.2 Flow Topology

Figure 8 shows how the flow topology is affected by $\langle \text{Re}_g \rangle$ and $\langle \phi_s \rangle$. The figure shows snapshots of the flow for $\langle \phi_s \rangle = 0.35, 0.45$ and 0.50 (columns), and gas Reynolds number ratios $\langle \text{Re}_g \rangle / \langle \text{Re}_g \rangle_{\text{susp}} = 1.00, 8.15, 16.30$ and 24.45 (rows), at statistical steady state conditions. The results are for the cases without enforced Interparticle friction coefficient, $C_f = 0$. As seen, the two macro-scale parameters considerably affect the flow topology. By increasing the domain average solid volume fraction $\langle \phi_s \rangle$ from 0.35 to 0.50 the solid structures become denser and heavier. On the other hand, while increasing the gas Reynolds number ratios $\langle \text{Re}_g \rangle / \langle \text{Re}_g \rangle_{\text{susp}}$ from 1.00 up to 24.45, the solid becomes more uniformly distributed throughout the domain and the flow tends to be more homogeneous.

Figure 8 – Plots of solid volume fraction in the domain inside the statistical steady state regime, for simulations with dense domain average solid fractions $\langle\phi_s\rangle = 0.35, 0.45$ and 0.50 (columns), and gas Reynolds number ratios $\langle\text{Re}_g\rangle/\langle\text{Re}_g\rangle_{\text{susp}} = 1, 8.15, 16.30$ and 24.45 (rows), and $C_f = 0$. (blue and red related to solid and gas phase, respectively).



Source: Elaborated by the author

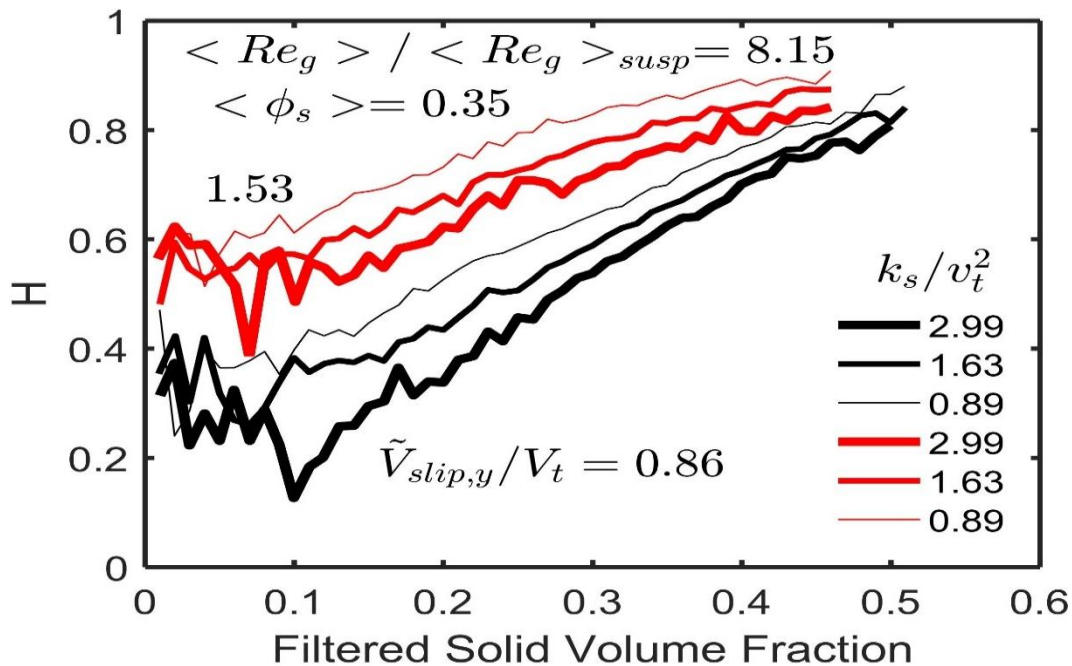
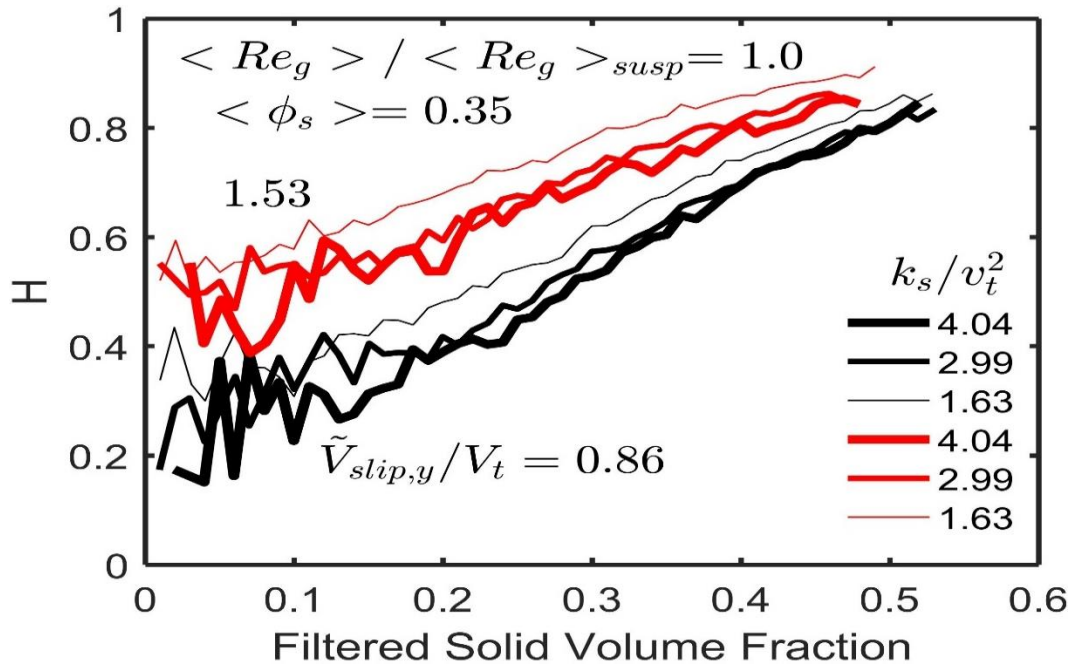
3.1.3 Drag Coefficient Correction

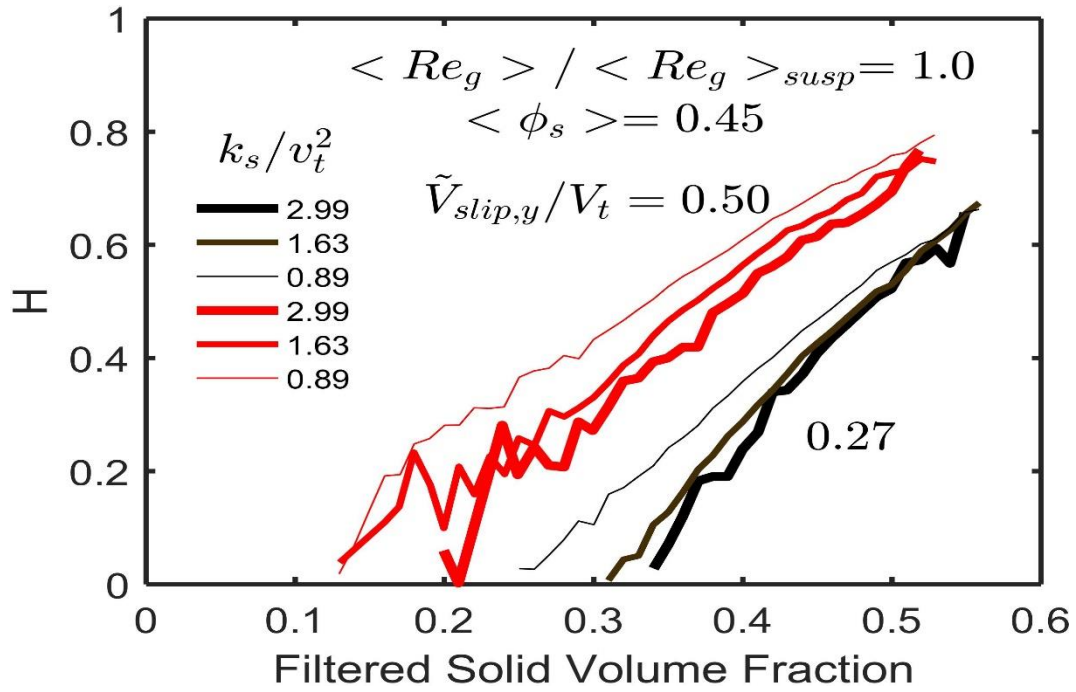
The drag coefficient correction H is a correction applied over the filtered Wen and Yu's drag coefficient, which stands for homogeneous flows. H closing to zero means a topology closing towards homogeneity. Otherwise, as a flow becomes more and more heterogeneous the effective drag progressively decreases and H grows higher.

Figure 9 shows H as a function of the filtered solid volume fraction $\bar{\phi}_s$ for the domain average solid volume fraction $\langle\phi_s\rangle = 0.35, 0.45$ and 0.50 , for gas Reynolds number ratios $\langle Re_g \rangle / \langle Re_g \rangle_{susp} = 1.00$ and 8.15 . The results stand for different dimensionless filtered axial slip velocities $\tilde{v}_{slip,y}/v_t$, for the dimensionless filter size $\Delta f/(v_t^2/g) = 4.112$, and for various dimensionless filtered kinetic energy of the solid velocity fluctuations k_s/v_t^2 . In the Appendix A results are also presented for $\langle Re_g \rangle / \langle Re_g \rangle_{susp} = 16.30$ and 24.45 .

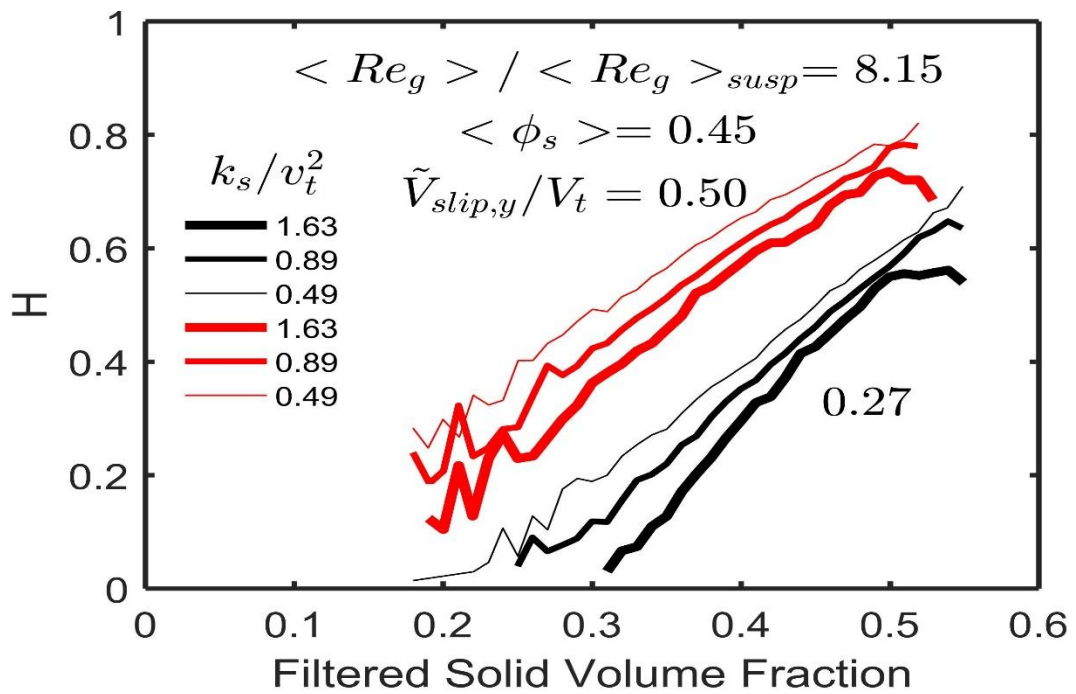
Figure 9 shows that H changes significantly with the variations of $\bar{\phi}_s$, k_s/v_t^2 and $\tilde{v}_{slip,y}/v_t$. As clearly seen, the higher the filtered solid volume fraction and the higher the filtered slip velocity, the higher H becomes for all $\langle\phi_s\rangle$ and $\langle Re_g \rangle / \langle Re_g \rangle_{susp}$. This implies that higher filtered solid volume fractions and higher filtered slip velocities are related to growing non-homogeneities on the flow. It is also that, for a particular $\tilde{v}_{slip,y}/v_t$, H decreases as k_s/v_t^2 grows higher, showing that the flow become more homogeneous as the solid velocity fluctuations (that define K_s) grow higher. This pattern is clear for $\langle\phi_s\rangle = 0.35$ and 0.45 , for both the values of $\langle Re_g \rangle / \langle Re_g \rangle_{susp}$ (Figures 9a, b, c, d). For $\langle\phi_s\rangle = 0.50$ K_s loses relevance as a marker (Figures 9e, f). Additionally, a systematic correlation is observed of H to all the three markers with the profiles coming closer as the filtered solid volume fraction grows higher. The results of H for higher $\langle Re_g \rangle / \langle Re_g \rangle_{susp}$ (16.30 and 24.45) in Appendix A are similar to those in Figure 9, except that the loosing relevance of K_s as a marker is anticipated to $\langle\phi_s\rangle = 0.45$.

Figure 9 – Drag Coefficient Correction, H , as a function of the filtered solid volume fraction $\bar{\phi}_s$ for the domain average solid volume fractions $\langle \phi_s \rangle = 0.35, 0.45$ and 0.50 and for gas Reynolds number ratios $\langle Re_g \rangle / \langle Re_g \rangle_{susp} = 1$ and 8.15 . The results stand for different dimensionless filtered axial slip velocities \tilde{v}_{slip} / v_t (black and red), for the dimensionless filter size $\Delta_f / (v_t^2 / g) = 4.112$, and for various dimensionless filtered kinetic energy of the solid velocity fluctuations k_s / v_t^2 (with different thickness). All graphs for $C_f = 0$.

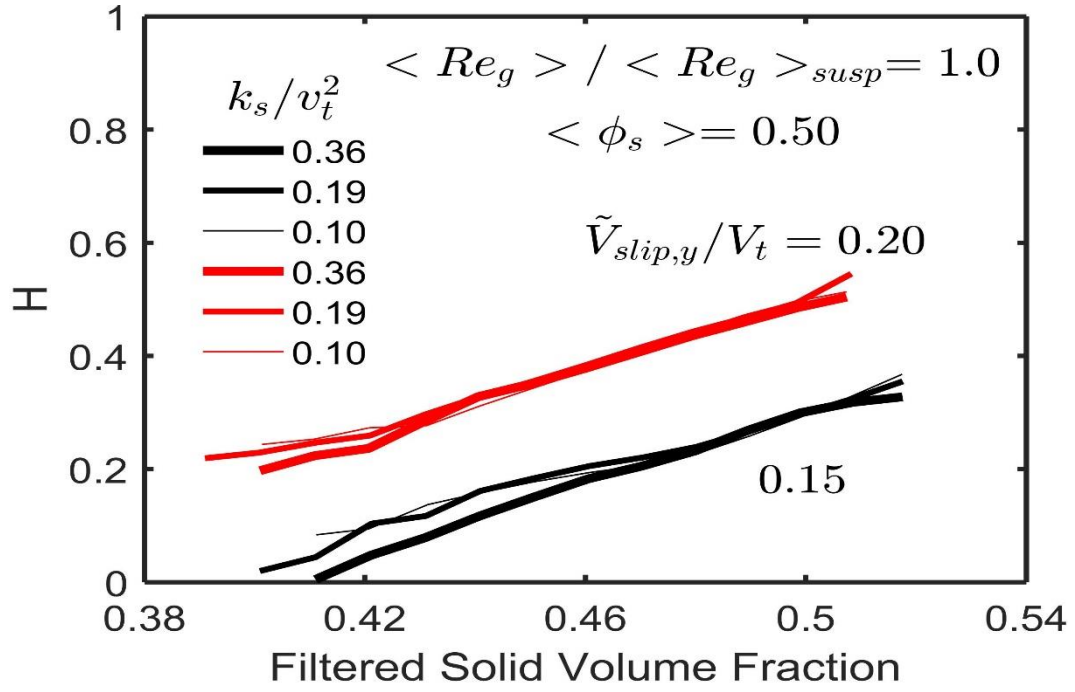




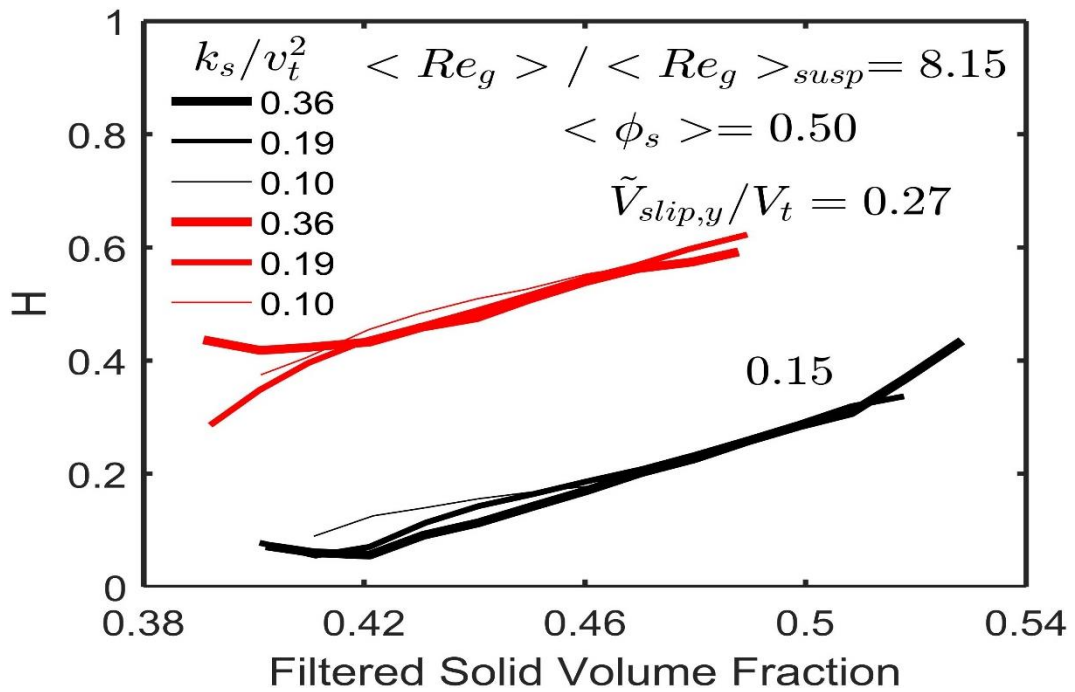
(c)



(d)



(e)



(f)

Source: Elaborated by the author

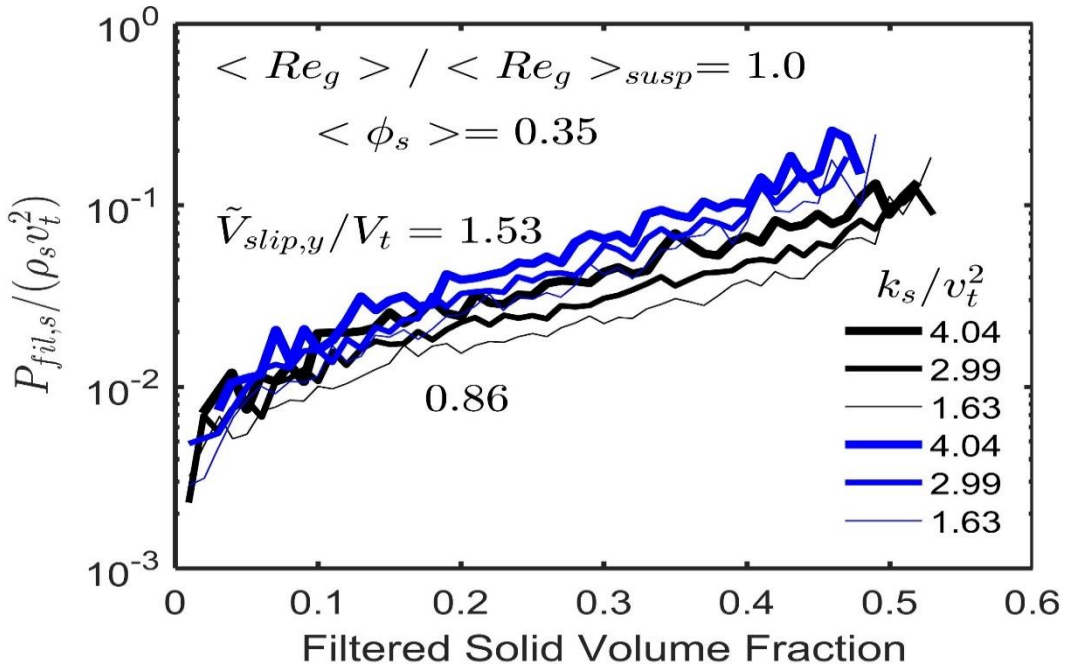
3.1.4 Filtered pressure and dynamic viscosity of the solid phase

Figures 10 and 11 show the variation of the dimensionless filtered solid pressure $P_{\text{fil},s}$ and dynamic viscosity $\mu_{\text{fil},s}$, respectively, for the same conditions as in figure 9. In the Appendix A results are also presented for $\langle \text{Re}_g \rangle / \langle \text{Re}_g \rangle_{\text{susp}} = 16.30$ and 24.45.

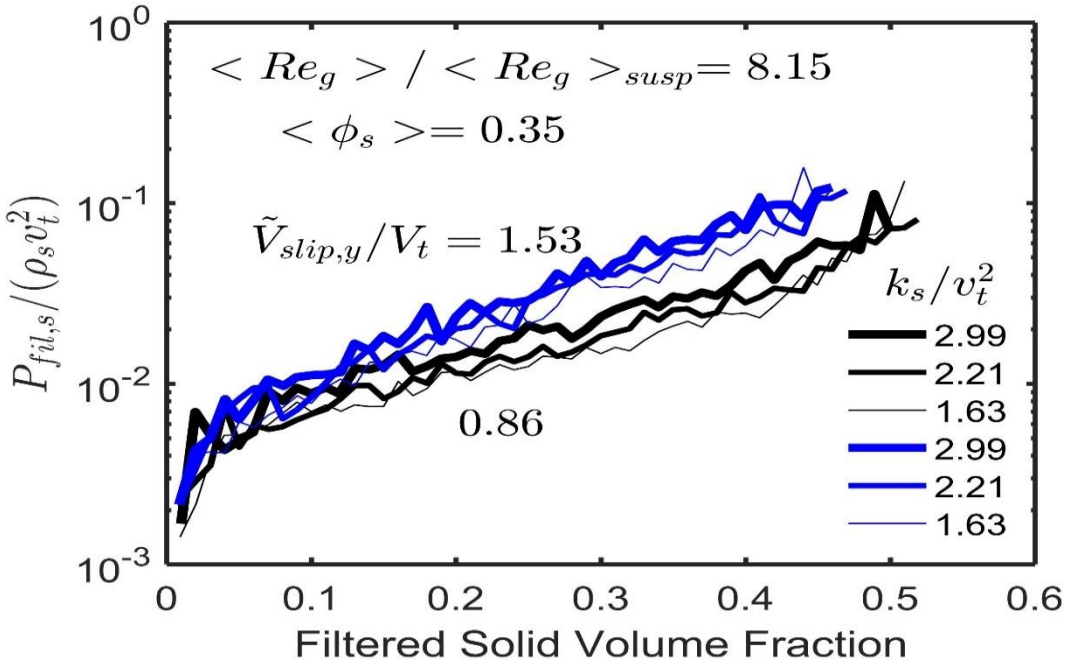
As seen, there are significant effects of the filtered solid volume fraction, filtered slip velocity and filtered kinetic energy of the solid velocity fluctuations over both the filtered parameters. The response of $P_{\text{fil},s}$ and $\mu_{\text{fil},s}$ to $\langle \text{Re}_g \rangle$ ultimately comes from the correlation of those parameters to the filtered granular temperature. At the micro-scale, the solid pressure and viscosity derived from the kinetic theory of granular flows are both strong functions of the granular temperature (Equations 2.14, 2.23 and 2.25). At the meso-scale, as a consequence, the counterpart filtered parameters also become strong functions of the filtered granular temperature. The observed decreasing of $P_{\text{fil},s}$ and $\mu_{\text{fil},s}$ as $\langle \text{Re}_g \rangle$ grows higher is, indeed, a consequence of the filtered granular temperature growing lower (not shown), owing to the more homogeneous conditions provided by the higher domain average gas Reynolds numbers (as seen in Figure 8). Under more homogeneous conditions all field fluctuations become smaller, including those of solid velocity fluctuations that define the granular temperature (not shown). As increase of $\langle \phi_s \rangle$ has the same effect of an increase of $\langle \text{Re}_g \rangle$, which is due to lower granular temperatures caused by lower solid velocity fluctuations, meaning more homogeneous flow conditions (as seen in Figure 8). This result is not clearly seen in Figures 10 and 11 because for the different $\langle \phi_s \rangle$ different values of $\tilde{v}_{\text{slip},y}/v_t$ were selected for conditions of higher occurrence in the flow field.

All the graphs in Figure 10 and 11 also show that, for particular values of $\tilde{v}_{\text{slip},y}/v_t$, both $P_{\text{fil},s}$ and $\mu_{\text{fil},s}$ increases as k_s/v_t^2 grows higher. Higher k_s/v_t^2 result from higher solid velocity fluctuations (that define k_s), which also mean higher granular temperature, and therefore higher $P_{\text{fil},s}$ and $\mu_{\text{fil},s}$. The results of $P_{\text{fil},s}$ and $\mu_{\text{fil},s}$ for higher $\langle \text{Re}_g \rangle / \langle \text{Re}_g \rangle_{\text{susp}}$ (16.30 and 24.45) presented in Appendix A are similar to those in Figures 10 and 11.

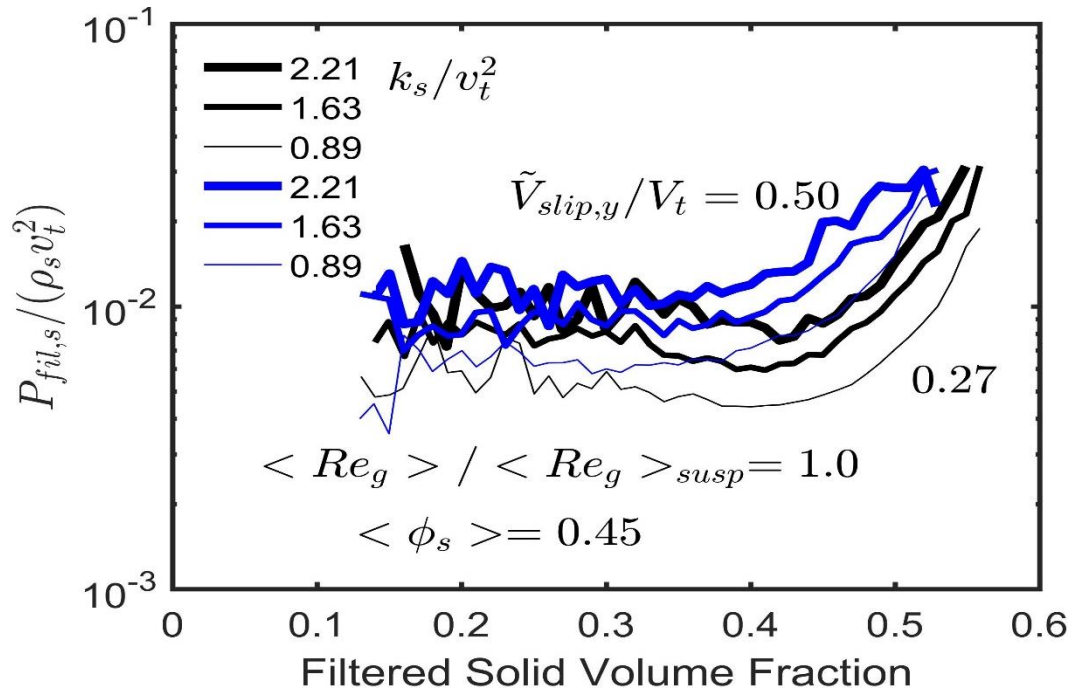
Figure 10 – Dimensionless filtered solid pressure, $P_{fil,s}/(\rho_s v_t^2)$, as a function of the filtered solid volume fraction $\bar{\phi}_s$ for the domain average solid volume fractions $\langle \phi_s \rangle = 0.35, 0.45$ and 0.50 and for gas Reynolds number ratios $\langle Re_g \rangle / \langle Re_g \rangle_{susp} = 1$ and 8.15 . The results stand for different dimensionless filtered axial slip velocities \tilde{v}_{slip}/v_t (black and blue), for the dimensionless filter size $\Delta_f/(v_t^2/g) = 4.112$, and for various dimensionless filtered kinetic energy of the solid velocity fluctuations k_s/v_t^2 (with different thickness). All graphs for $C_f = 0$.



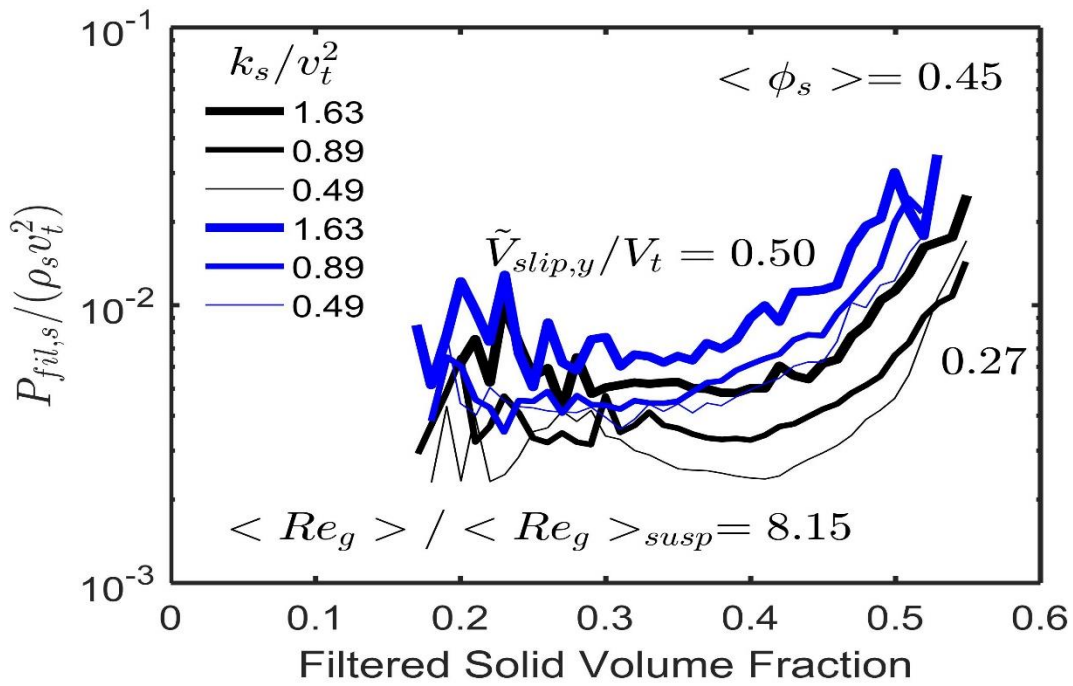
(a)



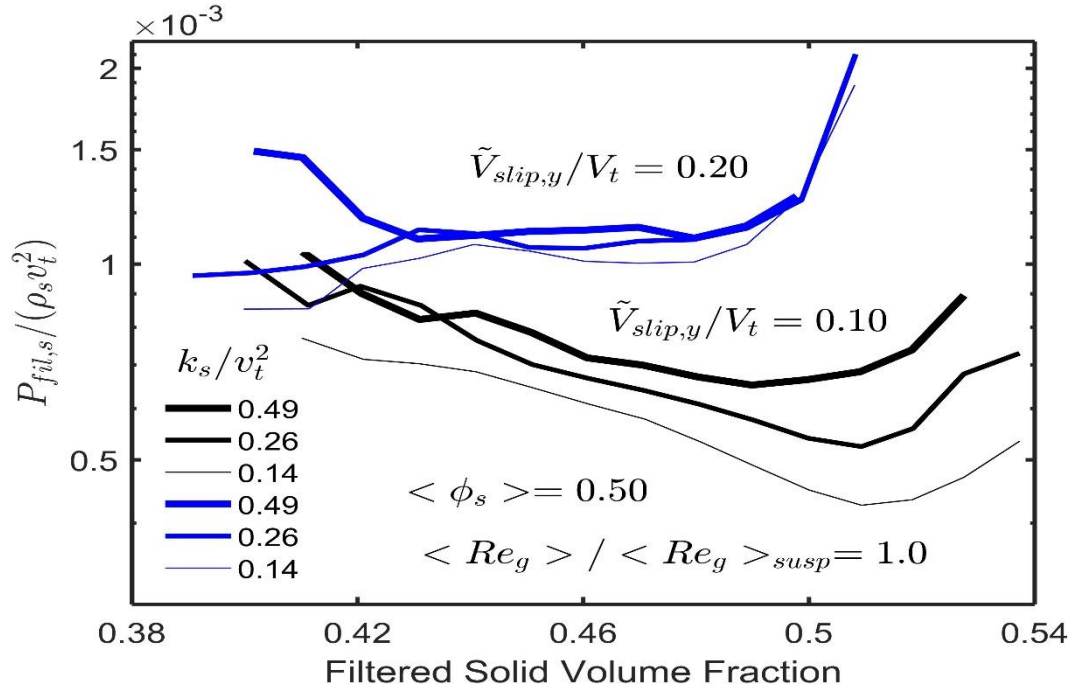
(b)



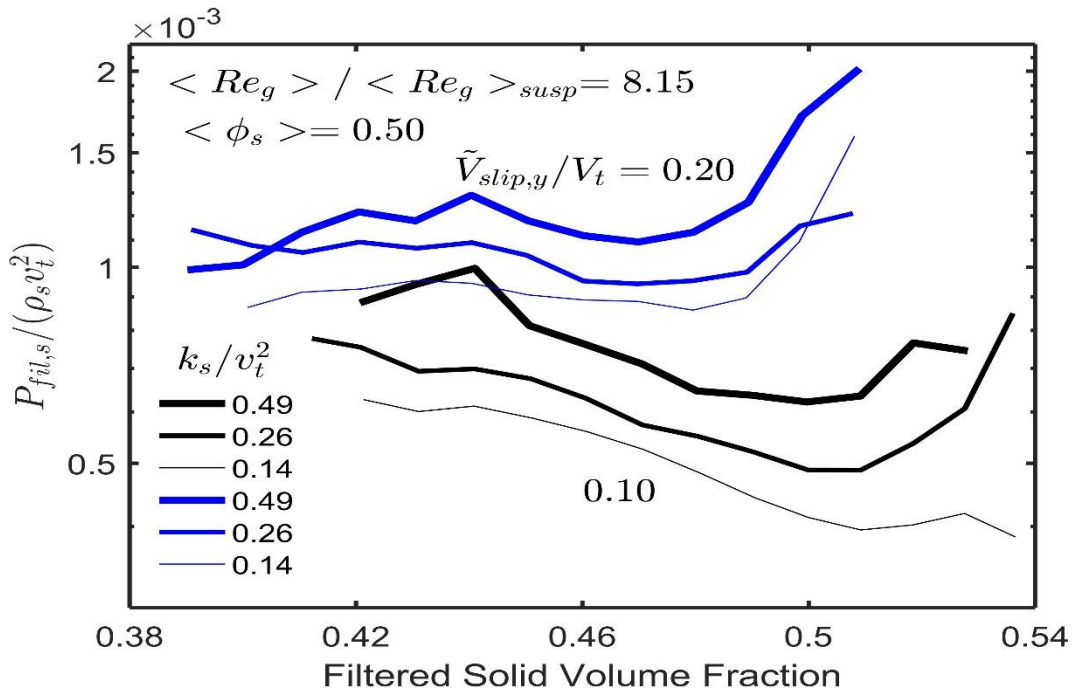
(c)



(d)



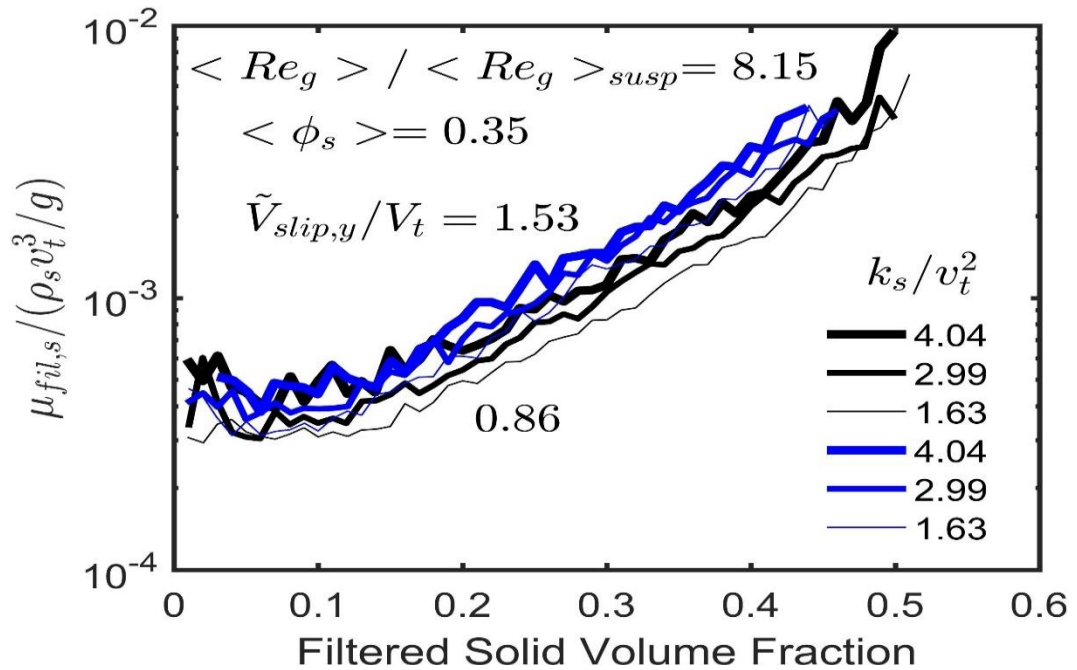
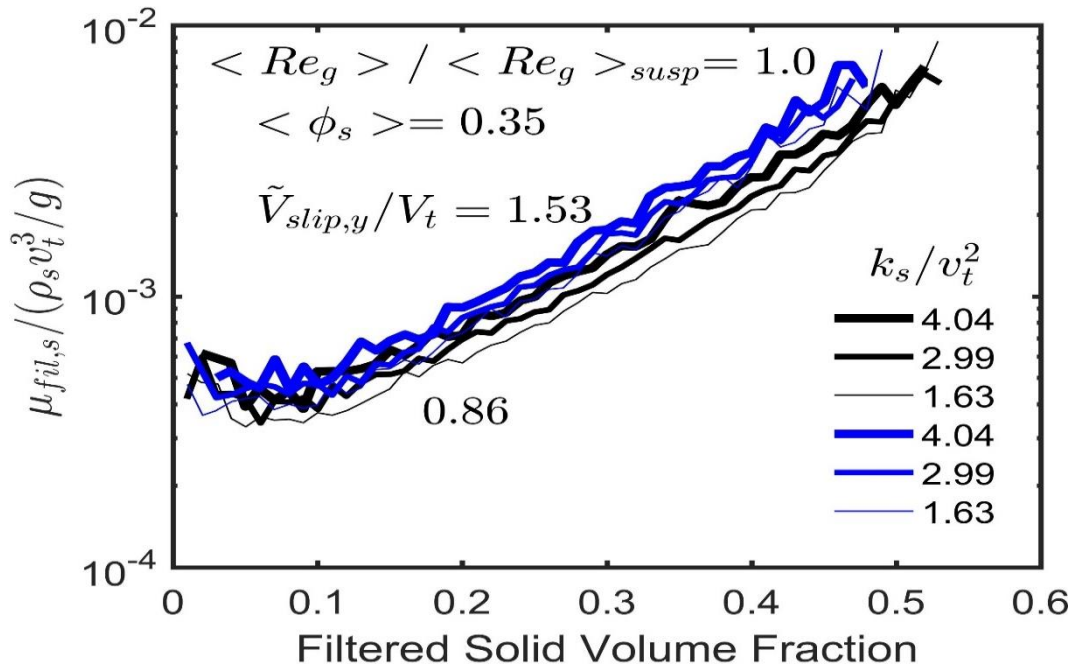
(e)

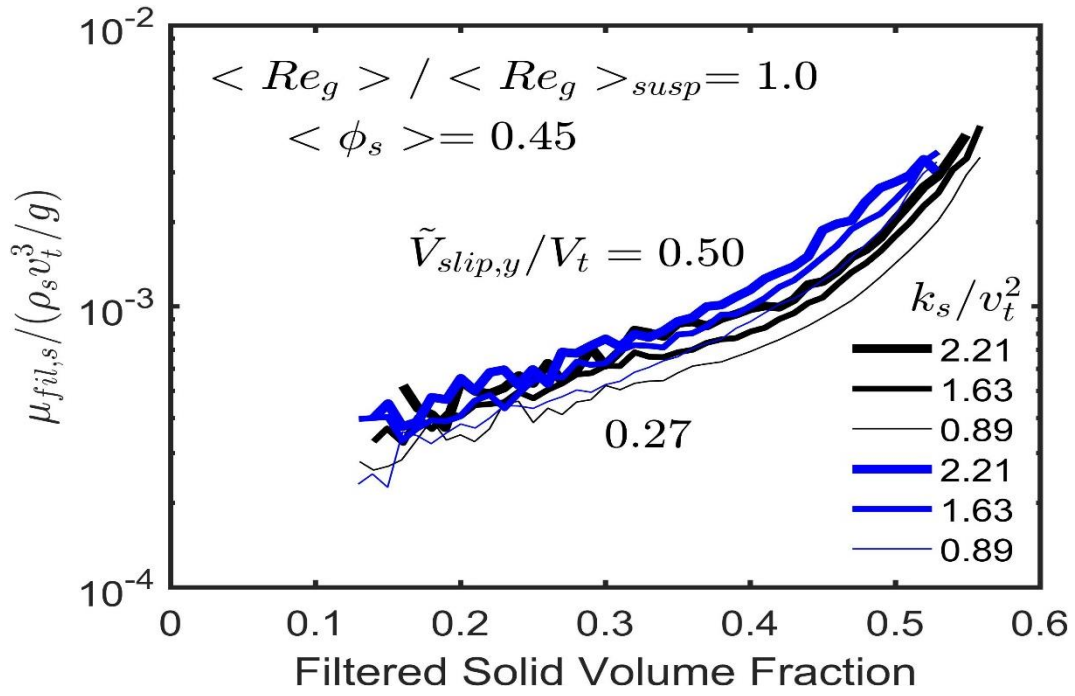


(f)

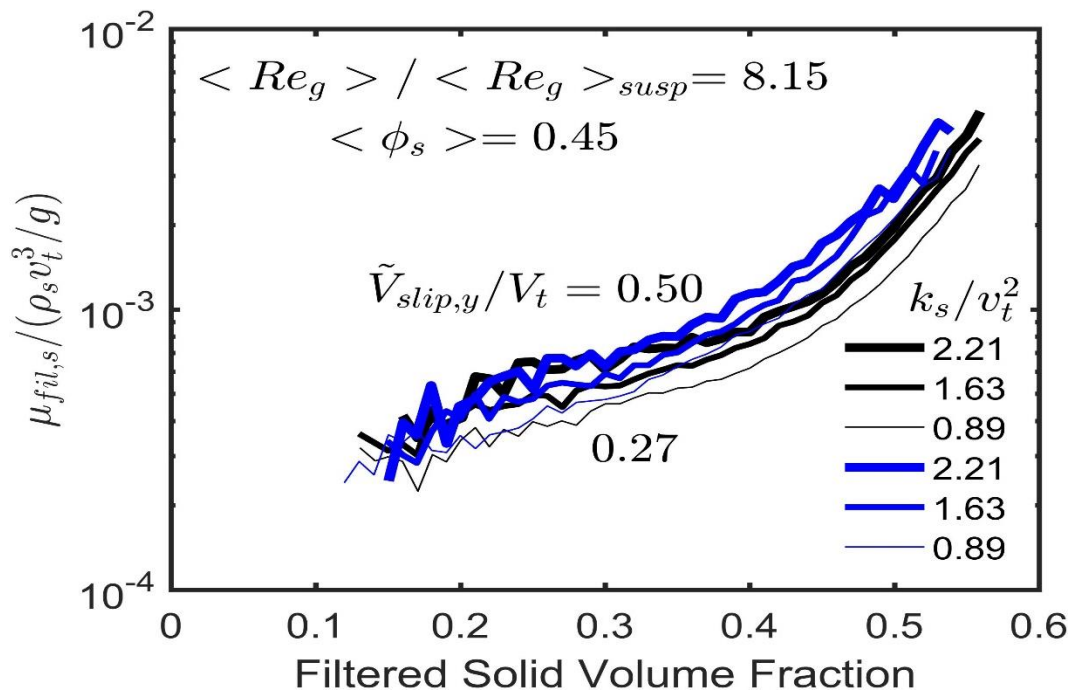
Source: Elaborated by the author

Figure 11 – Dimensionless filtered solid dynamic viscosities $\mu_{fil,s}/(\rho_s v_t^3/g)$, as a function of the filtered solid volume fraction $\bar{\phi}_s$, for the domain average solid volume fractions $\langle \phi_s \rangle = 0.35, 0.45$ and 0.50 and for gas Reynolds number ratios $\langle Re_g \rangle / \langle Re_g \rangle_{susp} = 1$ and 8.15 . The results stand for different dimensionless filtered axial slip velocities \tilde{v}_{slip}/v_t (black and blue), for the dimensionless filter size $\Delta_f/(v_t^2/g) = 4.112$, and for various dimensionless filtered kinetic energy of the solid velocity fluctuations k_s/v_t^2 (with different thickness). All graphs for $C_t = 0$.

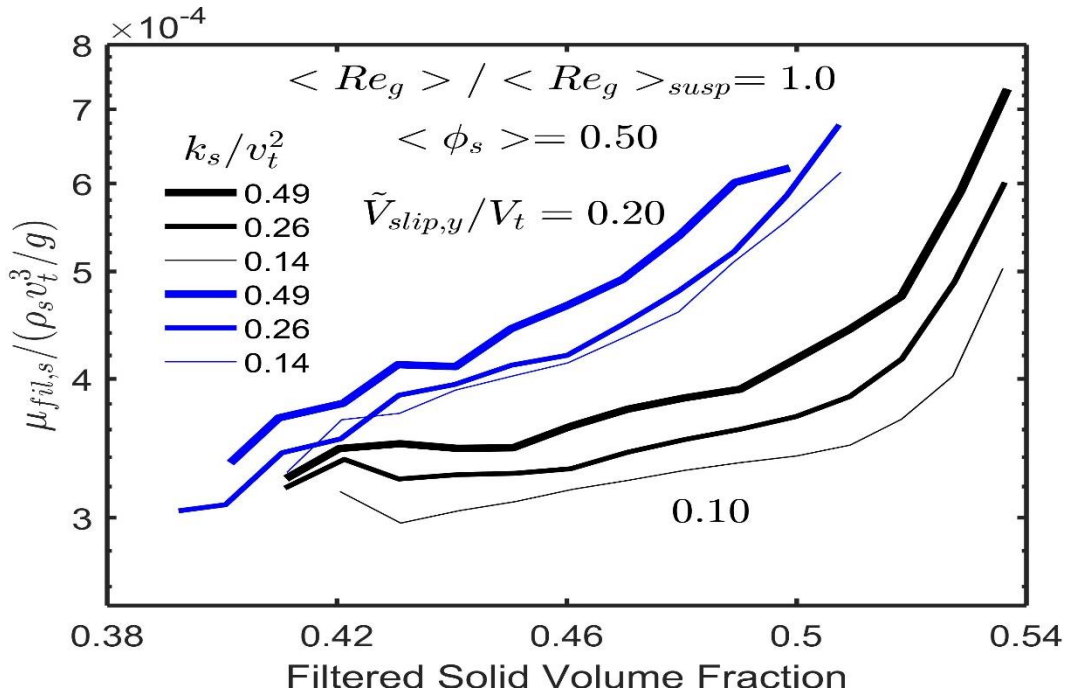




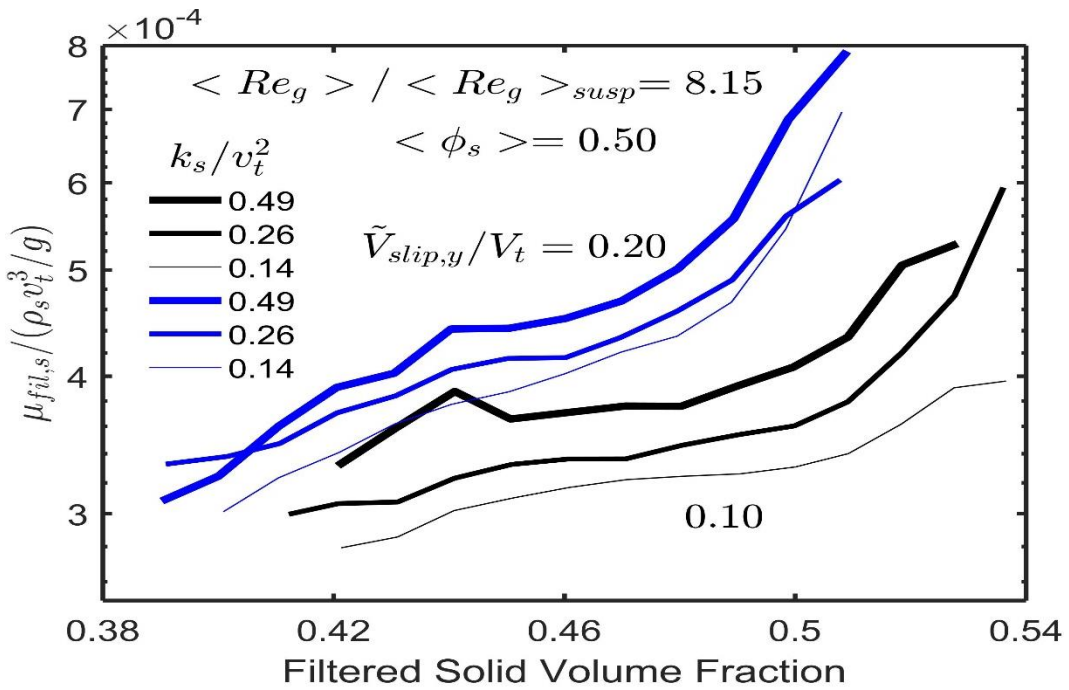
(c)



(d)



(e)



(f)

Source: Elaborated by the author

3.1.5 Residual pressure and dynamic viscosity of the solid phase

Figures 12 and 13 show the variation of the dimensionless residual solid pressure $P_{res,s}$ and dynamic viscosity $\mu_{res,s}$, respectively, for the same conditions as in Figures 9, 10 and 11. In Appendix A results are also presented for $\langle Re_g \rangle / \langle Re_g \rangle_{susp} = 16.30$ and 24.45.

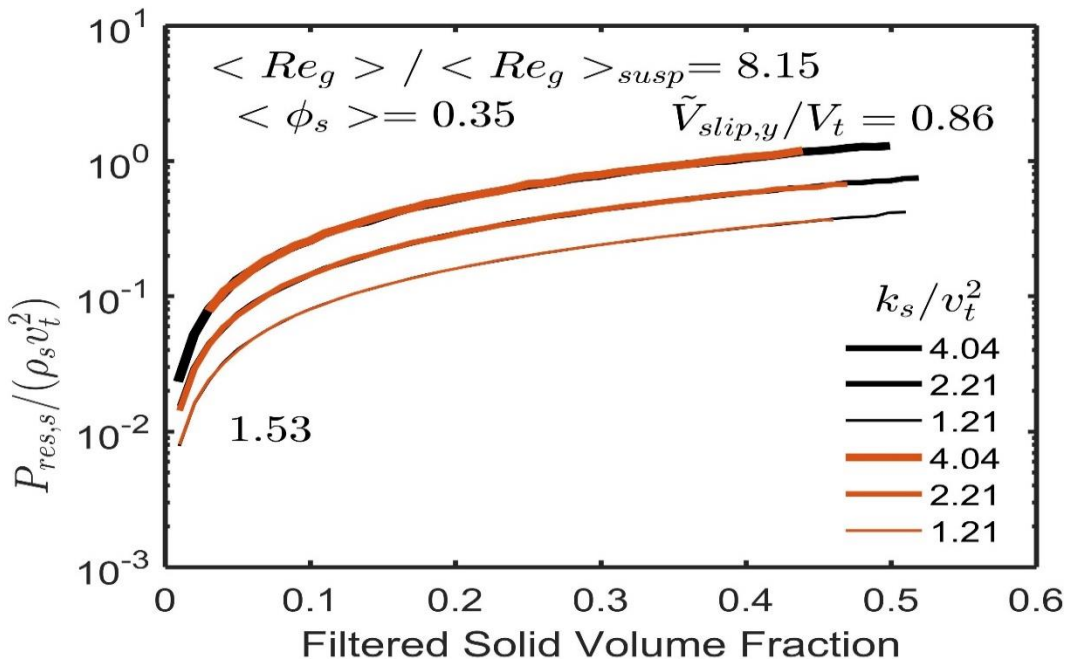
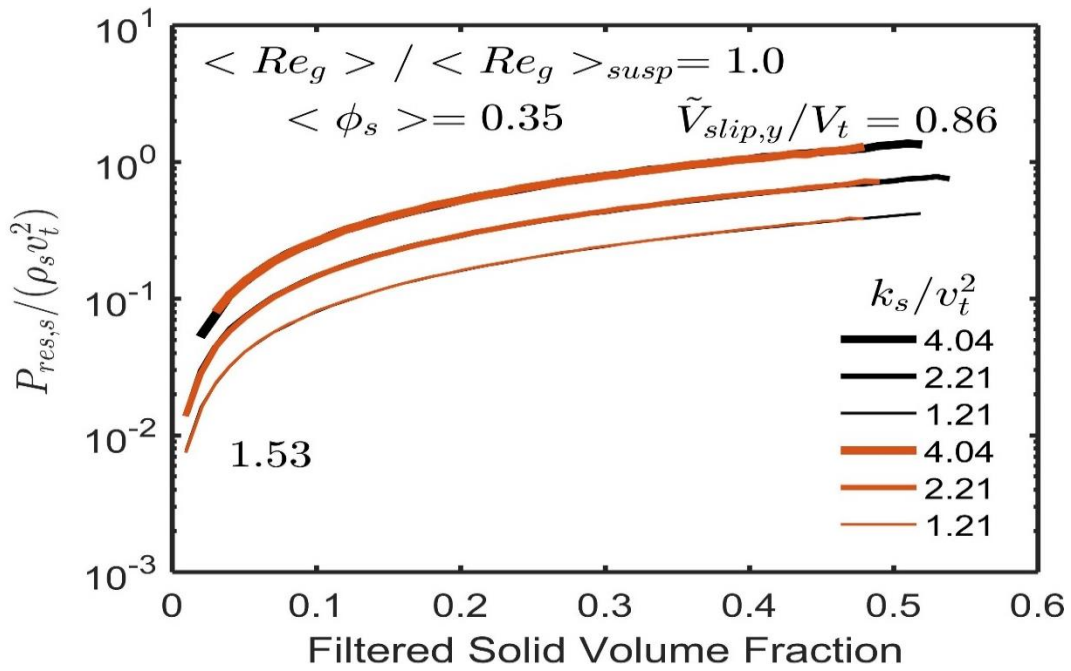
As seen, there are significant effects of the filtered solid volume fraction and filtered kinetic energy of the solid velocity fluctuations over both the residual parameters. Otherwise, the filtered slip velocity has no effect over both the residual parameters. Regarding, $P_{res,s}$, it is clear that this parameter is only a function of $\bar{\phi}_s$ and K_s , as seen by combining Equation 2.62 with Equation 2.66, which gives:

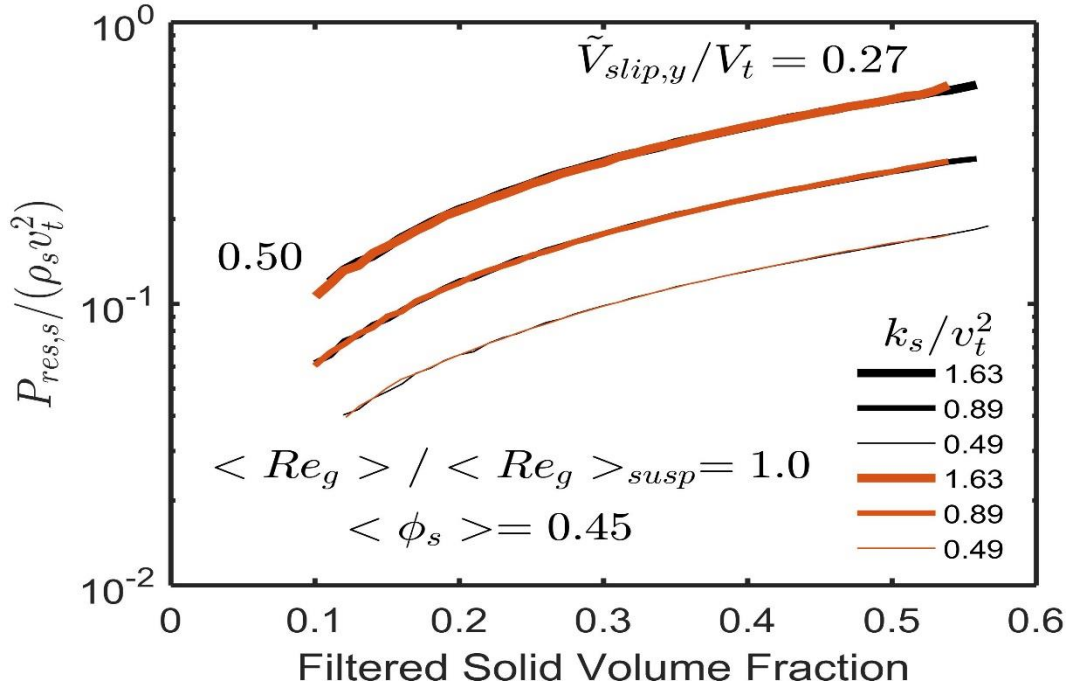
$$P_{res,s} \cong \frac{2}{3} \rho_s \bar{\phi}_s k_s \quad (3.1)$$

This linear correlation of $P_{res,s}$ to both $\bar{\phi}_s$ and K_s is clearly seen in Figure 12, except at lower $\bar{\phi}_s$ (here the simplifications leading to Equation 2.66, namely disregarding Leonard and cross like stresses and accounting only for Reynolds like stresses, seem to fail). The insensitivity of $\mu_{res,s}$ to $\tilde{v}_{slip,y}/v_t$ is not so explicit. It is clear that the ratio between the magnitude of the shear part of the residual stresses and the magnitude of the filtered shear deformation rate (see equation 2.63) is not sensitive to $\tilde{v}_{slip,y}/v_t$, meaning that both the parameters are equally affected by $\tilde{v}_{slip,y}/v_t$.

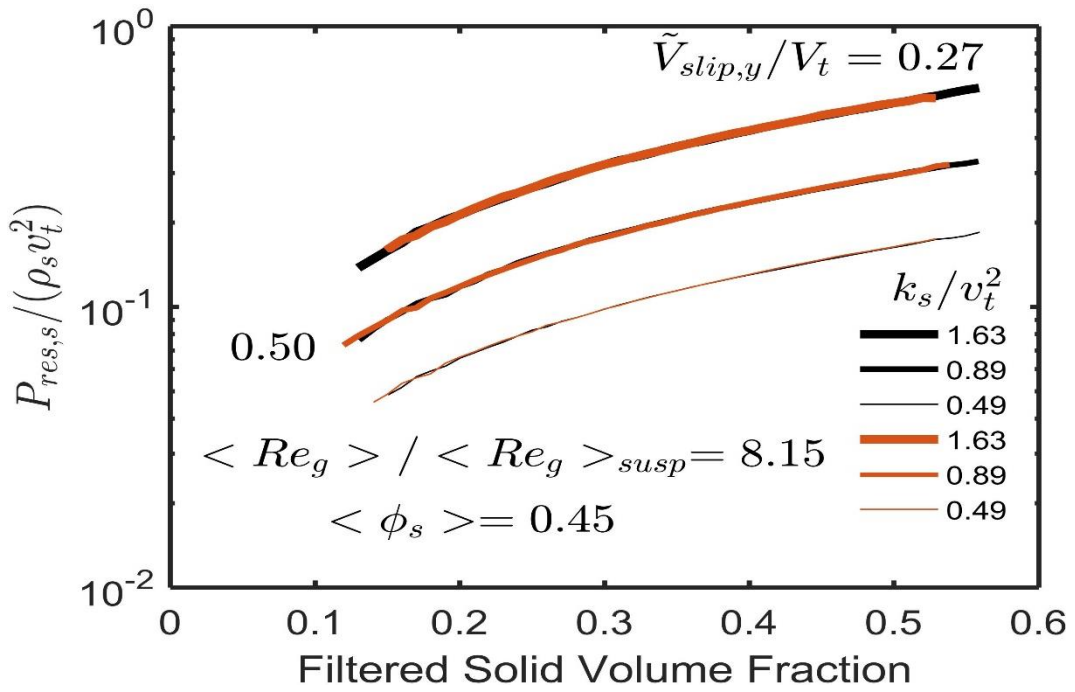
All the previous observations on the behavior of $P_{fil,s}$ and $\mu_{fil,s}$, ultimately related to the response of those parameters to the solid phase velocity fluctuations, also stand for $P_{res,s}$ and $\mu_{res,s}$. The lower solid velocity fluctuations that prevail at higher domain average gas Reynolds numbers and higher solid volume fractions, which give rise to lower filtered granular temperatures, also cause lower residual stresses in the solid phase and, therefore, lower residual pressure and dynamic viscosity of this phase. This behavior is clear for all $\langle \phi_s \rangle$ (0.35, 0.45 and 0.50), leading to increased $P_{res,s}$ and $\mu_{res,s}$ as k_s/v_t^2 grows higher owing to higher solid velocity fluctuations, for both $\langle Re_g \rangle / \langle Re_g \rangle_{susp} = 1.00$ and 8.15. The results for $\langle Re_g \rangle / \langle Re_g \rangle_{susp} = 16.30$ and 24.45, which are shown in Appendix A, are quite similar to those for $\langle Re_g \rangle / \langle Re_g \rangle_{susp} = 1$ and 8.15 reported in Figures 12 and 13.

Figure 12 – Dimensionless residual solid pressure, $P_{res,s}/(\rho_s v_t^2)$, as a function of the filtered solid volume fraction $\bar{\phi}_s$ for the domain average solid volume fractions $\langle \phi_s \rangle = 0.35, 0.45$ and 0.50 and for gas Reynolds number ratios $\langle Re_g \rangle / \langle Re_g \rangle_{susp} = 1$ and 8.15 . The results stand for different dimensionless filtered axial slip velocities \tilde{V}_{slip}/v_t (smaller: black and bigger: red), for the dimensionless filter size $\Delta f / (v_t^2/g) = 4.112$, and for various dimensionless filtered kinetic energy of the solid velocity fluctuations k_s/v_t^2 (with different thickness). All graphs for $C_f = 0$.

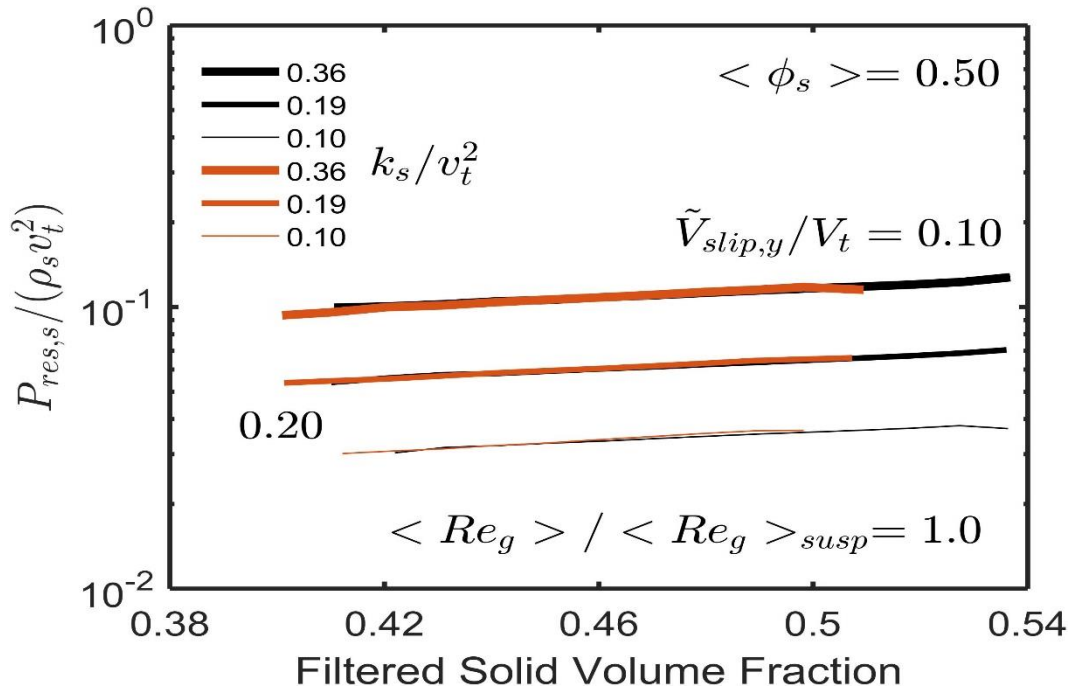




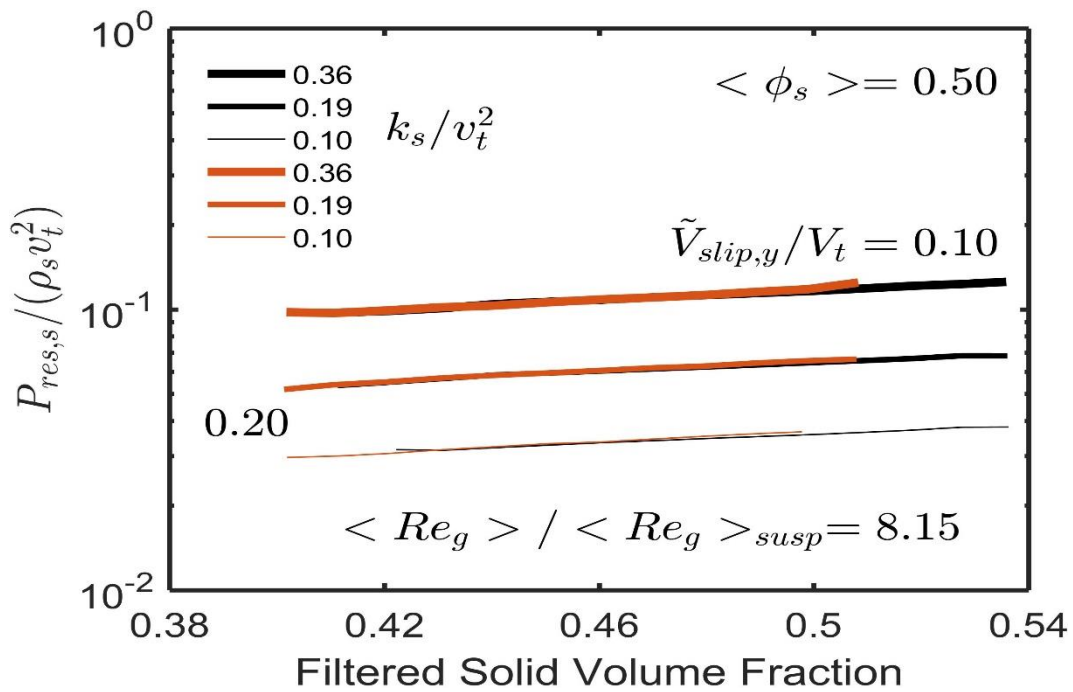
(c)



(d)



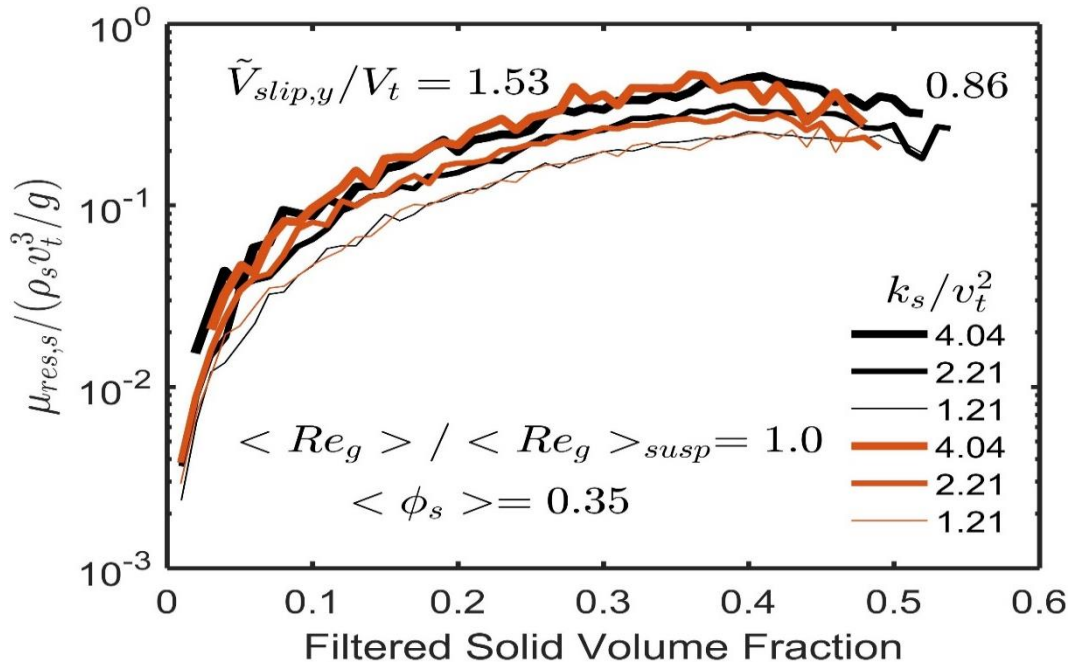
(e)



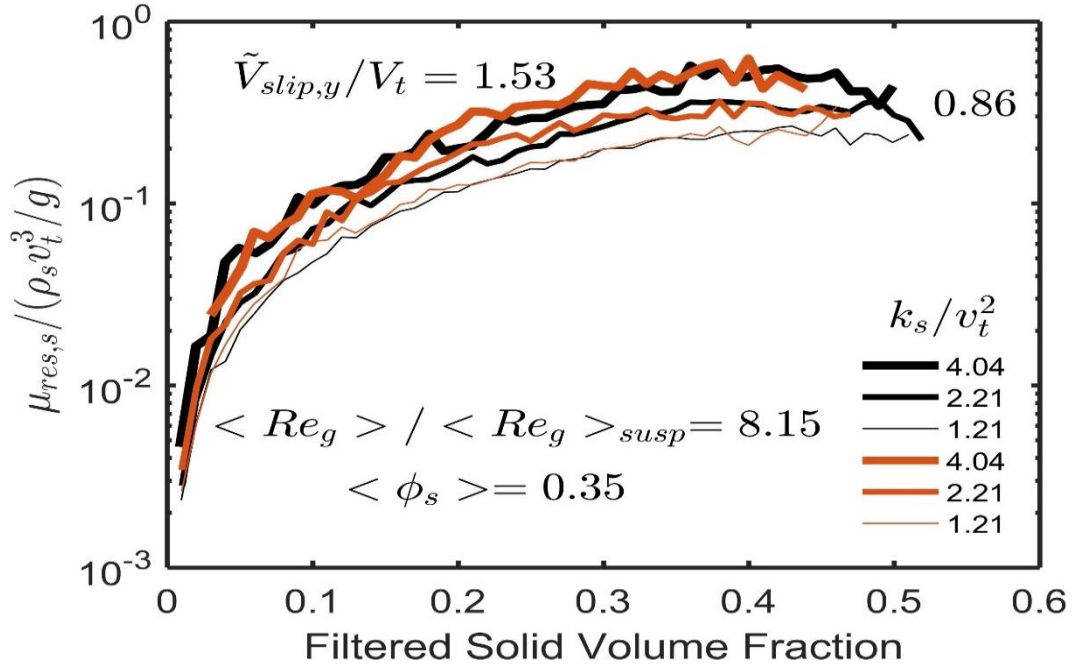
(f)

Source: Elaborated by the author

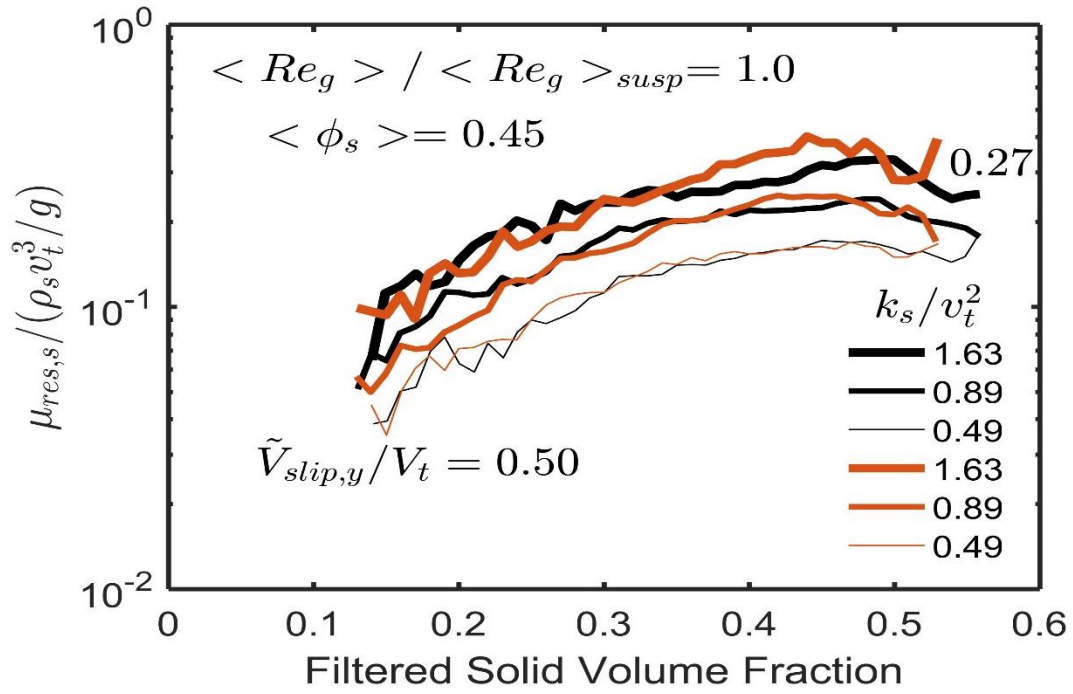
Figure 13 – Dimensionless residual solid dynamic viscosities, $\mu_{res,s}/(\rho_s v_t^3/g)$, as a function of the filtered solid volume fraction $\bar{\phi}_s$ for the domain average solid volume fractions $\langle \phi_s \rangle = 0.35, 0.45$ and 0.50 and for gas Reynolds number ratios $\langle Re_g \rangle / \langle Re_g \rangle_{susp} = 1$ and 8.15 . The results stand for different dimensionless filtered axial slip velocities \tilde{v}_{slip}/v_t (smaller: black and bigger: red), for the dimensionless filter size $\Delta f/(v_t^2/g) = 4.112$, and for various dimensionless filtered kinetic energy of the solid velocity fluctuations k_s/v_t^2 (with different thickness). All graphs for $C_f = 0$.



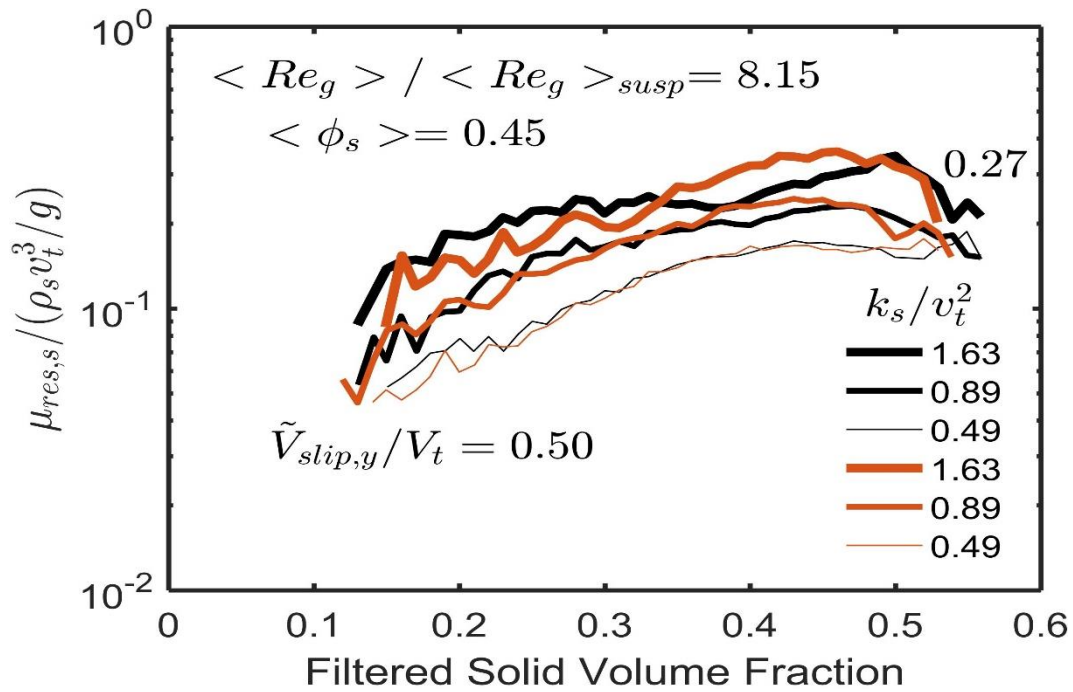
(a)



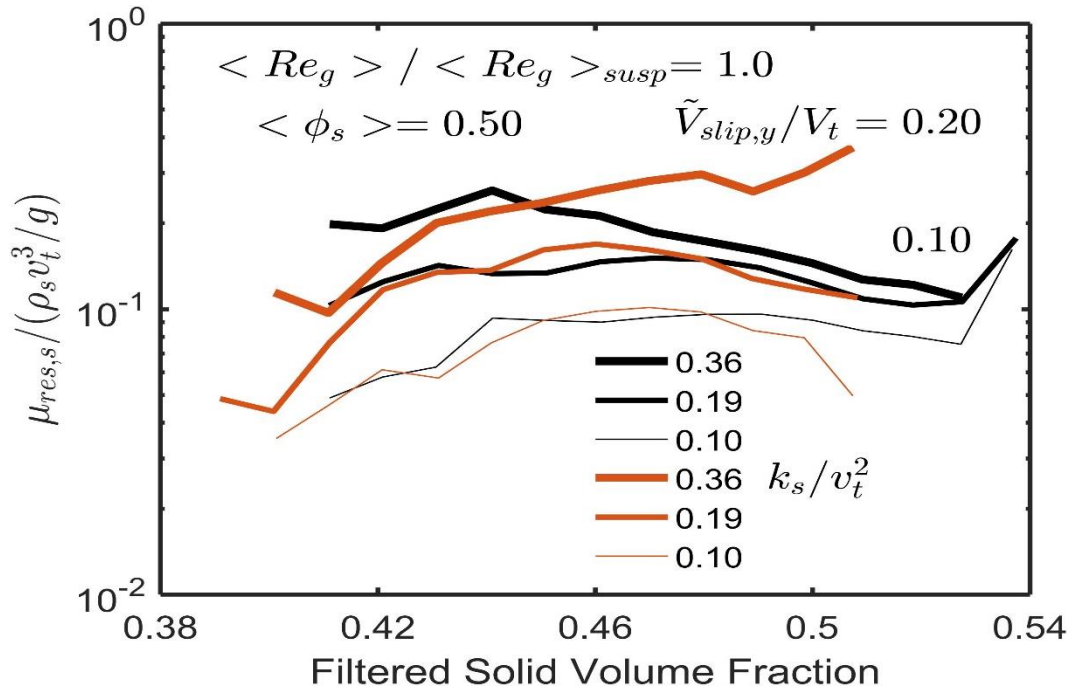
(b)



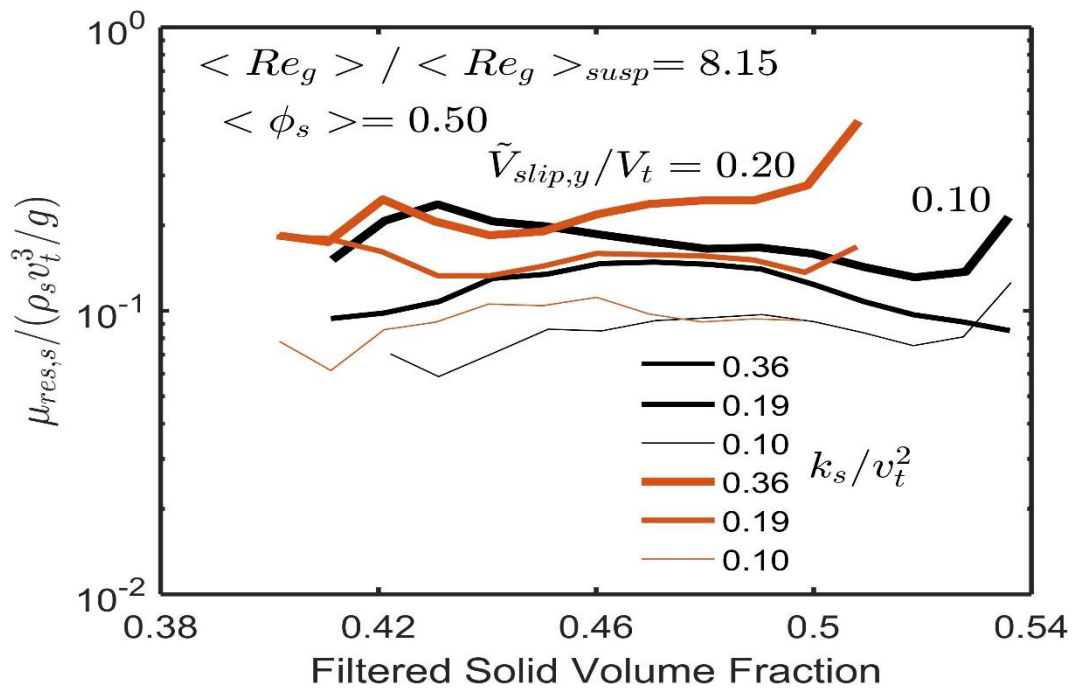
(c)



(d)



(e)



(f)

Source: Elaborated by the author

3.2 Case 2: interparticle friction analysis

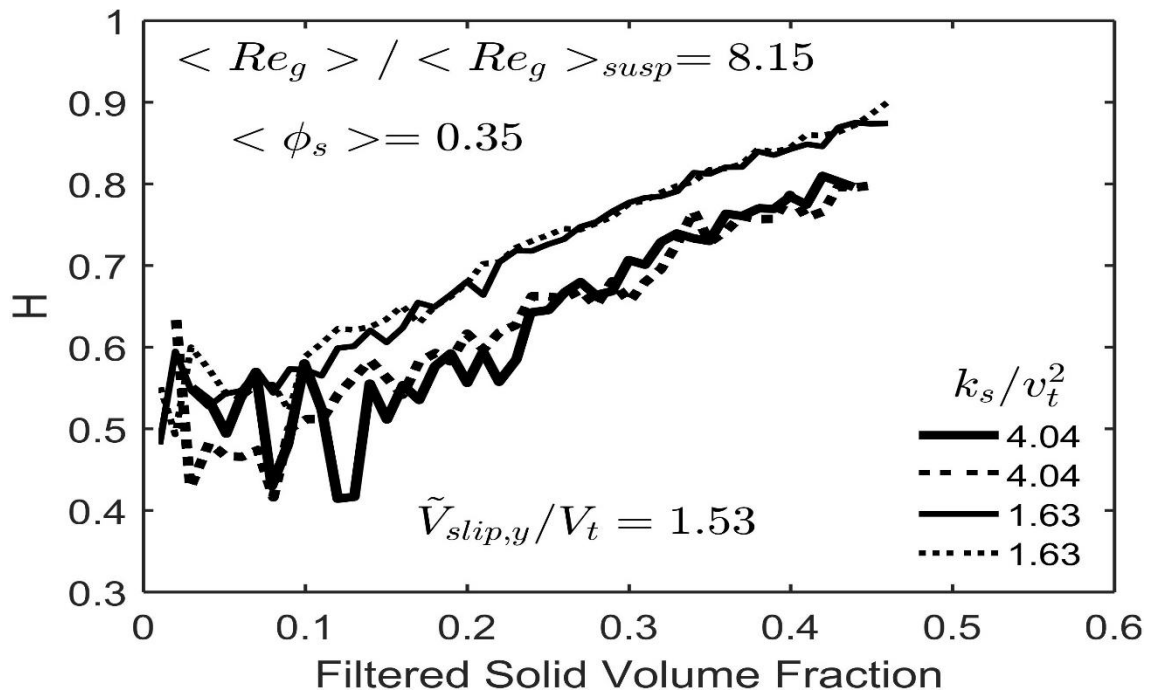
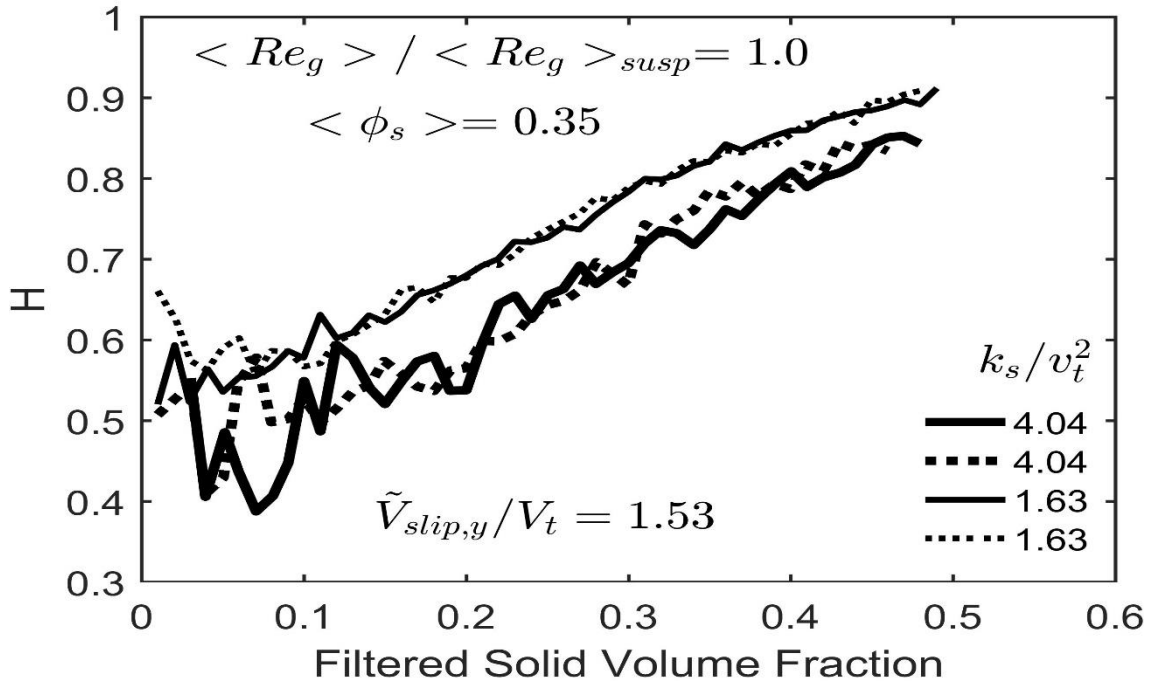
In this section same results without friction ($C_f = 0$) of section 3.1 are presented, but now in comparison to results under the same conditions, except for the inclusion of interparticle friction ($C_f = 0.3$). Figure 14 shows results of the drag coefficient correction, H . Figures 15 and 16 show results of the dimensionless filtered solid pressure $P_{\text{fil},s}/(\rho_s v_t^2)$ and dimensionless filtered solid dynamic viscosities $\mu_{\text{fil},s}/(\rho_s v_t^3/g)$. Figures 17 and 18 show results of the dimensionless residual solid pressure $P_{\text{res},s}/(\rho_s v_t^2)$ and dimensionless residual solid dynamic viscosities $\mu_{\text{res},s}/(\rho_s v_t^3/g)$. The graphs in the figures show the variation of the concerning parameters with the filtered solid volume fraction, and the filtered kinetic energy of the solid velocity fluctuations, for particular values of filtered slip velocity, and for conditions with and without interparticle friction.

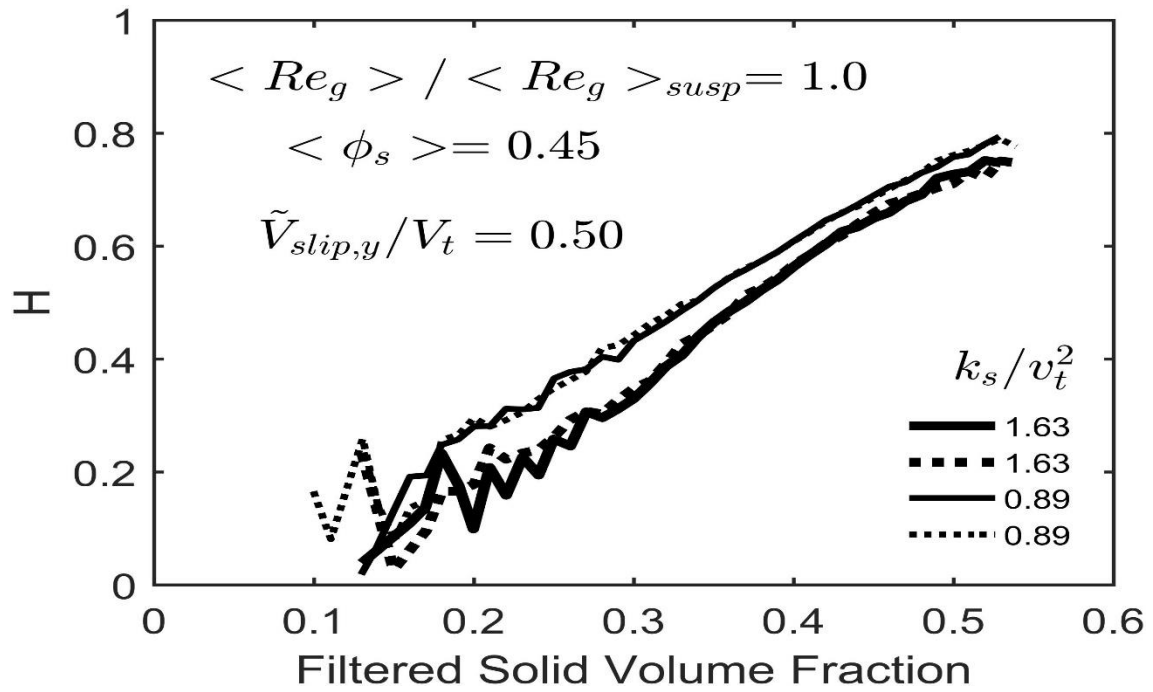
All the results stand for gas Reynolds number ratios $\langle \text{Re}_g \rangle / \langle \text{Re}_g \rangle_{\text{susp}} = 1.00$ and 8.15 and domain average solid volume fractions $\langle \phi_s \rangle = 0.35, 0.45$ and 0.50 . Further results are also presented for higher gas Reynolds number ratios, $\langle \text{Re}_g \rangle / \langle \text{Re}_g \rangle_{\text{susp}} = 16.30$ and 24.45 , in Appendix B.

As seen in Figures 14 to 18, the inclusion of interparticle friction had no effect over the concerning filtered and residual parameters under the various conditions that were applied. An exception was observed under the higher $\langle \phi_s \rangle = 0.50$ for $P_{\text{fil},s}$, $\mu_{\text{fil},s}$ and $\mu_{\text{res},s}$. For those case the inclusion of friction caused $\mu_{\text{res},s}$ to increase and $P_{\text{fil},s}$ and $\mu_{\text{fil},s}$ to decrease, but only slightly for all of them. The current results indicate that interparticle friction has no effect over the meso-scale hydrodynamics of dense gas-solid fluidized flows. The results for higher domain average gas Reynolds numbers presented in Appendix B show the same behavior, except that the smaller variations of $P_{\text{fil},s}$, $\mu_{\text{fil},s}$ and $\mu_{\text{res},s}$ were anticipated to $\langle \phi_s \rangle = 0.45$. Despite the current results, interparticle friction needs further research.

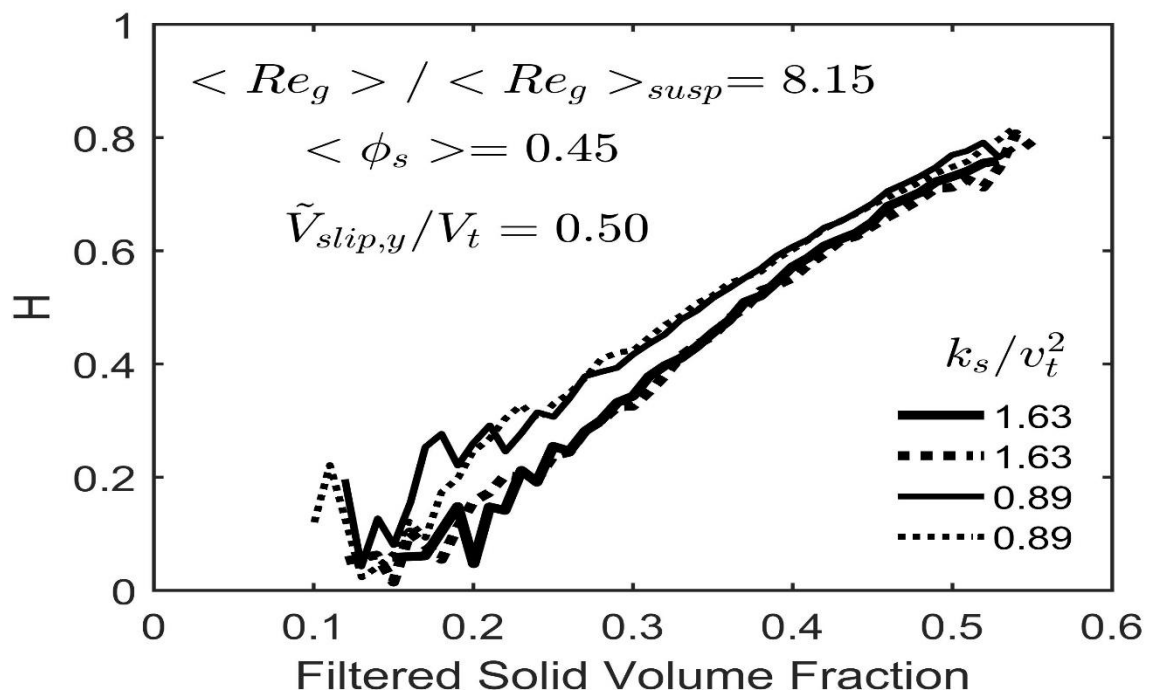
For instance, it is just possible that the filtered solid volume fraction, the filtered slip velocity and the filtered kinetic energy of the solid velocity fluctuations are either unsuitable or insufficient as markers, as they may be hiding hydrodynamic effects dissipated by the statistical averaging procedures that were performed in the current binning process. This is a matter for further verification.

Figure 14 – Drag Coefficient Correction, H , as a function of the filtered solid volume fraction $\bar{\phi}_s$ for the domain average solid volume fractions $\langle \phi_s \rangle = 0.35, 0.45$ and 0.50 and for gas Reynolds number ratios $\langle Re_g \rangle / \langle Re_g \rangle_{susp} = 1$ and 8.15 . The results stand for particular dimensionless filtered axial slip velocities \tilde{v}_{slip} / v_t , the dimensionless filter size $\Delta_f / (v_t^2 / g) = 4.112$, and for two different interparticle friction coefficient, $C_f = 0$ (full lines) and $C_f = 0.3$ (dash lines).

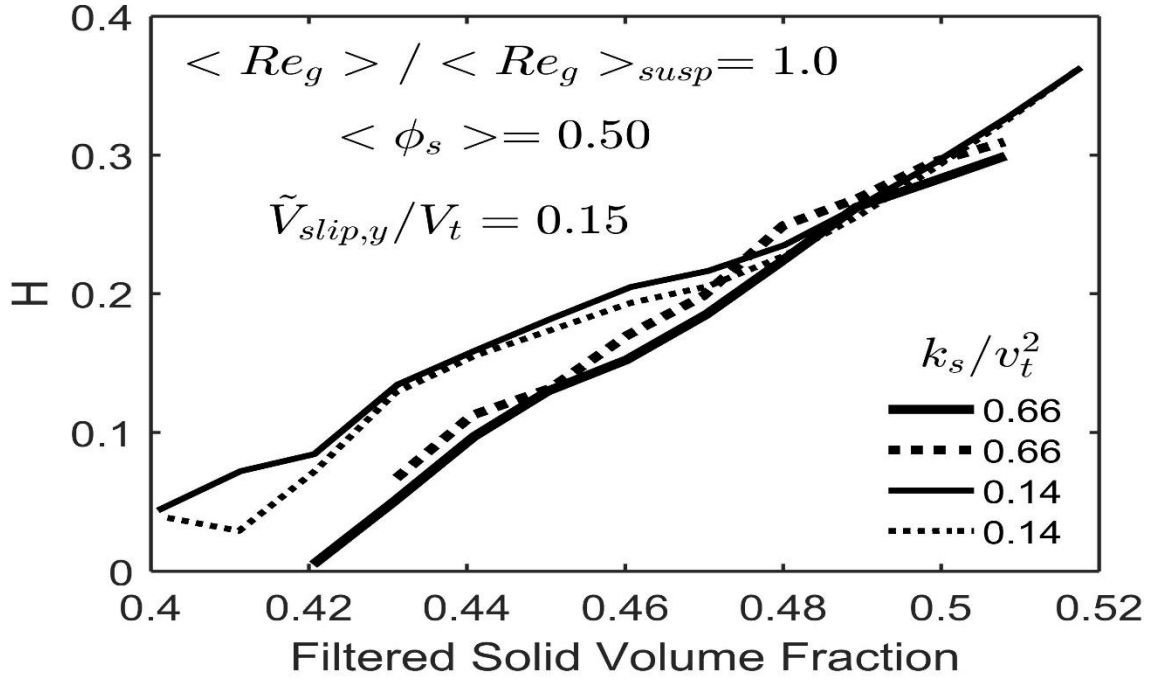




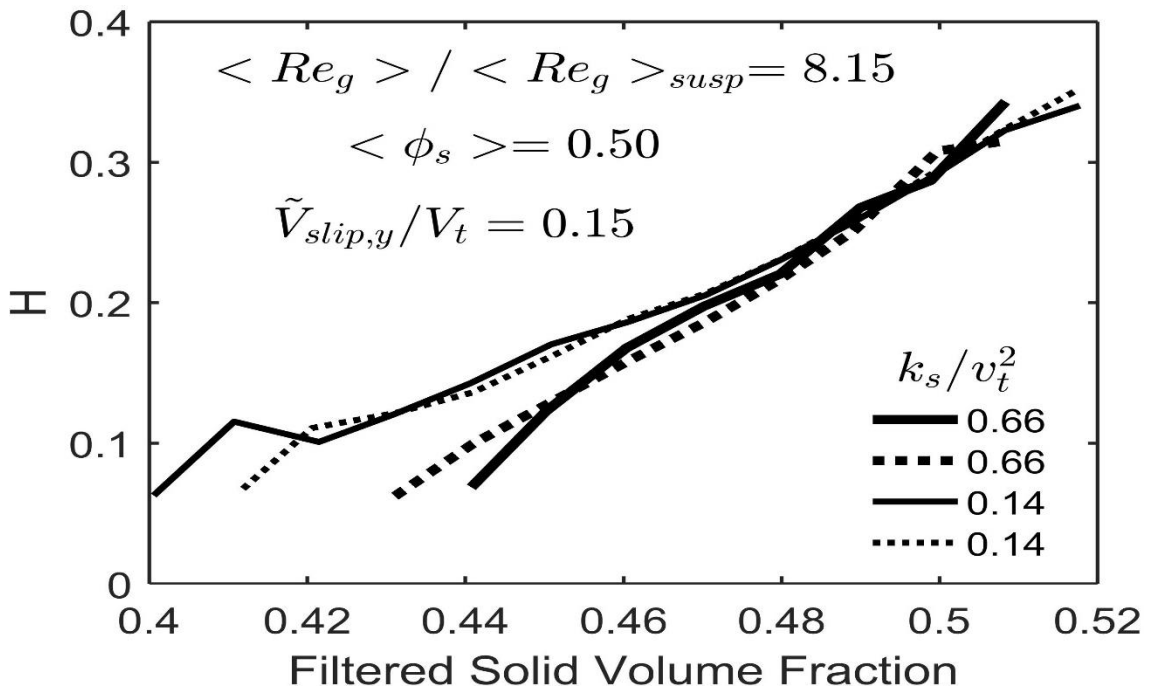
(c)



(d)



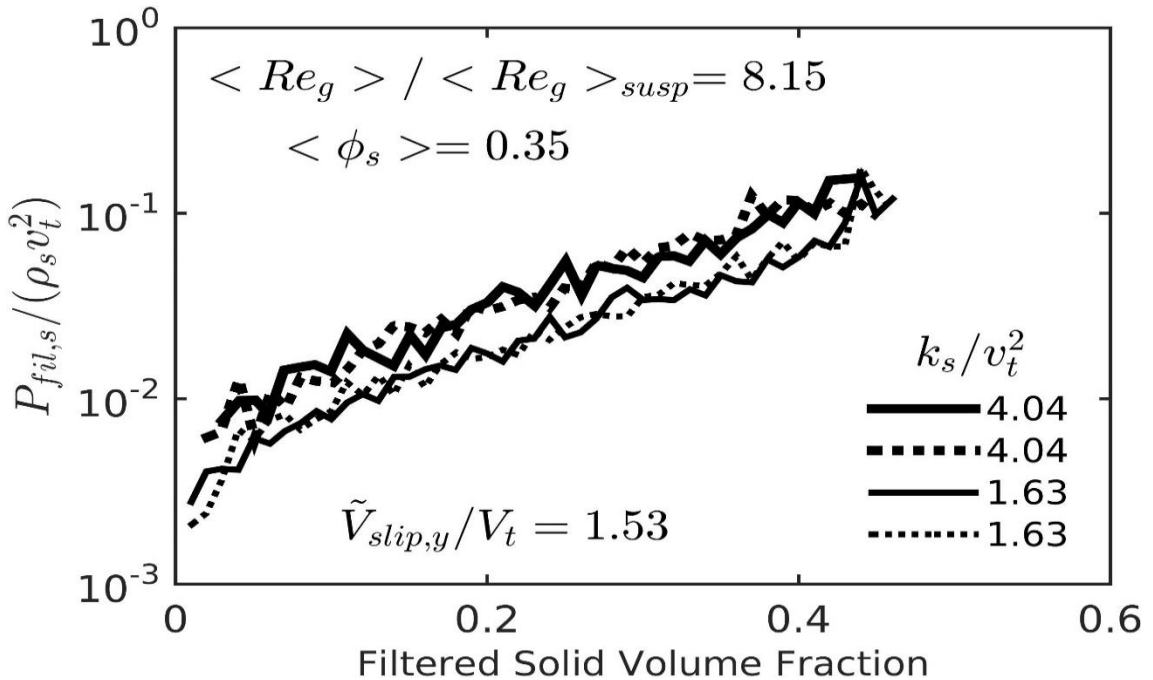
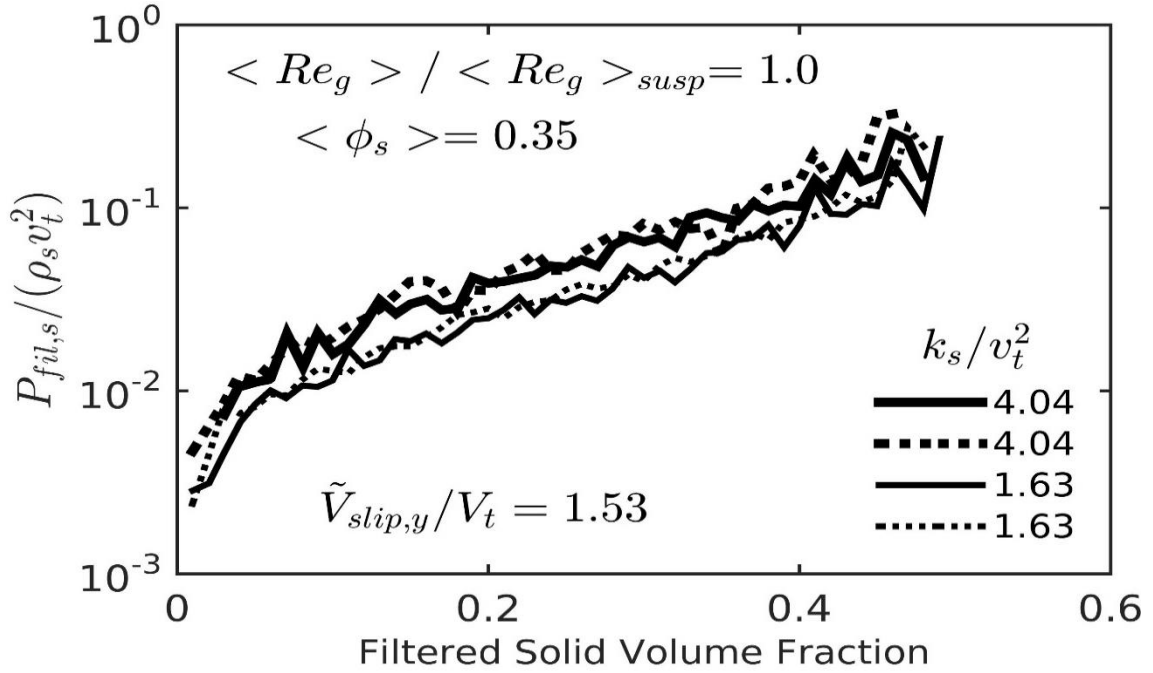
(e)

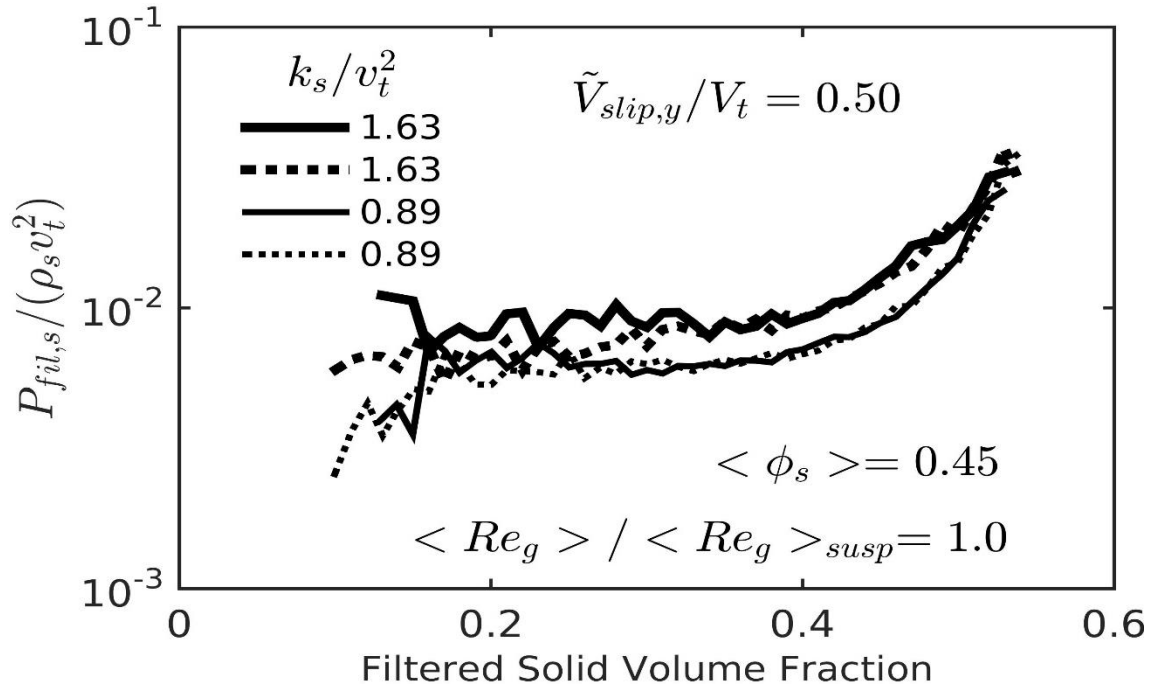


(f)

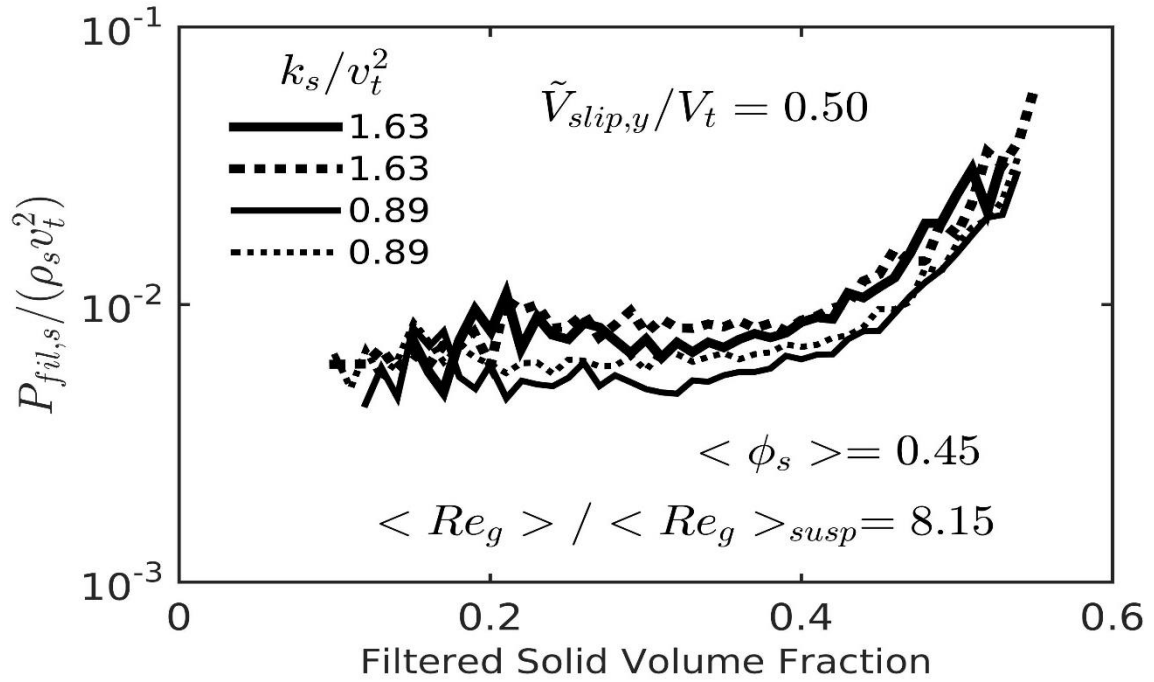
Source: Elaborated by the author

Figure 15 – Dimensionless filtered solid pressure, $P_{fil,s}/(\rho_s v_t^2)$, as a function of the filtered solid volume fraction $\bar{\phi}_s$ for the domain average solid volume fractions $\langle \phi_s \rangle = 0.35, 0.45$ and 0.50 and for gas Reynolds number ratios $\langle Re_g \rangle / \langle Re_g \rangle_{susp} = 1$ and 8.15 . The results stand for particular dimensionless filtered axial slip velocities \tilde{V}_{slip}/v_t , the dimensionless filter size $\Delta_f/(v_t^2/g) = 4.112$, and for two different interparticle friction coefficient, $C_f = 0$ (full lines) and $C_f = 0.3$ (dash lines).

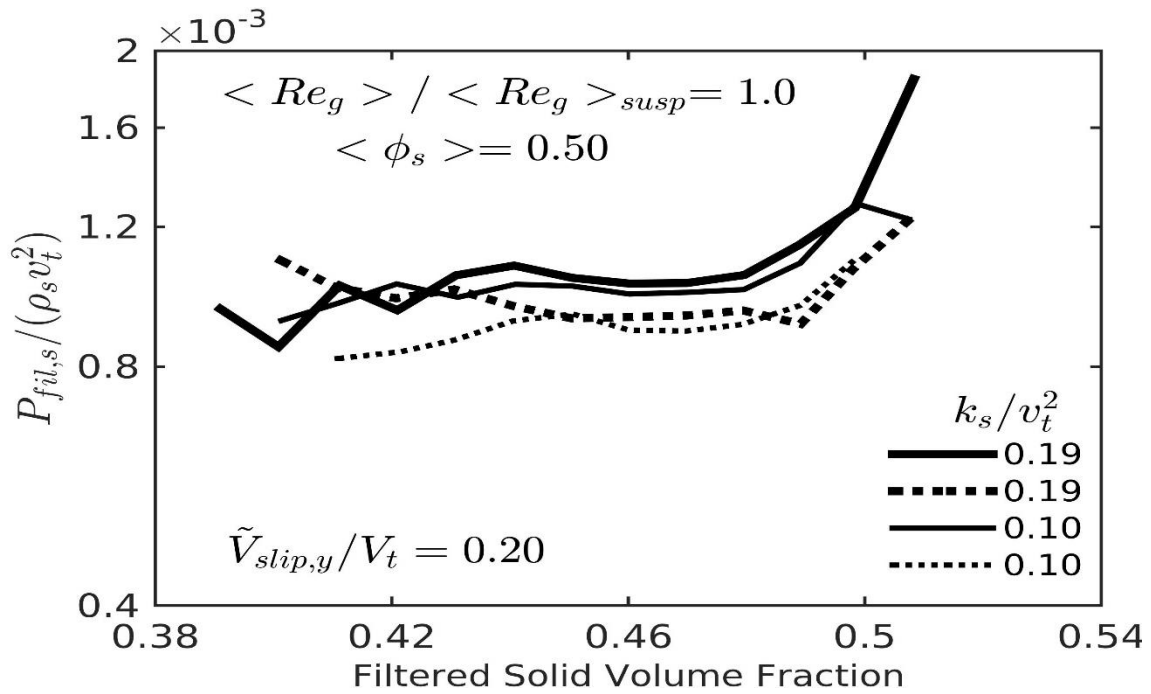




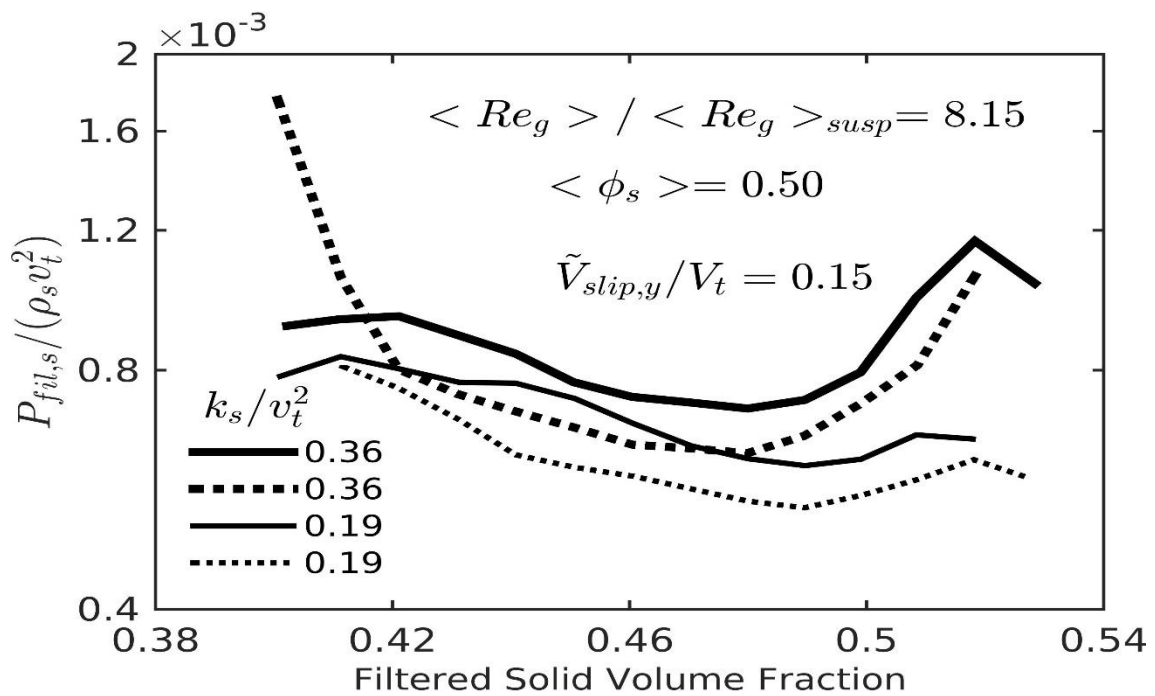
(c)



(d)



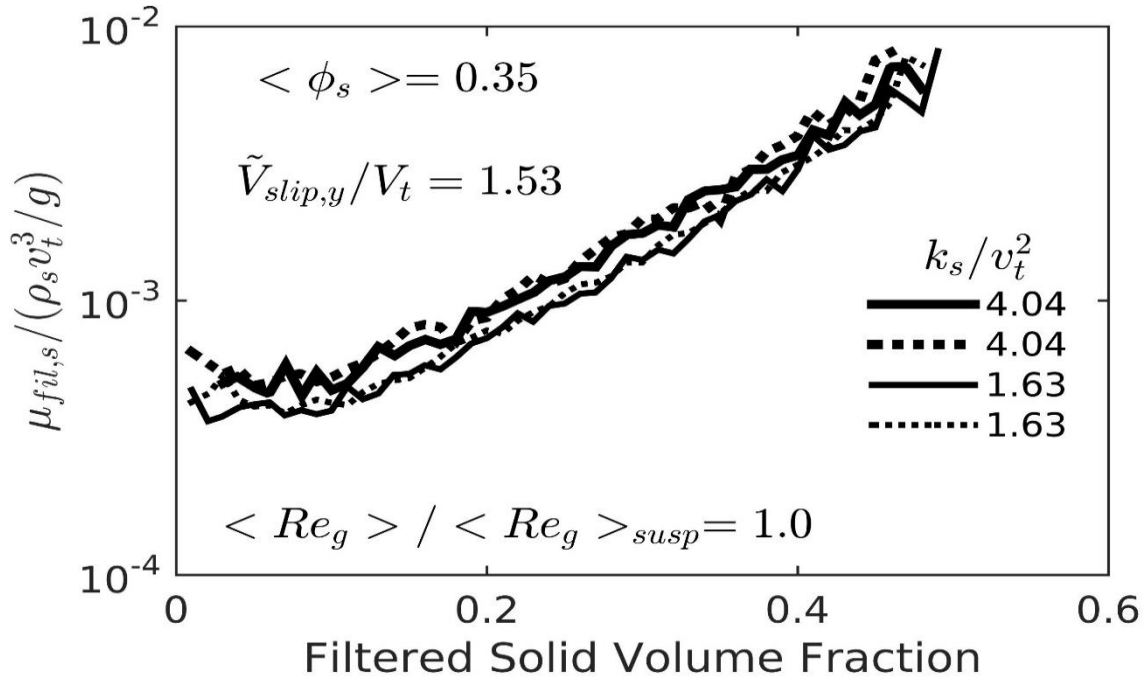
(e)



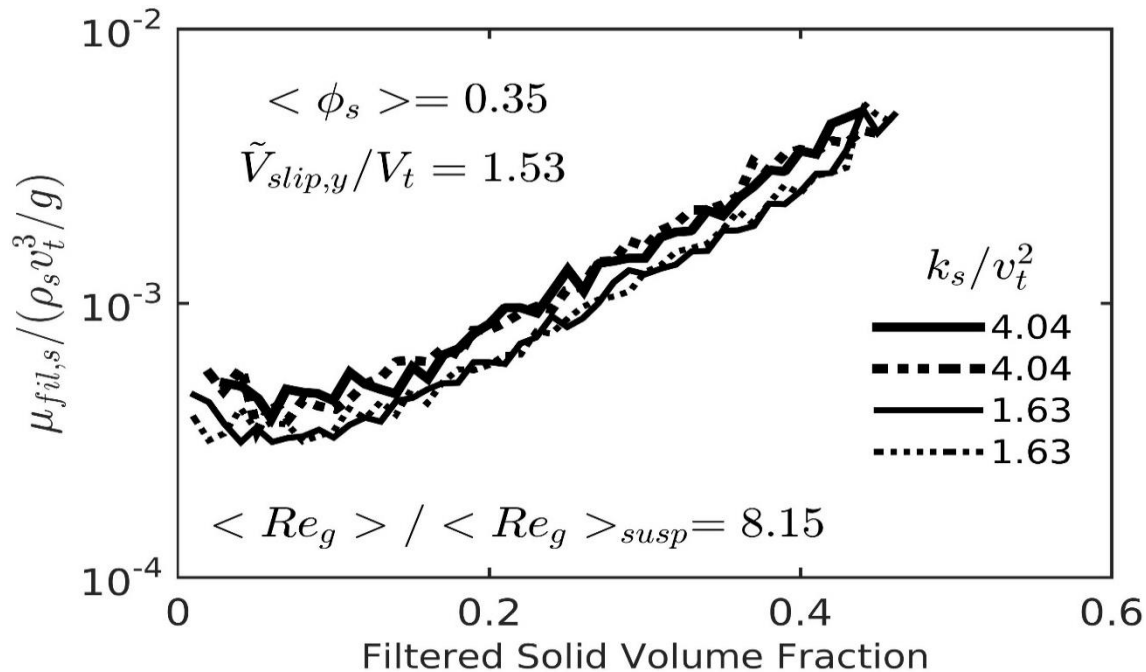
(f)

Source: Elaborated by the author

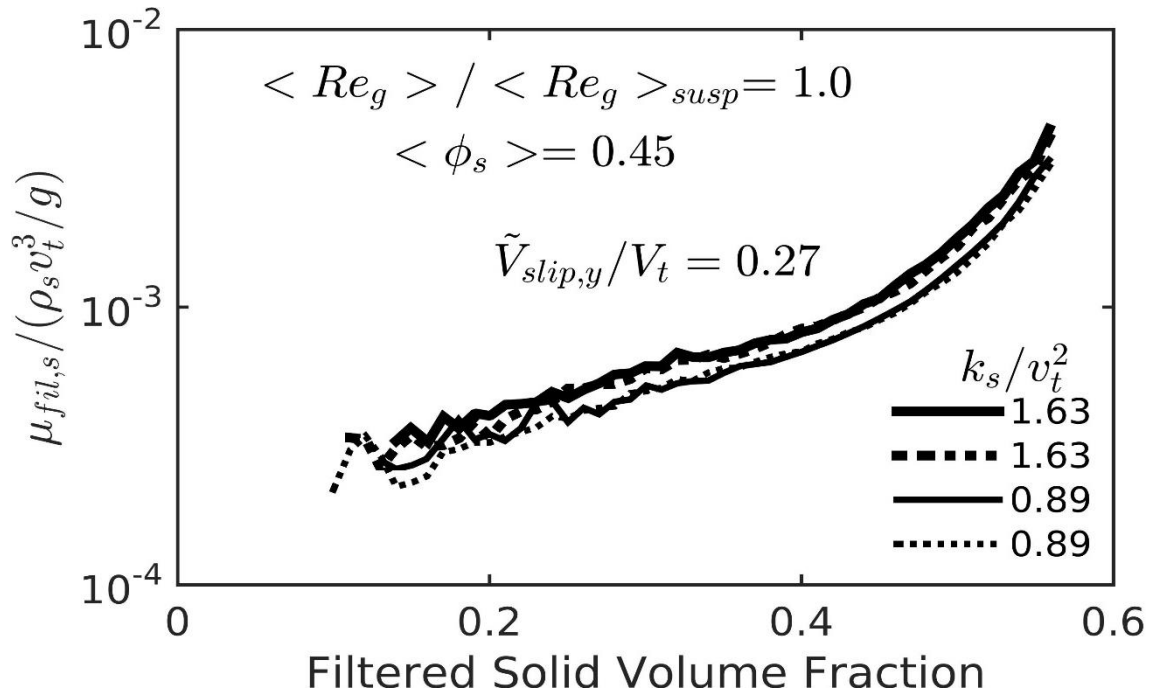
Figure 16 – Dimensionless filtered solid dynamic viscosities, $\mu_{fil,s}/(\rho_s v_t^3/g)$, as a function of the filtered solid volume fraction $\bar{\phi}_s$ for the domain average solid volume fractions $\langle \phi_s \rangle = 0.35, 0.45$ and 0.50 and for gas Reynolds number ratios $\langle Re_g \rangle / \langle Re_g \rangle_{susp} = 1$ and 8.15 . The results stand for particular dimensionless filtered axial slip velocities \tilde{V}_{slip}/V_t , the dimensionless filter size $\Delta_f/(v_t^2/g) = 4.112$, and for two different interparticle friction coefficient, $C_f = 0$ (full lines) and $C_f = 0.3$ (dash lines).



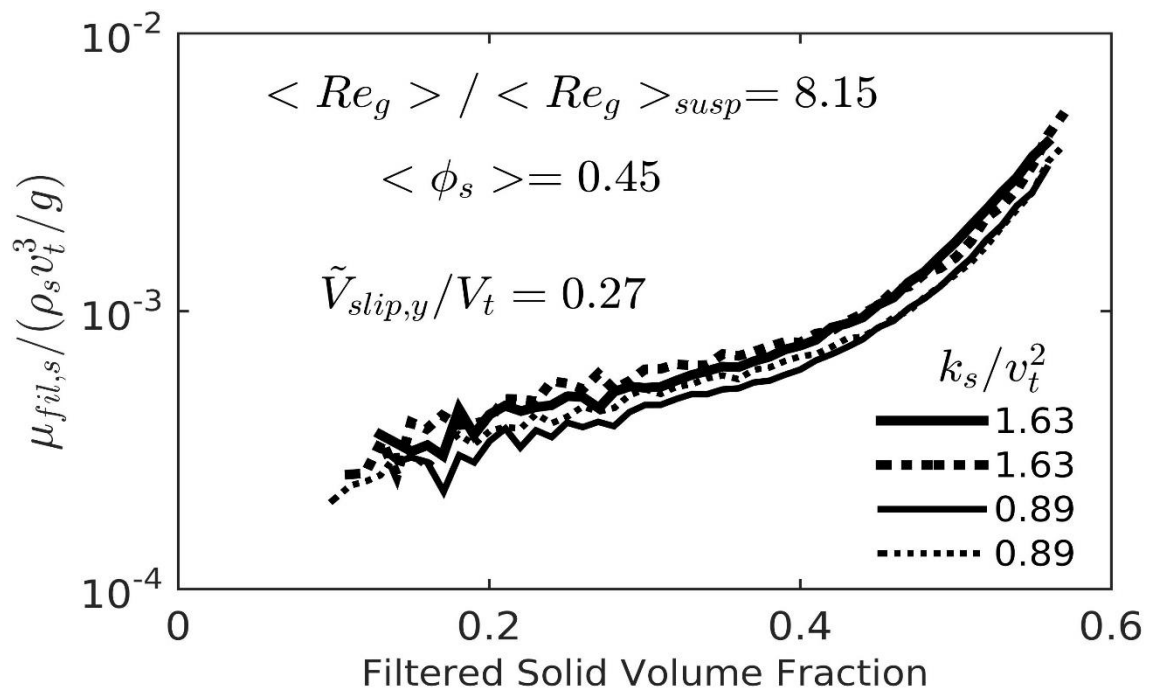
(a)



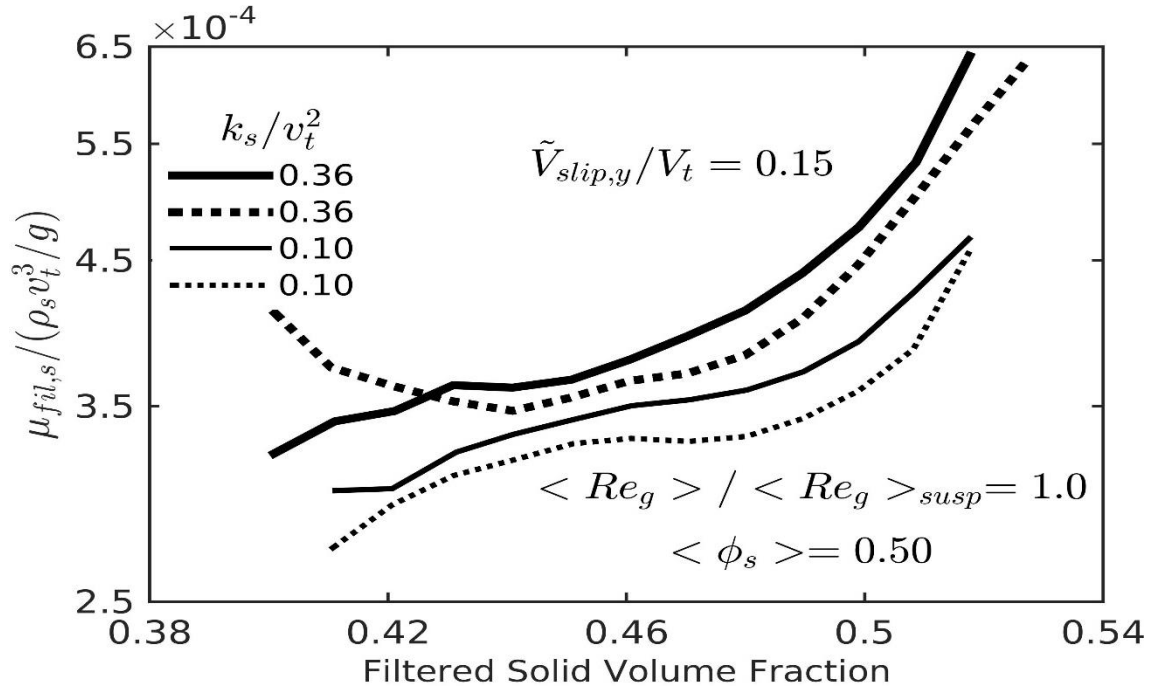
(b)



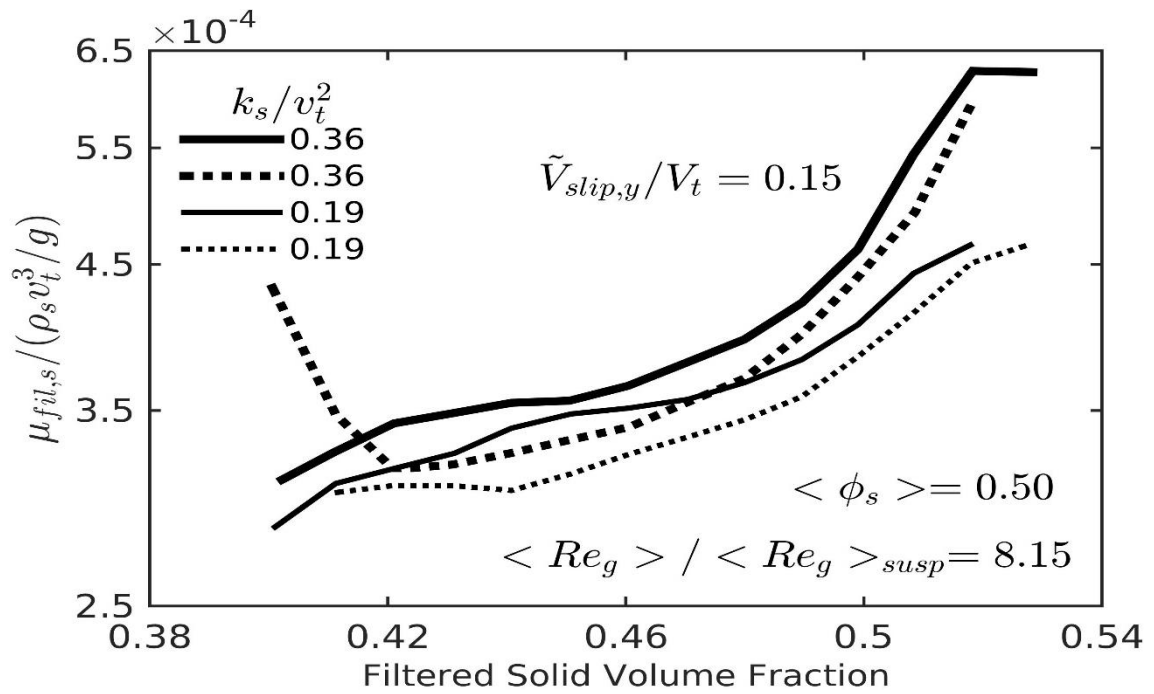
(c)



(d)



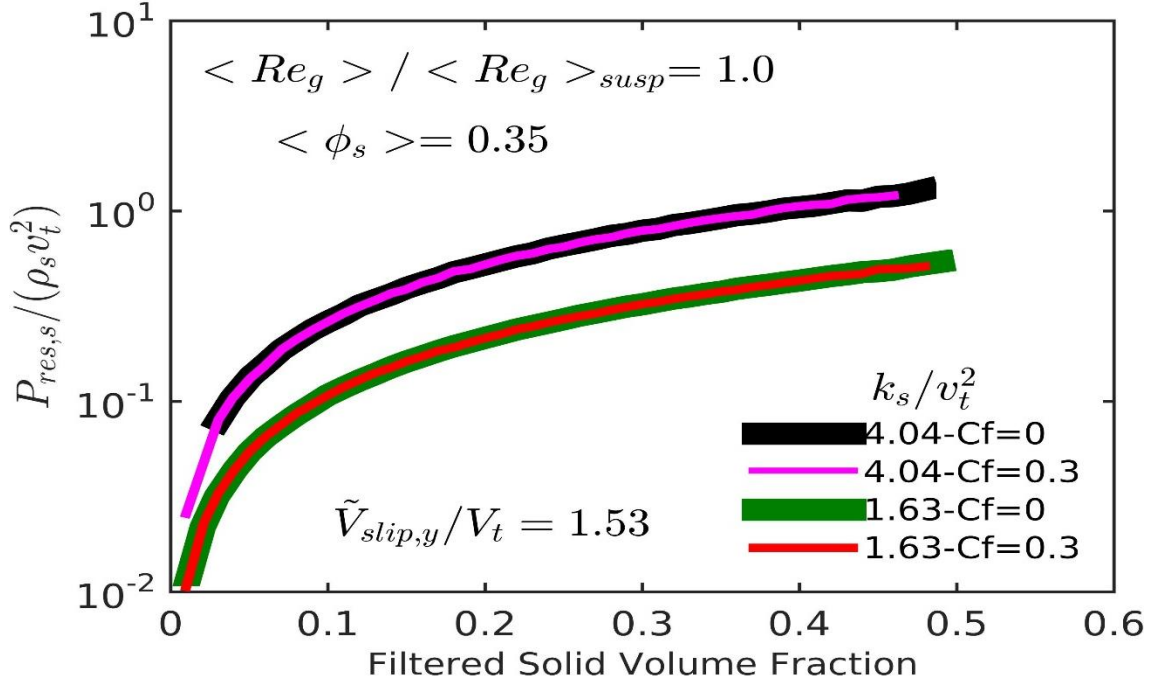
(e)



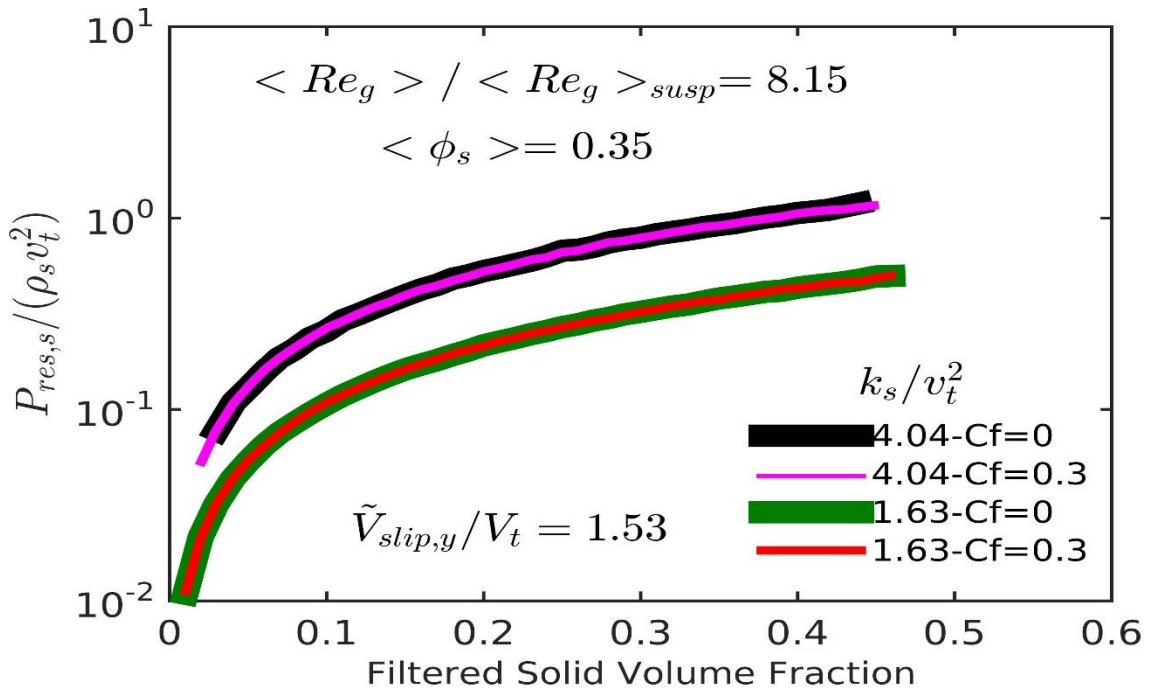
(f)

Source: Elaborated by the author

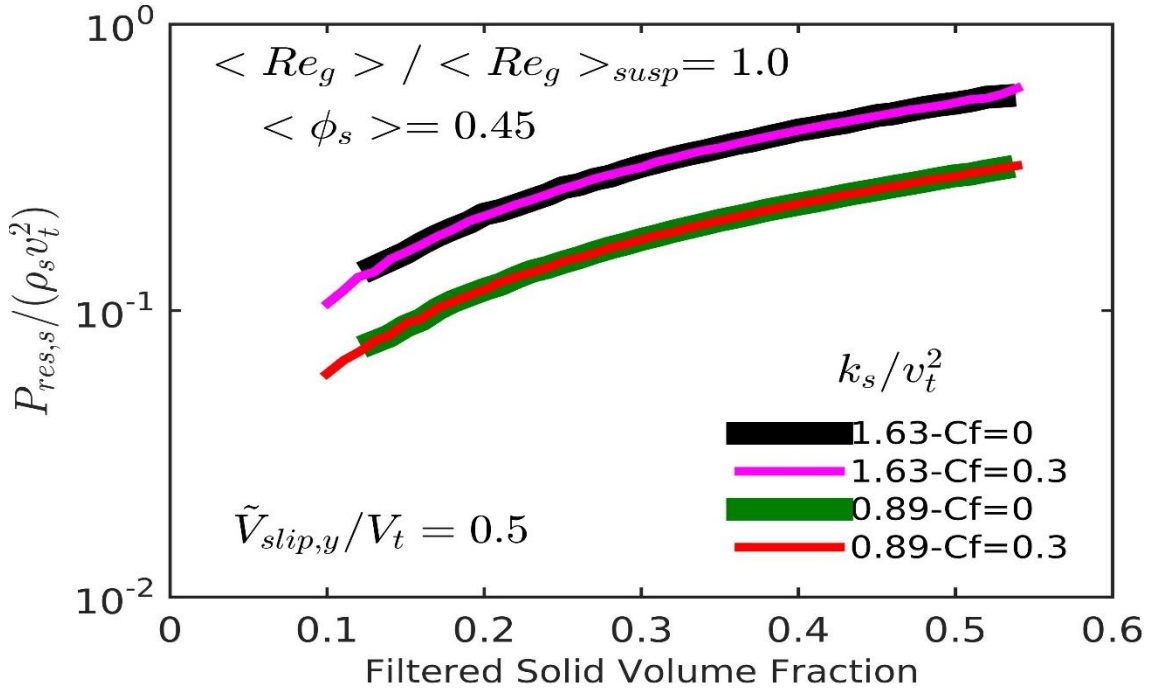
Figure 17 – Dimensionless residual solid pressure, $P_{res,s}/(\rho_s v_t^2)$, as a function of the filtered solid volume fraction $\bar{\phi}_s$ for the domain average solid volume fractions $\langle \phi_s \rangle = 0.35, 0.45$ and 0.50 and for gas Reynolds number ratios $\langle Re_g \rangle / \langle Re_g \rangle_{susp} = 1$ and 8.15 . The results stand for particular dimensionless filtered axial slip velocities $\tilde{V}_{slip,y}/V_t$, the dimensionless filter size $\Delta f / (v_t^2/g) = 4.112$, and for two different interparticle friction coefficients, $C_f = 0$ and 0.3 .



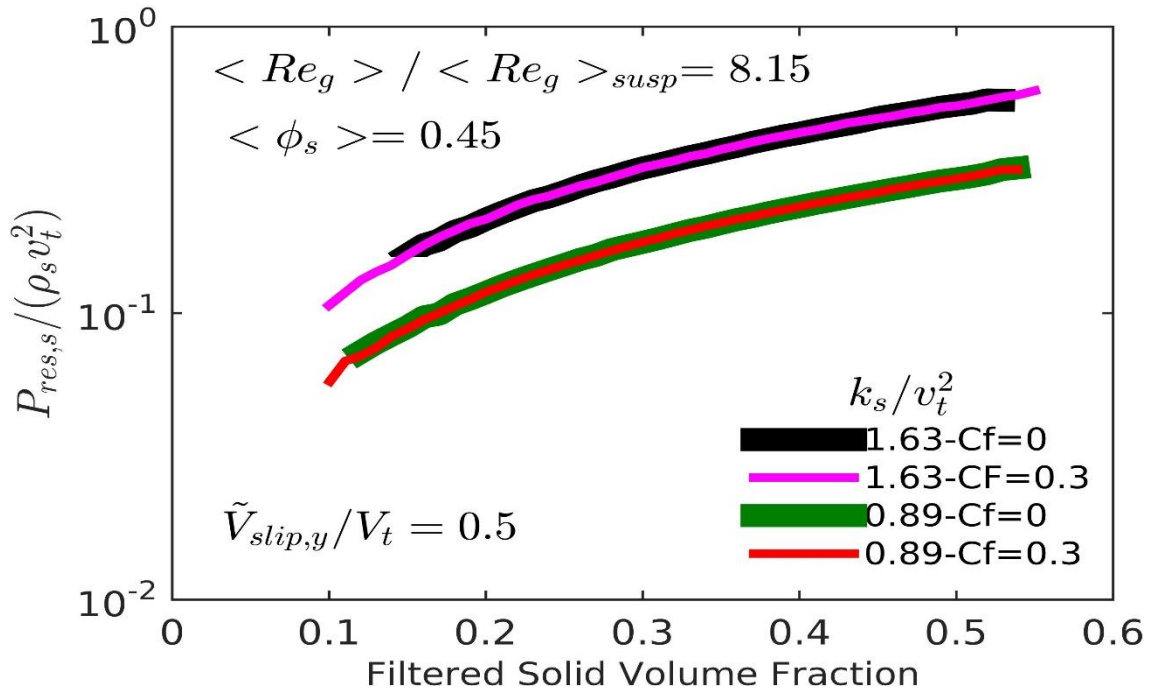
(a)



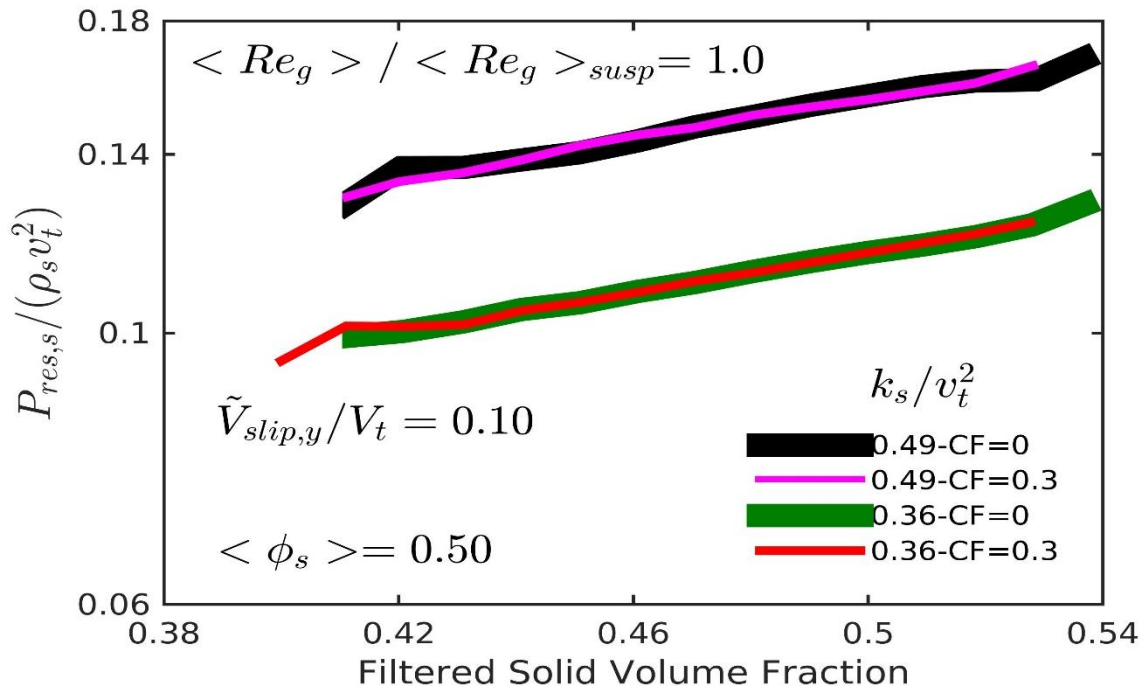
(b)



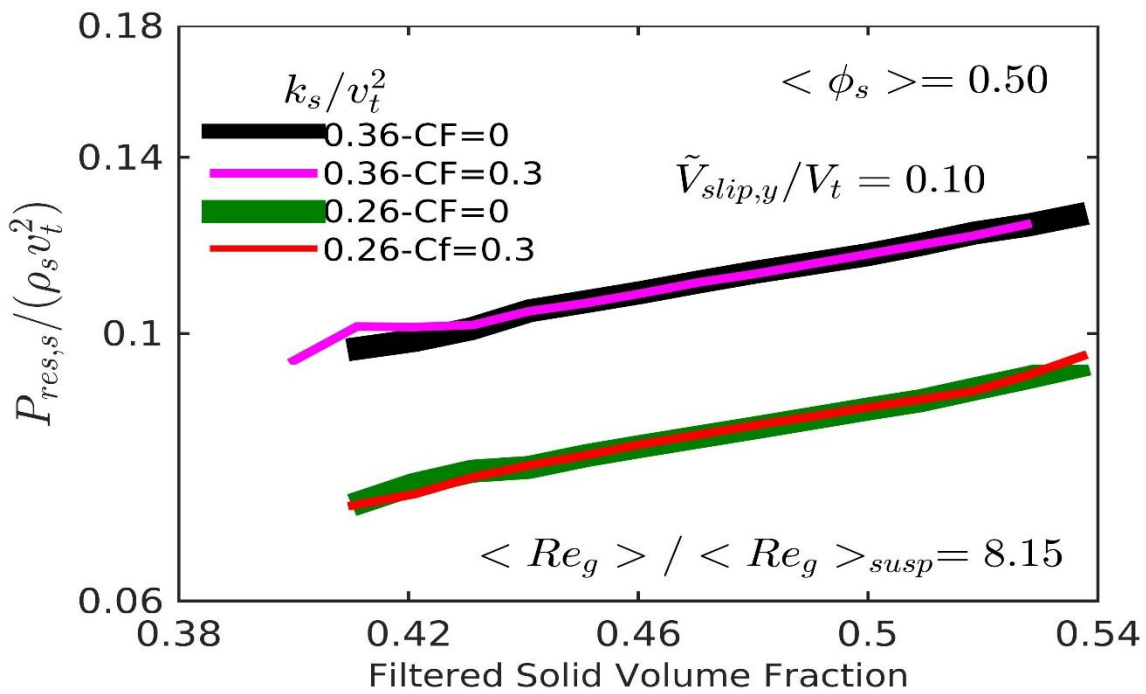
(c)



(d)

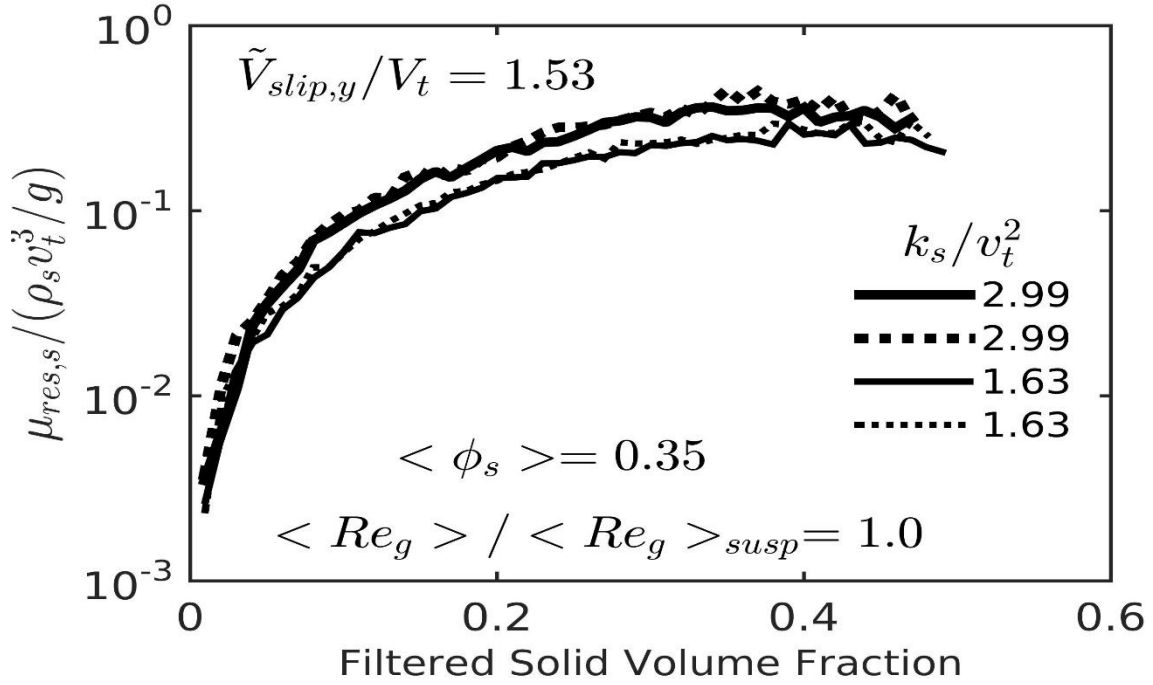


(e)

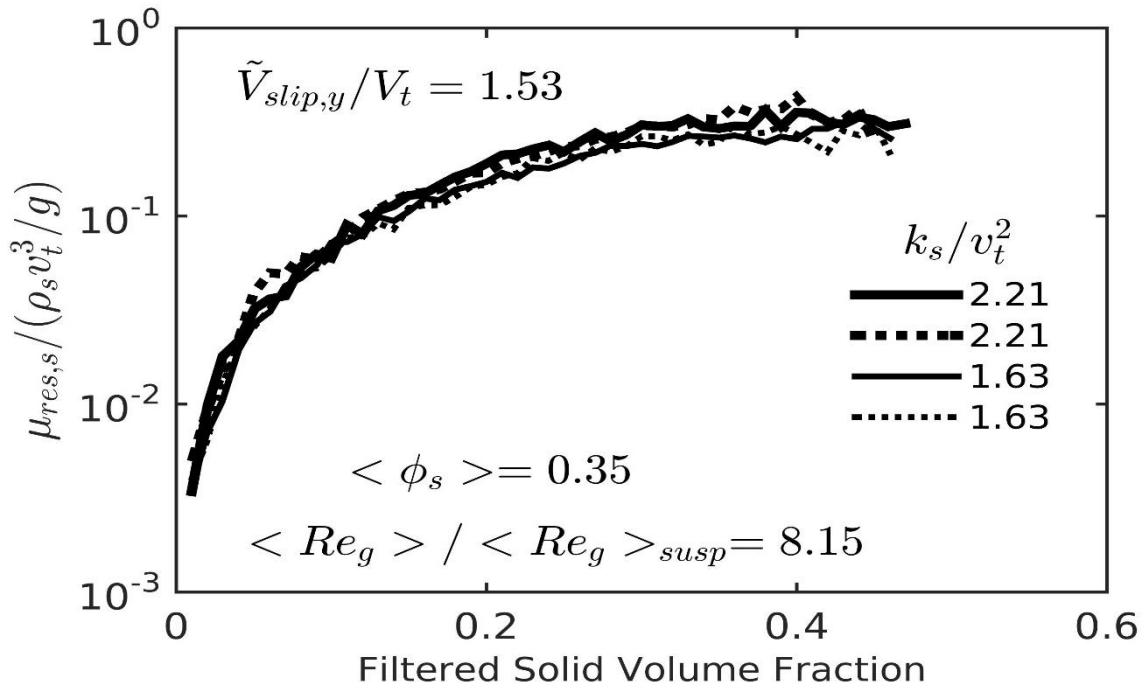


(f)

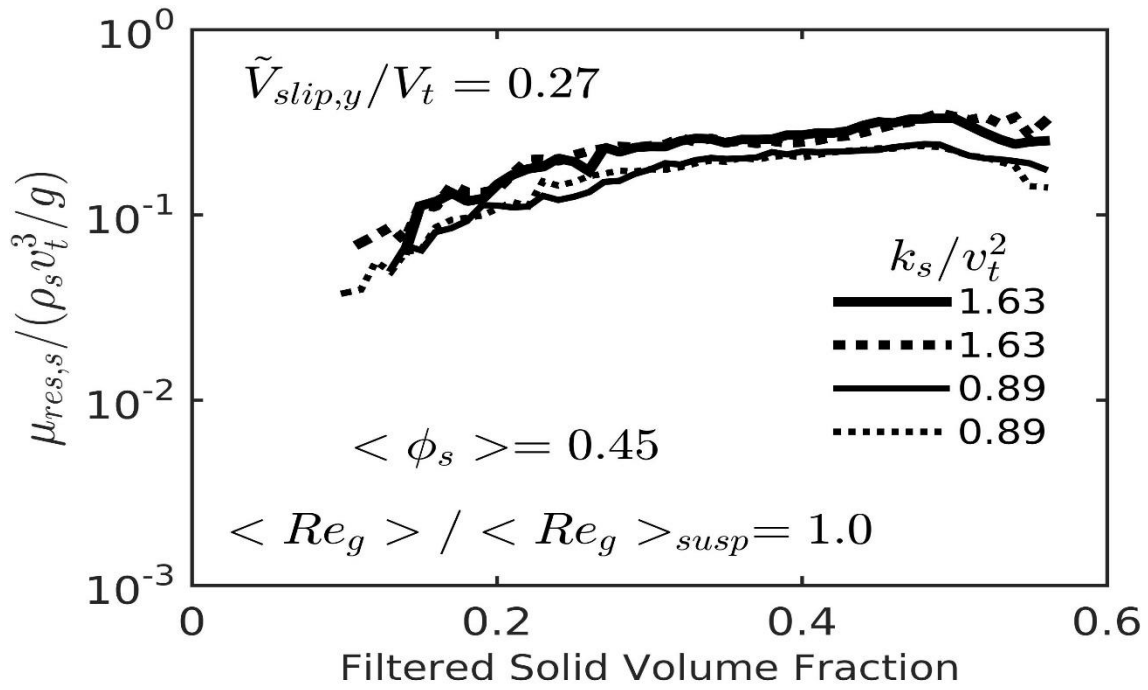
Figure 18 – Dimensionless residual solid dynamic viscosities, $\mu_{res,s}/(\rho_s v_t^3/g)$, as a function of the filtered solid volume fraction $\bar{\phi}_s$ for the domain average solid volume fractions $\langle \phi_s \rangle = 0.35, 0.45$ and 0.50 and for gas Reynolds number ratios $\langle Re_g \rangle / \langle Re_g \rangle_{susp} = 1$ and 8.15 . The results stand for particular dimensionless filtered axial slip velocities \tilde{V}_{slip}/V_t , the dimensionless filter size $\Delta_f/(v_t^2/g) = 4.112$, and for two different interparticle friction coefficient, $C_f = 0$ (full lines) and $C_f = 0.3$ (dash lines).



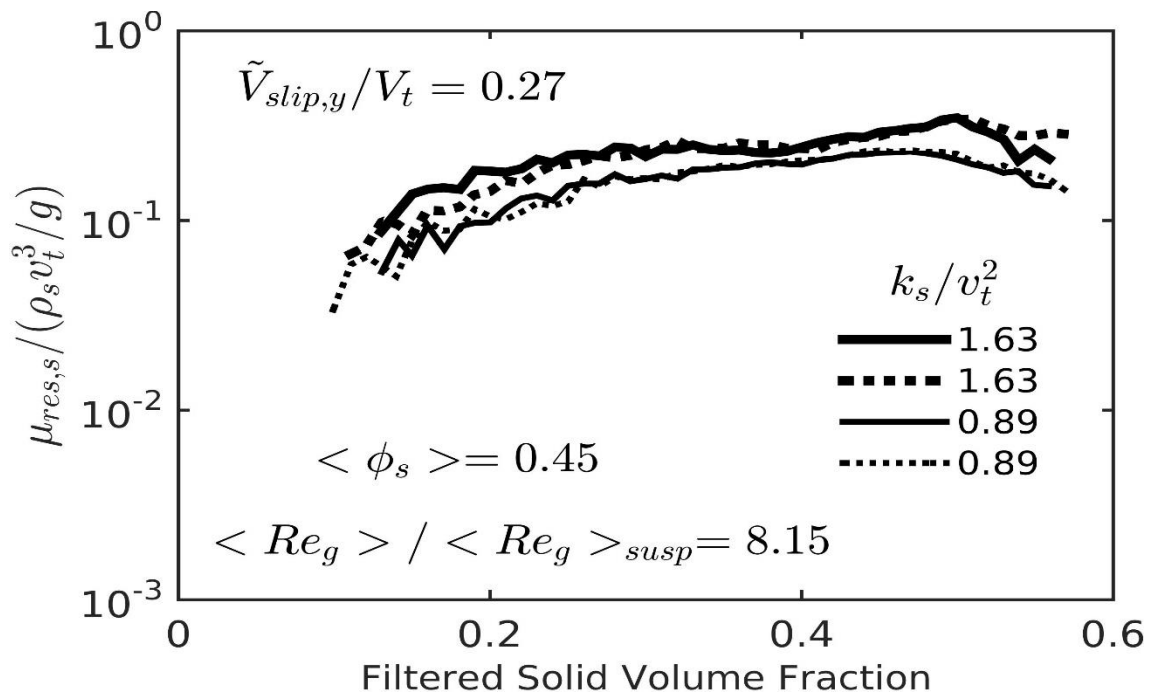
(a)



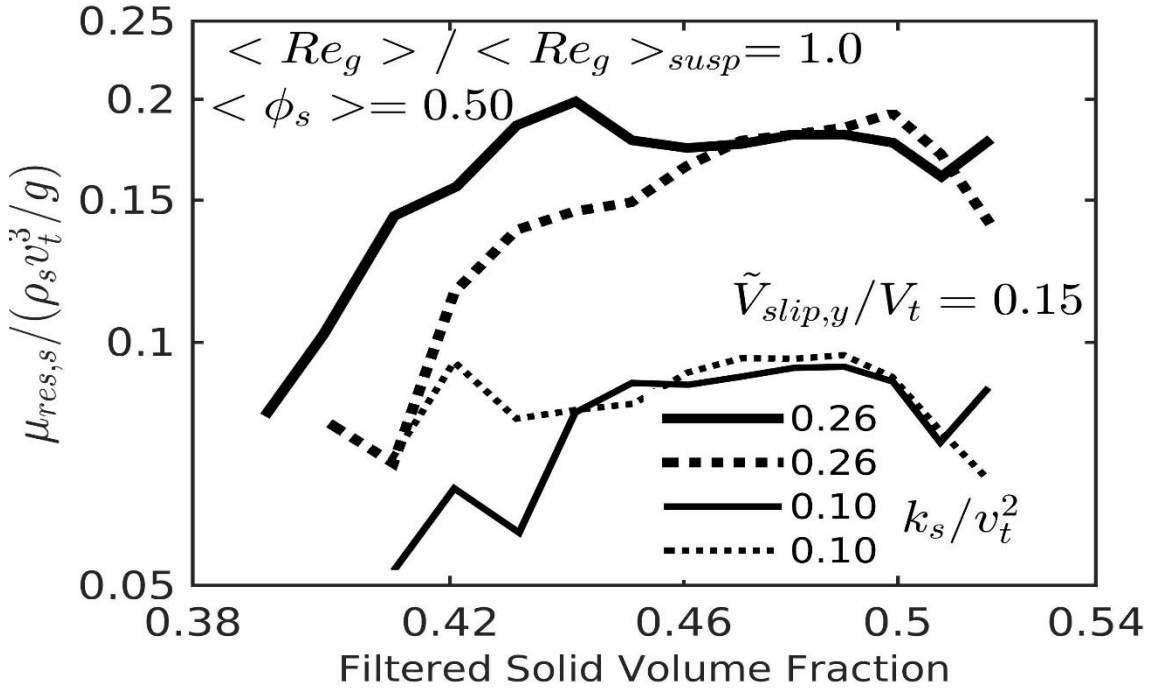
(b)



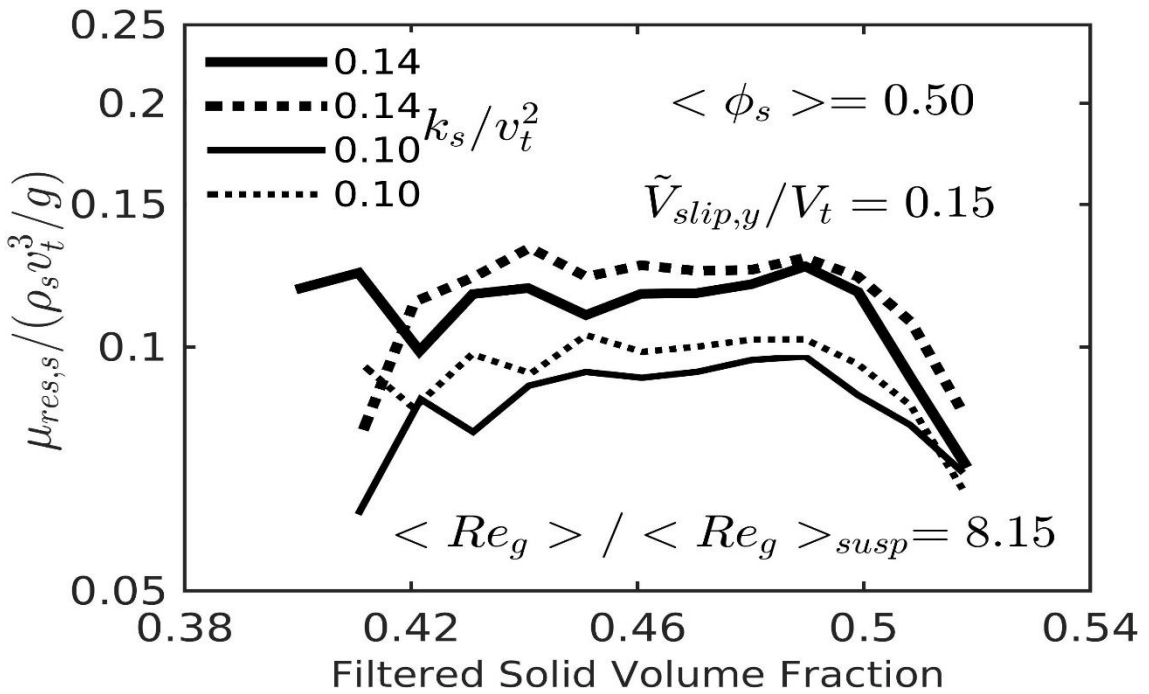
(c)



(d)



(e)



(f)

Source: Elaborated by the author

4 CONCLUSION

The current work was intended as a contribution for the improvement of sub-grid closure models for Large Scale Simulations (LSS) of gas-solid fluidized flows. Sub-grid filtered data were derived by filtering over results of highly resolved simulations under microscopic two-fluid modeling. Filtered parameters, like drag coefficient correction, residual and filtered solid pressure and viscosity were derived as a function of filtered solid volume fraction, filtered slip velocity and filtered kinetic energy of the solid velocity fluctuations.

In the simulations different macro-scale conditions were enforced by imposing various domain average solid volume fractions and gas Reynolds numbers, covering high density topology from suspensions up to pneumatic transport.

The conventional kinetic theory of granular flows (KTGF) was applied providing closures for solid phase stresses in the microscopic two-fluid formulation, accounting for kinetic-collisional effects only. A modified version of KTGF was also applied including interparticle frictional effects, which was advanced by Berzi and Vescovi (2015) following a previous approach developed by Chialvo and Sundaresan (2013). All the current simulations were performed with the open source code MFIX, which was modified to include frictional effects on its microscopic two-fluid model. The frictional implementation was tested by simulating a bin discharge problem described by Schneiderbauer et al. (2012). The modification of the MFIX code to add interparticle friction was performed by Milioli (2016), who also carried out the referred bin discharge simulation test. In this work such test was repeated confirming the results reported by Milioli (2016).

All the simulations were implemented in 2D periodic domains, for a single particle size and Froude and number, and for a unique friction coefficient following experimental data of Schneiderbauer et al. (2012). Highly Resolved Simulation (HRS) results were collected for a time interval of 32s inside the statistical steady-state regime, which was found enough to provide suitable statistics. Filtered results were derived and analysed for a unique filter size under a three marker binning procedure, where the filtered solid volume fraction was taken as the first marker, the filtered slip velocity as the second marker, and the filtered kinetic energy of the solid velocity fluctuations as the third marker. For the macro-scale variables taken into account, i.e. the domain average solid volume fraction and the domain average gas Reynolds number ratio, three values of the former (0.35, 0.45, 0.50) and four of the latter (1, 8.15, 16.30, 24.45) were considered.

Gray-scale plots of solid volume fraction in the domain showed that denser and heavier solid structures are formed for higher domain average solid fractions, while the flow field became more homogeneous at higher domain average gas Reynolds numbers. Filtered results were derived for two different situations:

The first aiming to evaluate the impact of the macro-scale flow conditions as a 3rd marker is accounted for; the second aiming to evaluate the impact of including interparticle friction effects. Regarding the analysis on the macro-scale effects, higher $\langle\phi_s\rangle$ and higher $\langle Re_g\rangle$ caused higher flow homogeneity, which led to: i) lower drag coefficient corrections, which are indeed a measure of the departure from homogeneity; ii) lower filtered and residual pressures and viscosities of the solid phase, owing to the lower solid velocity fluctuations that prevail at more homogeneous conditions. Regarding the 3rd marker analysis, results showed that the drag coefficient correction, the filtered and residual pressure and viscosity of the solid phase were all significantly affected by the filtered kinetic energy of the solid velocity fluctuations. This showed that the two-marker approach available in literature, considering the filtered solid volume fraction and filtered slip velocity as marker, is insufficient to correlate filtered parameters. While the current three-marker approach is, for sure, relatively more accurate, it does not prove to be enough, nor that the current markers are the more relevant to account for. Further investigations on those issues are required.

For any particular $\langle\phi_s\rangle$, $\langle Re_g\rangle$, \tilde{v}_{slip} and $\bar{\phi}_s$, a growing k_s cause: i) lower H; ii) higher $P_{fil,s}$, $\mu_{fil,s}$, $P_{res,s}$ and $\mu_{res,s}$. The first effect means more homogeneity at higher K_s ; the second effect is due to the higher solid velocity fluctuations of higher k_s . It was also observed that K_s loses relevance as a marker for H at higher $\langle\phi_s\rangle$, an effect that was anticipated for higher $\langle Re_g\rangle$.

Regarding the analysis of interparticle friction effects, the results showed no significant impact of its inclusion for all the macro-scale conditions that were practiced. In fact, very slight impact were observed on filtered and residual pressure and viscosities of the solid phase at higher $\langle\phi_s\rangle$ an effect that was anticipated for higher $\langle Re_g\rangle$.

There was an expectation that frictional effects could affect cluster mechanisms through altering the pattern of the particles contact, leading to changes in meso-scale filtered parameters. That expectation did not prevail, at least at the light of the current simulations. Of course, the accuracy of the method of investigation must be considered as a possible cause for mispredictions, for instance regarding the markers that were assumed in the analyses of the filtered parameters. In the present studies, filtered data were classified by narrow ranges of filtered solid volume fraction,

filtered slip velocity and filtered kinetic energy of the solid velocity fluctuations, which were assumed as suitable independent variables relevant to the meso-scale flow filtered parameters (named markers). It is just possible that those markers are either unsuitable or insufficient, as they may be hiding hydrodynamic effects dissipated by the statistical averaging procedures that are performed in the current binning process.

Regarding future research in sub-grid correlation for gas-solid fluidized flows under microscopic two-fluid modeling, there are two major aspects to be considered: i. the first concerns the accuracy of the microscopic two-fluid modeling itself; ii. the second concerns the accurate correlation of sub-grid filtered parameters.

Regarding the first aspect, some possible issues to be addressed may be:

- In two-fluid modeling both gas and solid phases are assumed as Newtonian fluids. Regarding the gas phase this is a trivial straightforward assumption. Otherwise, there is no guarantee that the Newtonian rheology equally holds for the solid phase. This is an open matter waiting for further research.
- The Wen and Yu (1966) drag model is widely applied as closure for drag in microscopic two-fluid modeling. This model, however, are better suited to homogeneous conditions, and does not quite apply to the heterogeneous micro-scale of the gas-solid fluidized flows. New more realistic micro-scale models are needed for drag which can be derived, for instance, by applying discrete element methods
- Besides drag and friction, other interphase interactive effects such as cohesive electrostatic and moisture may also become relevant in gas-solid fluidization. Such effects may be issues for future analyses.
- In microscopic two-fluid modeling, closures for solid phases are usually derived from the kinetic theory of granular flows, which still requires validation. This is a big challenge to be tackled.
- In highly resolved simulations gas turbulence is filtered, so that any effects it may have over solid phase coherent structures are lost. Some initial studies have been developed on the effects of gas sub-grid turbulence over the meso-scale hydrodynamics of gas-solid fluidized flows, as well as on the effects of the solid phase over the turbulence of the gas (i.e. gas turbulence

modulation by the solid phase), which are described in Mouallem (2018). Those are only initial studies that require further extension.

Regarding the second aspect, some possible issues to be addressed may be:

- The question of the markers taken as independent variables for the correlation of filtered parameters must be rigorously addressed. An in-depth analysis is missing in literature regarding the suitability and sufficiency of the markers that are usually considered.
- A variety of macro-scale conditions alongside with ranges of Froude numbers must be accounted for. This would be crucial regarding hydrodynamic scaling, an issue that remains as a big challenge in gas-solid fluidization. The establishment of physically meaningful hydrodynamic scales would be essential for future accurate correlation efforts.
- Literature presents highly resolved simulations of gas-solid fluidized flows mostly for monodisperse particulates (unique size and density). However, real gas-solid fluidized flows present wide granulometry and even density distributions. Therefore, polydisperse analyses are needed to enhance correlation accuracy.
- Gas-solid fluidized flows are 3D in nature. Therefore, having in view correlation accuracy, any attempt for advancing new sub-grid models, in the current line of research, should be based on 3D simulations.

REFERENCES

- Agrawal, Kapil. 2001. "The role of mesoscale structures in rapid granular and gas-solid flows."
- Anderson, TB, and Roy Jackson. 1968. "Fluid mechanical description of fluidized beds. Stability of state of uniform fluidization." *Industrial & Engineering Chemistry Fundamentals* 7 (1):12-21.
- Andrews IV, Arthur T, Peter N Loezos, and Sankaran Sundaresan. 2005. "Coarse-grid simulation of gas-particle flows in vertical risers." *Industrial & engineering chemistry research* 44 (16):6022-6037.
- Arnold, GS, DA Drew, and RT Lahey Jr. 1990. "An assessment of multiphase flow models using the second law of thermodynamics." *International journal of multiphase flow* 16 (3):481-494.
- Berzi, Diego, and Dalila Vescovi. 2015. "Different singularities in the functions of extended kinetic theory at the origin of the yield stress in granular flows." *Physics of fluids* 27 (1):013302.
- Cabezas-Gómez, L, RC Silva, and FE Milioli. 2006. "Some modeling and numerical aspects of the two-fluid simulation of the gas-solids flow in a CFB riser." *Brazilian Journal of Chemical Engineering* 23 (4):487-496.
- Chialvo, Sebastian, and Sankaran Sundaresan. 2013. "A modified kinetic theory for frictional granular flows in dense and dilute regimes." *Physics of Fluids* 25 (7):070603.
- Cocco, Ray, SB Reddy Karri, and Ted Knowlton. 2014. "Introduction to fluidization." *Chem. Eng. Prog* 110 (11):21-29.
- Drew, DA, and RT Lahey. 1993. "In particulate two-phase flow." *ButterworthL Heinemann, Boston* 509 (0):566.
- Enwald, Hans, Eric Peirano, and A-E Almstedt. 1996. "Eulerian two-phase flow theory applied to fluidization." *International Journal of Multiphase Flow* 22:21-66.
- Garzó, V, and JW Dufty. 1999. "Dense fluid transport for inelastic hard spheres." *Physical Review E* 59 (5):5895.
- Gidaspow, Dimitri. 1994. *Multiphase flow and fluidization: continuum and kinetic theory descriptions*: Academic press.
- Goldhirsch, I, M-L Tan, and G Zanetti. 1993. "A molecular dynamical study of granular fluids I: The unforced granular gas in two dimensions." *Journal of Scientific Computing* 8 (1):1-40.
- Igci, Yesim, Arthur T Andrews, Sankaran Sundaresan, Sreekanth Pannala, and Thomas O'Brien. 2008. "Filtered two-fluid models for fluidized gas-particle suspensions." *AIChE Journal* 54 (6):1431-1448.

- Igci, Yesim, and Sankaran Sundaresan. 2011a. "Constitutive models for filtered two-fluid models of fluidized gas–particle flows." *Industrial & Engineering Chemistry Research* 50 (23):13190-13201.
- Igci, Yesim, and Sankaran Sundaresan. 2011b. "Verification of filtered two-fluid models for gas-particle flows in risers." *AIChE Journal* 57 (10):2691-2707.
- Ishii, M. 1975. "Thermo-Fluid Theory of Two-Phase Flows." *Eyrolles, Paris*.
- Jenkins, James T, and Stuart B Savage. 1983. "A theory for the rapid flow of identical, smooth, nearly elastic, spherical particles." *Journal of fluid mechanics* 130:187-202.
- Johnson, Paul C, and Roy Jackson. 1987. "Frictional–collisional constitutive relations for granular materials, with application to plane shearing." *Journal of fluid Mechanics* 176:67-93.
- Kunii, Daizo, and Octave Levenspiel. 1991. "Phase interchange coefficients in bubbling fluidized beds." *Journal of chemical engineering of Japan* 24 (1):138-141.
- Kunii, Daizo, and Octave Levenspiel. 2013. *Fluidization engineering*: Elsevier.
- Leva, Max, Milton Grummer, Murray Weintraub, and Morris Pollchik. 1948. "Introduction to fluidization." *Chemical Engineering Progress* 44 (7):511-520.
- Lun, CKK, S Br Savage, DJ Jeffrey, and N Chepurniy. 1984. "Kinetic theories for granular flow: inelastic particles in Couette flow and slightly inelastic particles in a general flowfield." *Journal of fluid mechanics* 140:223-256.
- Milioli, C.C. 2016. research report proc. FAPESP 2014/11359-2, Princeton University-USA.
- Milioli, Christian C, Fernando E Milioli, William Holloway, Kapil Agrawal, and Sankaran Sundaresan. 2013. "Filtered two-fluid models of fluidized gas-particle flows: new constitutive relations." *AIChE Journal* 59 (9):3265-3275.
- Ozel, A, Pascal Fede, and Olivier Simonin. 2013. "Development of filtered Euler–Euler two-phase model for circulating fluidised bed: high resolution simulation, formulation and a priori analyses." *International Journal of Multiphase Flow* 55:43-63.
- Pangarkar, Vishwas G. 2014. *Design of multiphase reactors*: John Wiley & Sons.
- Parmentier, Jean-François, Olivier Simonin, and Olivier Delsart. 2012. "A functional subgrid drift velocity model for filtered drag prediction in dense fluidized bed." *AIChE Journal* 58 (4):1084-1098.
- Sarkar, Avik, Fernando E Milioli, Shailesh Ozarkar, Tingwen Li, Xin Sun, and Sankaran Sundaresan. 2016. "Filtered sub-grid constitutive models for fluidized gas-particle flows constructed from 3-D simulations." *Chemical Engineering Science* 152:443-456.

Schaeffer, David G. 1987. "Instability in the evolution equations describing incompressible granular flow." *Journal of differential equations* 66 (1):19-50.

Schneiderbauer, Simon. 2017. "Validation study on Spatially Averaged Two Fluid Model for dense gassolids flows." *CFB-12, Krakow, Poland*.

Schneiderbauer, Simon, Andreas Aigner, and Stefan Pirker. 2012. "A comprehensive frictional-kinetic model for gas-particle flows: Analysis of fluidized and moving bed regimes." *Chemical Engineering Science* 80:279-292.

Schneiderbauer, Simon, and Stefan Pirker. 2014. "Filtered and heterogeneity-based subgrid modifications for gas-solid drag and solid stresses in bubbling fluidized beds." *AIChE Journal* 60 (3):839-854.

Srivastava, Anuj, and Sankaran Sundaresan. 2003. "Analysis of a frictional-kinetic model for gas-particle flow." *Powder technology* 129 (1-3):72-85.

Sundaresan, Sankaran. 2000. "Modeling the hydrodynamics of multiphase flow reactors: current status and challenges." *AIChE Journal* 46 (6):1102-1105.

Syamlal, Madhava, William Rogers, and Thomas J OBrien. 1993. MFIx documentation theory guide. USDOE Morgantown Energy Technology Center, WV (United States).

Tan, ML, and I Goldhirsch. 1997. "Intercluster interactions in rapid granular shear flows." *Physics of Fluids* 9 (4):856-869.

Wang, XS, NA Akhtar, BM Gibbs, and MJ Rhodes. 1999. "Abatement of NO_x emission from a circulating fluidized bed combustor." *Clean Combustion Technologies: Proceedings of the Second International Conference, Part 2*.

Wen, C-Y. 1966. "Mechanics of fluidization." *Chem. Eng. Prog. Symp. Ser.*

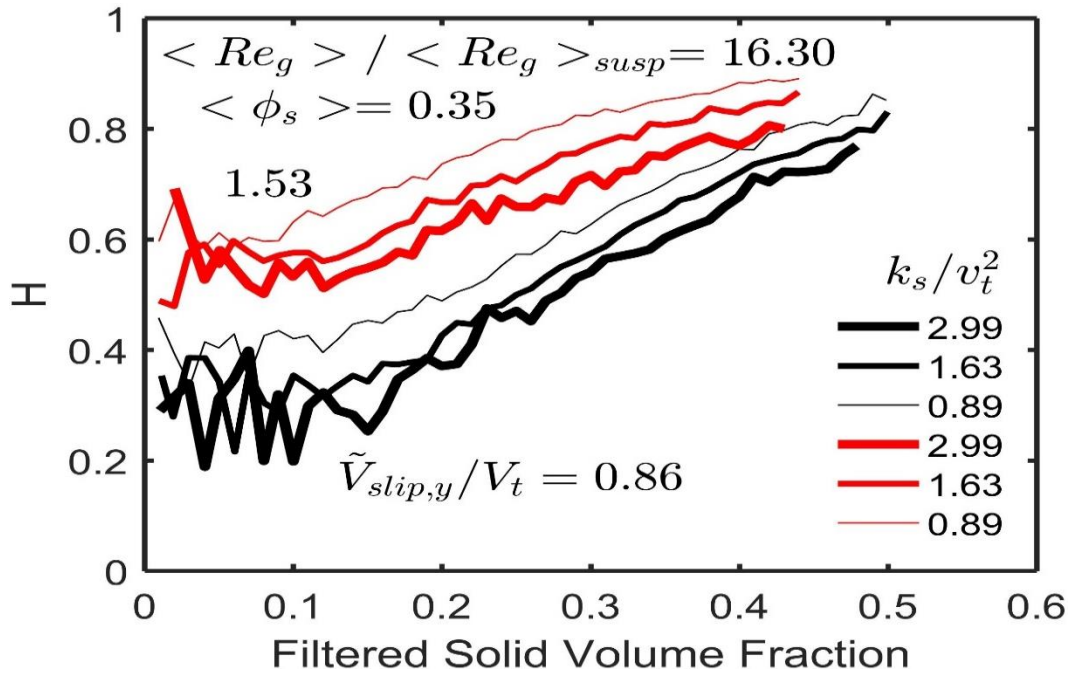
Appendices

Appendix A – Case 1: Third marker analysis – results for high Reynolds number ratios

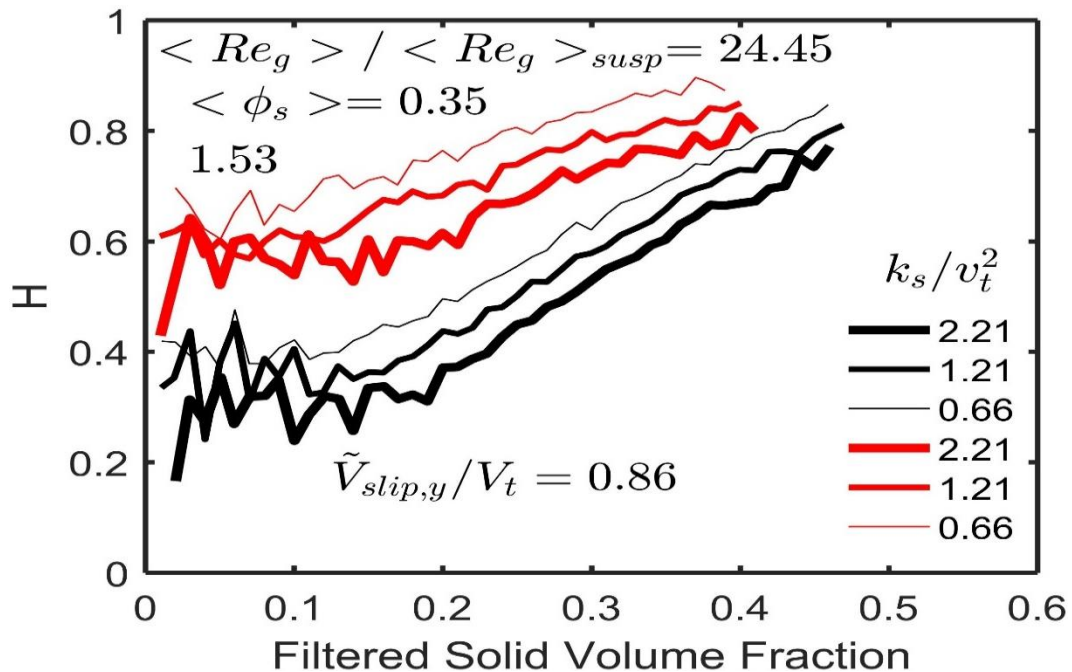
Figure 19 shows results of the drag coefficient correction, H . Figures 20 and 21 show results of the dimensionless filtered solid pressure, $P_{\text{fil},s}/(\rho_s v_t^2)$, and dimensionless filtered solid dynamic viscosity, $\mu_{\text{fil},s}/(\rho_s v_t^3/g)$. Figures 22 and 23 show results of the dimensionless residual solid pressure, $P_{\text{res},s}/(\rho_s v_t^2)$, and dimensionless residual solid dynamic viscosity, $\mu_{\text{res},s}/(\rho_s v_t^3/g)$.

The results stand for gas Reynolds number ratios $\langle \text{Re}_g \rangle / \langle \text{Re}_g \rangle_{\text{susp}} = 16.30$ and 24.45 , domain average solid volume fractions $\langle \phi_s \rangle = 0.35, 0.45$ and 0.50 and dimensionless filter size of 4.112 . Each graph shows the variation of the concerning parameter with the solid volume fraction and the filtered kinetic energy of the solid velocity fluctuations, for particular values of filtered slip velocity.

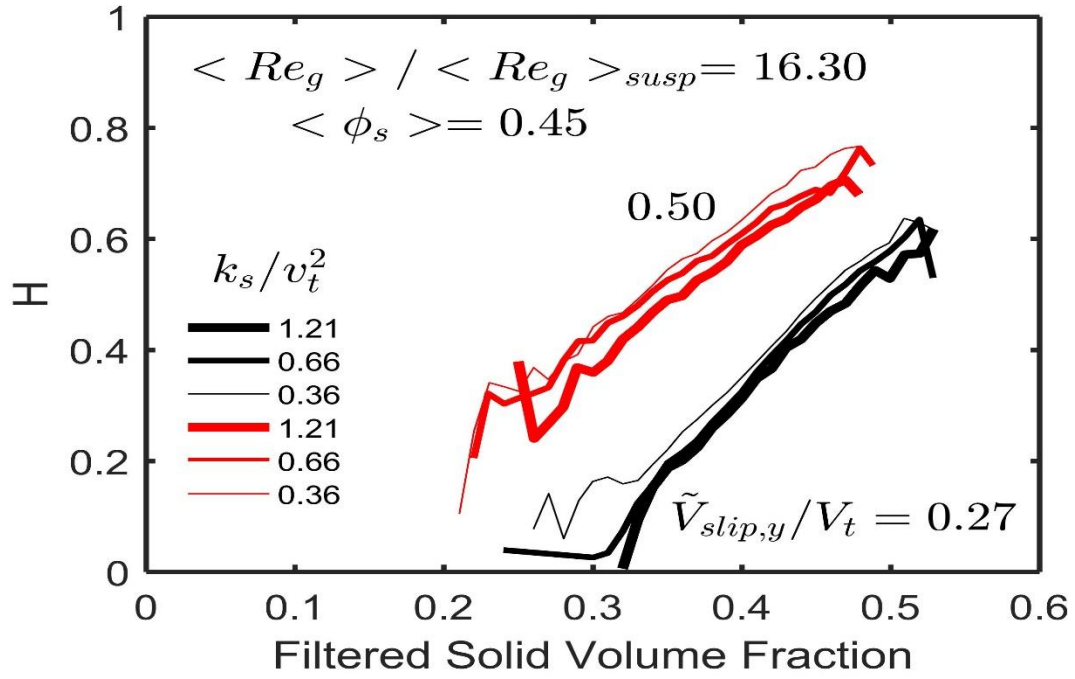
Figure 19 – Drag Coefficient Correction, H , as a function of the filtered solid volume fraction $\bar{\phi}_s$ for the domain average solid volume fractions $\langle \phi_s \rangle = 0.35, 0.45$ and 0.50 and for gas Reynolds number ratios $\langle Re_g \rangle / \langle Re_g \rangle_{susp} = 16.30$ and 24.45 . The results stand for different dimensionless filtered axial slip velocities \tilde{v}_{slip} / v_t (black and red), the dimensionless filter size $\Delta_f / (v_t^2 / g) = 4.112$, and for various dimensionless filtered kinetic energy of the solid velocity fluctuations k_s / v_t^2 (with different thickness). All graphs for $C_f = 0$.



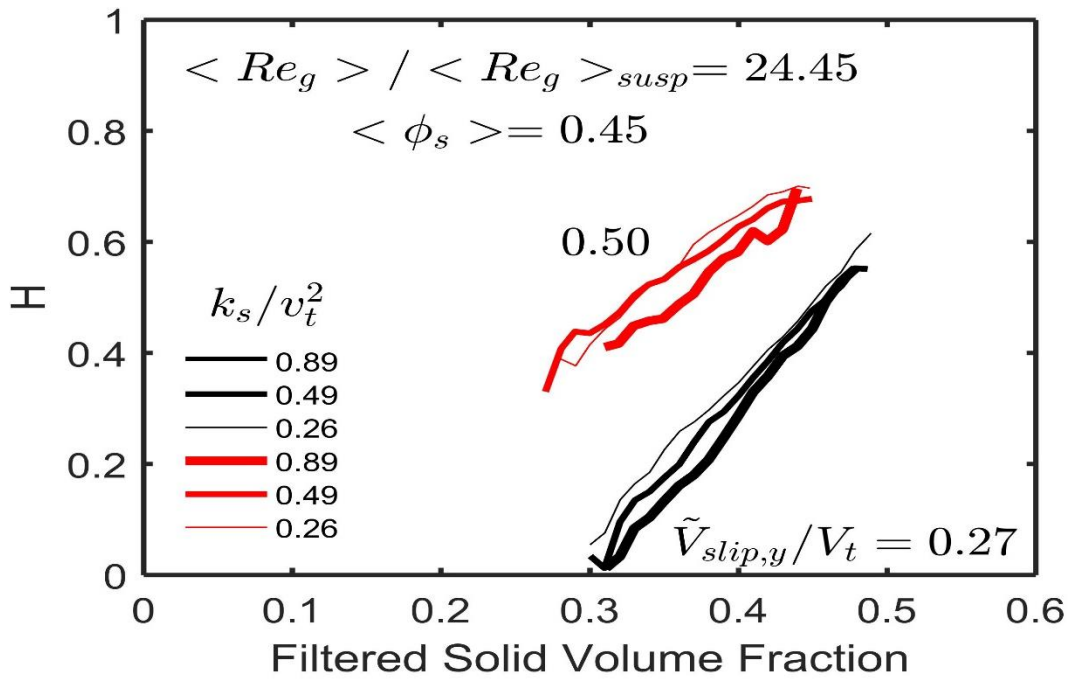
(a)



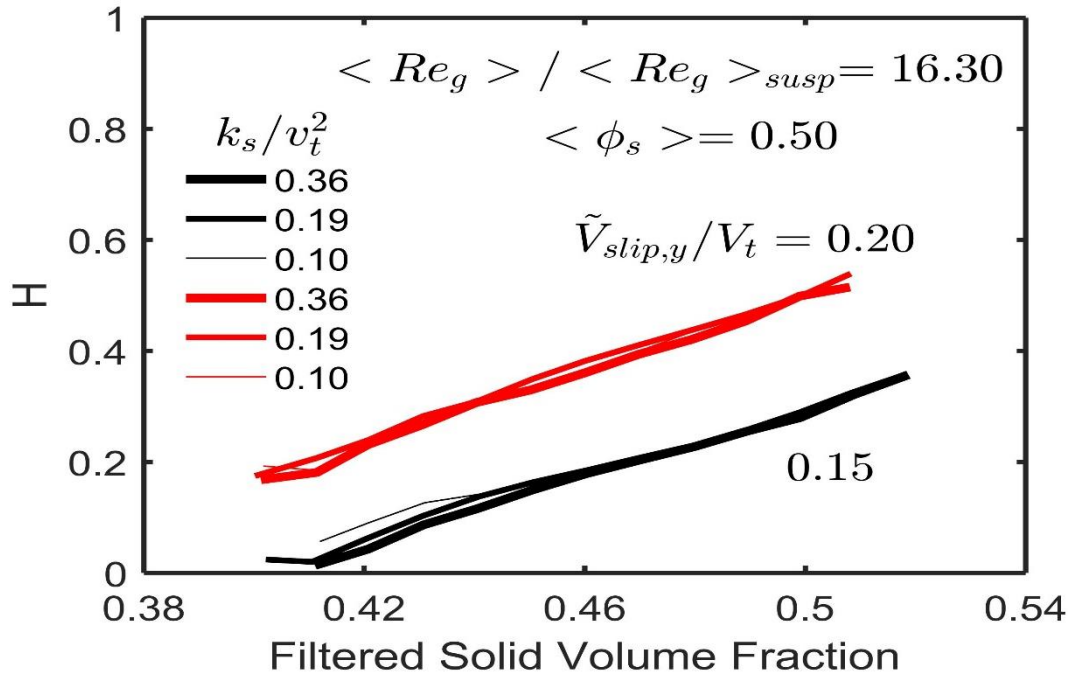
(b)



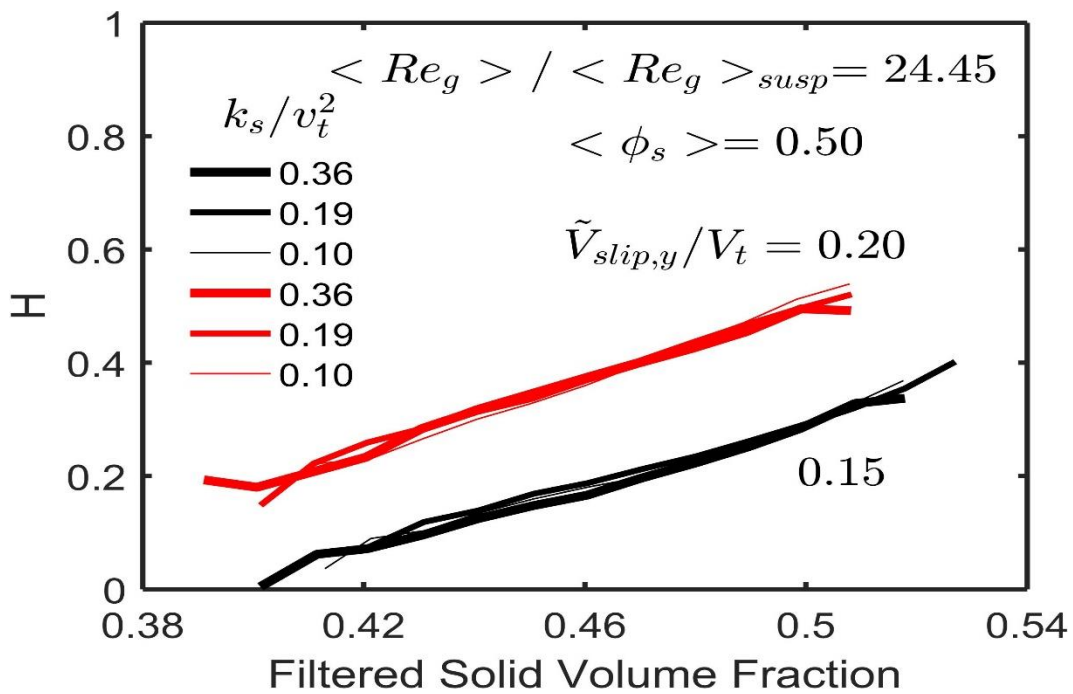
(c)



(d)



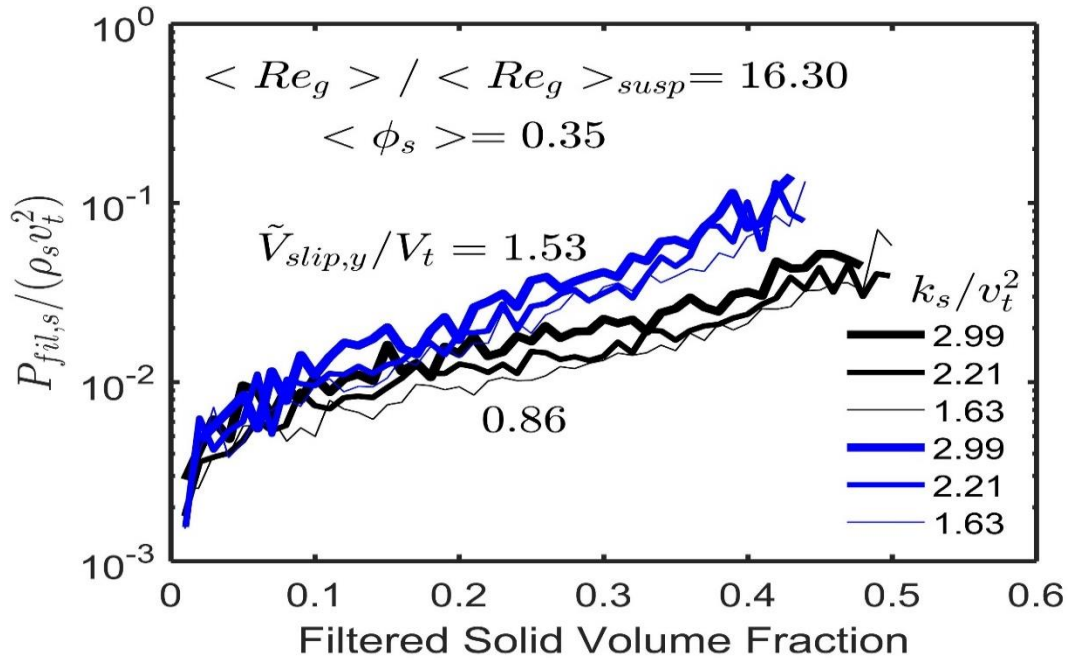
(e)



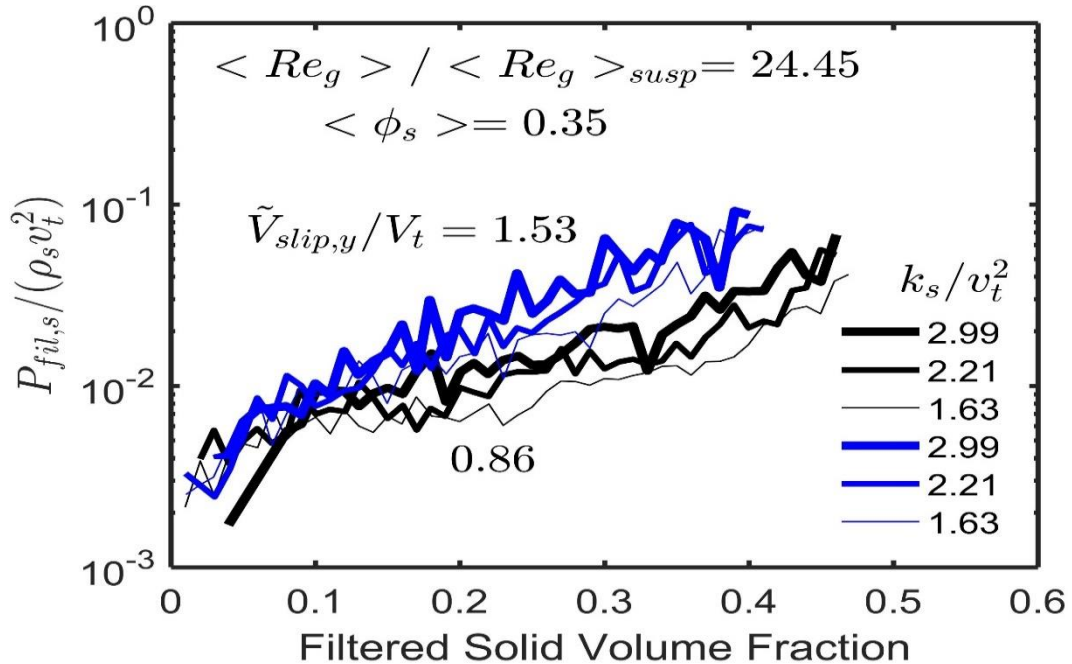
(f)

Source: Elaborated by the author

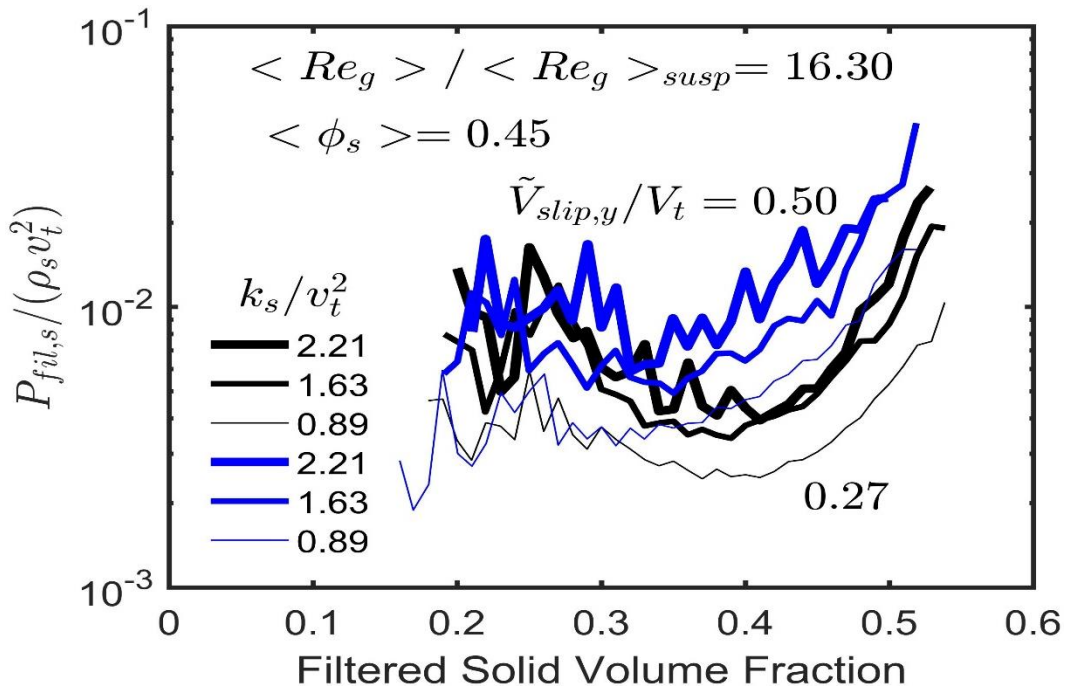
Figure 20 – Dimensionless filtered solid dynamic viscosities $P_{fil,s}/(\rho_s v_t^2)$, as a function of the filtered solid volume fraction $\bar{\phi}_s$ for the domain average solid volume fractions $\langle \phi_s \rangle = 0.35, 0.45$ and 0.50 and for gas Reynolds number ratios $\langle Re_g \rangle / \langle Re_g \rangle_{susp} = 16.30$ and 24.45 . The results stand for different dimensionless filtered axial slip velocities \tilde{V}_{slip}/V_t (black and blue), the dimensionless filter size $\Delta_f/(v_t^2/g) = 4.112$, and for various dimensionless filtered kinetic energy of the solid velocity fluctuations k_s/v_t^2 (with different thickness). All graphs for $C_f = 0$.



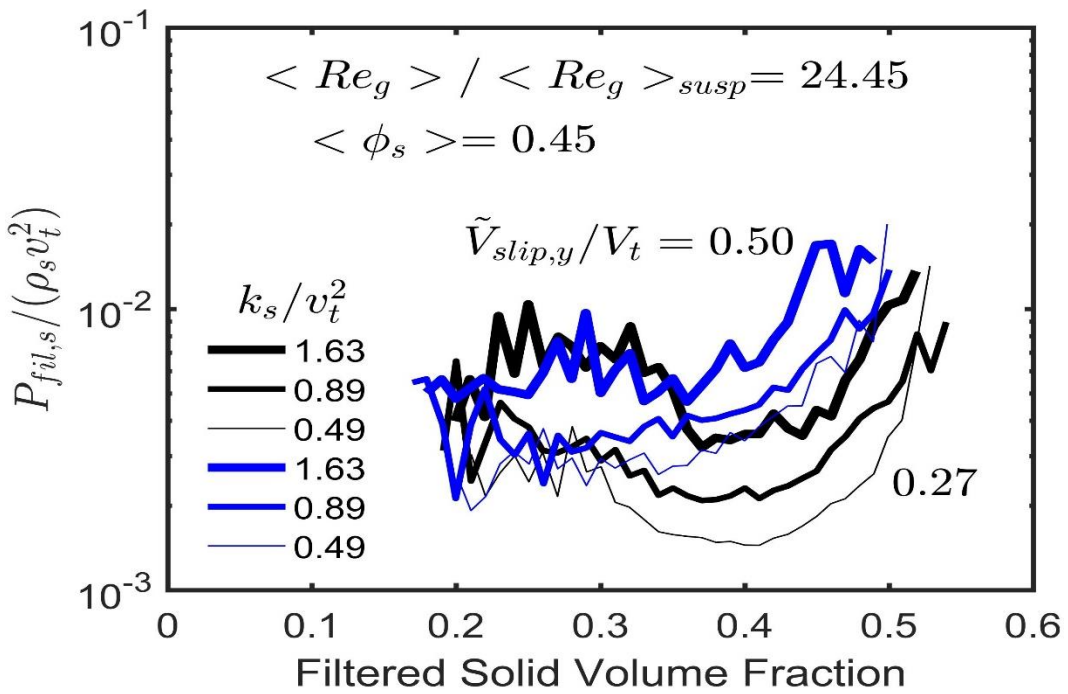
(a)



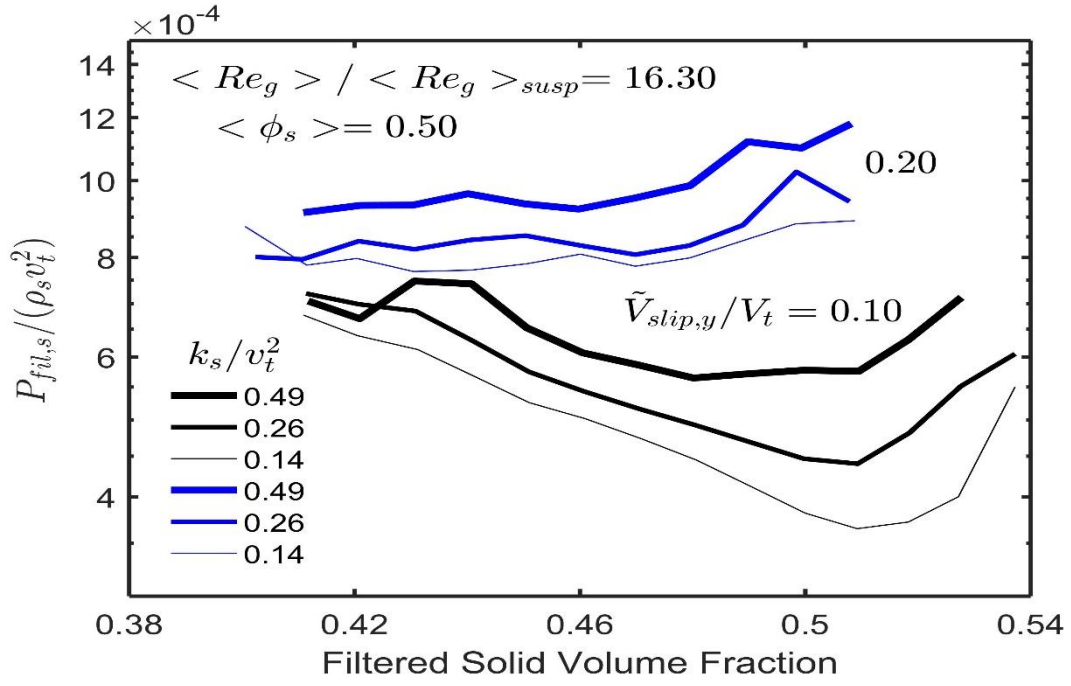
(b)



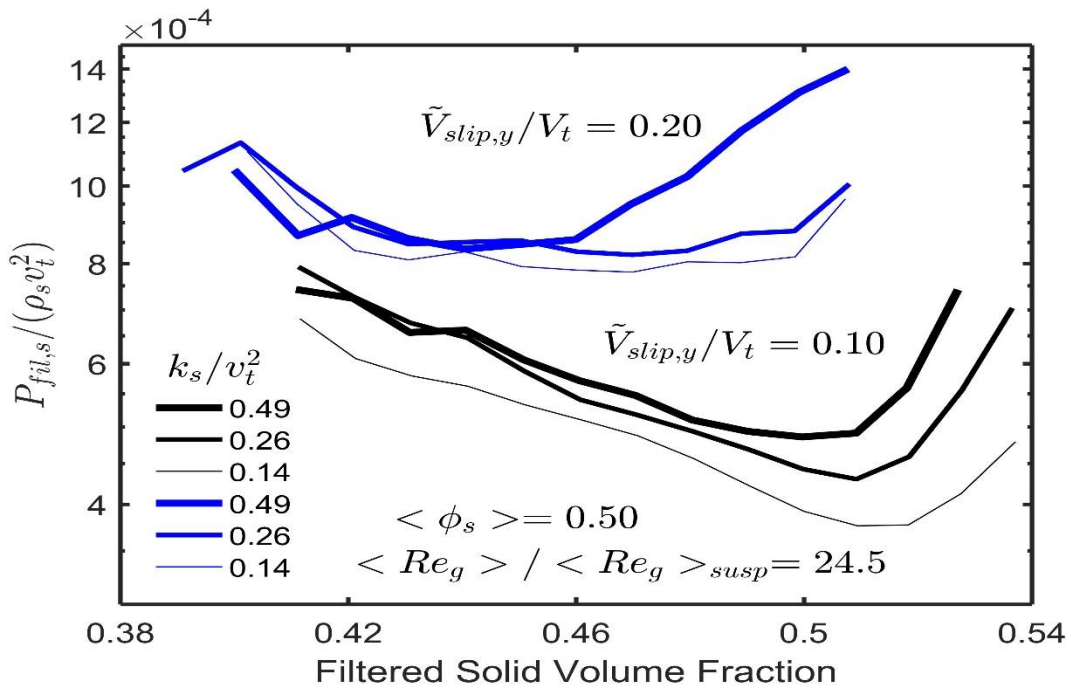
(c)



(d)



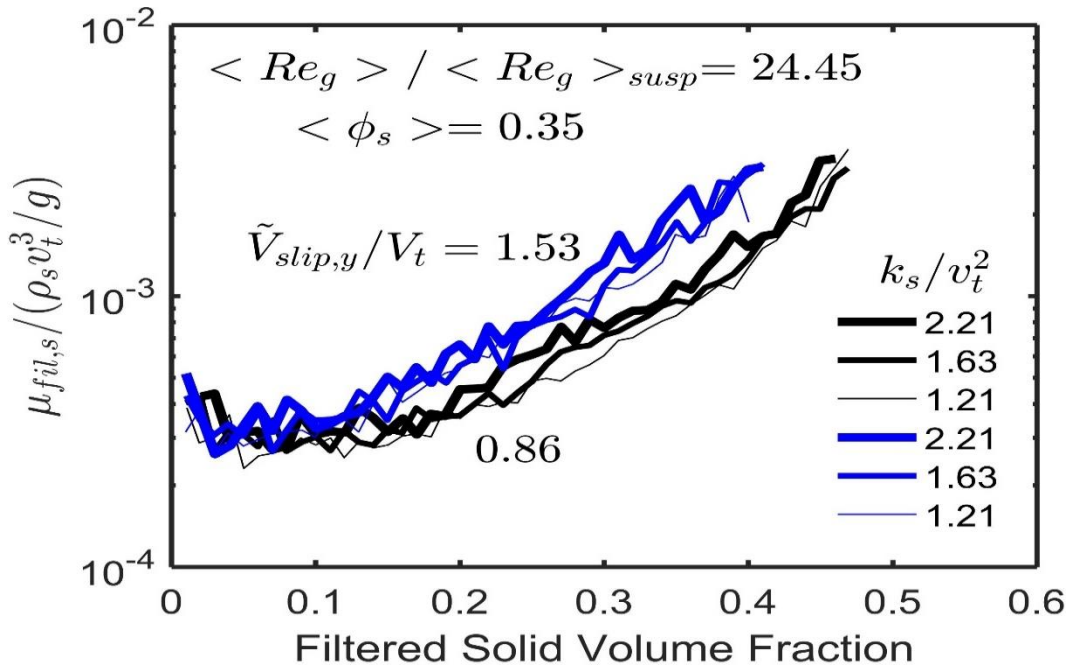
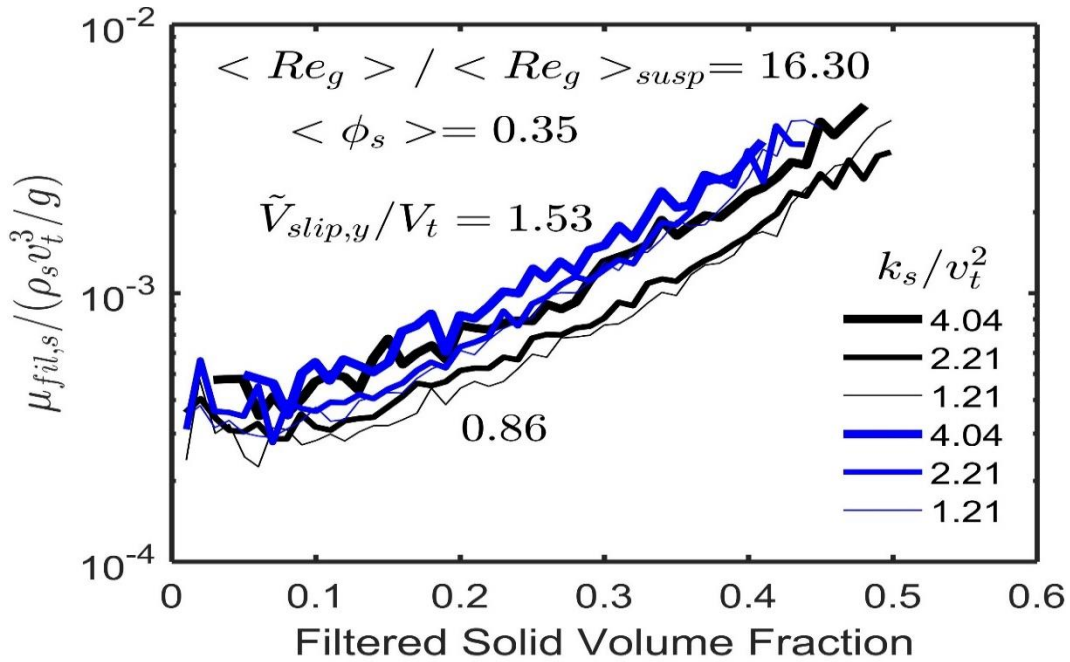
(e)

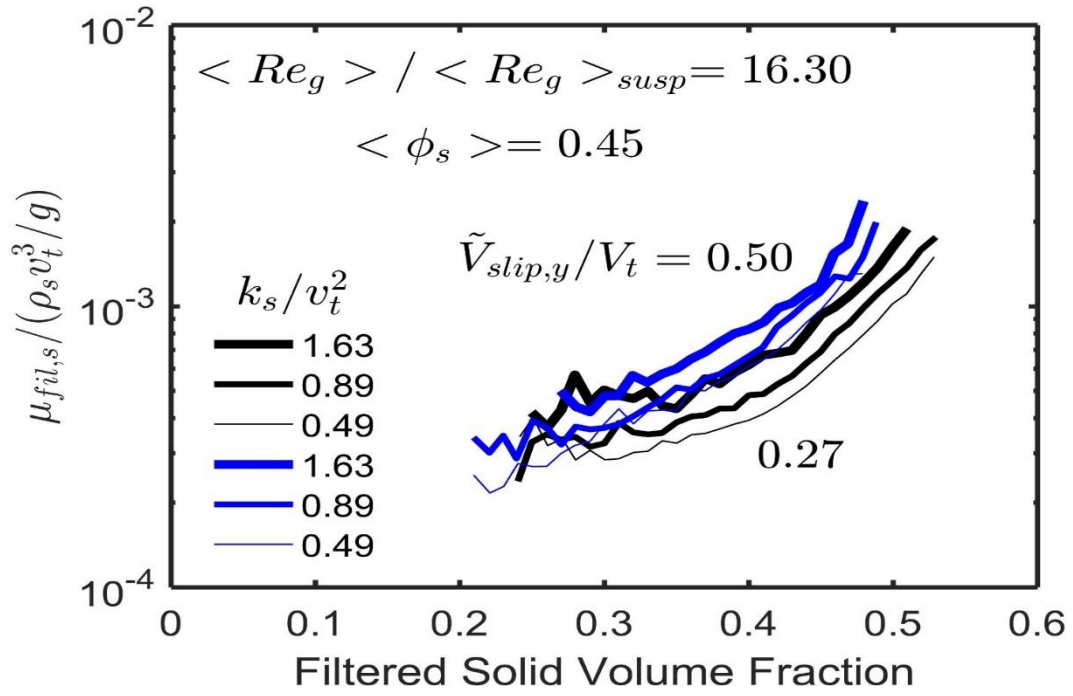


(f)

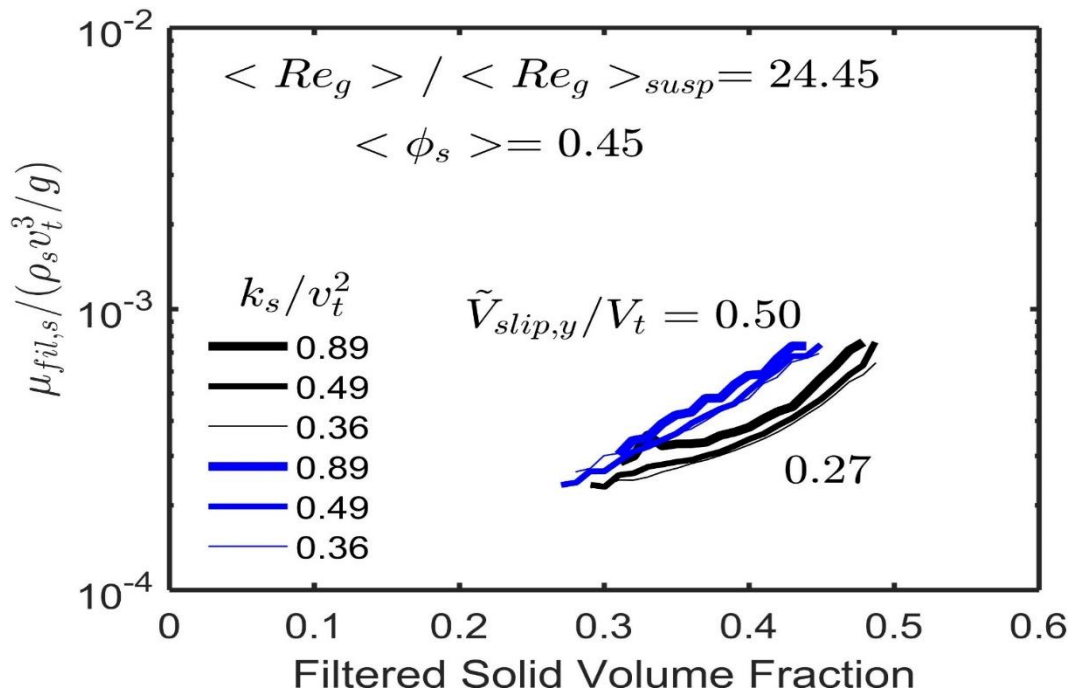
Source: Elaborated by the author

Figure 21 – Dimensionless filtered solid dynamic viscosities $\mu_{fil,s}/(\rho_s v_t^3/g)$, as a function of the filtered solid volume fraction $\bar{\phi}_s$ for the domain average solid volume fractions $\langle \phi_s \rangle = 0.35, 0.45$ and 0.50 and for gas Reynolds number ratios $\langle Re_g \rangle / \langle Re_g \rangle_{susp} = 16.30$ and 24.45 . The results stand for different dimensionless filtered axial slip velocities \tilde{V}_{slip}/V_t (black and blue), the dimensionless filter size $\Delta_f/(v_t^2/g) = 4.112$, and for various dimensionless filtered kinetic energy of the solid velocity fluctuations k_s/v_t^2 (with different thickness). All graphs for $C_f = 0$.

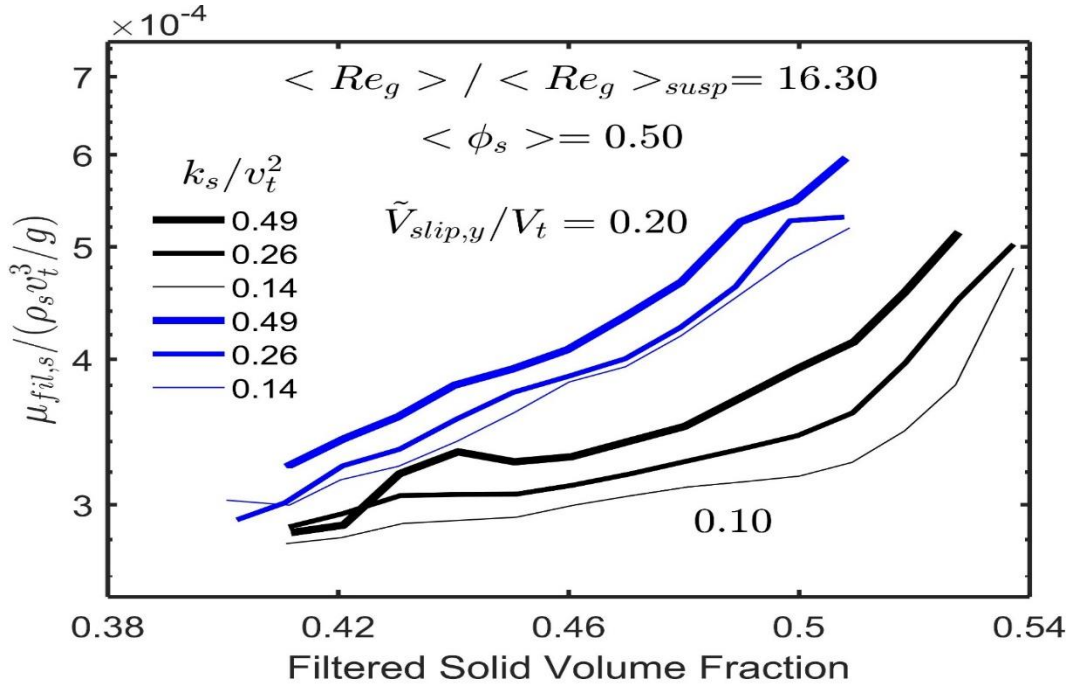




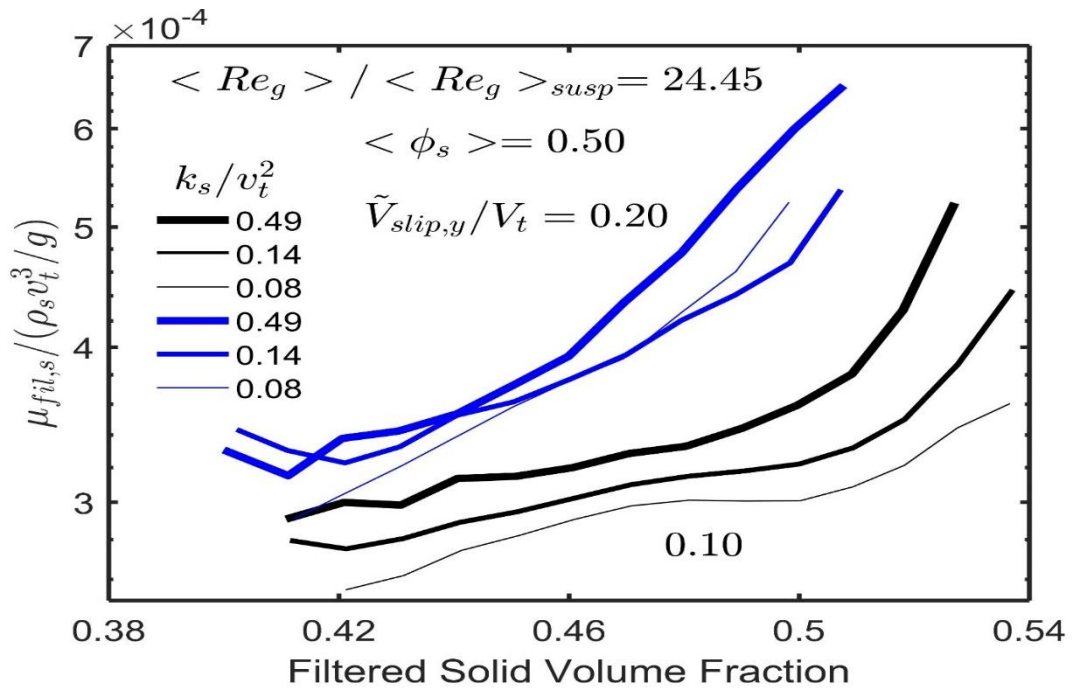
(c)



(d)



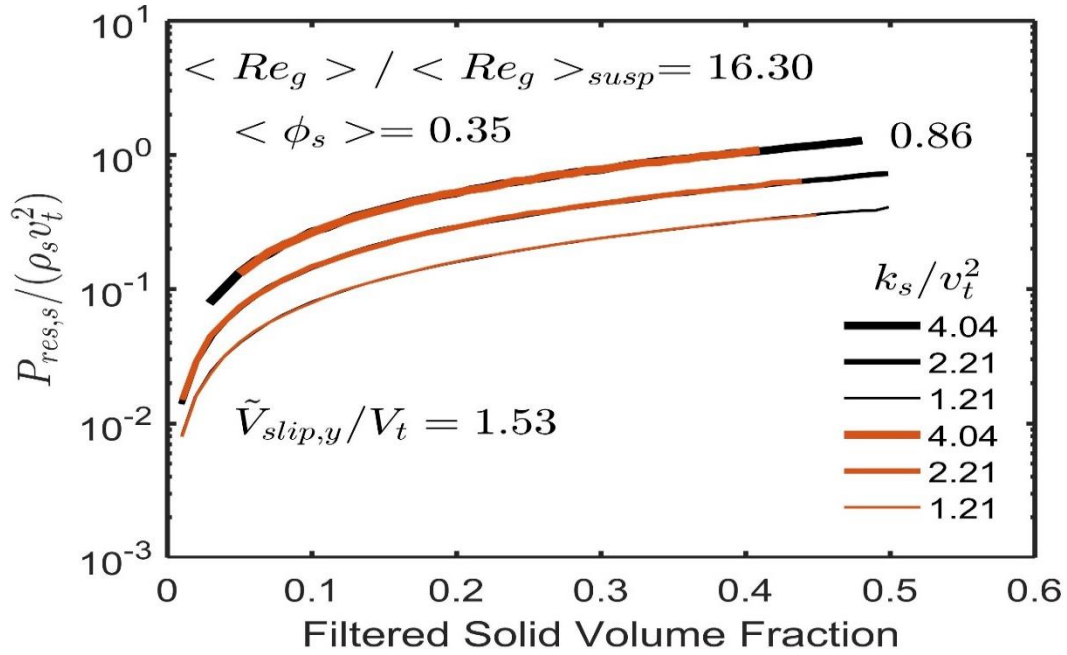
(e)



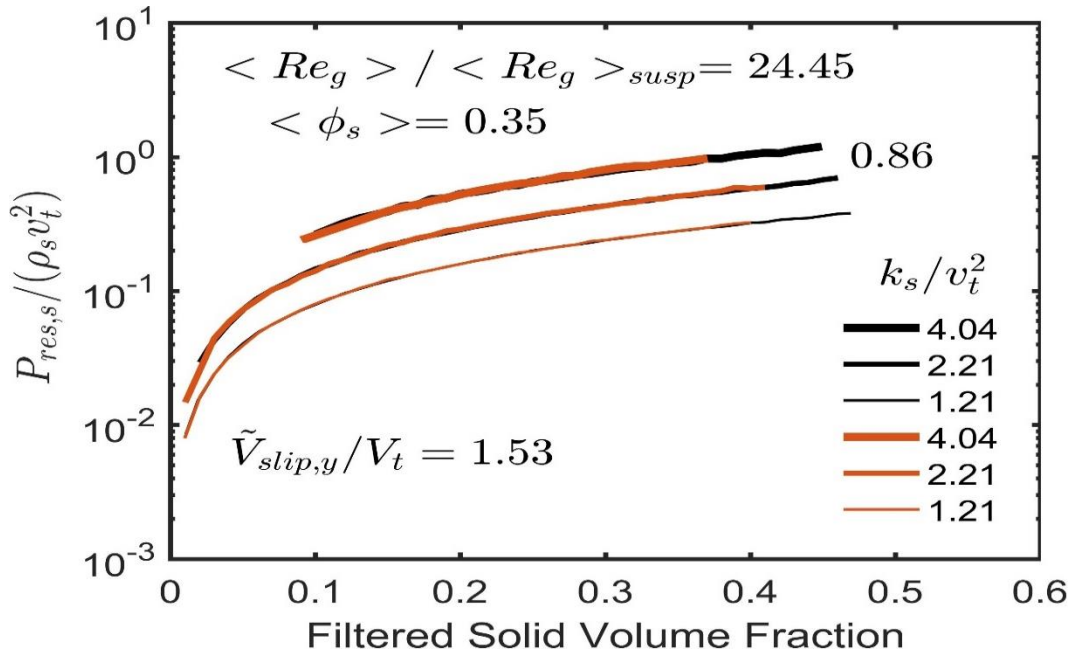
(f)

Source: Elaborated by the author

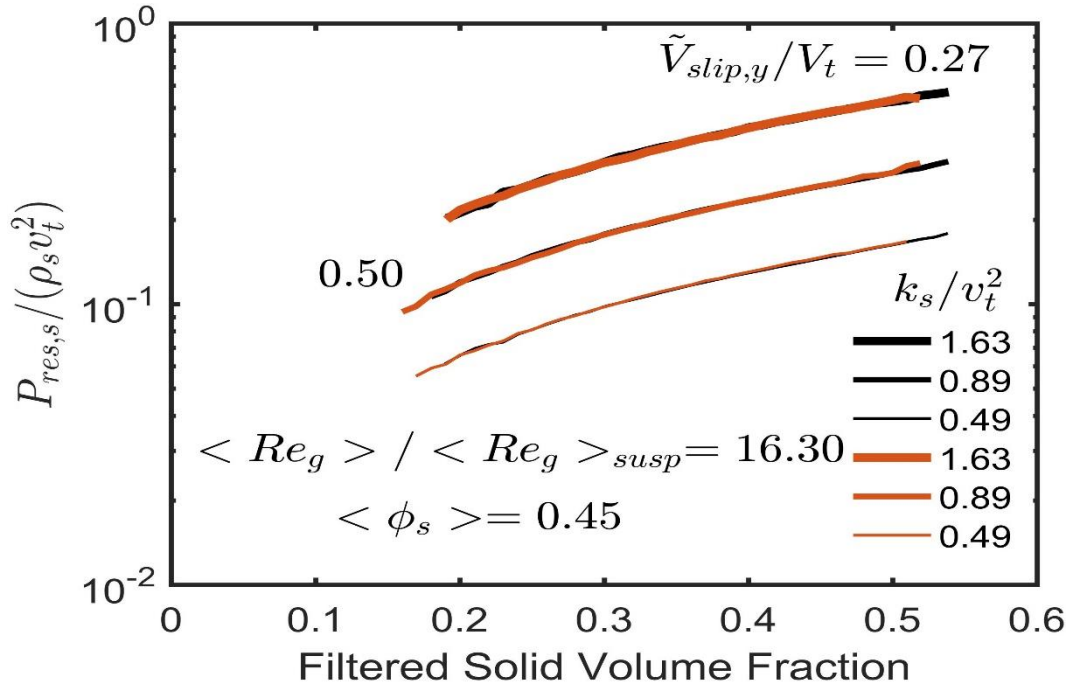
Figure 22 – Dimensionless residual solid pressure, $P_{res,s}/(\rho_s v_t^2)$, as a function of the filtered solid volume fraction $\bar{\phi}_s$ for the domain average solid volume fractions $\langle \phi_s \rangle = 0.35, 0.45$ and 0.50 and for gas Reynolds number ratios $\langle Re_g \rangle / \langle Re_g \rangle_{susp} = 16.30$ and 24.45 . The results stand for different dimensionless filtered axial slip velocities \tilde{V}_{slip}/V_t (smaller: black and bigger: red), for the dimensionless filter size $\Delta f/(v_t^2/g) = 4.112$, and for various dimensionless filtered kinetic energy of the solid velocity fluctuations k_s/v_t^2 (with different thickness). All graphs for $C_f = 0$.



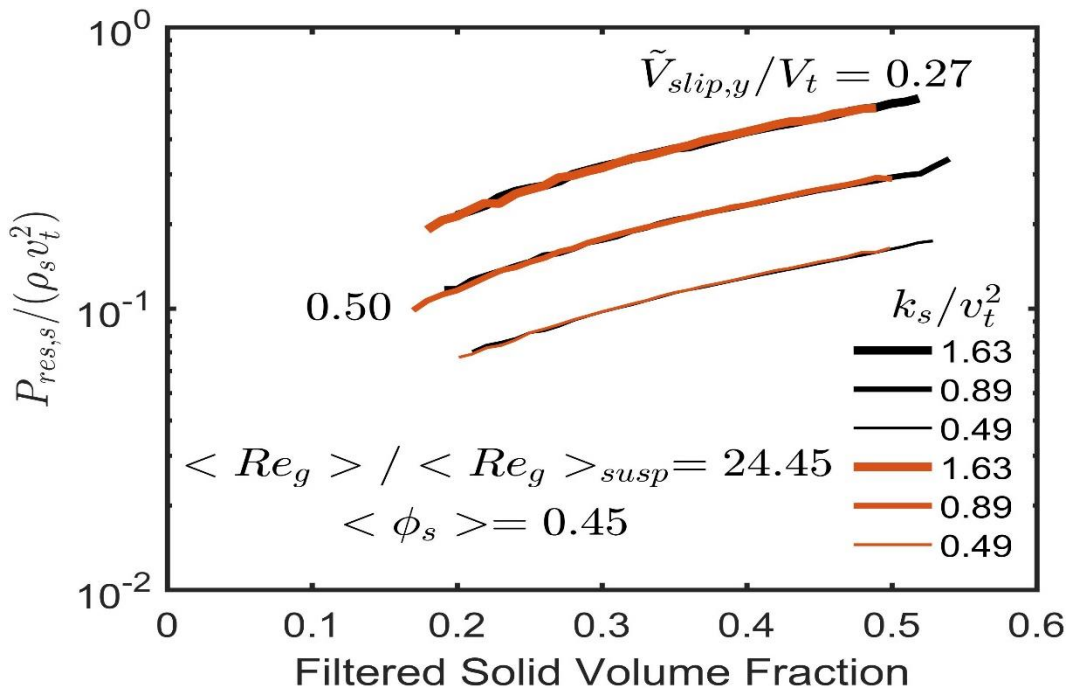
(a)



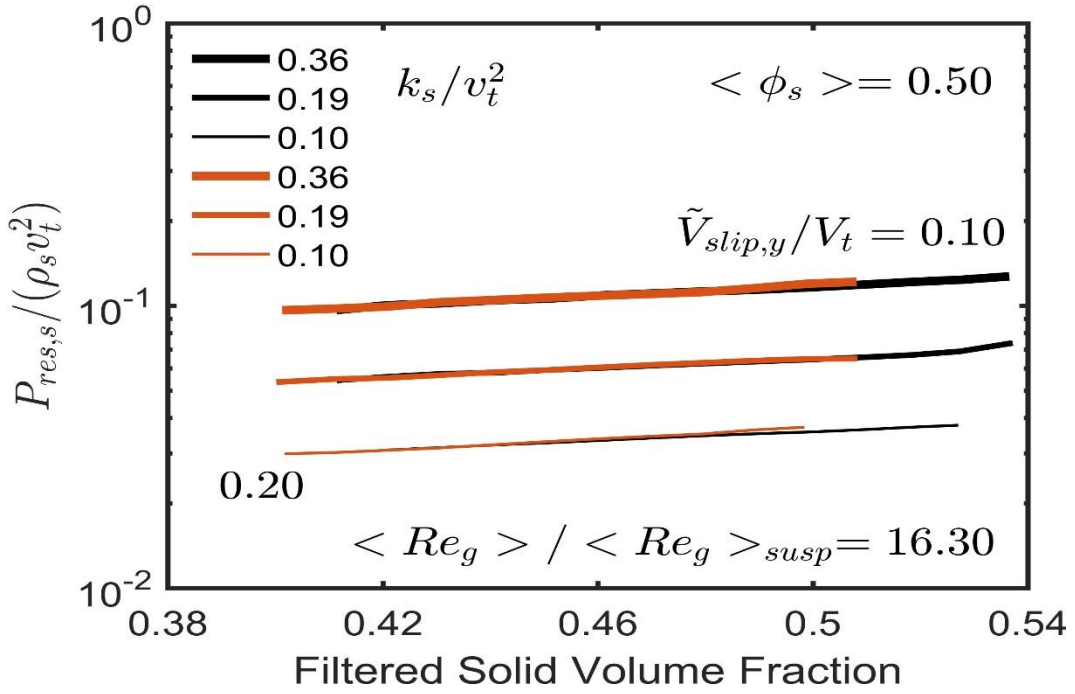
(b)



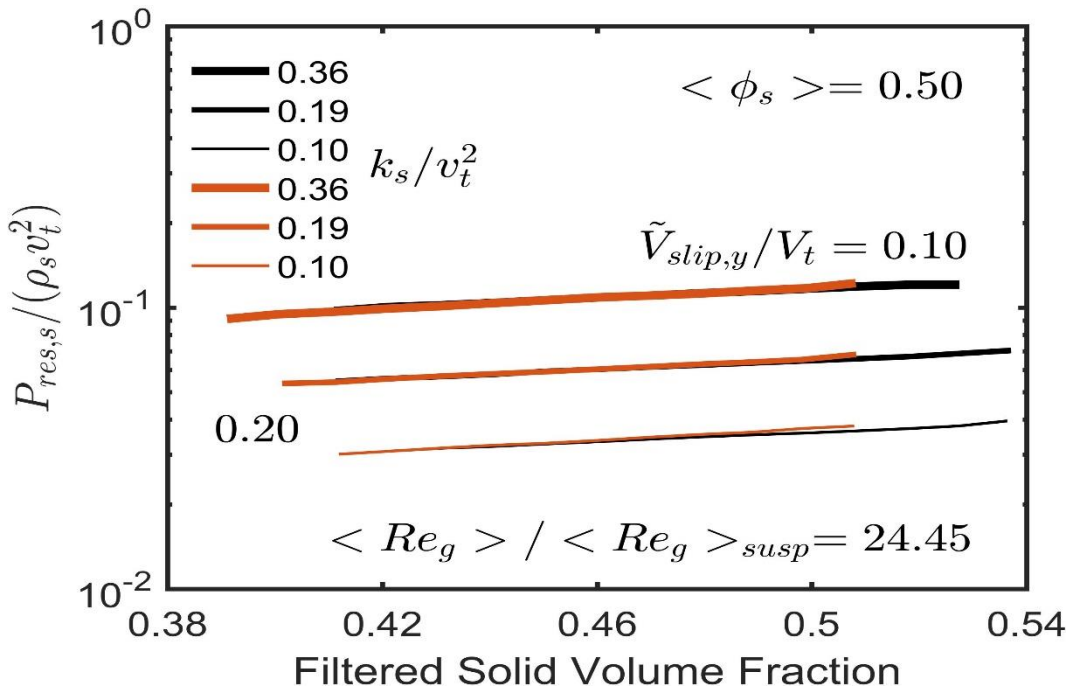
(c)



(d)



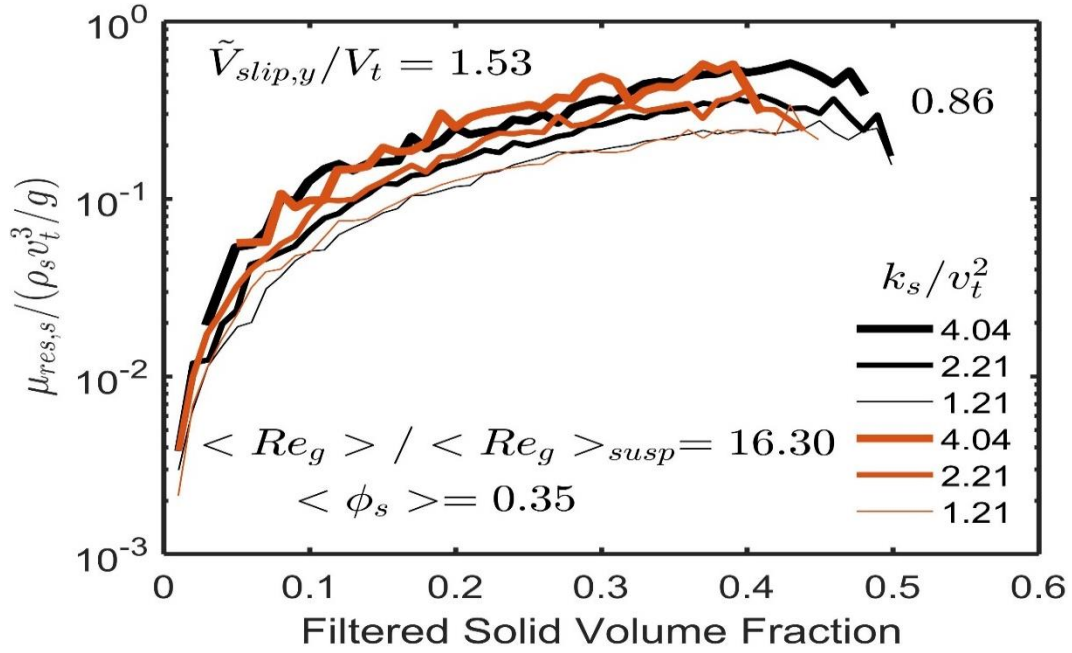
(e)



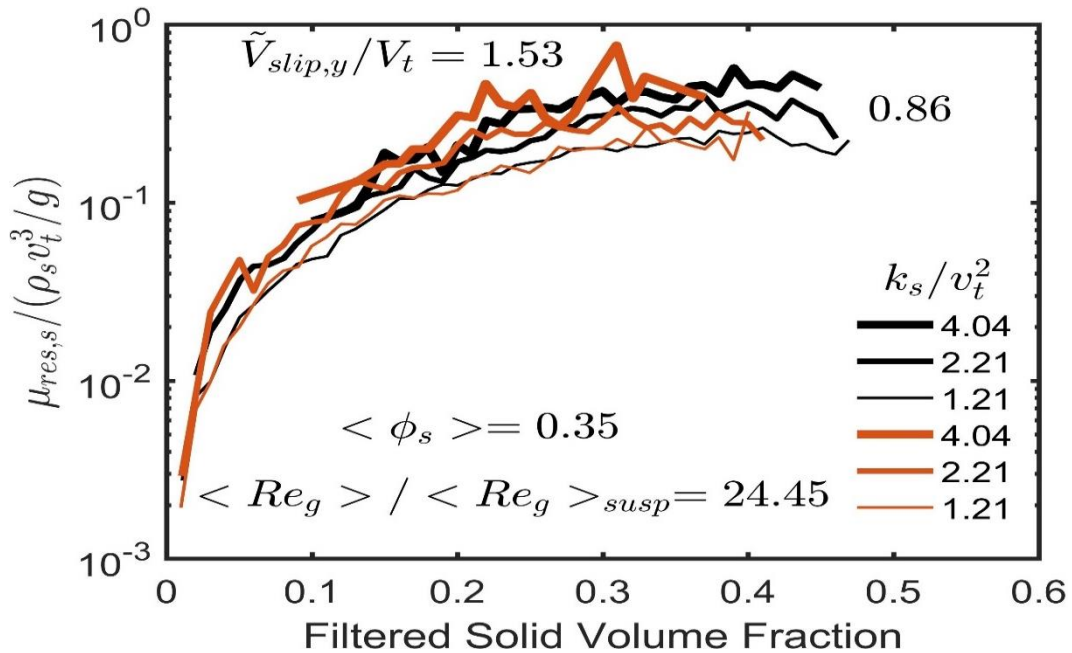
(f)

Source: Elaborated by the author

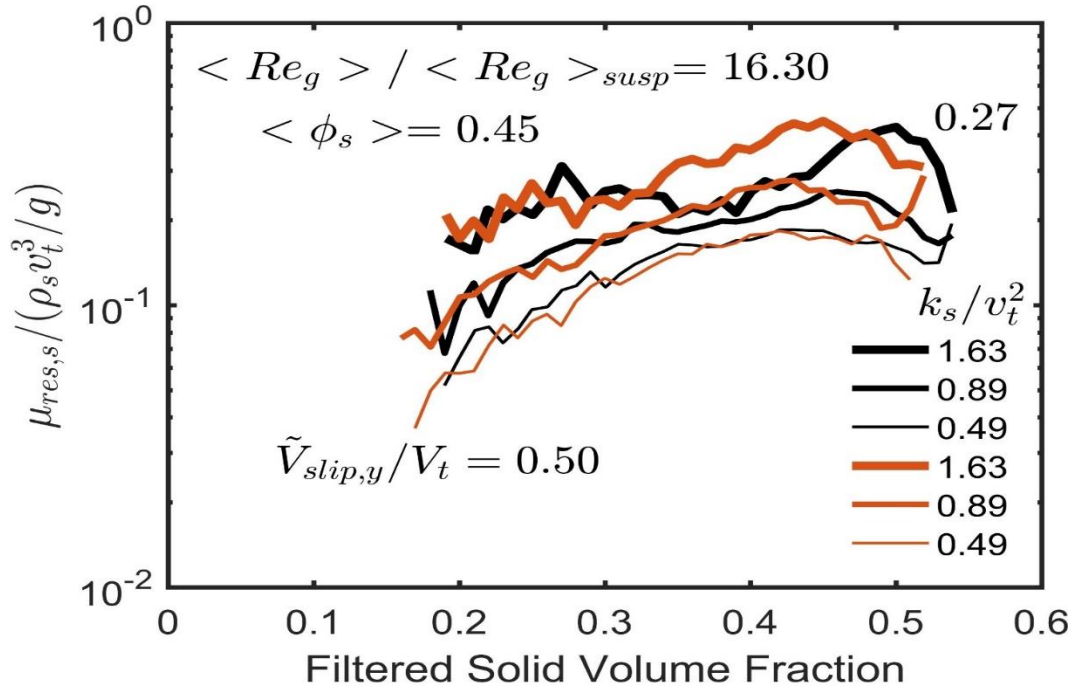
Figure 23 – Dimensionless residual solid dynamic viscosities, $\mu_{res,s}/(\rho_s v_t^3/g)$, as a function of the filtered solid volume fraction $\bar{\phi}_s$ for the domain average solid volume fractions $\langle \phi_s \rangle = 0.35, 0.45$ and 0.50 and for gas Reynolds number ratios $\langle Re_g \rangle / \langle Re_g \rangle_{susp} = 16.30$ and 24.45 . The results stand for different dimensionless filtered axial slip velocities \tilde{V}_{slip}/V_t (smaller: black and bigger: red), for the dimensionless filter size $\Delta f / (v_t^2/g) = 4.112$, and various dimensionless filtered kinetic energy of the solid velocity fluctuations k_s/v_t^2 (with different thickness). All graphs for $C_f = 0$.



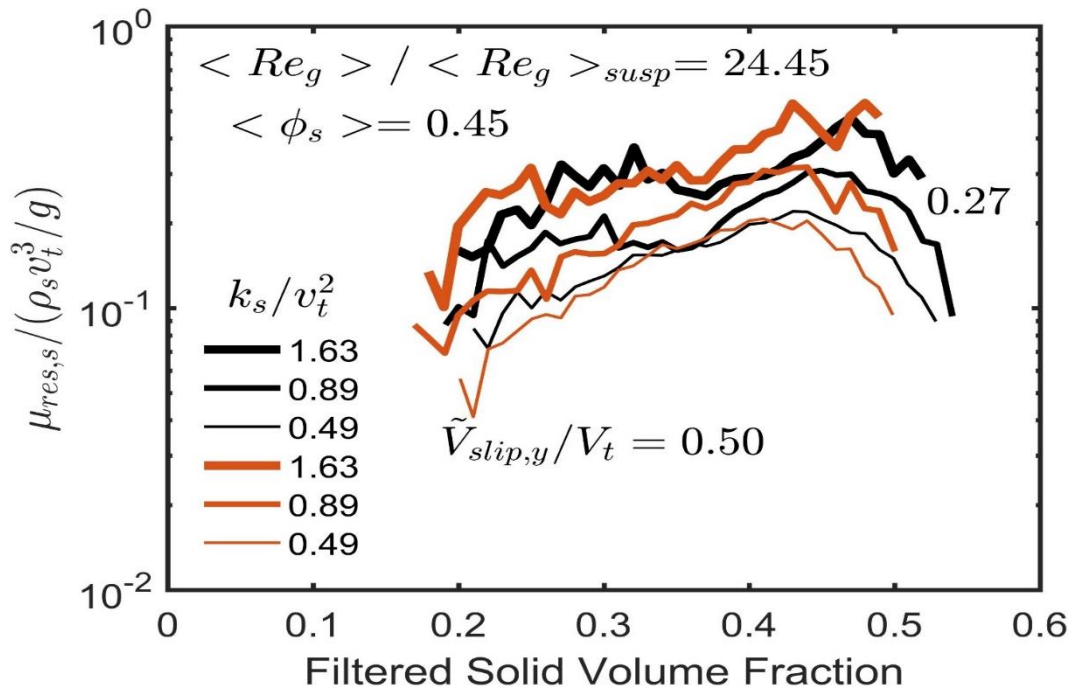
(a)



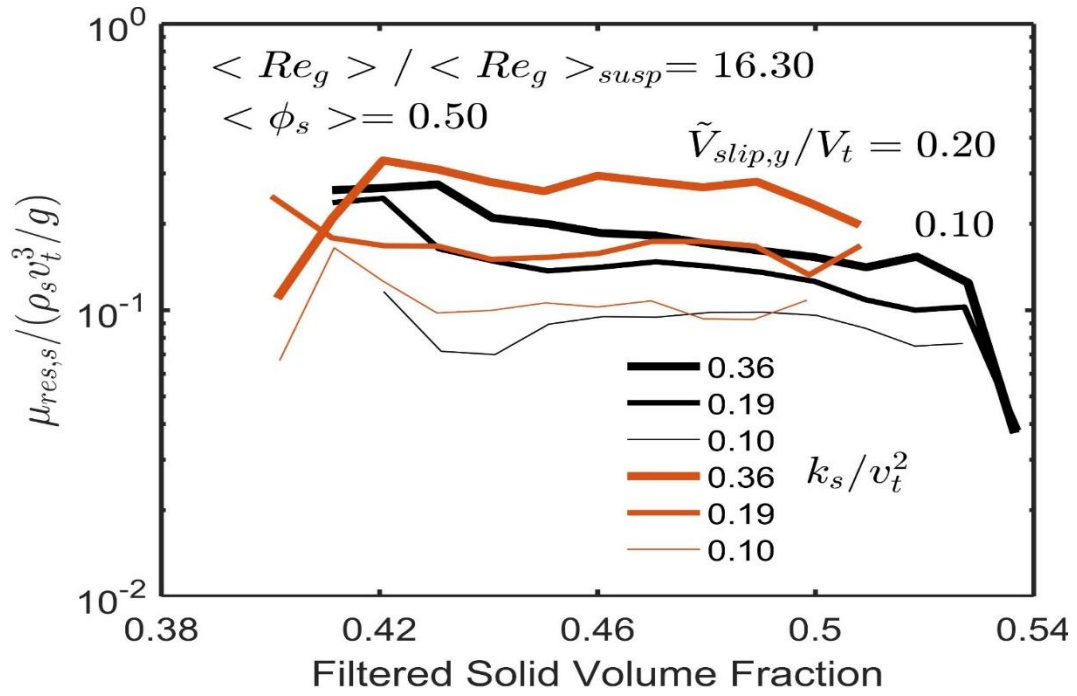
(b)



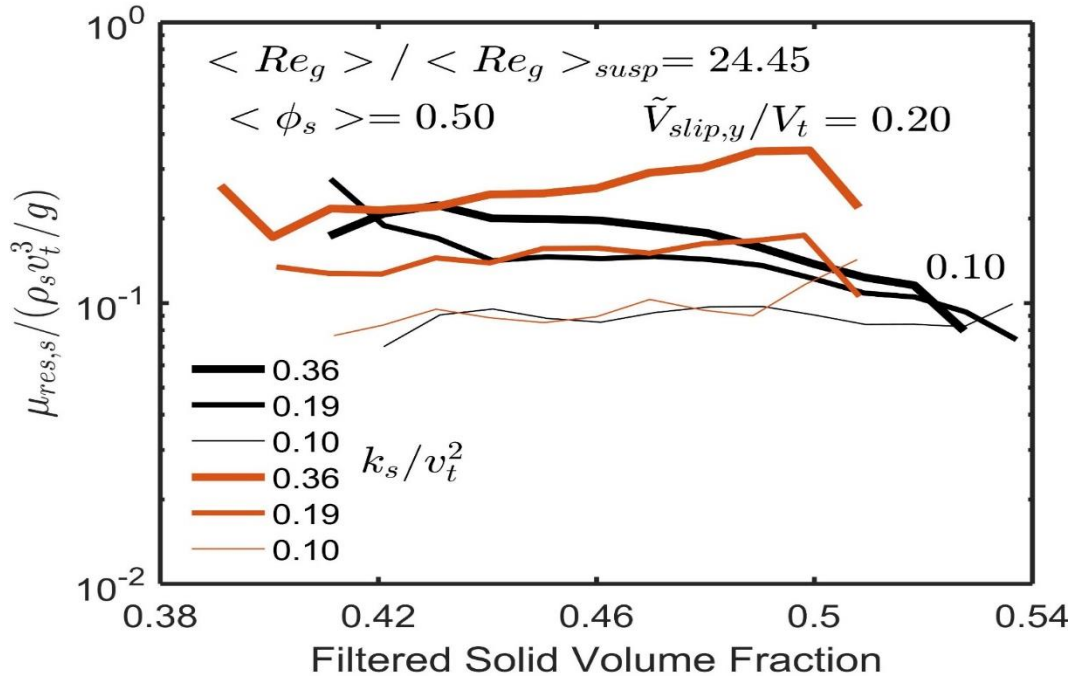
(c)



(d)



(e)



(f)

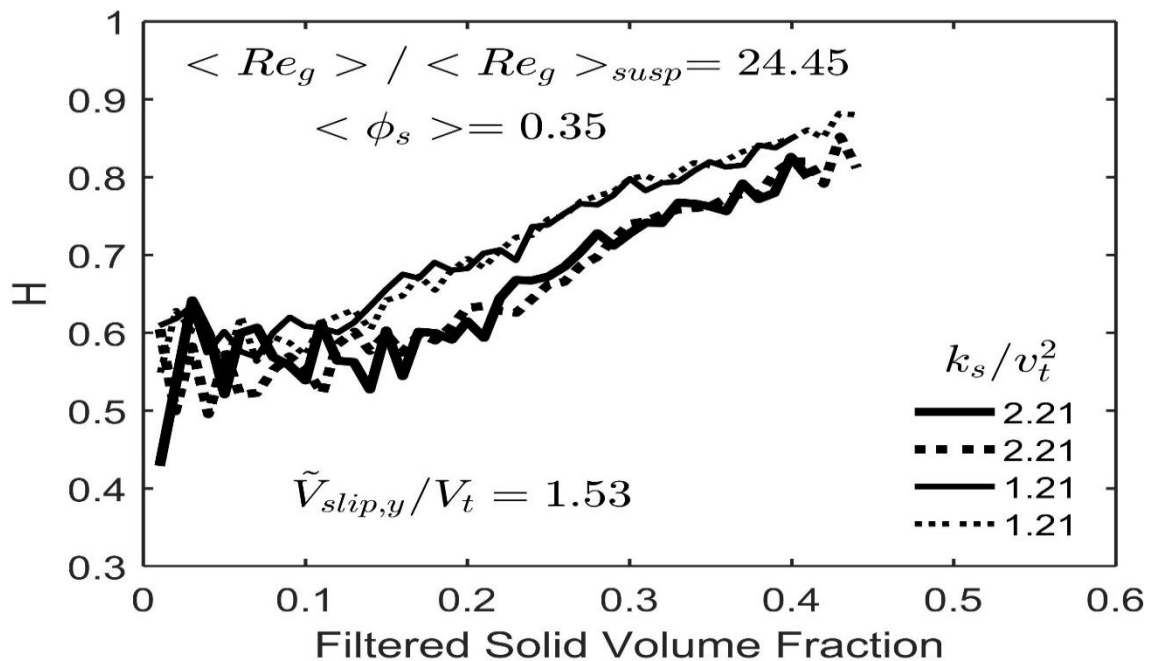
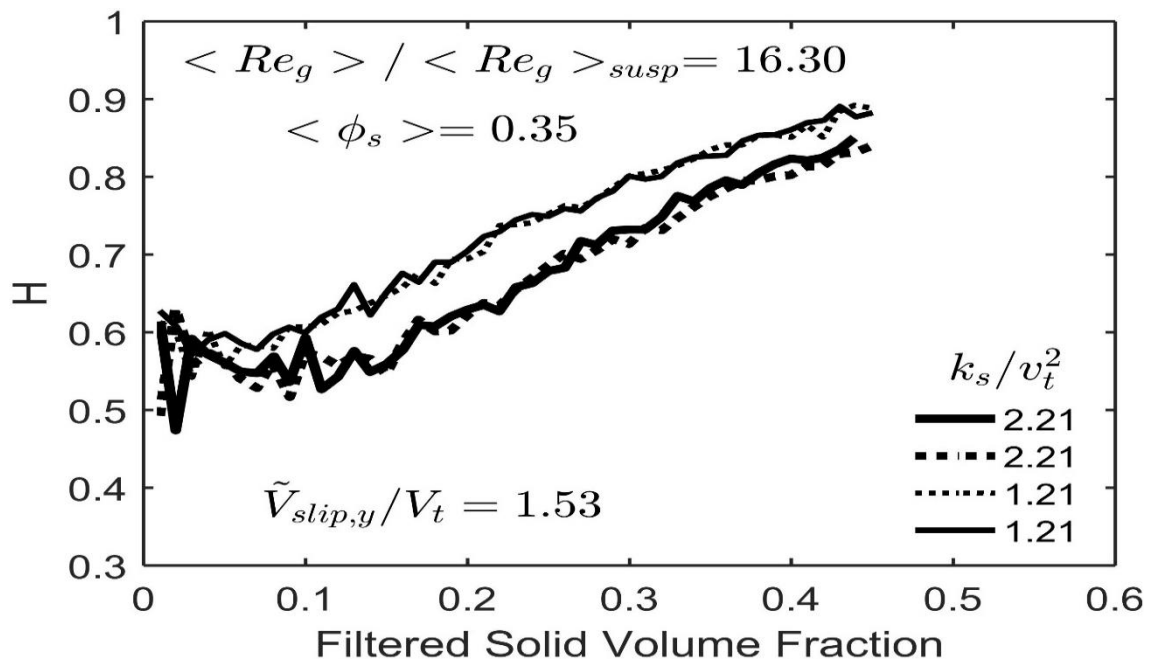
Source: Elaborated by the author

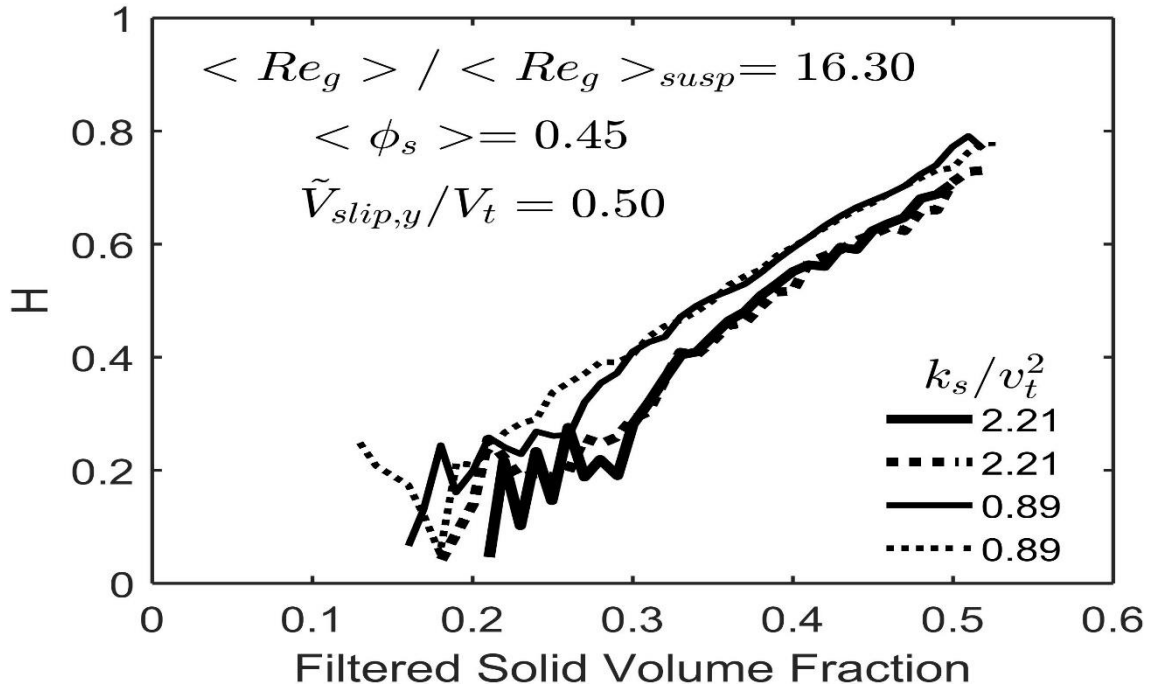
Appendix B – Case 2: Interparticle friction analysis – results for high Reynolds number ratios

Figure 24 shows results of the drag coefficient correction, H . Figures 25 and 26 show results of the dimensionless filtered solid pressure, $P_{\text{fil},s}/(\rho_s v_t^2)$, and dimensionless filtered solid dynamic viscosity, $\mu_{\text{fil},s}/(\rho_s v_t^3/g)$. Figures 27 and 28 show results of the dimensionless residual solid pressure, $P_{\text{res},s}/(\rho_s v_t^2)$, and dimensionless residual solid dynamic viscosity, $\mu_{\text{res},s}/(\rho_s v_t^3/g)$.

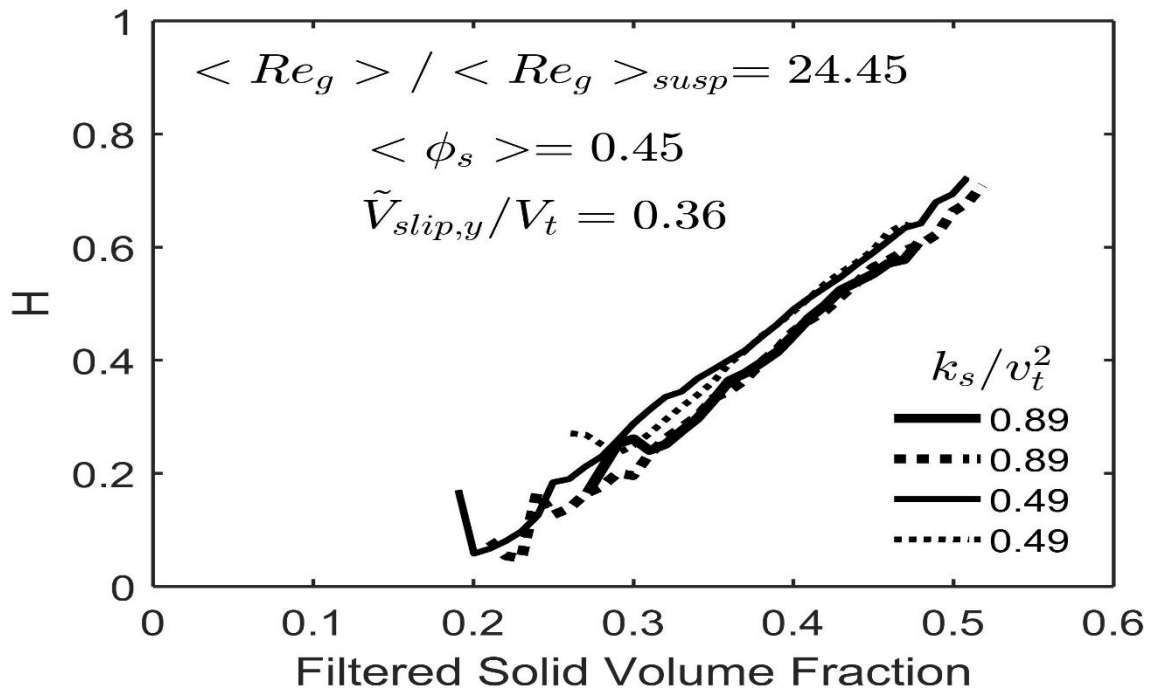
The results stand for gas Reynolds number ratios $\langle \text{Re}_g \rangle / \langle \text{Re}_g \rangle_{\text{susp}} = 16.30$ and 24.45 , domain average solid volume fraction $\langle \phi_s \rangle = 0.35, 0.45$ and 0.50 , interparticle friction coefficients, $C_f = 0$ and 0.3 . Each graph shows the variation of the concerning parameter with the solid volume fraction and the filtered kinetic energy of the solid velocity fluctuations, for particular values of filtered slip velocity.

Figure 24 – Drag Coefficient Correction, H , as a function of the filtered solid volume fraction $\bar{\phi}_s$ for the domain average solid volume fractions $\langle \phi_s \rangle = 0.35, 0.45$ and 0.50 and for gas Reynolds number ratios $\langle Re_g \rangle / \langle Re_g \rangle_{susp} = 16.30$ and 24.45 . The results stand for particular dimensionless filtered axial slip velocities \tilde{V}_{slip}/V_t , for the dimensionless filter size $\Delta_f/(v_t^2/g) = 4.112$, and two different interparticle friction coefficient, $C_f = 0$ (full lines) and $C_f = 0.3$ (dash lines).

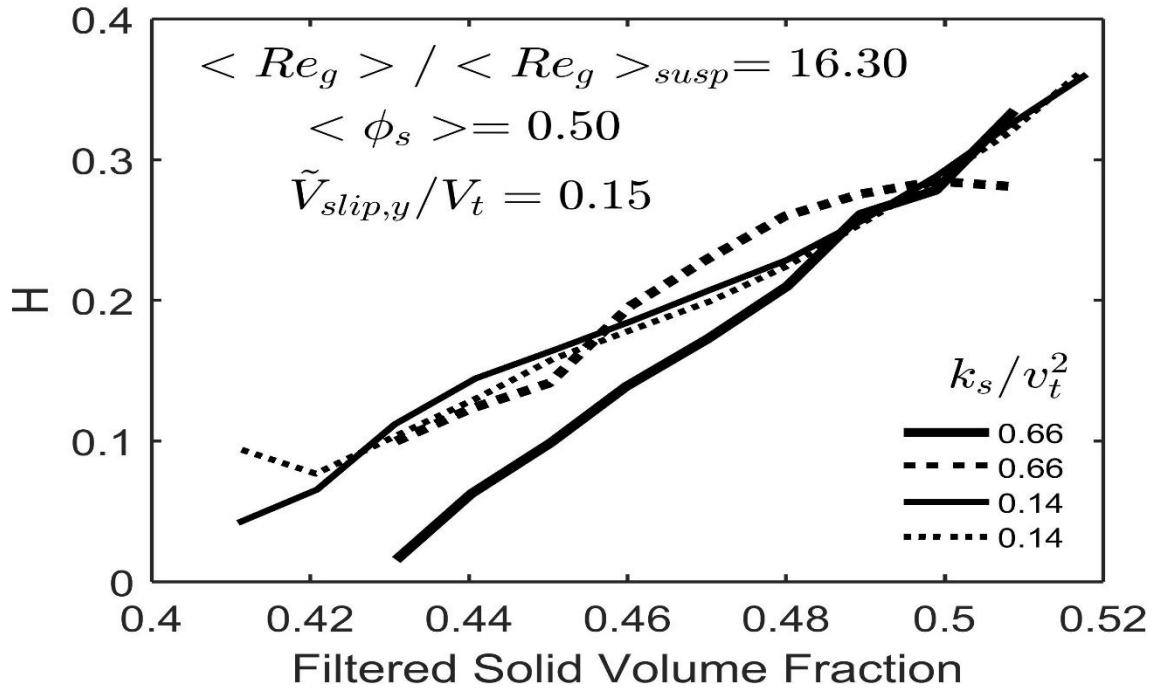




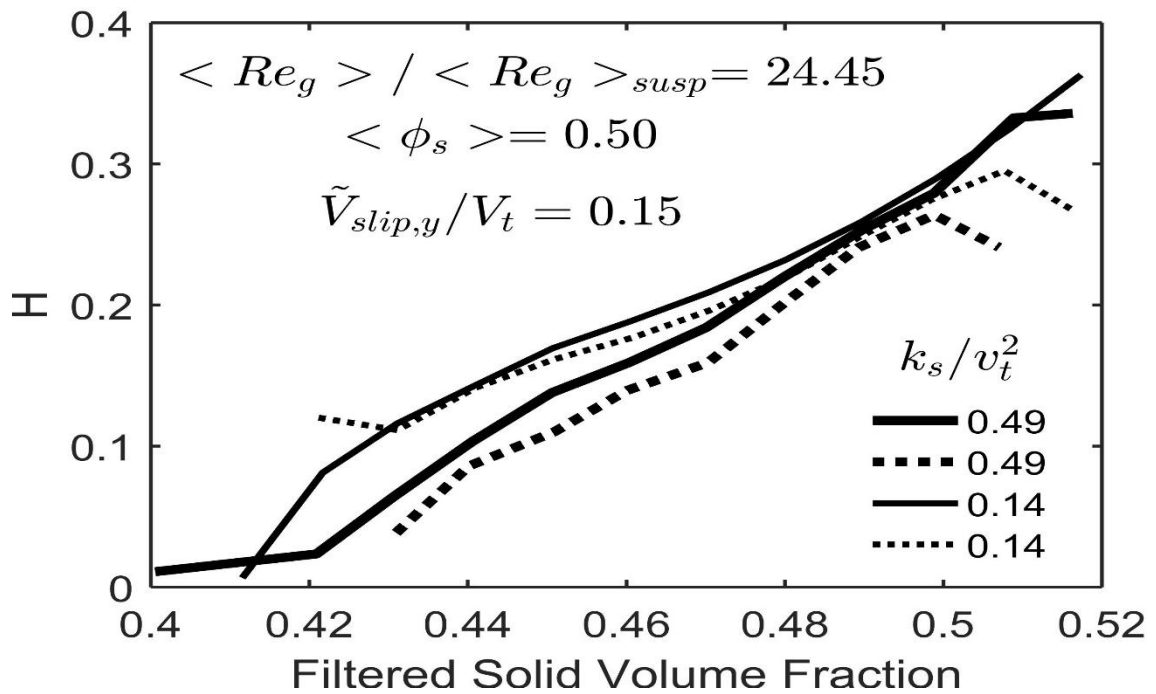
(c)



(d)



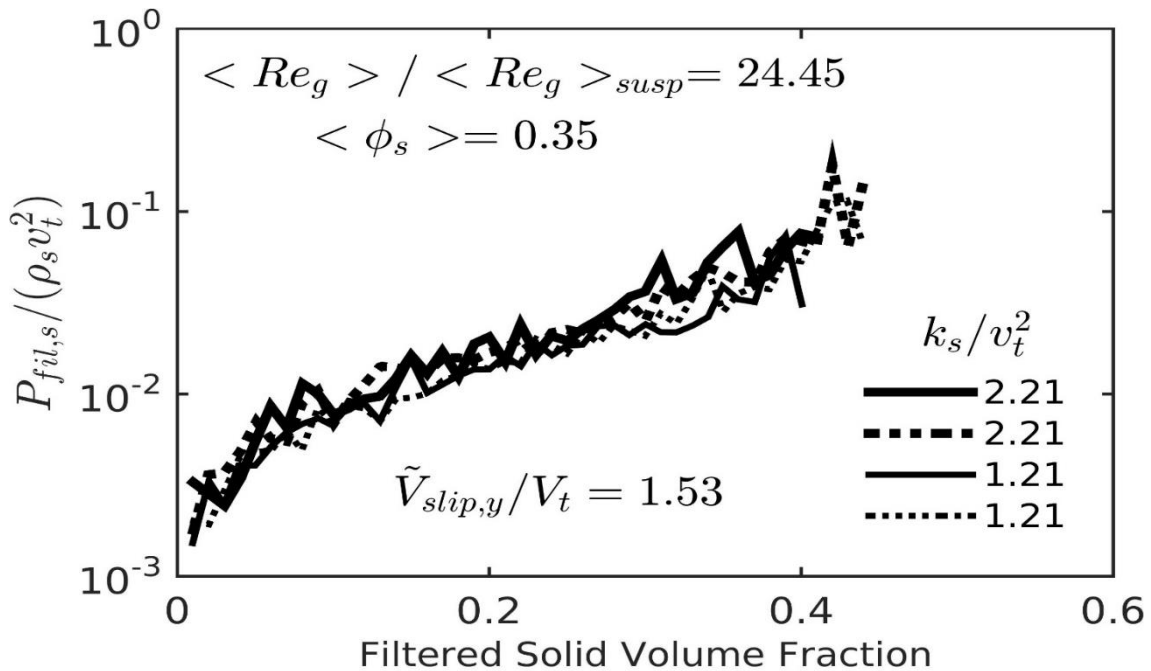
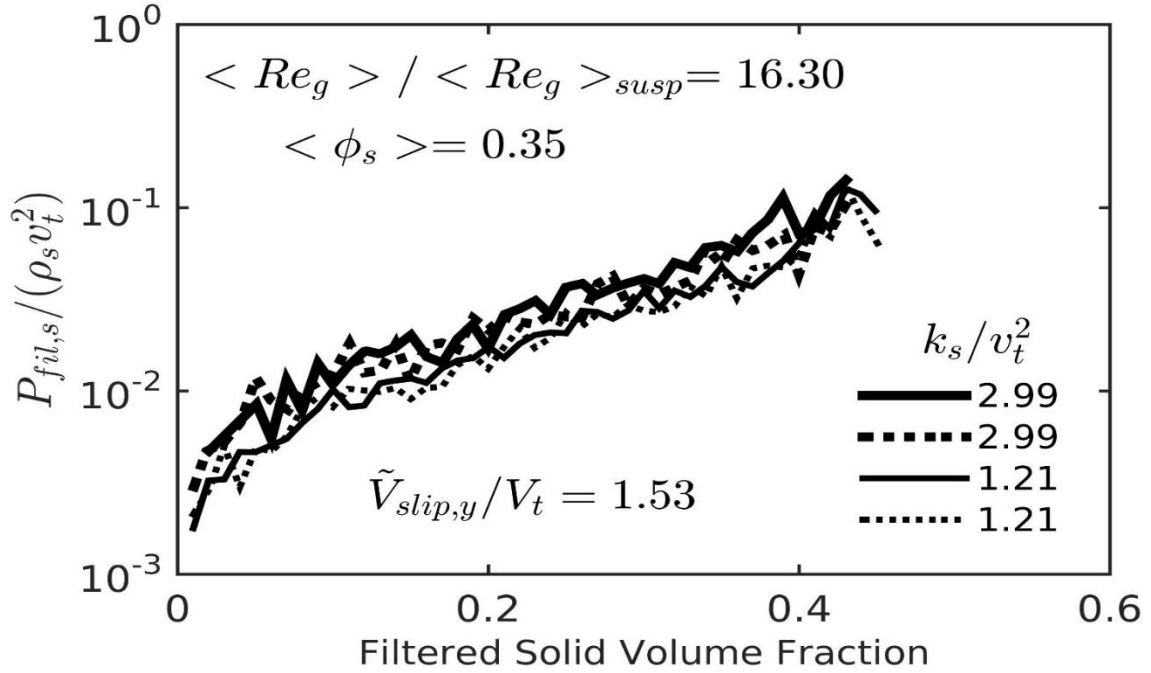
(e)

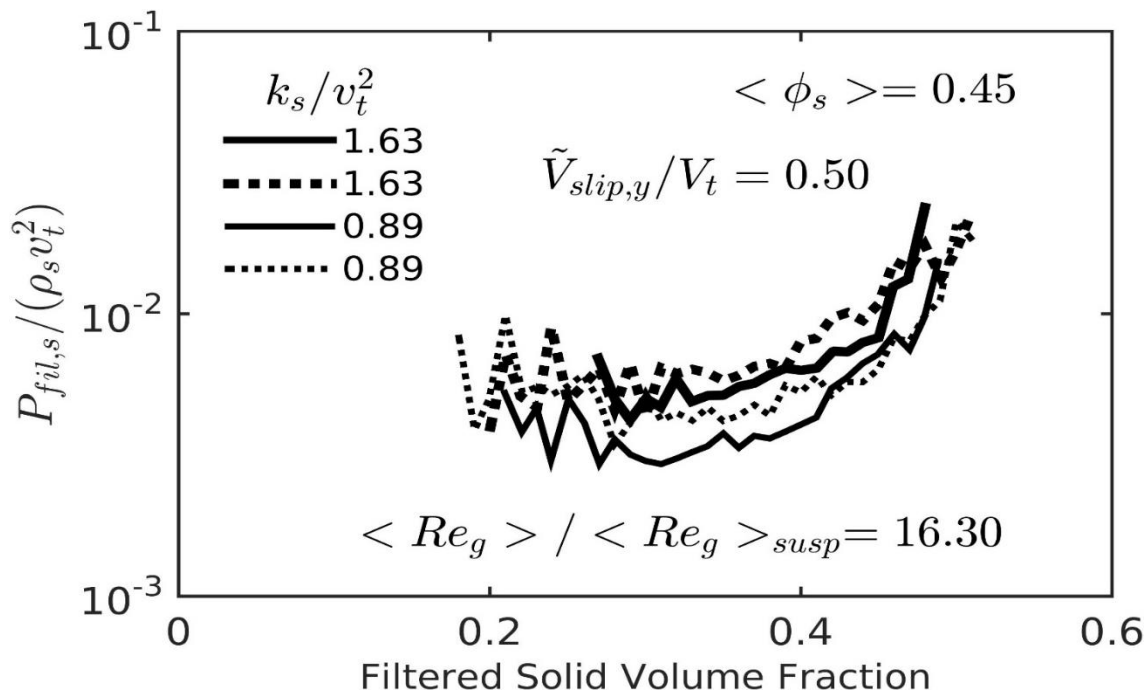


(f)

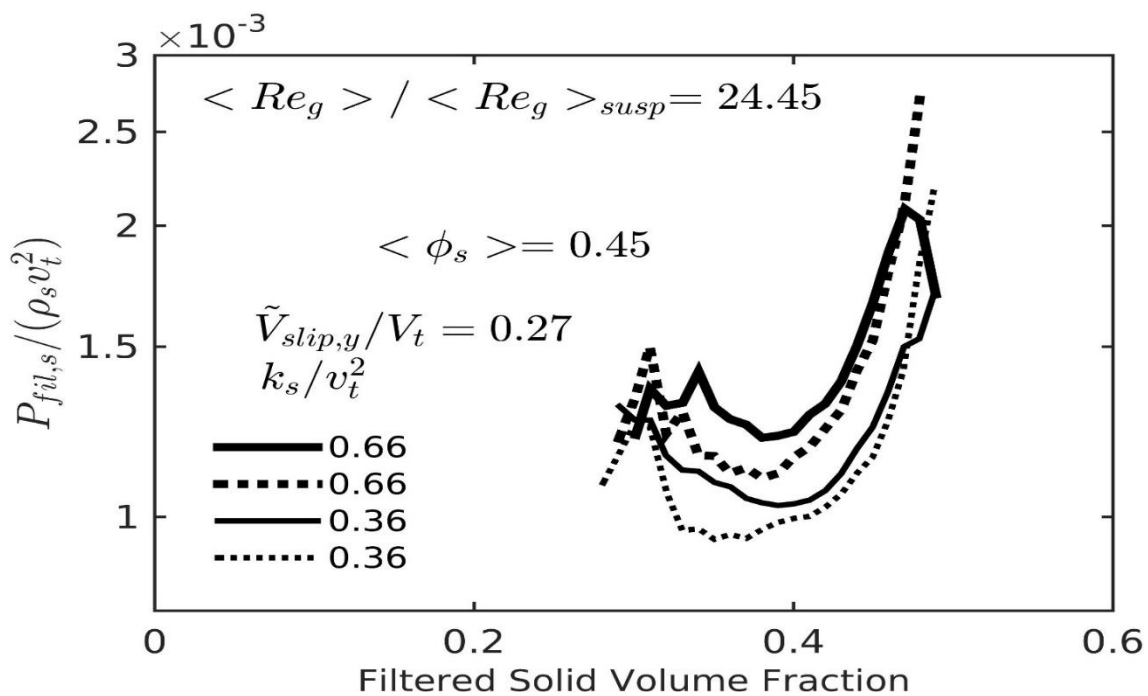
Source: Elaborated by the author

Figure 25 – Dimensionless filtered solid pressure, $P_{fil,s}/(\rho_s v_t^2)$, as a function of the filtered solid volume fraction $\bar{\phi}_s$ for the domain average solid volume fractions $\langle \phi_s \rangle = 0.35, 0.45$ and 0.50 and for gas Reynolds number ratios $\langle Re_g \rangle / \langle Re_g \rangle_{susp} = 16.30$ and 24.45 . The results stand for particular dimensionless filtered axial slip velocities \tilde{V}_{slip}/V_t , for the dimensionless filter size $\Delta f / (v_t^2/g) = 4.112$, and two different interparticle friction coefficient, $C_f = 0$ (full lines) and $C_f = 0.3$ (dash lines).

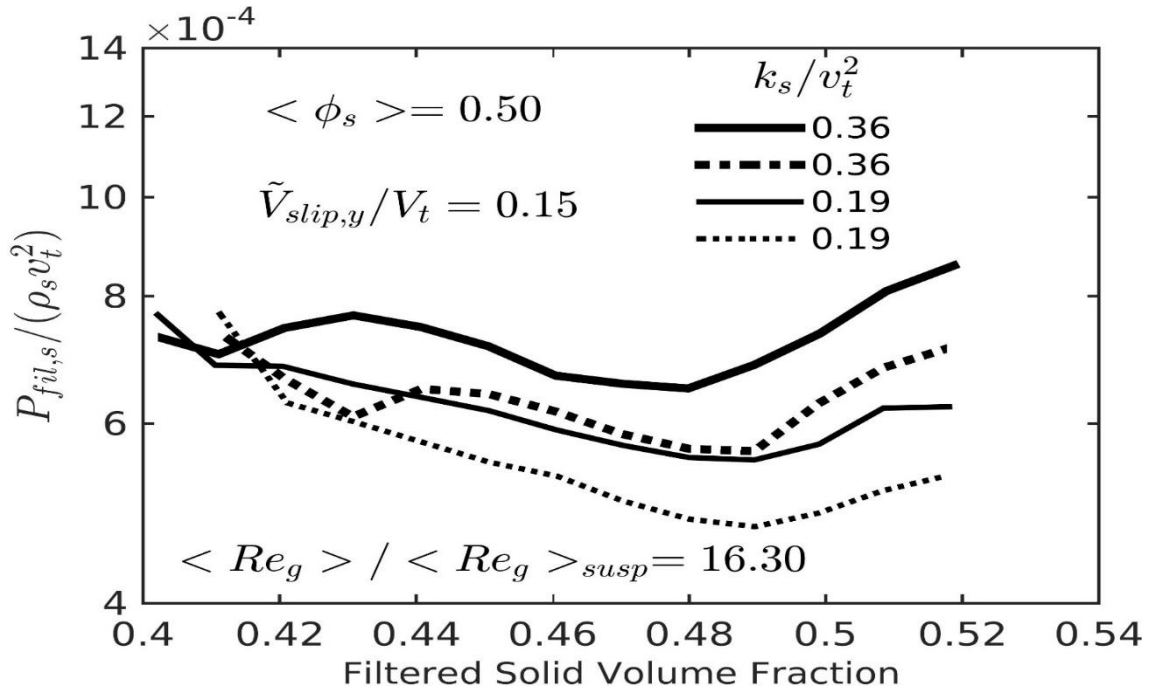




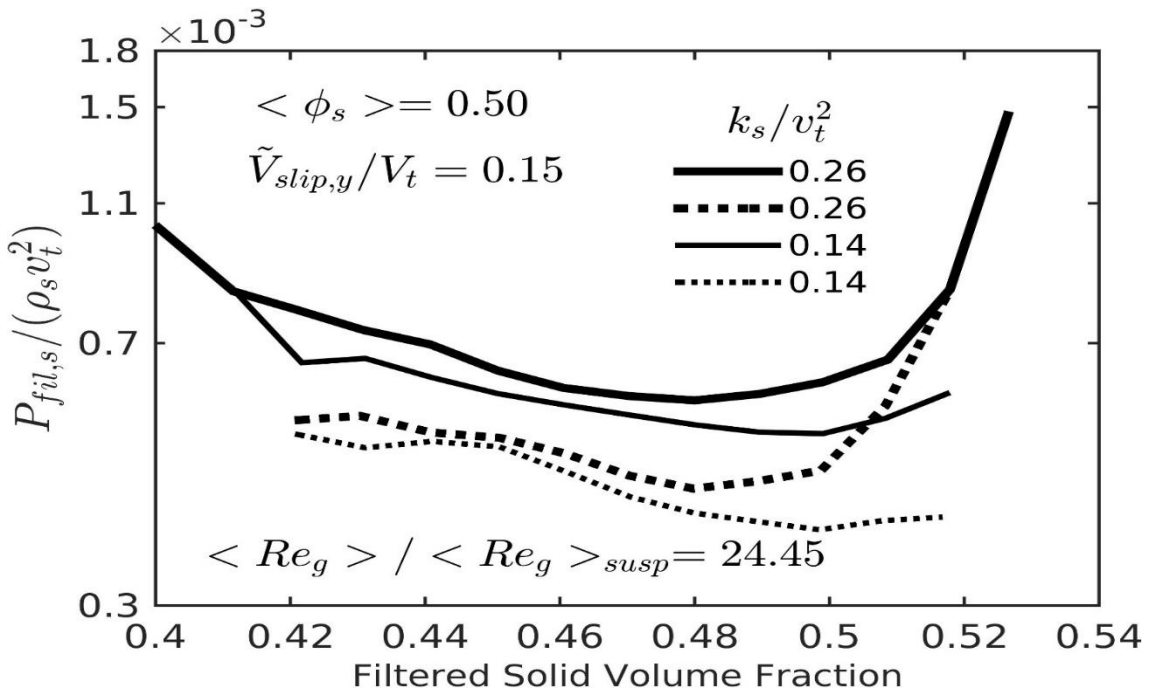
(c)



(d)



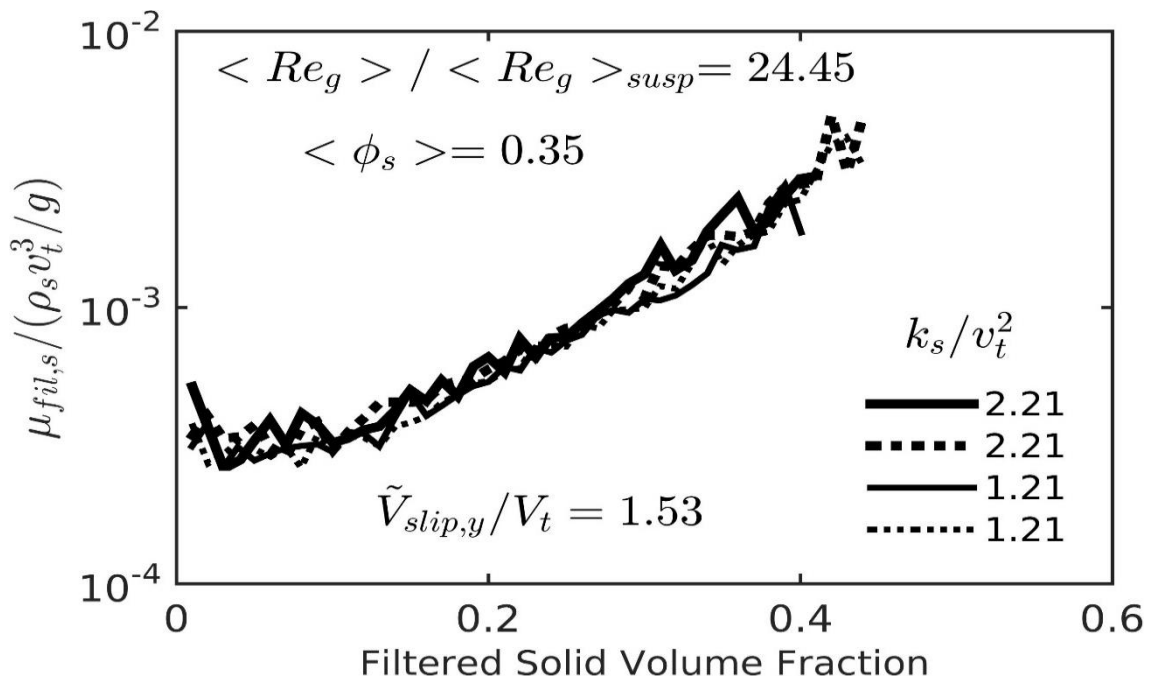
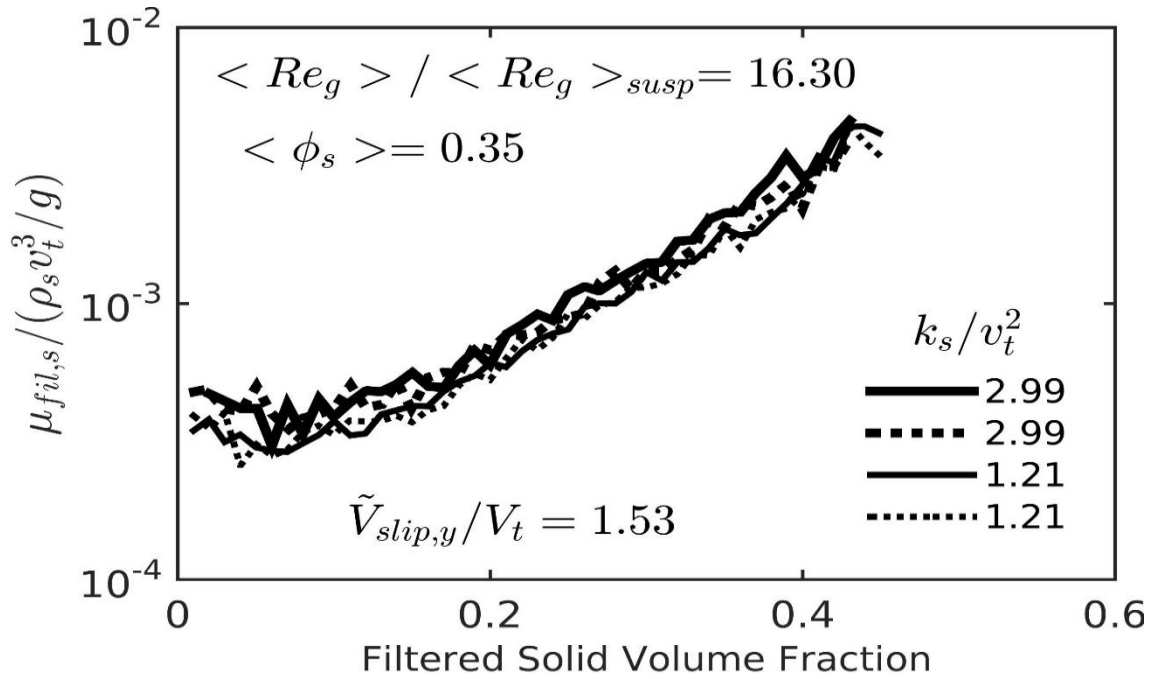
(e)

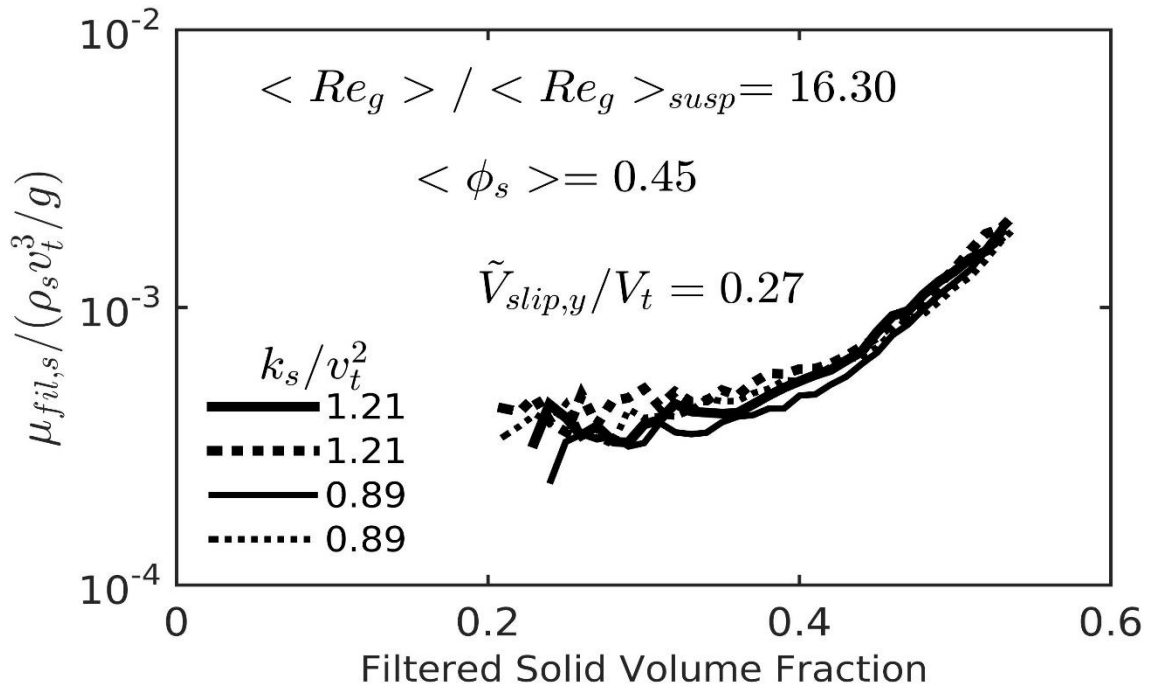


(f)

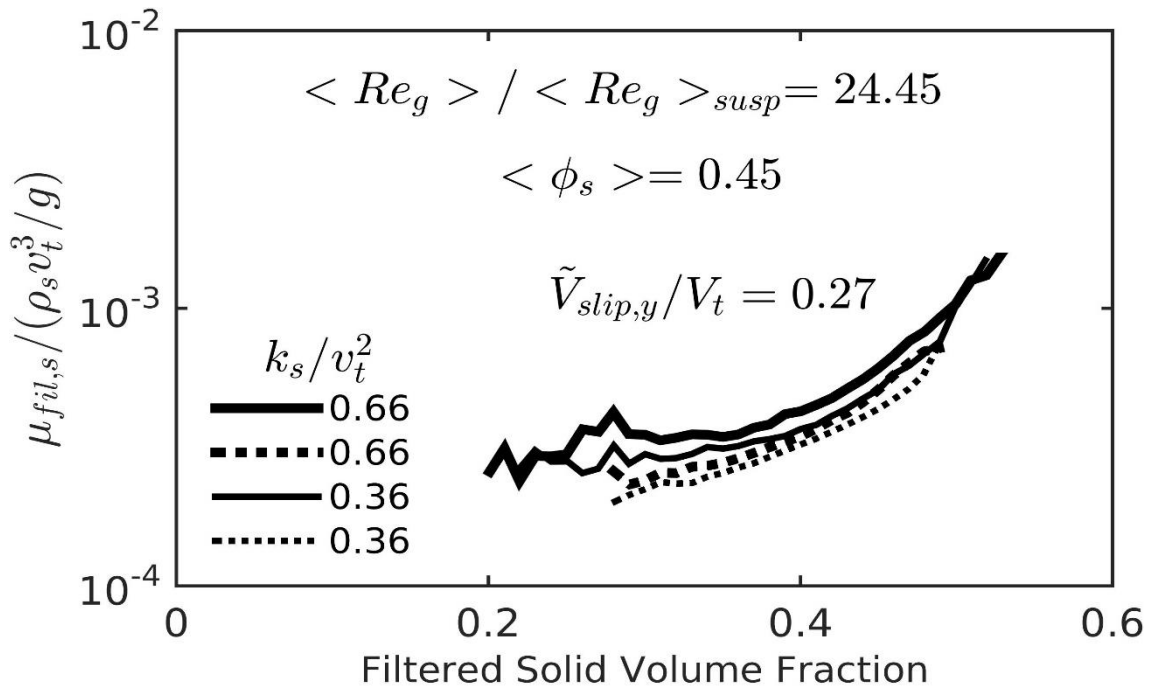
Source: Elaborated by the author

Figure 26 - Dimensionless filtered solid dynamic viscosities, $\mu_{fil,s}/(\rho_s v_t^3/g)$, as a function of the filtered solid volume fraction $\bar{\phi}_s$ for the domain average solid volume fractions $\langle \phi_s \rangle = 0.35, 0.45$ and 0.50 and for gas Reynolds number ratios $\langle Re_g \rangle / \langle Re_g \rangle_{susp} = 16.30$ and 24.45 . The results stand for particular dimensionless filtered axial slip velocities \tilde{V}_{slip}/V_t , for the dimensionless filter size $\Delta_f/(v_t^2/g) = 4.112$, and two different interparticle friction coefficient, $C_f = 0$ (full lines) and $C_f = 0.3$ (dash lines).

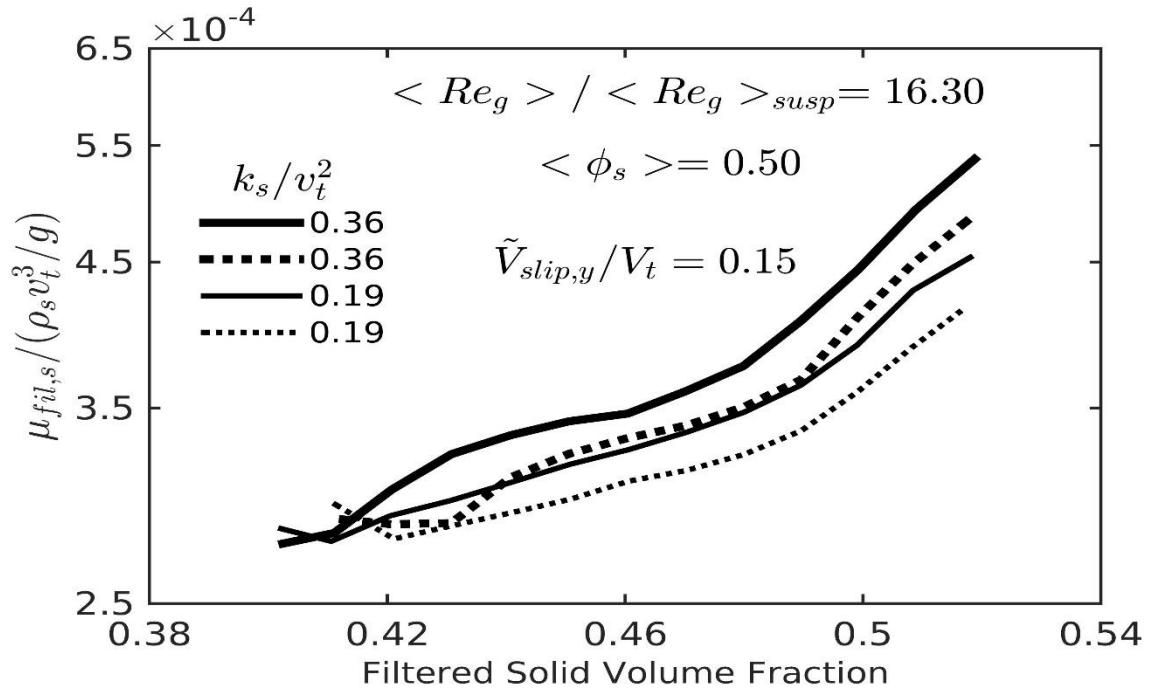




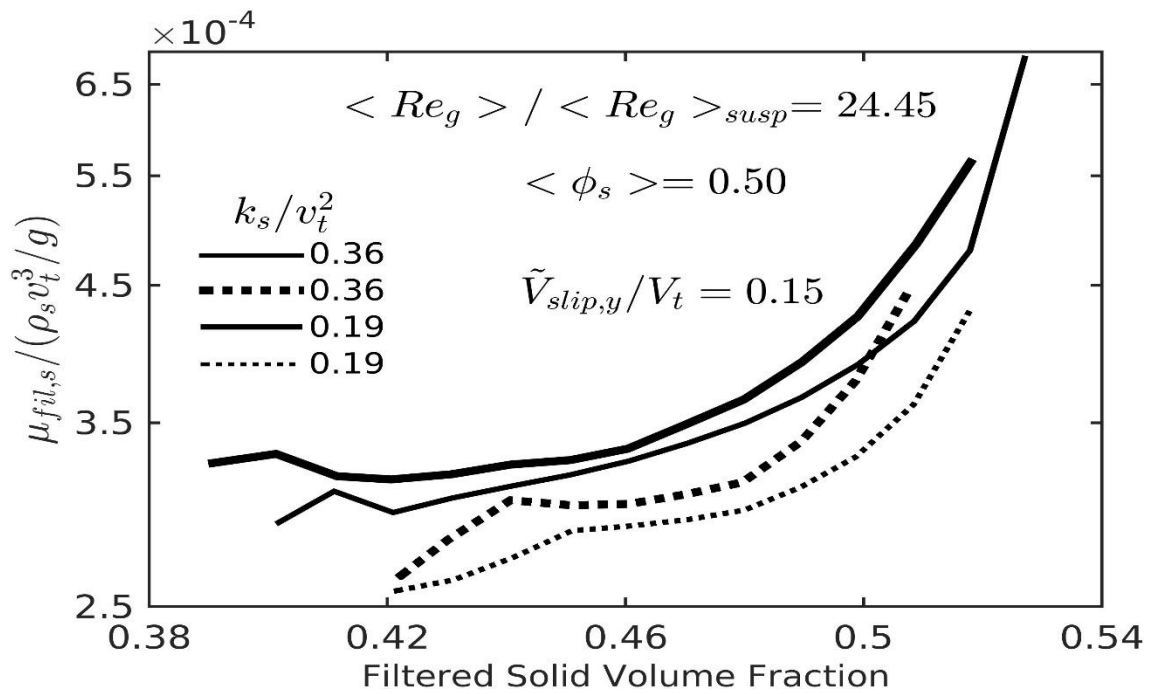
(c)



(d)



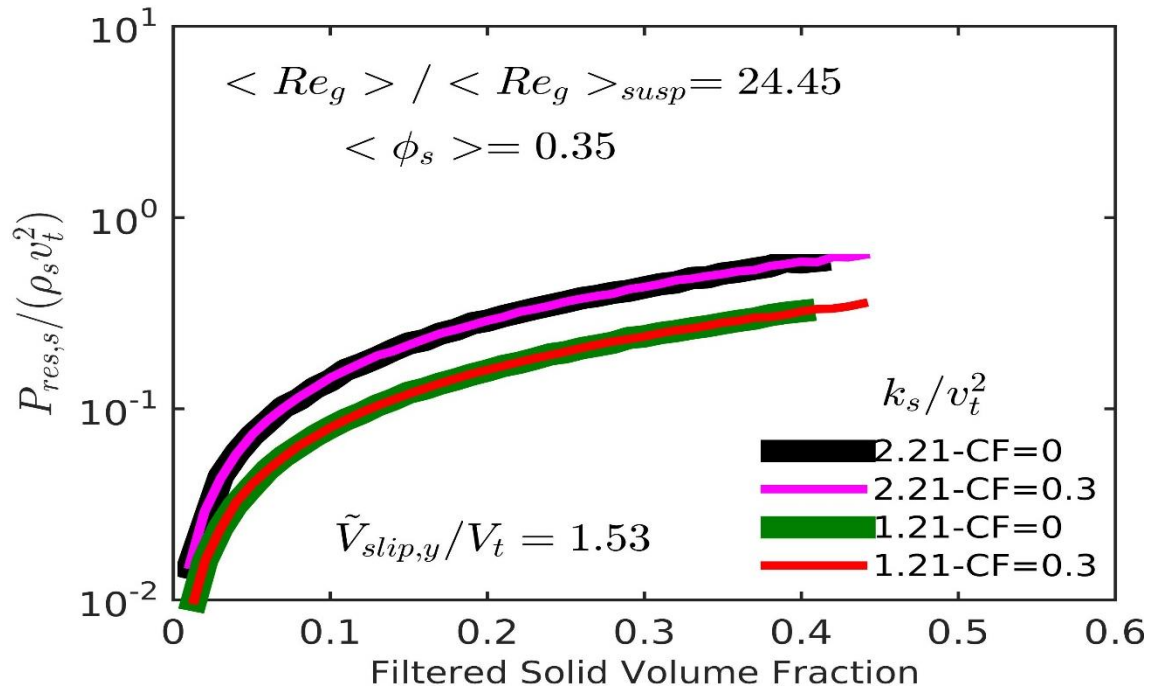
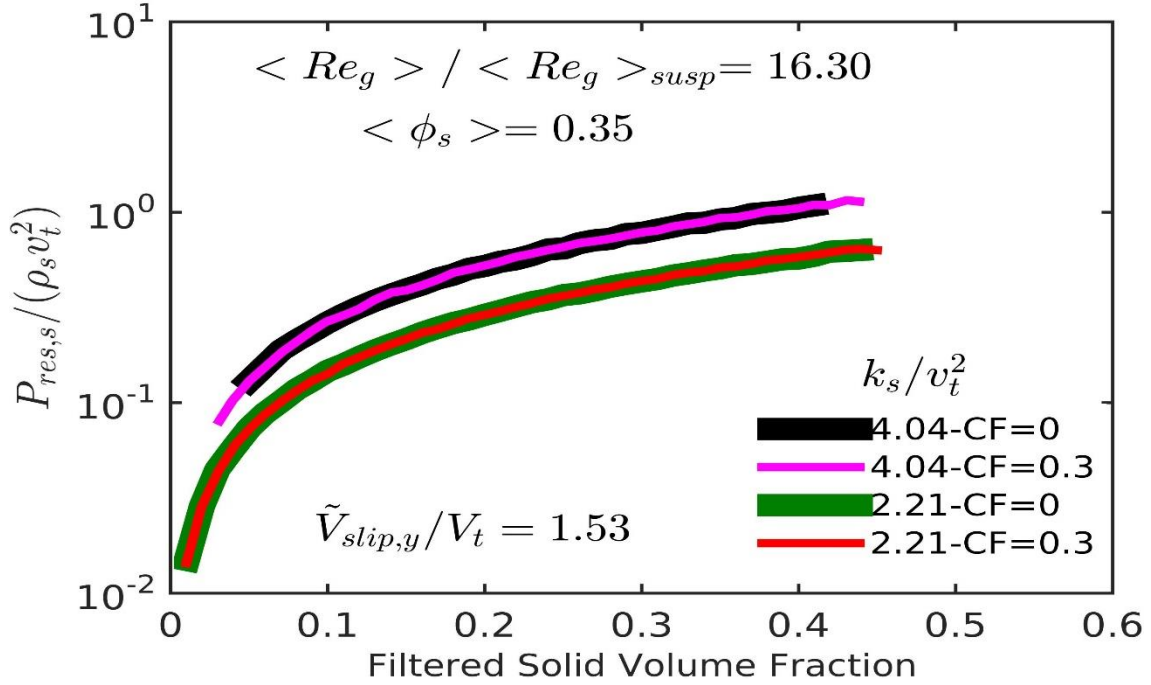
(e)

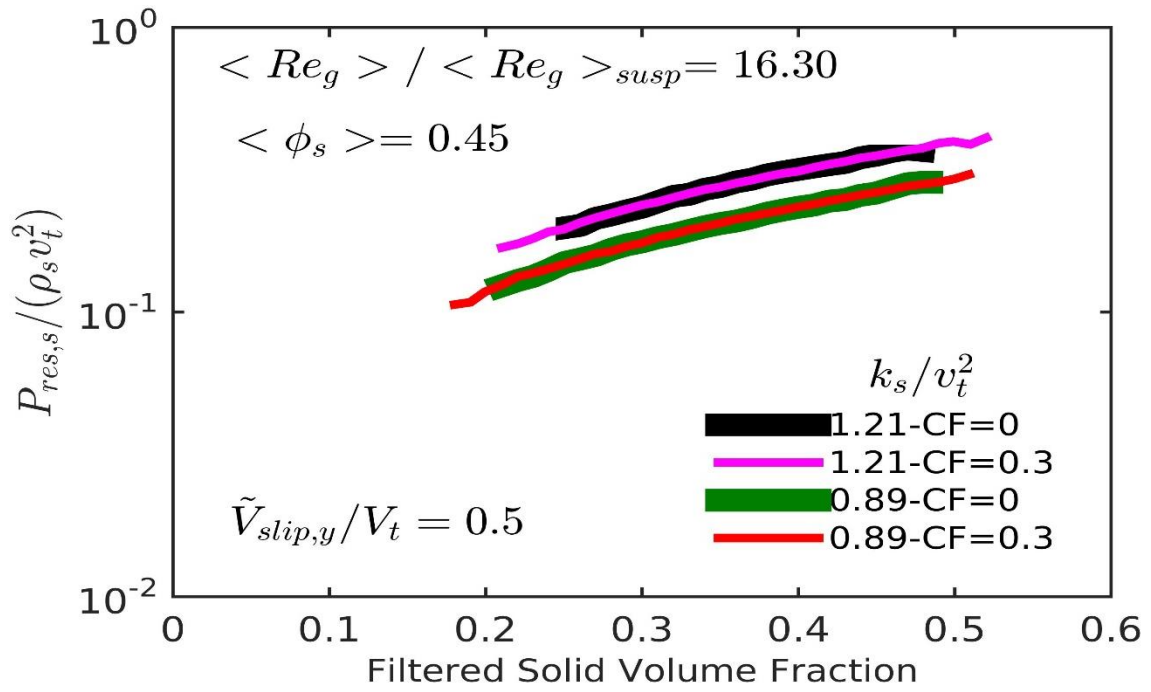


(f)

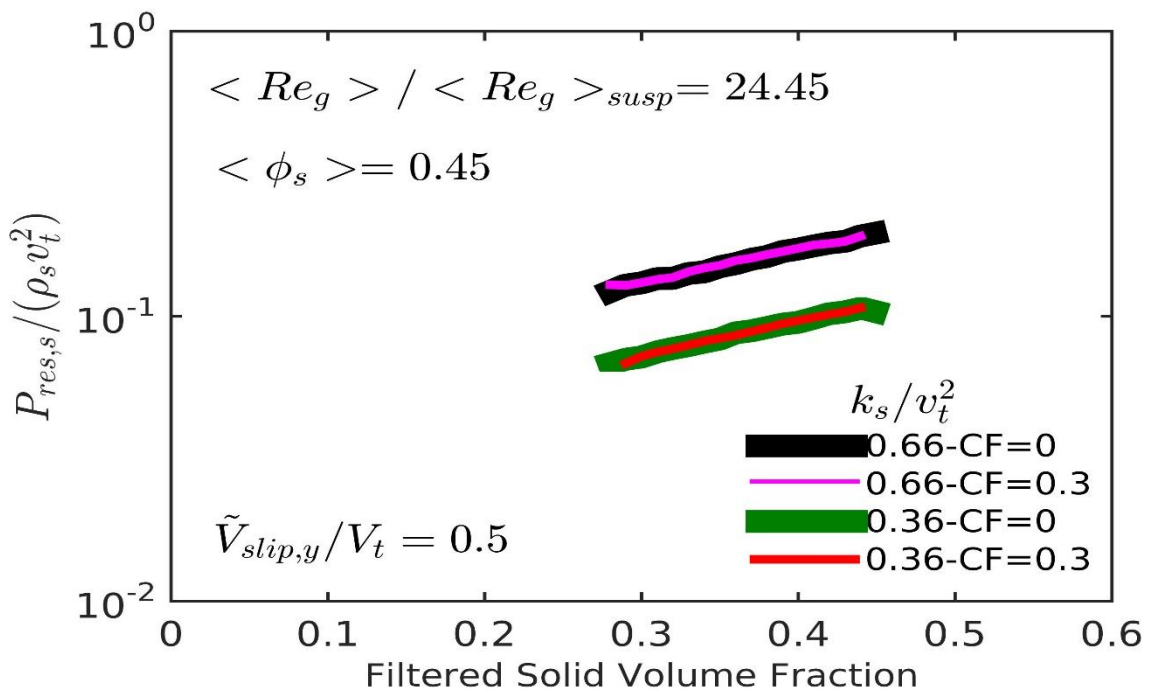
Source: Elaborated by the author

Figure 27 – Dimensionless residual solid pressure, $P_{res,s}/(\rho_s v_t^2)$, as a function of the filtered solid volume fraction $\bar{\phi}_s$ for the domain average solid volume fractions $\langle \phi_s \rangle = 0.35, 0.45$ and 0.50 and for gas Reynolds number ratios $\langle Re_g \rangle / \langle Re_g \rangle_{susp} = 16.30$ and 24.45 . The results stand for particular dimensionless filtered axial slip velocities \tilde{V}_{slip}/V_t , for the dimensionless filter size $\Delta_f/(v_t^2/g) = 4.112$, and two different interparticle friction coefficients, $C_f = 0$ and 0.3 .

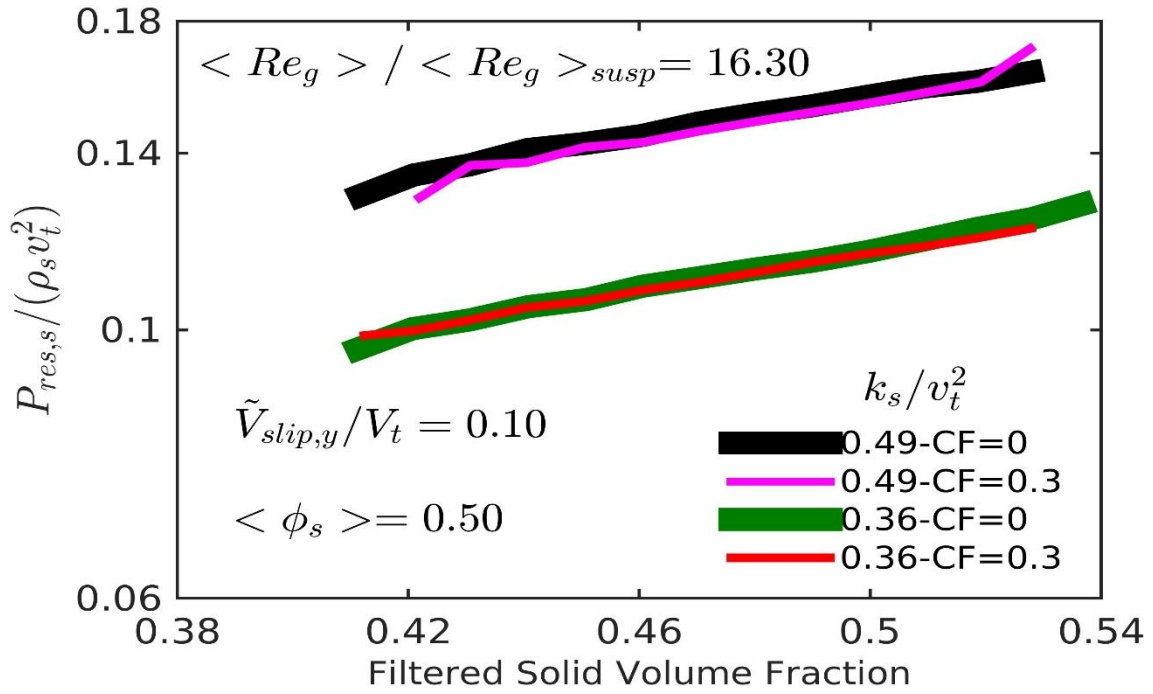




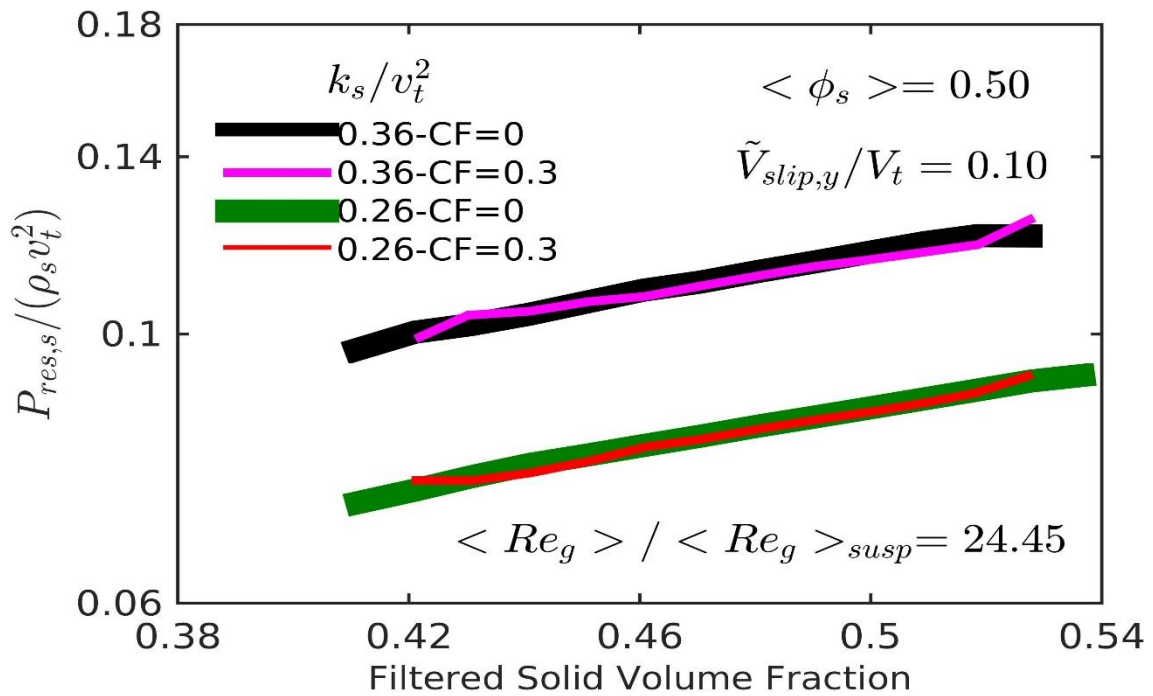
(c)



(d)



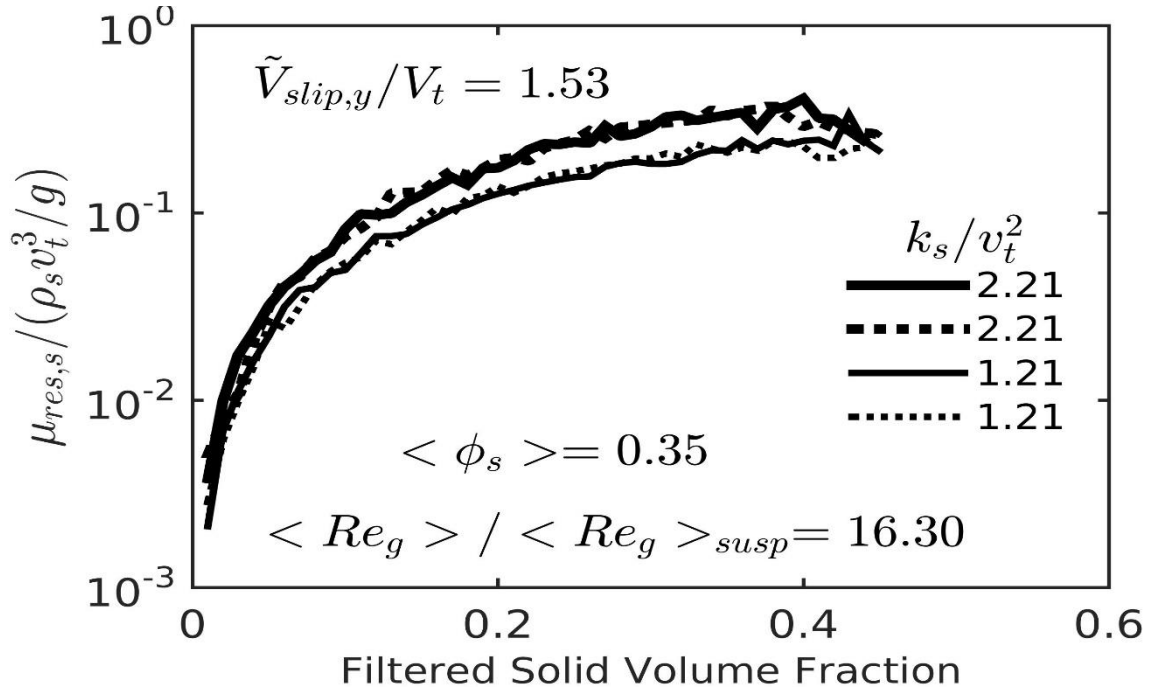
(e)



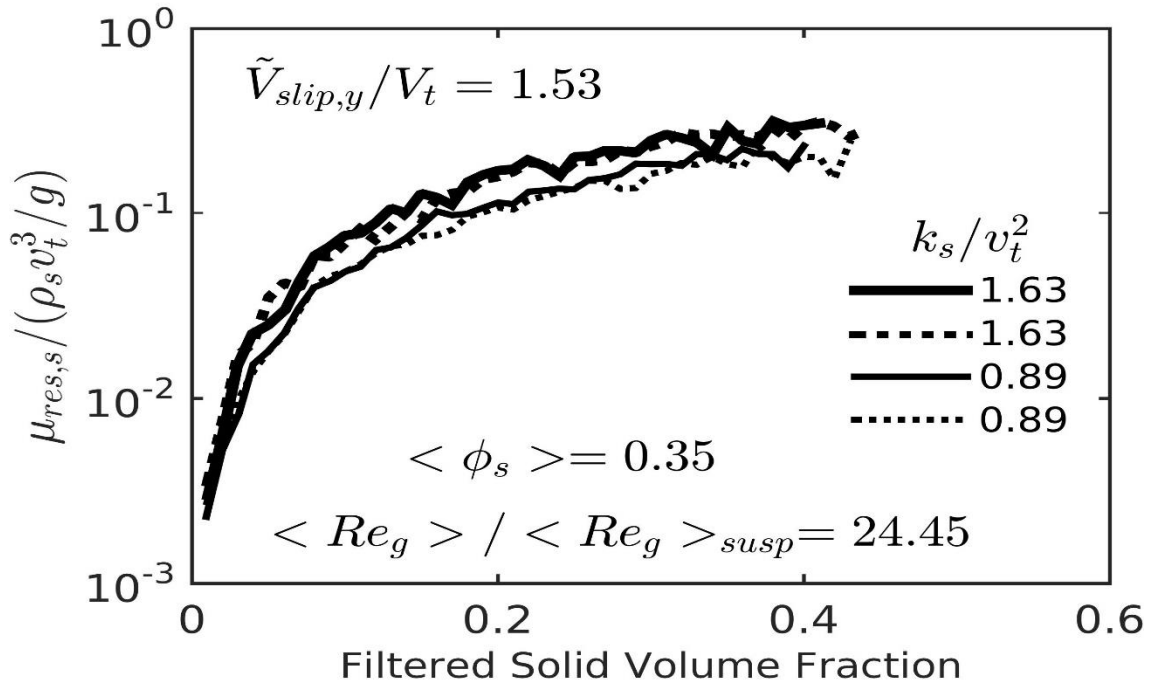
(f)

Source: Elaborated by the author

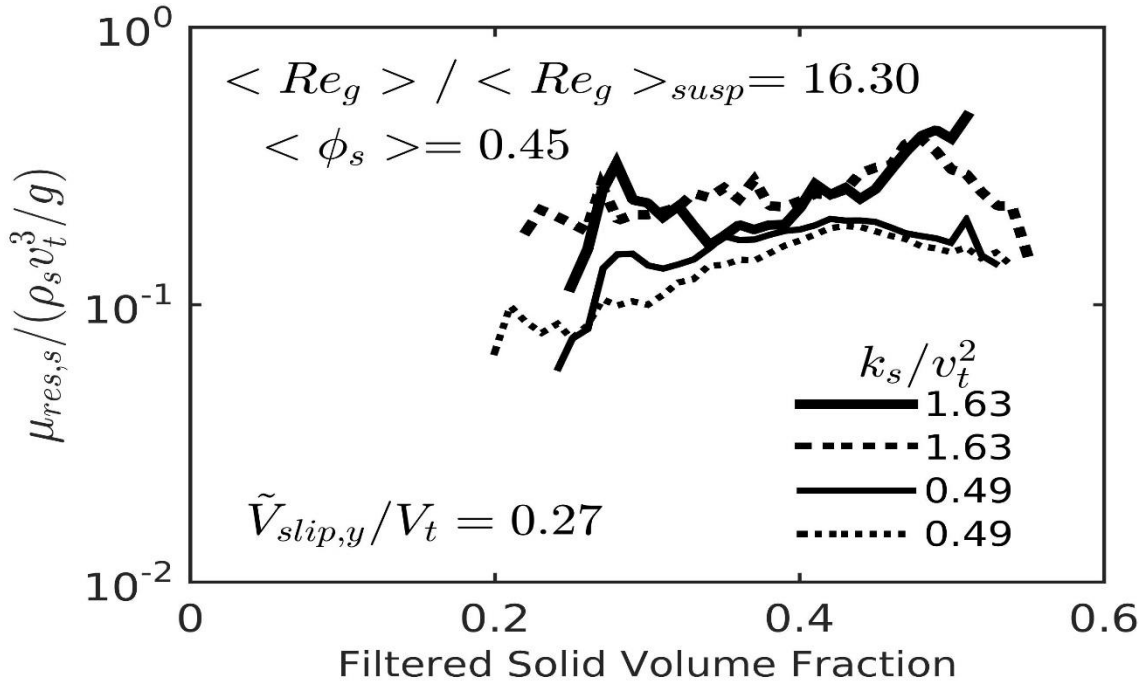
Figure 28 – Dimensionless residual solid dynamic viscosities, $\mu_{res,s}/(\rho_s v_t^3/g)$, as a function of the filtered solid volume fraction $\bar{\phi}_s$ for the domain average solid volume fractions $\langle \phi_s \rangle = 0.35, 0.45$ and 0.50 and for gas Reynolds number ratios $\langle Re_g \rangle / \langle Re_g \rangle_{susp} = 16.30$ and 24.45 . The results stand for particular dimensionless filtered axial slip velocities \tilde{v}_{slip}/V_t , for the dimensionless filter size $\Delta_f/(v_t^2/g) = 4.112$, and two different interparticle friction coefficient, $C_f = 0$ (full lines) and $C_f = 0.3$ (dash lines).



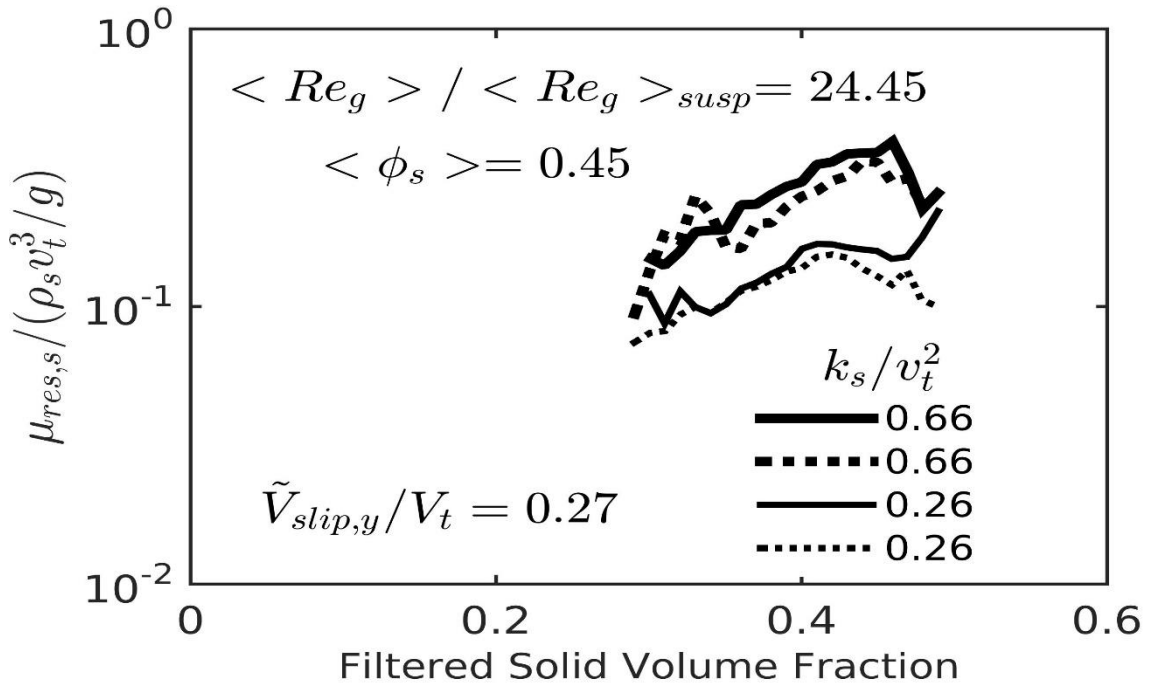
(a)



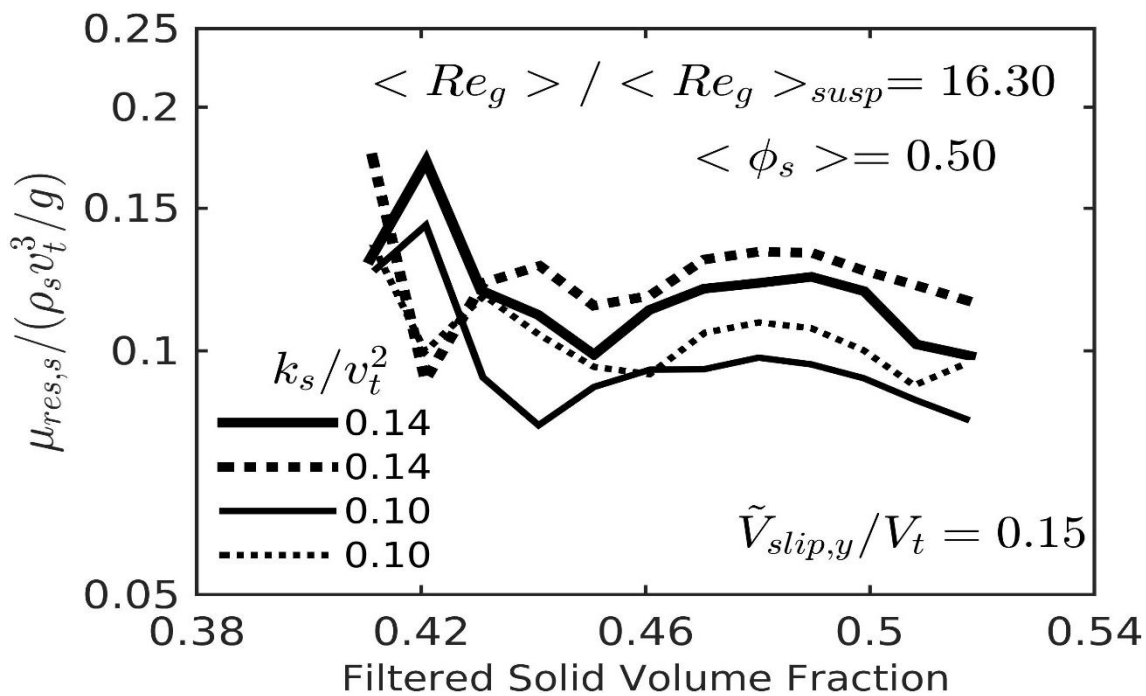
(b)



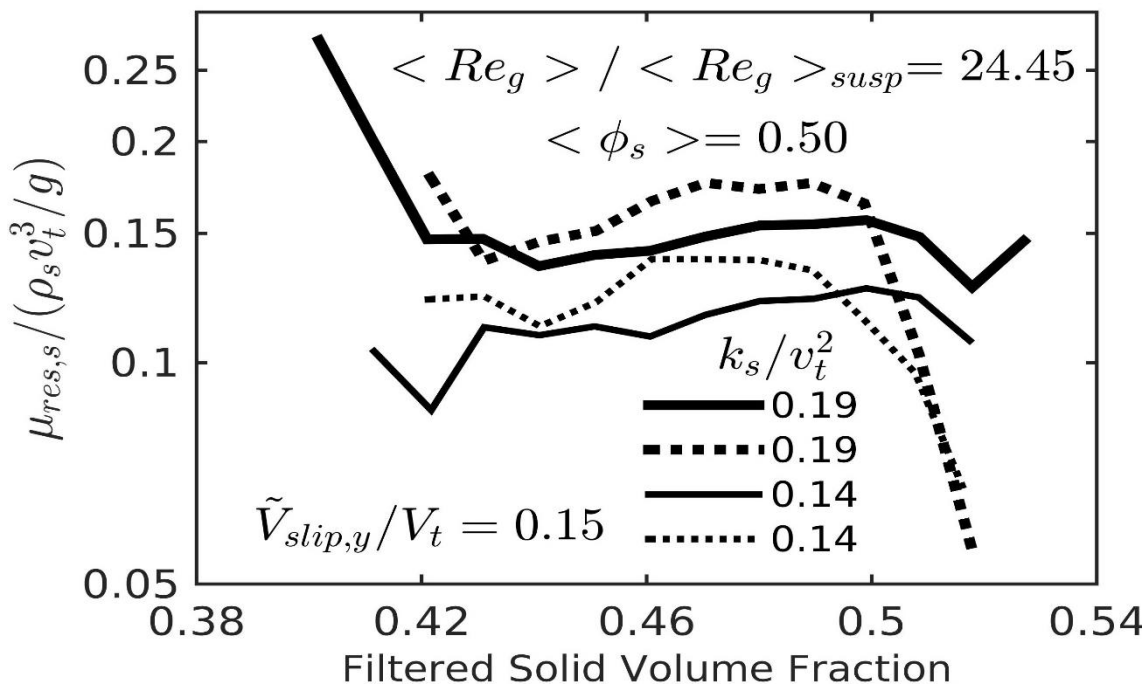
(c)



(d)



(e)



(f)

Source: Elaborated by the author